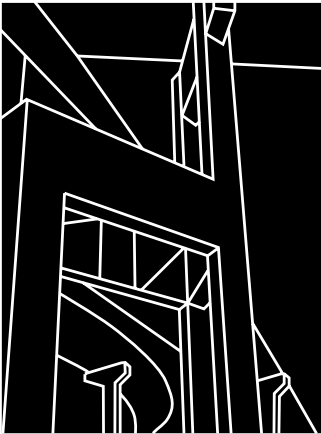


RESEARCH REPORT 580-6

TIME-DEPENDENT DEFORMATION BEHAVIOR OF
PRESTRESSED HIGH PERFORMANCE CONCRETE
BRIDGE BEAMS

K. A. Byle, Ned H. Burns, and Ramón L. Carrasquillo



CENTER FOR TRANSPORTATION RESEARCH
BUREAU OF ENGINEERING RESEARCH
THE UNIVERSITY OF TEXAS AT AUSTIN

OCTOBER 1997

1. Report No. FHWA/TX-98/580-6	2. Government Accession No.	3. Recipient's Catalog No.	
4. Title and Subtitle TIME-DEPENDENT DEFORMATION BEHAVIOR OF PRESTRESSED HIGH PERFORMANCE CONCRETE BRIDGE BEAMS		5. Report Date October 1997	
		6. Performing Organization Code	
7. Author(s) K. A. Byle, Ned H. Burns, and R. L. Carrasquillo		8. Performing Organization Report No. 580-6	
9. Performing Organization Name and Address Center for Transportation Research The University of Texas at Austin 3208 Red River, Suite 200 Austin, TX 78705-2650		10. Work Unit No. (TRAIS)	
		11. Contract or Grant No. 9-580	
12. Sponsoring Agency Name and Address Texas Department of Transportation Research and Technology Transfer Section/Construction Division P.O. Box 5080 Austin, TX 78763-5080		13. Type of Report and Period Covered Research Report (9/96 — 8/97)	
		14. Sponsoring Agency Code	
15. Supplementary Notes Project conducted in cooperation with the Federal Highway Administration.			
16. Abstract Twelve full-scale prestressed high performance concrete Texas Type U54 bridge beams with span lengths ranging from 35.55 to 41.25 meters were instrumented and monitored in the field. The instrumented U-beams were fabricated using 15.2 mm-diameter low-relaxation prestressing strands and concrete with design compressive strengths between 80.0 and 90.3 MPa. Time-dependent camber, deflection, strain at the center of gravity of the prestressing strands, and strain distributions at midspan were measured from transfer of the prestressing force until 5 months after completion of the composite deck. Internal beam temperatures at midspan were also measured during that time period, allowing for the measurement of temperature gradients over the beam depth. The measured time-dependent camber, deflection, and prestress losses at midspan were compared with results obtained using AASHTO and PCI prediction techniques. Predictions were also made using an analytical time-step method that was developed on a computer spreadsheet program. The analytical time-step method predicted the time-dependent behavior of the instrumented beams fairly accurately, while the AASHTO and PCI methods yielded inaccurate predictions. A set of camber and deflection multipliers were developed based on the analytical time-step method and the measured prestress losses and material properties for the instrumented beams. The equations for these multipliers were well suited for programming on a computer, although they could also be used for hand calculations. The sensitivity of camber prediction to the modulus of elasticity at release and the prestressing force transferred to the beams was investigated using the proposed multipliers.			
17. Key Words High performance concrete bridges, time-dependent deformation behavior, Texas Type U54 girders		18. Distribution Statement No restrictions. This document is available to the public through the National Technical Information Service, Springfield, Virginia 22161.	
19. Security Classif. (of report) Unclassified	20. Security Classif. (of this page) Unclassified	21. No. of pages 236	22. Price

**TIME-DEPENDENT DEFORMATION BEHAVIOR OF PRESTRESSED
HIGH PERFORMANCE CONCRETE BRIDGE BEAMS**

by

Kenneth Arlan Byle,

Ned H. Burns,

and

Ramón L. Carrasquillo

Research Report 580-6

Research Project 9-580

“High Performance Concrete for Bridges”

Conducted for the

TEXAS DEPARTMENT OF TRANSPORTATION

in cooperation with the

**U.S. DEPARTMENT OF TRANSPORTATION
FEDERAL HIGHWAY ADMINISTRATION**

by the

**CENTER FOR TRANSPORTATION RESEARCH
BUREAU OF ENGINEERING RESEARCH
THE UNIVERSITY OF TEXAS AT AUSTIN**

September 1998

DISCLAIMERS

The contents of this report reflect the views of the authors, who are responsible for the facts and the accuracy of the data presented herein. The contents do not necessarily reflect the official views or policies of the Federal Highway Administration (FHWA) or the Texas Department of Transportation (TxDOT). This report does not constitute a standard, specification, or regulation.

There was no invention or discovery conceived or first actually reduced to practice in the course of or under this contract, including any art, method, process, machine, manufacture, design or composition of matter, or any new and useful improvement thereof, or any variety of plant, which is or may be patentable under the patent laws of the United States of America or any foreign country.

NOT INTENDED FOR CONSTRUCTION, BIDDING, OR PERMIT PURPOSES

R. L. Carrasquillo, P.E. (Texas No. 63881)
Research Supervisor

ACKNOWLEDGMENTS

The researchers acknowledge the invaluable assistance provided by Mary Lou Ralls (DES), TxDOT project director for this study. Also appreciated is the guidance provided by the other members of the project monitoring committee, which includes J. P. Cicerello (DES), A. Cohen (DES), W. R. Cox (CMD), N. Friedman (DES), D. Harley (FHWA), G. Lankes (MAT), L. Lawrence (MAT), L. M. Wolf (DES), and T. M. Yarbrough (CSTR).

Prepared in cooperation with the Texas Department of Transportation and the U.S.
Department of Transportation, Federal Highway Administration.

TABLE OF CONTENTS

CHAPTER 1. INTRODUCTION	1
1.1 Background	1
1.1.1 Historical Overview	1
1.1.2 Developments in the Prestressed Concrete Industry	1
1.1.3 Development of High Performance Concrete	2
1.1.4 High Performance Concrete in Bridges.....	2
1.2 Deformation Behavior of Prestressed Concrete Beams	3
1.2.1 Causes of Camber and Deflection.....	3
1.2.2 Parameters Affecting Camber and Deflection.....	6
1.2.3 Prestress Losses.....	7
1.3 Research Program	8
1.4 Objectives of This Study.....	9
1.5 Organization of Report.....	9
CHAPTER 2. REVIEW OF LITERATURE	11
2.1 Introduction	11
2.2 High Strength Concrete.....	11
2.2.1 Production and Implementation of High Strength Concrete	11
2.2.2 Material Properties of High Strength Concrete.....	12
2.3 Field Instrumentation Programs	14
2.4 Previous Studies of Time-Dependent Behavior	14
2.5 Methods of Estimating Time-Dependent Behavior	15
2.5.1 Code Provisions	15
2.5.2 Analytical Methods	16
CHAPTER 3. BRIDGE DETAILS, INSTRUMENTATION, AND COMPANION TESTS	19
3.1 Introduction	19
3.2 Bridge Details.....	19
3.2.1 General	19
3.2.2 Bridge Girder Details	22
3.2.3 Composite Bridge Details and Support Conditions	24
3.2.4 Instrumented Beams.....	26
3.3 Instrumentation.....	29
3.3.1 Selection of Instrumentation	29
3.3.2 Concrete Surface Strain Measurement	31
3.3.3 Internal Strain Measurement	33
3.3.4 Internal Temperature Measurement	35
3.3.5 Long-Term Camber and Deflection Measuring System	39
3.4 Data Acquisition.....	41

3.4.1	General	41
3.4.2	Data Acquisition System	41
3.4.3	Data Reduction	42
3.5	Materials	43
3.5.1	Precast U-Beams	43
3.5.2	Precast Deck Panels	43
3.5.3	Cast-in-Place Deck Slabs	44
3.6	Companion Tests	44
3.6.1	General	44
3.6.2	Modulus of Elasticity	45
3.6.3	Compressive Strength	45
3.6.4	Creep and Shrinkage	46
3.6.5	Coefficient of Thermal Expansion	47
CHAPTER 4. FIELD WORK		49
4.1	Introduction	49
4.1.1	Coordination with Contractors	49
4.1.2	Chapter Format	49
4.2	Preparation of Instrumentation	49
4.3	Precast Operations	51
4.3.1	Precast Beams	51
4.3.2	Precast Deck Panels	57
4.4	Cast-in-Place Decks	59
4.4.1	Preparation	59
4.4.2	Instrumentation	60
4.4.3	Casting	61
4.5	Problems Encountered in the Field	62
4.5.1	Difficulties with Instrumentation Placement	62
4.5.2	Damaged Instrumentation	63
4.5.3	Measurements	64
CHAPTER 5. OBSERVED BEHAVIOR		67
5.1	Introduction	67
5.2	Companion Test Results	67
5.2.1	Concrete Compressive Strength	67
5.2.2	Elastic Modulus of Concrete	70
5.2.3	Creep and Shrinkage Properties of Concrete	72
5.3	Field Measurements	76
5.3.1	Camber and Deflection	76
5.3.2	Surface Strain at the Center of Gravity of the Prestressing Strands	86
5.3.3	Internally Measured Strain at the Center of Gravity of the Prestressing Strands	88
5.3.4	Measured Strain Profiles at Midspan	95

5.3.5 Temperature Gradients	101
5.3.6 Thermally Induced Camber and Deflection	107
5.4 Comparison of Measured Behavior.....	110
5.4.1 Camber and Deflection.....	110
5.4.2 Prestressing Strand Strain.....	124
5.4.3 Midspan Strain Profiles at Release.....	134
CHAPTER 6. ANALYTICAL METHODS FOR PREDICTING TIME-DEPENDENT BEHAVIOR.....	139
6.1 Introduction	139
6.2 AASHTO.....	139
6.3 PCI Design Handbook: Prestress Losses, Camber, and Deflection	151
6.3.1 Prestress Losses.....	151
6.3.2 Camber and Deflection.....	159
6.4 Analytical Time-Step Method.....	172
6.4.1 General	172
6.4.2 Prestress Losses.....	172
6.4.3 Camber and Deflection.....	182
6.5 Proposed Multipliers for Estimating Time-Dependent Camber and Deflection.....	195
6.5.1 Development of Proposed Multipliers	195
6.5.2 Prediction of Camber and Deflection using Proposed Multipliers	199
CHAPTER 7. SUMMARY, CONCLUSIONS, AND RECOMMENDATIONS.....	211
7.1 Summary	211
7.2 Conclusions	211
7.3 Recommendations	214
REFERENCES.....	215
APPENDIX A: DEBONDING DETAILS.....	221

CHAPTER 1. INTRODUCTION

1.1 BACKGROUND

1.1.1 Historical Overview

Most of the bridges that are currently part of the United States infrastructure were constructed following the passage of the Federal Aid Highway Act in 1956 (1). Today, many of these bridges do not meet current federal and state design standards for geometry, strength, or average daily vehicular traffic. This can be attributed to the excessive demand placed on the infrastructure over the 20- to 30-year period following construction. During that time period, the use of the infrastructure system rapidly increased as tourism, the interstate trade of goods by truck, and the mobilization of people across the nation grew to be economic forces. Yesterday's bridges were not designed for the size, weight, and volume of today's car and truck traffic. Consequently, a large percentage of these bridge structures are in need of substantial improvement or complete replacement.

It was also shortly after 1956 that the prestressed concrete industry began to flourish. A construction project as large as the interstate system demanded cost-effective structural systems. The development of standardized beam sections, most notably the I-shaped section, made prestressed concrete an efficient alternative for bridge superstructures. However, the strength and durability properties of the concrete used in those bridges are inferior to those of the high strength concrete being developed and implemented today.

1.1.2 Developments in the Prestressed Concrete Industry

Recent developments in the prestressing industry can be utilized to provide economical design solutions to satisfy the increasing demand for bridge replacement. One such development is the use of 15.2 mm-diameter low-relaxation prestressing strand in place of the more common 12.7 mm-diameter strand. The 15.2 mm-diameter strand has 40 percent more area than the 12.7 mm-diameter strand. When it is used in the standard 50 mm by 50 mm grid spacing, the larger strand has the potential for providing 40 percent more prestressing force.

In order to efficiently utilize the larger force that can be developed with the 15.2 mm-diameter strands, concrete with higher compressive strength needed to be developed. The typical compressive strength of concrete used for prestressed beams in the 1950's was between 27.6 and 34.5 MPa. Peterman and Carrasquillo (2) were able to produce high quality concrete with compressive strengths in the 62.1 MPa to 82.7 MPa range at 56 days using conventional batching procedures and materials that were readily available in the state of Texas. To utilize the benefits afforded by high strength concrete, the ability to produce it in the field on a consistent basis is needed. Additionally, it is important to be able to produce high strength concrete using materials that are readily available in the region of the project. The use of high strength concrete along with the 15.2 mm-diameter strands can result in

longer spans, fewer beams per span, more efficient cross-sections, and fewer substructure units. As a direct result, construction costs can be reduced significantly.

In addition to the development of larger diameter prestressing strands and higher strength concrete, the development of more efficient beam cross-sections has helped increase the cost effectiveness of prestressed concrete bridge structures. The Texas U40 and U54 beam sections were developed to provide more structural efficiency than that of the standard Texas Type C and AASHTO Type IV, respectively (1). The results of a parametric study by Russell (3) showed that the use of high strength concrete and 15.2 mm-diameter strands with the Texas Type U54B section would result in wider beam spacing and longer spans than with the AASHTO Type IV section. The Texas Type U54A and U54B sections were utilized for the bridge in this study.

1.1.3 Development of High Performance Concrete

High *performance* concrete, as opposed to high *strength* concrete, refers to concrete that satisfies any number of significant long-term performance requirements rather than compressive strength alone. High performance concrete (HPC) differs from normal concrete in that it is engineered to meet specific strength and durability requirements, depending on the particular application. A working definition of high performance concrete (HPC) based on long-term performance criteria has been developed by Goodspeed et al. (4) under direction of the Federal Highway Administration (FHWA). The objective of this definition was to assist in the implementation of HPC in highways and bridge structures by making specification of HPC more straightforward for engineers.

The proposed HPC definition was based on four strength and four durability parameters. The strength parameters were compressive strength, elastic modulus, shrinkage, and creep. The durability parameters were freeze-thaw, scaling resistance, abrasion resistance, and chloride penetration. For each of these parameters, performance grades from one to four were defined based on a relationship between severity of the field condition and recommended performance level. In addition, standard testing methods were defined to measure performance for each parameter (4). The development of the HPC definition allows engineers to specify concrete strength and durability requirements based on the structural application (beam, deck, or substructure) and environmental conditions of the project site. Quality assurance and quality control are vital to the implementation and success of high performance concrete.

1.1.4 High Performance Concrete in Bridges

High performance concrete used in bridge structures can provide an increase in long-term durability coupled with several economic benefits. The use of HPC for bridge beams and decks can result in initial benefits, such as fewer spans, beams, and substructures, as well as long-term benefits, such as reduced maintenance, longer service life, and lower life-cycle costs.

Widespread use of HPC in bridge structures requires the monitoring of several bridges in the field to develop a data base of knowledge on the long-term performance of

bridge beams and decks. Currently there is very little information for the engineer or contractor to turn to for guidance in predicting the behavior of structural members constructed with high performance concrete.

During the design and construction of a bridge, the engineer and contractor must estimate the long-term deflection behavior of the prestressed concrete beams. Because of the uncertainty in determining properties of concrete, the prediction of camber at the beginning of service life for a composite bridge deck is very difficult. Factors such as creep, shrinkage, the elastic modulus of the concrete, and relaxation of the prestressing strands continually change with time. This makes an accurate estimation of long-term behavior difficult to accomplish. The use of HPC in bridge beams and decks can only increase this difficulty. As more information is gathered, better estimates of long-term behavior can be made for bridge structures constructed using HPC; at the same time, engineers and contractors may become more comfortable using this new technology for bridges.

1.2 DEFORMATION BEHAVIOR OF PRESTRESSED CONCRETE BEAMS

For composite prestressed concrete beam bridges with span lengths exceeding 40 meters, the serviceability limit state becomes very important. In many cases it becomes the controlling limit state, rather than the allowable stress or ultimate strength limit states that usually control designs. The accurate prediction of camber and deflection behavior of prestressed concrete beams becomes essential when considering the serviceability limit state. Camber differentials between adjacent beams upon erection cause the contractor to add more concrete to the cast-in-place slab to level it out while maintaining minimum thickness requirements at the same time. The additional concrete needed to level out the deck slab produces an increase in the deflection of the beams. If the beams have too much camber or deflection, the driving surface will be rough and unpleasant for motorists using the bridge. Also, a downward deflection creates an aesthetically displeasing bridge for the public. The accurate prediction of long-term camber and deflection can reduce or eliminate these problems and ease the construction of the bridge.

1.2.1 Causes of Camber and Deflection

Long-term camber and deflection in prestressed concrete beams are caused by a combination of sustained loads, transient loads, and time-dependent material properties that affect sustained loads. Precise prediction of long-term camber is extremely difficult because the net camber is usually the small difference between several large components of camber and deflection.

At transfer of the prestressing force, the downward deflection caused by the beam self-weight (Δ_{beam}) is opposed by a larger upward deflection caused by the prestressing force (Δ_{ps}), whose line of action is a distance 'e' below the center of gravity of the beam cross-section. These components of camber and deflection are given in Eqs. 1.1 and 1.2.

$$\Delta_{\text{beam}} = \frac{5wL_s^4}{384E_c I} \quad (1.1)$$

$$\Delta_{ps} = \frac{PeL_s^2}{8E_c I} \quad (1.2)$$

A net upward deflection (camber) is induced in the beam immediately after transfer due to elastic action only. The magnitude of the initial camber is the difference between the upward component due to prestressing and the downward component due to the beam weight ($\Delta_{ps} - \Delta_{beam}$). The magnitude of this camber can be rather small for long spans, even though each individual component is quite large.

Figure 1.1 illustrates the components of initial camber at release for the beams in this study. The strands in these beams were debonded at the ends. The debonded strands reduce the eccentricity and prestressing force at the ends of the beam. The effect that the debonded strands have on Δ_{ps} is minimal. Therefore, the equation for initial camber due to the prestressing force has been simplified in Figure 1.1 to exclude the effects of debonding. Each component of camber and deflection increases with time, due to the effects of creep. The beam camber will continue to increase up to the time of additional loading. Figure 1.2 shows how each component increases with time.

After the beams are erected in the bridge, additional sustained loads are applied which cause immediate elastic deflection in the beams. These sustained loads include precast deck panels, cast-in-place slabs, guardrails, and surface overlays. The first two sources are usually resisted by the beam alone, while the last two sources are resisted by the composite deck section. The deflections caused by each sustained load increase with time due to the effects of the time-dependent material properties. However, the increase is usually small because the beam concrete is quite mature by that time and some of the additional load is resisted by a stiffer composite section. The composite section will also slow down the growth of the initial camber and deflection components that occur just after release. Figure 1.2 shows how the beam deflection is affected by superimposed loads.

Other sources of deflection can be classified as transient in nature because the loads are applied to the beams for only a short period of time. Temperature gradients in the composite bridge section can induce daily fluctuations in camber. If the top portion of the section is heated more than the bottom portion, the top tends to expand more, which induces additional camber in the beam. Maximum thermally induced camber occurs on sunny days during the afternoon when solar radiation is the most intense. The effects of thermal gradients are removed at night when the temperature of the cross-section becomes uniform. Another temporary source of deflection is due to live loads caused by vehicular traffic on the bridge during its service life. These types of loads are not considered in determining the net long-term camber in the bridge. However, temporary camber induced by thermal gradients can have an impact on the roughness of the riding surface.

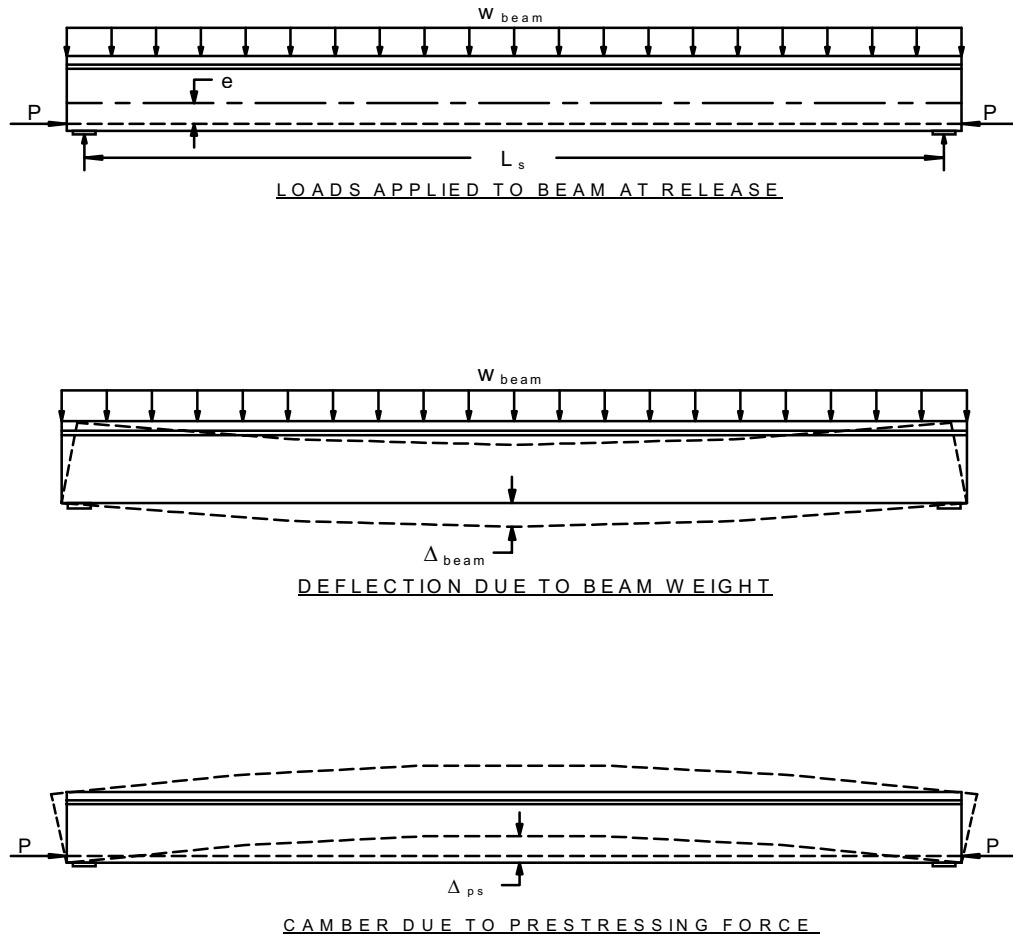


Figure 1.1 Elastic components of beam camber and deflection immediately after release

A final source of deflection that cannot be classified as a sustained dead load or as a transient load is shrinkage of the cast-in-place slab. As the slab concrete becomes composite with the deck panels and beams, it begins to lose moisture and shrink. The mature beam concrete resists the shrinkage of the slab, causing tension to develop in the bottom fiber of the cross-section. This action results in a time-dependent deflection component. This type of response is very difficult to estimate and is generally ignored during prediction of long-term camber.

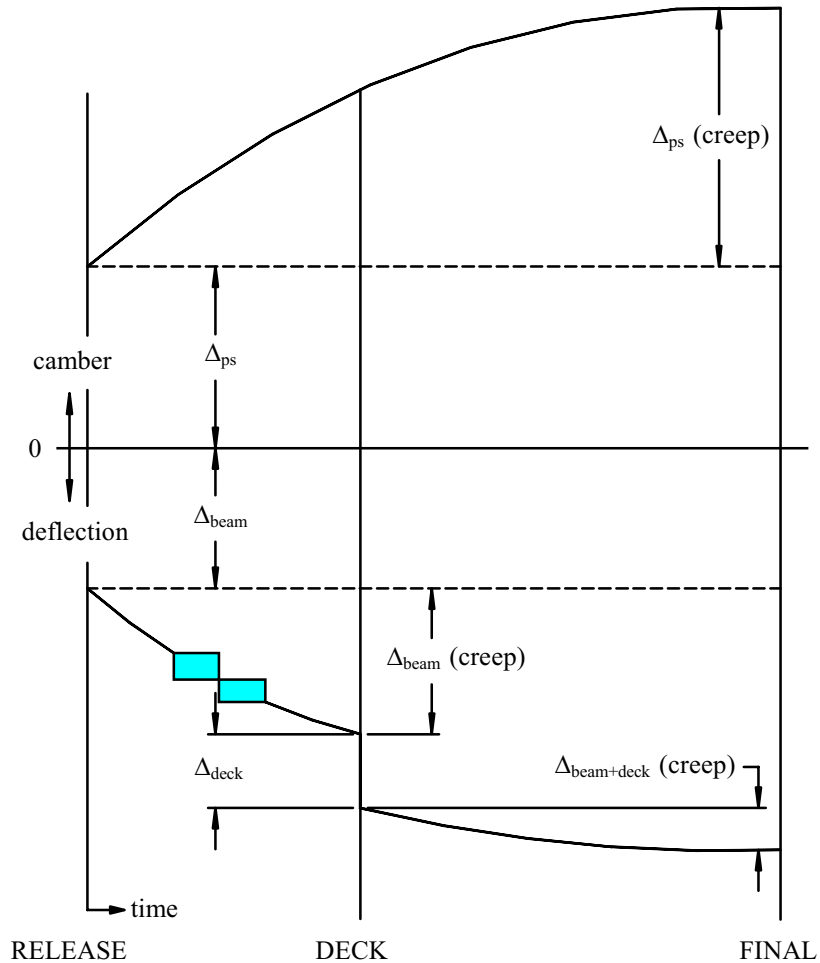


Figure 1.2 Components of time-dependent camber and deflection

1.2.2 Parameters Affecting Camber and Deflection

There are several geometric and material properties that affect the magnitudes of the various sources of camber and deflection discussed in Sec. 1.2.1. These properties make accurate prediction of long-term camber in prestressed beams extremely difficult.

Careful examination of Eqs. 1.1 and 1.2 indicates that the magnitude of camber owing to the prestressing force and the magnitude of deflection owing to the beam weight (and other superimposed dead loads) are inversely proportional to the elastic modulus of the concrete (E_c). Because concrete is not a homogeneous material, variations can exist between the measured and actual elastic modulus in a beam. In addition, the elastic modulus is a time-dependent property of concrete, making camber and deflection predictions difficult. Another

material parameter, namely the unit weight of the concrete, directly affects the deflection components due to the beam and other superimposed distributed loads. This property can be estimated with relatively high accuracy.

Creep of concrete affects the time-dependent growth of camber and deflection due to sustained loads, as shown in Figure 1.2. Creep, shrinkage, and relaxation of the prestressing strands interact with each other to affect the prestressing force over time. This is discussed further in Sec. 1.2.3.

Several geometric parameters shown in the equations in Figure 1.1 can have a significant effect on camber and deflection. The moment of inertia of the cross-section (I) is inversely proportional to the camber and deflection components. The combination of the elastic modulus (E_c) and the moment of inertia (I) represents the stiffness of the beam in the elastic range. A more significant parameter that affects camber and deflection is the span length (L_s). Camber due to the prestressing force is proportional to the square of the span length. Deflections due to the beam, panel, and slab uniform loads are proportional to the fourth power of the span length. For long spans, the camber and deflection components can become extremely sensitive to small variations in the span length.

1.2.3 Prestress Losses

Prestress losses reduce the total prestressing force applied to the beam over time, resulting in a reduction of the beam camber over time. Several different sources of prestress loss occurring at different times contribute to the long-term prestress loss in a beam.

The initial loss of prestress is due to elastic shortening when transfer occurs. Since the strands are bonded to the beam during transfer, they will shorten with the beam as the force is applied to the beam cross-section.

Thermal losses may occur prior to release if the temperature of the strands is lower at the time of stressing than at the time of casting. During that time period, heating of the free strand results in a loss of stress because the strand tends to lengthen as it increases in temperature. A portion of strand relaxation, which is a loss of stress due to a constant strain applied to the strand, also occurs prior to transfer.

It is the time-dependent properties of the steel and the concrete that make the loss of prestress over time a complex issue. Creep of the concrete is the increase in deformation, or compressive strain, caused by the presence of an applied stress. Shrinkage of the concrete is a volume change in the concrete that occurs as moisture leaves the beam, resulting in a compressive strain. Additional relaxation of the strand occurs over a long period of time. All of these factors affect the loss of prestress over time. A complex interaction exists between creep, shrinkage, and steel relaxation as they pertain to prestress loss. A reduction in the steel stress due to relaxation causes less creep loss to occur, which in turn causes less steel relaxation to occur. Furthermore, the existing environmental conditions greatly affect the time-dependent creep and shrinkage properties of concrete. Prestress losses are also reduced when superimposed loads are placed on the beam or composite section. Because of their complexity, long-term prestress losses can only be estimated, and the amount of loss attributed to each source is impossible to determine with precision.

1.3 RESEARCH PROGRAM

The primary objective of this research program was to develop guidelines for the design and construction of highway bridge structures that utilize high performance concrete. These guidelines were developed by monitoring the entire construction process for an actual bridge project. Furthermore, this study documented several benefits that could be realized through the use of high performance concrete. The site that has been chosen for the implementation of this research was the Louetta Road Overpass on State of Texas Highway 249 in Houston, Texas.

Initial research for this study by Cetin and Carrasquillo (5) consisted of the development of several high performance concrete mixes to be used in the design of the proposed structure. The tested compressive strengths for specimens made with these high performance concrete mixes were between 55.2 MPa and 82.7 MPa. Once the structural design of the bridge girders was completed, Barrios et al. (6) tested full scale prototypes of the Texas Type U54 beam to determine the adequacy of end zone structural details during transfer of the prestressing force. The specimens in that study were pretensioned with 15.2 mm-diameter strands arranged on a grid with 50 mm spacing. The transfer length for these strands in the high performance concrete was determined by measurement of the concrete surface strain.

Carlton and Carrasquillo (7) assessed the adequacy of current quality control procedures for predicting in-situ strength of structural members cast with high performance concrete. The effects of different curing conditions and testing methods on high performance concrete cylinders were examined. In addition, the temperature development and in-situ strength of the Texas Type U54 beams, which were cast with high performance concrete, were monitored and compared to standard quality control procedures. Match-cured cylinders, which were cured based on the internal temperatures at various locations in the beams, were used to determine the in-situ strength of the beams. Strength results for the match-cured cylinders were compared with strength results for moist-cured cylinders and cylinders that were cured next to beams on the casting bed.

Farrington et al. (8) reported on the creep and shrinkage properties of the high performance concrete mix used for the pretensioned bridge girders. Creep specimens were cured at two different temperatures and tested under applied loads of 6.9, 20.7, and 34.5 MPa at the ages of 1, 2, and 28 days. Shrinkage specimens that were kept in the same environment as the creep specimens were monitored to determine the shrinkage portion of the measured concrete surface strains for the creep specimens. Data from that study were reported for up to 120 days after casting. Further creep and shrinkage data for the high performance concrete used in the beams, deck panels, and cast-in-place decks were gathered throughout the remainder of the research program.

Also continuing throughout this study was the establishment and implementation of a quality control and quality assurance program for concrete production and construction practices using high performance concrete. The study included the monitoring of short-term and long-term structural performance of the pretensioned high performance concrete bridge girders and the cast-in-place decks. Additional work included preliminary testing for the

establishment of the necessary design and material requirements for the construction of bridges utilizing concrete with compressive strengths in the 103.4 to 117.2 MPa range. Finally, recommendations and guidelines pertaining to the design and construction of high performance concrete bridges would be developed.

1.4 OBJECTIVES OF THIS STUDY

The objective of this portion of the research program was to monitor the long-term deformation behavior of pretensioned high performance concrete bridge girders. This study focused on the field instrumentation of twelve high performance concrete Texas Type U54 beams pretensioned with 15.2 mm-diameter low-relaxation strands. Beam cambers and deflections, concrete strains, and concrete temperatures were monitored from transfer of prestressing force through placement of the precast concrete deck panels and cast-in-place concrete deck on the girders in the bridge. The measured cambers and prestress losses were compared to predicted values obtained using current design and analysis procedures. This study presents preliminary design considerations for estimating the long-term behavior of pretensioned high performance concrete girders.

1.5 ORGANIZATION OF REPORT

Chapter 2 reviews previous experimental studies in high strength concrete production, implementation, and properties. Reviews of previous studies on time-dependent behavior of prestressed concrete beams and several analytical methods for estimating time-dependent behavior are also given in Chapter 2. Chapter 3 presents the bridge beam and composite section details, the details of the field instrumentation plan, and the laboratory tests performed on the companion cylinders for the bridge girders. Chapter 4 describes the field operations, including placement of instrumentation, fabrication and casting of the girders, and a summary of the problems encountered in the field. The results from the laboratory tests and the measured time-dependent camber and strain in the bridge girders are presented in Chapter 5. The results of several analytical techniques for estimating time-dependent camber and prestress losses for the beams in this study are given in Chapter 6. Comparison between the observed and predicted behavior and the development of multipliers for estimating beam camber are also presented in Chapter 6. The conclusions for this study are given in Chapter 7, which includes recommendations for estimating the long-term behavior of the pretensioned high performance concrete U-beams in this study.

CHAPTER 2. REVIEW OF LITERATURE

2.1 INTRODUCTION

This chapter reviews some of the most recent research in the areas of high strength concrete production, implementation, and time-dependent material properties, such as modulus of elasticity, creep, and shrinkage. A review of research conducted on the measurement of long-term camber, deflection, and prestress losses for prestressed concrete beams fabricated with both normal and high strength concrete is also presented. In addition, some recent studies on field instrumentation of precast concrete members are reviewed. Finally, a review of the current code provisions used in design and several methods of analysis developed for estimating long-term camber, deflection, and prestress losses is presented. The previous research reviewed in this chapter is not exhaustive but gives sufficient background for the work presented in this study.

2.2 HIGH STRENGTH CONCRETE

For this research study, the high compressive strength of the beam concrete was the main performance characteristic considered in the mix design. Because of this, the review of previous research was focused on high *strength* concrete production and properties, rather than exclusively on high *performance* concrete.

2.2.1 Production and Implementation of High Strength Concrete

The ability to commercially produce high strength concrete under plant conditions has been the first step toward the implementation of high strength concrete in bridge structures. Peterman and Carrasquillo (2) were able to produce high quality concrete with compressive strengths in the 62.1 MPa to 82.7 MPa range at 56 days using conventional batching procedures and materials that were readily available in Texas. Only commercially available cements, aggregates and admixtures, and conventional production techniques were used in the study. The concrete mixes had low water-to-cement ratios, which were necessary for attaining high strengths. High-range water reducers were utilized to keep these concrete mixes workable. The results of this report indicated that to achieve consistent production of high strength concrete, a set of guidelines for materials selection and mix proportioning needed to be developed and utilized by engineers. It was concluded that high strength concrete could be produced in other parts of the country, although materials and mix design guidelines would vary among regions.

Durning and Rear (9) reported on the successful implementation of high strength concrete in the design and construction of the Braker Lane Bridge in Austin, Texas. The bridge consisted of two spans, each having eleven 1016-mm deep Texas Type C girders with span lengths of 26 meters. The required design strength for these beams was 66.2 MPa. The design parameters for this bridge were based on the research work of Castrodale et al. (10,

11), which showed that longer span lengths and fewer beams per span (larger beam spacing) could be achieved by using high strength concrete with typical precast beam sections. The high strength concrete mix was based on the results of research work done by Carrasquillo and Carrasquillo (12). In that study, methods for producing high strength concrete in the field were examined and trial mix designs were developed to attain a release strength of 51.0 MPa and a 28-day strength of 66.2 MPa. These mix designs utilized Type III cement, Type C fly ash, microsilica, and high-range water reducers. The actual mix designs that were developed and tested had 28-day strengths that averaged 92 MPa.

2.2.2 Material Properties of High Strength Concrete

Some of the material properties of high strength concrete, such as the modulus of elasticity, early-age strength gain, creep, and shrinkage, are notably different from that of normal strength concrete. Since many equations used for determining the time-dependent properties of concrete are empirically derived from tests on concrete with strength at or below approximately 41 MPa, further data on high strength concrete is needed to revise these equations (13). Knowledge of the basic properties of high strength concrete is needed to make better estimates of the long-term behavior of prestressed beams cast with high strength concrete.

2.2.2.1 Elastic Modulus of Concrete

The elastic modulus of concrete is dependent upon several factors, such as the compressive strength of the concrete, age of the concrete, and the properties of the aggregate and cement in the concrete mixture. The definition of elastic modulus, whether tangential or secant modulus, also affects the determination of elastic modulus. For design and analysis in prestressed and reinforced concrete, the initial slope of the approximately straight, or elastic, portion of the stress-strain curve is used as the modulus of elasticity of the concrete. This is also known as the secant modulus (14).

Several studies have been conducted to investigate the modulus of elasticity of high strength concrete. The ACI Committee 363 report on high strength concrete (13) summarizes the results of some of these studies and offers a recommendation for the prediction of modulus of elasticity for high strength concrete. The recommended prediction for modulus of elasticity is based on the work of Carrasquillo, Nilson, and Slate (15). They found that for concretes with compressive strengths greater than 41 MPa, the ACI 318-77 and AASHTO expression for modulus of elasticity, shown in Eq. 2.1, tended to overestimate the measured values for modulus of elasticity. (Eq. 2.1 is also used in the latest editions of the AASHTO Specifications [16] and ACI 318 Code [17].) They also found that the modulus of elasticity measurements were quite dependent on the type of aggregate used in the concrete. The recommended expression for modulus of elasticity for concrete with compressive strengths greater than 41 MPa is shown in Eq. 2.2. This equation was based on test data obtained from gravel and crushed limestone concrete specimens and on a dry unit weight of 2320 kg/m³.

$$E_c = 4730\sqrt{f'_c} \quad (\text{MPa}) \quad (2.1)$$

$$E_c = 3320\sqrt{f'_c} + 6900 \quad (\text{MPa}) \quad (2.2)$$

$$\text{for } 21 \text{ MPa} \leq f'_c \leq 83 \text{ MPa}$$

2.2.2.2 Creep and Shrinkage

Creep of concrete is defined as the time-dependent strain in the concrete resulting from an applied constant stress. Shrinkage of concrete is defined as the contraction of concrete due to the loss of water and due to chemical changes, both of which are dependent upon time and moisture conditions. Both creep and shrinkage create additional compressive strain in a prestressed concrete beam. The additional compressive strain causes a loss in the initial prestress force. The creep of concrete causes time-dependent changes in the camber and deflection of prestressed concrete beams (14,18). In order to estimate the long-term behavior of prestressed concrete beams cast with high strength concrete, knowledge of the creep and shrinkage properties of high strength concrete must be acquired.

Several studies have been conducted to determine the creep and shrinkage properties of concrete. The ACI Committee 209 report (19) summarizes the findings of many of these studies and recommends methods for calculating time-dependent creep and shrinkage. However, the recommendations of the ACI 209 report were based primarily on data for normal strength concrete. That report also contains an extensive list of references on creep and shrinkage of concrete.

Ngab, Nilson, and Slate (20) found that the creep coefficient in high strength concrete was approximately 50 to 75 percent of that of normal strength concrete. The shrinkage of high strength concrete was found to be greater than that of normal strength concrete, though not considerably greater. These results were based on drying conditions, meaning that the creep specimens were allowed to dry while under sustained load.

Farrington et al. (8) studied the creep and shrinkage properties of the high performance concrete mix used for the fabrication of the Texas Type U54 beams monitored in this study. They examined the effects of curing temperature, applied stress level, and loading age on creep and shrinkage. They found that the ultimate shrinkage strain was approximately 55 percent lower and the ultimate creep coefficient was approximately 60 percent lower than that of the predicted values made using the ACI Committee 209 procedures. They also found that a higher curing temperature had little effect on the creep coefficient but increased the ultimate shrinkage strain. In addition, the specimens loaded at later ages showed less creep. These results were based on 120 days of data.

Farrington et al. also provided a thorough review of the ACI Committee 209 procedures for estimating time-dependent creep and shrinkage of concrete. In addition, the reports by the ACI Committee 517 (21) and Hanson (22) on the effects of curing temperature on creep and shrinkage and the report by Swamy and Anand (23) on the effects of age at loading on creep were reviewed.

2.3 FIELD INSTRUMENTATION PROGRAMS

There are a limited number of studies that report on guidelines for implementing a field instrumentation program for monitoring the long-term behavior of a full-scale bridge. The reports by Arellaga (24) and Russell (25) are presented as background for the instrumentation plan that was implemented to monitor the time-dependent behavior of the Louetta Road Overpass.

Arellaga (24) reported on a number of instrumentation systems that could be used in a field instrumentation program. An extensive review of many types of instrumentation was conducted, and field and laboratory testing was performed to determine an ideal instrumentation system for monitoring the behavior of post-tensioned segmental box girder bridges. Recommendations were made for the instrumentation to be used to monitor three spans of the San Antonio Y segmental box girder bridge project.

The types of instrumentation that were reviewed and tested included embedded strain measuring devices, surface strain measuring devices, temperature measuring devices, and deflection measuring systems. Automated data acquisition system components were also reviewed. This report provides a sizable amount of information on the various types of instrumentation that can be used for monitoring long-term behavior in precast, post-tensioned (or prestressed) concrete bridge structures. Several of the instrumentation devices and data acquisition system components that were reviewed in the study by Arellaga were implemented in the Louetta Road Overpass instrumentation plan.

Russell (25) developed a set of guidelines for the instrumentation of bridges. The guidelines were developed in conjunction with the Federal Highway Administration's (FHWA) implementation program on high performance concrete.

Russell (25) gives recommendations for the types of measurements to be obtained in the field instrumentation of a bridge, such as internal temperatures, short and long-term strains at the centroid of the prestressing force, surface strains, deflections, and prestressing forces. The types of instrumentation that should be used to measure the above mentioned quantities are included in the guidelines. In addition, an automated data acquisition system is recommended for the gathering of data from the instrumentation. This makes interpretation and reduction of the data easier. Finally, a basic instrumentation program is suggested with the option of additions to the basic program.

The recommendations outlined by Russell for the types of measurements to obtain and the corresponding measuring devices to use were considered during the instrumentation of the Louetta Road Overpass.

2.4 PREVIOUS STUDIES OF TIME-DEPENDENT BEHAVIOR

There have been a limited number of field studies conducted to monitor the time-dependent behavior of prestressed concrete beams that were part of a full-scale highway bridge. In addition, there have been even fewer field or laboratory studies that included the use of high strength concrete in the production of the monitored prestressed concrete bridge girders.

Kelly, Bradberry, and Breen (26) reported on the field instrumentation and monitoring of eight 38.7-m long AASHTO Type IV bridge beams with low relaxation strands and design compressive strengths of 45.5 MPa. The measured average 28-day compressive strengths were 59.4 MPa, classifying the beam concrete as high strength. The strands in the beams were draped at the ends rather than debonded.

Long-term deformations were monitored from casting through one year into service life for the completed bridge. Camber and deflection at midspan and the quarter points, surface strain and prestressing strand strain at midspan, and internal temperature gradients were measured during that period.

The measured time-dependent camber and deflection responses of the eight beams were compared to results obtained from the PCI design handbook (27) multipliers for estimating long-term camber and deflection, which were developed from the work by Martin (28). They were also compared to predictions made with the computer program PBEAM, which was developed by Suttikan (29).

A modified PCI multiplier method was developed by Kelly et al. (26) to accurately predict the long-term camber and deflection of the beams in that study. The proposed multipliers were used to conduct a sensitivity analysis for camber and deflection by varying the material properties and the construction schedule to determine maximum variations in expected camber or deflection at the end of service life.

The results of this sensitivity analysis for the instrumented beams showed that the maximum cambers could range between 50 and 150 millimeters, and the service life camber could range between -20 and 50 millimeters. They found that for the typical construction schedule, beams fabricated with high strength concrete showed the smallest camber at erection, the smallest time-dependent increase in camber, and the greatest camber during service life.

Kelly et al. (26) reviewed several laboratory and field investigations of time-dependent behavior of pretensioned concrete beams, including the works of Rao and Dilger (30), Corley et al. (31), Sinno and Furr (32, 33), Branson, Meyers, and Kripanarayanan (34), and Gamble et al. (35, 36, 37). These investigations were limited to normal strength concrete and typical span lengths.

2.5 METHODS OF ESTIMATING TIME-DEPENDENT BEHAVIOR

2.5.1 Code Provisions

The AASHTO Standard Specification for Highway Bridges (16) is the primary set of guidelines for designing prestressed concrete bridge beams. The ACI Code (17) also treats the design of prestressed concrete members, although those specifications were developed primarily for prestressed structural members used in building applications. Thus, the ACI Code will not be considered in this review of code provisions.

The AASHTO Specification does not provide a method for estimating the short and long-term deflections of prestressed concrete beams. Section 9.11.1 of the AASHTO Specification states, “Deflection calculations shall consider dead load, live load, prestressing, erection loads, concrete creep and shrinkage, and steel relaxation.” However, there are no

guidelines given for limits on long-term camber or deflection of the bridge. A table of minimum allowable span-to-depth ratios is presented in Sec. 8.9, which is part of the chapter on the design of reinforced concrete members. This type of table is not included in the section on prestressed concrete.

Limitations on live load deflections are given in Sec. 10.6.2, which is part of the chapter on the design of steel bridge superstructures. In that section, the deflection due to live load is limited to 1/800 of the span length for bridges without pedestrian traffic and 1/1000 of the span length for bridges with pedestrian traffic.

The AASHTO Specification provides a simple method for calculating the loss of prestress. The equations for estimating the creep and shrinkage are for normal weight concrete. Equations for estimating relaxation losses are given for both low relaxation and stress-relieved strands. As an alternative to using the equations that are given, the AASHTO Specification provides for a lump sum estimate of the prestress losses. The lump sum estimate is applicable for concretes with compressive strengths between 27.6 and 34.5 MPa.

2.5.2 Analytical Methods

In addition to the AASHTO Specification, there are several other methods available for computing the time-dependent camber (or deflection) and loss of prestress for prestressed concrete beams. These methods range from straightforward hand calculations to complex computer programs that have the capability of including user-input time-dependent material properties for their analysis.

Initial camber and deflection of prestressed concrete members resulting from superimposed loads (such as prestress force, beam weight, and additional dead and live loads) can be easily estimated using moment-curvature analysis, because the section generally remains uncracked under these loads. For the uncracked section conditions, gross cross-section properties can be used for computation. Estimation of long-term camber, deflection, and prestress loss becomes more complicated because the material properties of the concrete and steel, which are time-dependent, become important factors in the calculation procedure.

The PCI Design Handbook (27) contains a procedure for estimating long-term camber by using multipliers that are applied to the immediate elastic camber due to the prestressing force, to the immediate elastic deflections due to the beam weight, and to other superimposed dead loads. The multipliers given in the PCI Design Handbook were derived by Martin (28).

A method for calculating the long-term loss of prestress is also given in the PCI Design Handbook. The equations for losses due to creep, shrinkage, and steel relaxation are based upon the recommendations of the ACI-ASCE Committee 423 (38). The PCI Committee on Prestress Losses (39) also recommends a straightforward method for calculation losses.

Several other methods of calculating time-dependent camber, deflection, and loss of prestress have been recommended. Both an approximate method and a detailed step-by-step procedure for calculating long-term deflection of prestressed concrete beams is suggested by ACI Committee 435 (40). Tadros, Ghali, and Dilger (41) recommend a procedure that can be

used to calculate the prestress loss, curvature, and deflection at any time in both non-composite and composite prestressed beams. Tadros, Ghali, and Meyer (42) developed deflection multipliers, similar to the PCI approach, that can be used for the simple prediction of long-term deflection. They also considered the immediate deflection of cracked members and the effects that non-prestressed steel has on time-dependent deflection behavior. This procedure can be used in conjunction with any method for calculating prestress losses.

The AASHTO Specification procedure for estimating prestress losses and the PCI Design Handbook methods for estimating both prestress losses and camber and deflection are presented in more detail in Chapter 6. These methods were used as a comparison to the measured camber and prestress losses for the instrumented U-beams in this study. In addition, a time-step method based on the work of Branson and Kripanarayanan (43) was used to predict time-dependent behavior of the instrumented U-beams. This method is presented in Chapter 6.

There are several methods of calculating time-dependent behavior of prestressed concrete beams that consider the material properties of the concrete and steel as continuous time functions, and consider the interdependence of prestress force, creep, shrinkage, and steel relaxation over time. These methods are generally too complex and time consuming to be performed by hand and are of more use when programmed on a computer.

Computer programs and procedures that are applicable for programming have been developed by Suttikan (29), Sinno and Furr (44), Branson and Kripanarayanan (43), Rao and Dilger (30), Hernandez and Gamble (45), Grouni (46), and Huang (47). The work of Ingram and Butler (48) resulted in the development of PSTRS14 (49), which is the computer program used by the Texas Department of Transportation (TxDOT) for the design of simply-supported prestressed concrete I-beams. This program was created in 1970 and has been updated several times since then.

CHAPTER 3. BRIDGE DETAILS, INSTRUMENTATION, AND COMPANION TESTS

3.1 INTRODUCTION

This chapter presents the details and specifications for the twelve high performance concrete U-beams that were instrumented for this study. Details are also given for the precast deck panels and cast-in-place decks that were instrumented to monitor composite behavior. Included in this chapter are brief summaries of information about the bridge structure, instrumented beams, material specifications, locations and types of instrumentation used to monitor behavior, the data acquisition system used for reading the instrumentation, and the companion tests necessary for the study of the long-term behavior of the pretensioned high performance concrete beams.

3.2 BRIDGE DETAILS

3.2.1 General

The site chosen for this research project was the Louetta Road Overpass on SH 249 located in Harris County near Houston, Texas. This project was part of a cooperative research agreement established in 1993 between the Texas Department of Transportation (TxDOT) and the Federal Highway Administration (FHWA). The bridge structure was designed by TxDOT bridge engineers and the project was let in February of 1994. Williams Brothers Incorporated of Houston, Texas, was the general contractor on the project and was responsible for the precast pier segments and precast deck panels for the bridge structure. Texas Concrete Company in nearby Victoria, Texas, was the fabricator of the pretensioned concrete bridge girders.

The Louetta Road Overpass consists of two main lane bridges, one in the northbound direction and one in the southbound direction, each having three spans. Figure 3.1 shows a plan view of the bridges and the corresponding span lengths and widths. While Figure 3.1 provides the span lengths as measured along the centerline of SH 249, Table 3.1 summarizes the maximum span lengths for each bridge as measured from centerline to centerline of bents. The length of each beam is unique because there is a different skew angle at each bent.

The clear widths of the northbound and southbound bridges vary as well. The clear width is taken as the distance between the outside faces of the guardrails. Both bridges were designed to carry three lanes of traffic, and the southbound bridge was also designed to accommodate an exit ramp. For this reason, the beam lines of the southbound bridge flare out more than those of the northbound bridge. Table 3.1 provides a summary of the maximum and minimum clear widths for each bridge.

Each span in the northbound bridge has five Texas Type U54 beams, and each span in the southbound bridge has six beams. The beam spacing varies for each span because of the varying widths of the bridges. The maximum and minimum spacings for each span are given in Table 3.2. The beams bear on individual piers at bents two and three rather than on the traditional continuous pier cap. This design concept is well-suited for the U-beam section

since much larger beam spacings can be achieved, resulting in a more visually appealing substructure.

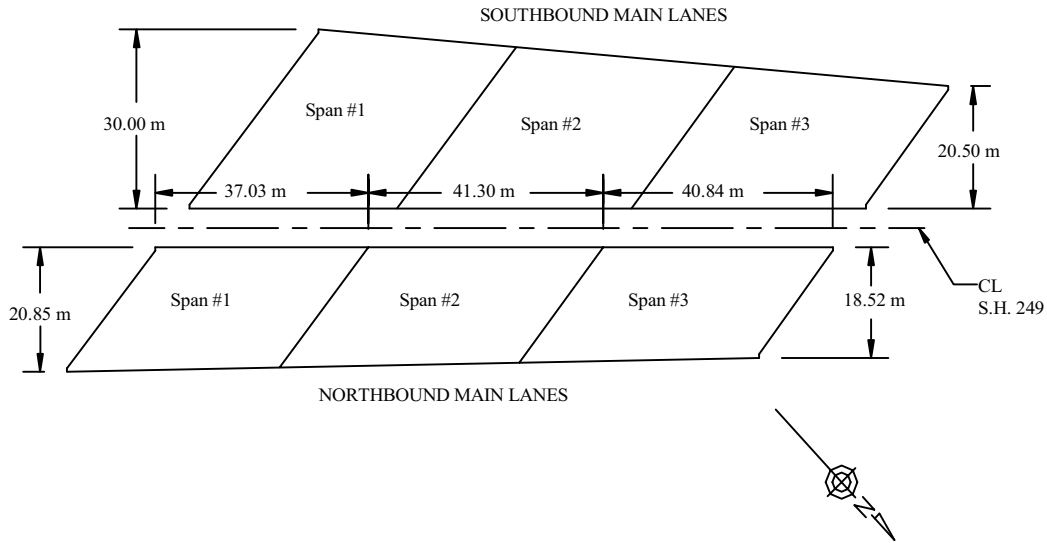


Figure 3.1 Plan view of Louetta Road Overpass

Table 3.1 Maximum span lengths and clear widths for the Louetta Road Overpass

Bridge	Maximum Span Lengths (m)			Clear Widths (m)	
	Span #1	Span #2	Span #3	Maximum	Minimum
Northbound	37.75	42.04	41.50	20.86	18.52
Southbound	37.01	41.28	40.82	30.00	20.83

Table 3.2 Maximum and minimum bridge girder spacings

Spacing ¹ (m)	Southbound Bridge			Northbound Bridge		
	Span 1	Span 2	Span 3	Span 1	Span 2	Span 3
Minimum ² (m)	4.62	3.95	3.34	3.81	3.61	3.44
Maximum ² (m)	5.26	4.64	3.96	4.02	3.84	3.64
Midspan ² (m)	4.94	4.30	3.65	3.92	3.73	3.54

Notes:

1. Beam spacings are determined by taking the average of the perpendicular distances between centerlines of beams in each span.
2. The average minimum and maximum spacings occur at the ends of the beams.
3. The average midspan spacing is only approximate because of the varying bridge skews.

The nomenclature used for the instrumented bridge beams in this study is straight-forward. For example, one bridge beam that was instrumented in this study is designated as

S14. The first letter in the beam designation tells where it is located. The location of a beam will be in either the southbound main lane (S) or northbound main lane (N) bridge. The second label identifies the span in which the beam is located. For this example, Beam S14 is located in the first span of the southbound bridge. The third label tells exactly which lateral position that beam occupies in its particular span. Beam S14 is the fourth beam in the span where beam one corresponds to the west exterior girder. Figures 3.2 and 3.3 show the beam nomenclature system for each bridge. The darkened beam locations identify the twelve beams that were instrumented for this study.

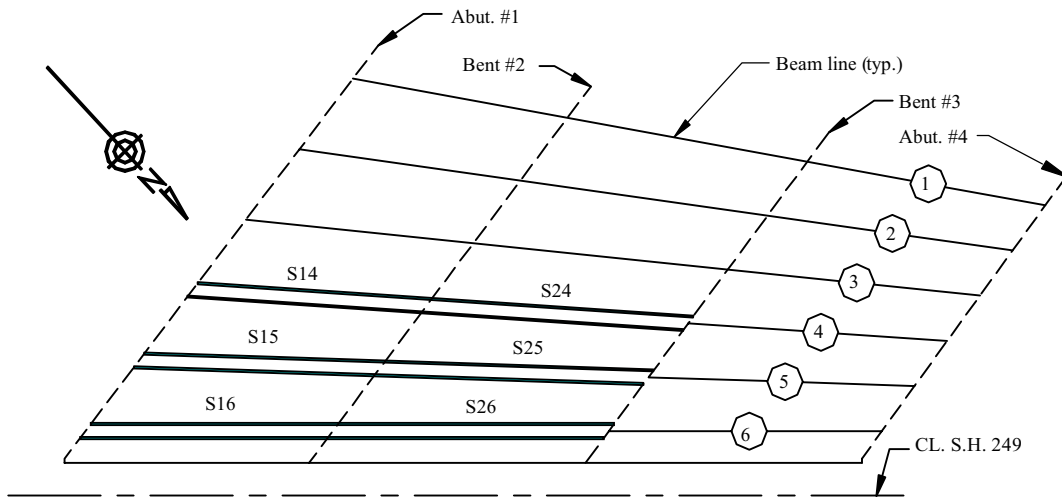


Figure 3.2 Instrumented beams in the southbound main lanes bridge

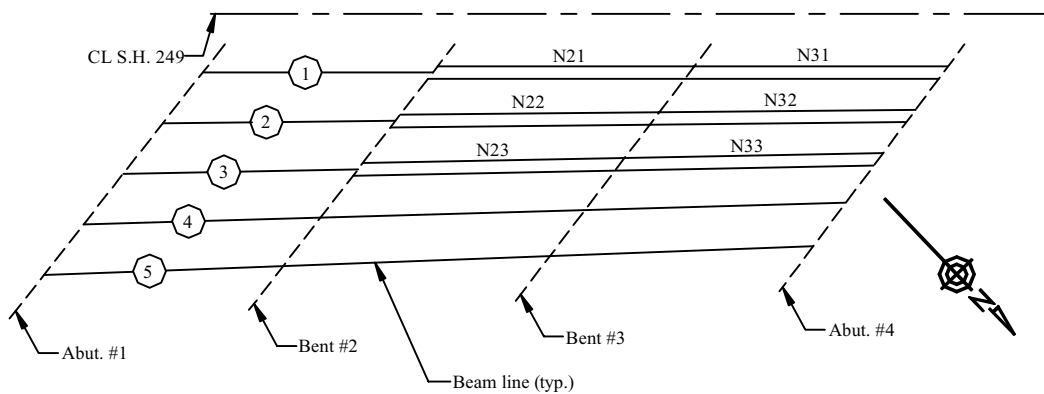


Figure 3.3 Instrumented beams in the northbound main lanes bridge

3.2.2 Bridge Girder Details

As previously mentioned, the Louetta Road Overpass was designed using the newly developed Texas U-beam. As indicated by Ralls et al. (1), the Texas U-beam cross section was developed with a renewed focus on aesthetics while emphasizing the need for the economical, durable, and functional qualities that are inherent to structures constructed using the standard I-shaped beams. The aesthetic advantages of the U-beam are apparent from consideration of the shape and spacing of the girder. The standard AASHTO I-shaped girders have several horizontal break lines on their web faces. The trapezoidal shape of the U-beam eliminates those visual breaklines and gives the bridge smoother lines. Larger beam spacing can be achieved with the Type U54 beam because it has nearly twice the moment of inertia as the AASHTO Type IV girder. The larger spacing will result in a more open and attractive superstructure. It will also create more options for the substructure, such as beams being supported on individual piers, as is the case in this project.

While the transportation and fabrication costs of the U-beam exceed those of the standard I-shaped girders, several economical advantages can be realized with the U-beam (1). One advantage is that fewer beams per span are needed to complete a bridge superstructure. This may result in savings in material, transportation, and fabrication costs for the whole project. Additionally, longer spans and larger spacing can be achieved with the U-beam. When combined with high performance materials, such as high strength concrete and 15.2 mm-diameter prestressing strand, the advantage of longer spans will result in a reduction in the number of substructure units. Russell (3) points out that a cost savings can be realized with high strength concrete U-beams when shallower superstructures can be used for longer spans. The savings resulting from shallower sections will come from reductions in pier, abutment, and approach work costs. The practical limitations imposed on span length, such as girder self-weight and difficulty in transportation and handling of very long beams, indicate that the greatest advantage may come from larger beam spacing and shallower sections.

The cross-sectional dimensions of the U54A and U54B girders are shown in Figure 3.4. These sections were developed in metric units to comply with the Federal Highway Administration (FHWA) initiative that all federally funded projects have construction documents that are produced using the International System of units (metric system) by September of 1996 (1). Both of these sections were used in the Louetta Road Overpass and both were included as part of the twelve instrumented beams in this research study.

At first glance the U54A and U54B cross sections look identical. Both sections have an overall top width of 2440 mm, two top flanges that are 400 mm wide and 150 mm thick, and a bottom flange width of 1400 mm. The Type U54 beam is 1372 mm deep, matching the depth of the AASHTO Type IV beam. The reason for this was to allow for widening of existing I-shaped girder bridges with the more visually appealing Type U54. There are two webs in the Type U54 beam, each with a width of 126 mm. The outside web faces taper downwards at a 4-to-1 slope, as shown in Figure 3.4, resulting in the attractive trapezoidal shape.

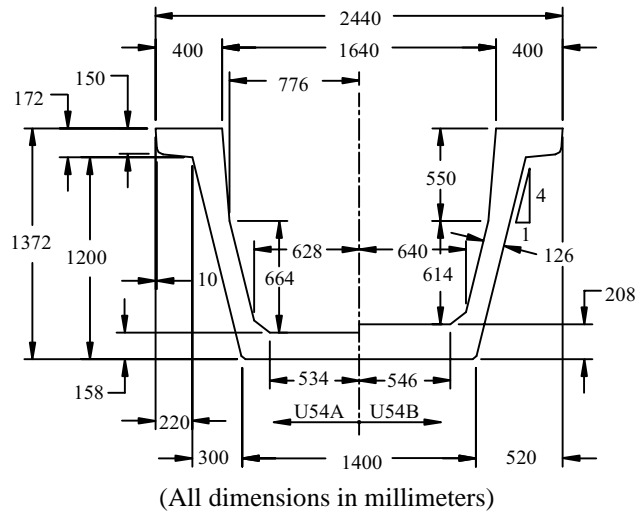


Figure 3.4 Cross-section dimensions for Texas U54 beam

The main difference between the two sections is the thickness of the bottom flange. The U54A section has a bottom flange thickness of 158 mm, which allows for two rows of prestressing strands. The U54B section has a slightly larger bottom flange thickness of 208 mm. This means that a third row of strands can be added for the U54B section. Additional strands can be placed in single vertical rows located in each web. The maximum number of strands that can be placed in the U54A and U54B sections are 74 and 99 strands, respectively. Figure 3.5 shows the maximum strand patterns for both cross sections. The strands are positioned on a grid with 50 mm spacings in the horizontal and vertical directions. Both the 12.7 mm-diameter and the 15.2 mm-diameter seven-wire prestressing strands can be used with the Type U54 beam.

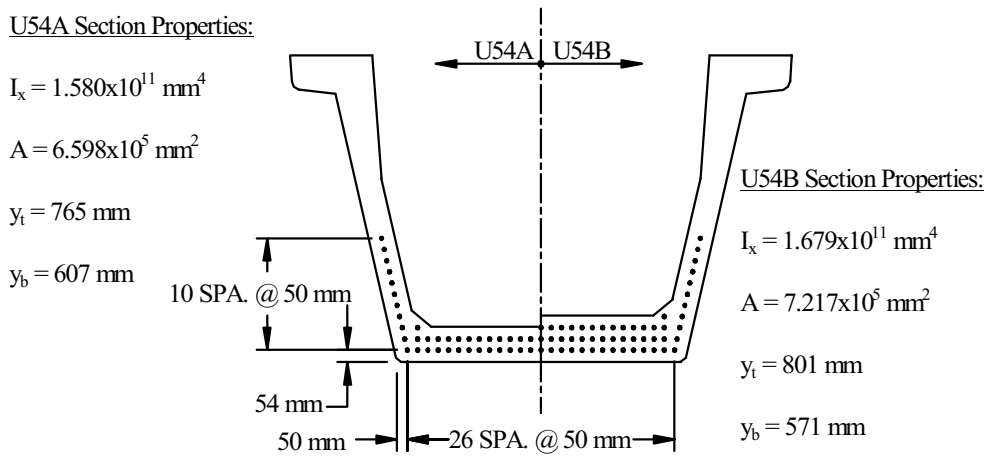


Figure 3.5 Maximum prestressing strand patterns for Texas U54 beam

The U-beam also has two internal diaphragms that vary in thickness and are located approximately 0.4L and 0.6L from one end of the beam. These diaphragms help to stiffen the two separated webs. The beams also had solid end blocks which varied in thickness (minimum thickness of 457 mm) because of the bridge skew.

3.2.3 Composite Bridge Details and Support Conditions

Both bridge superstructures in the Louetta Road Overpass were designed as prestressed concrete beam sections acting compositely with precast prestressed concrete deck panels and a reinforced concrete deck cast over the panels. The details of the composite bridge section are shown in Figure 3.6. The composite deck was designed to be 184 mm thick. The thickness of the precast panels is 89 mm, and the thickness of the cast-in-place slab is 95 mm. The use of precast panels in deck construction is just as advantageous with the U-Beam bridge as it is with the I-shaped girder bridges. The precast panels make the deck easier to construct because less formwork preparation is needed and contractors frequently select this option for Texas bridges. Figure 3.7 gives details and dimensions for the precast deck panels.

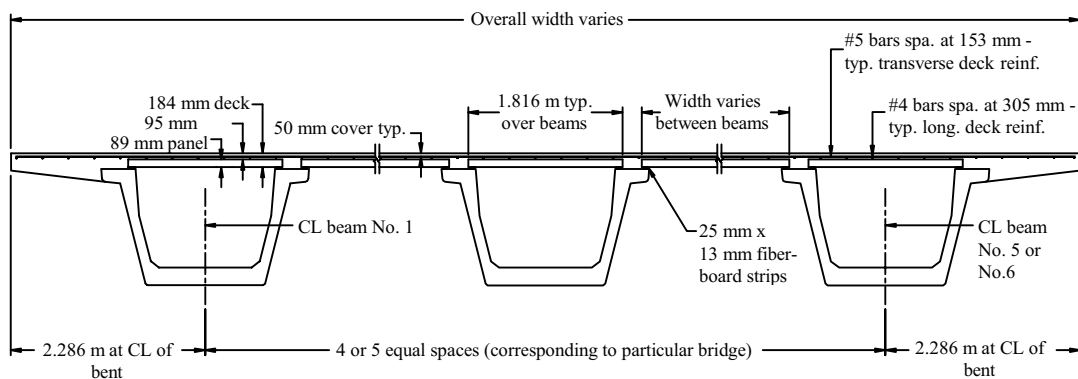
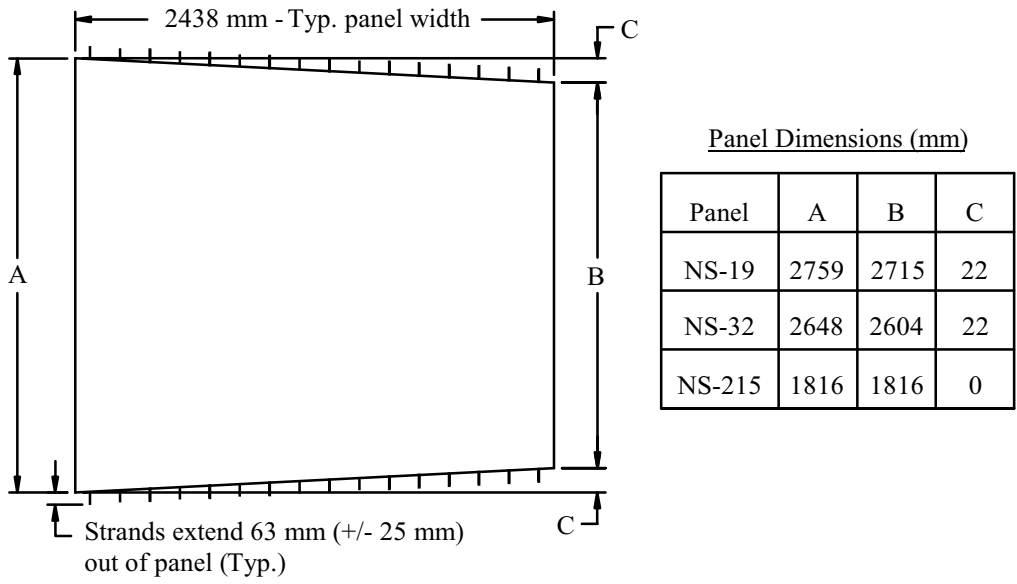
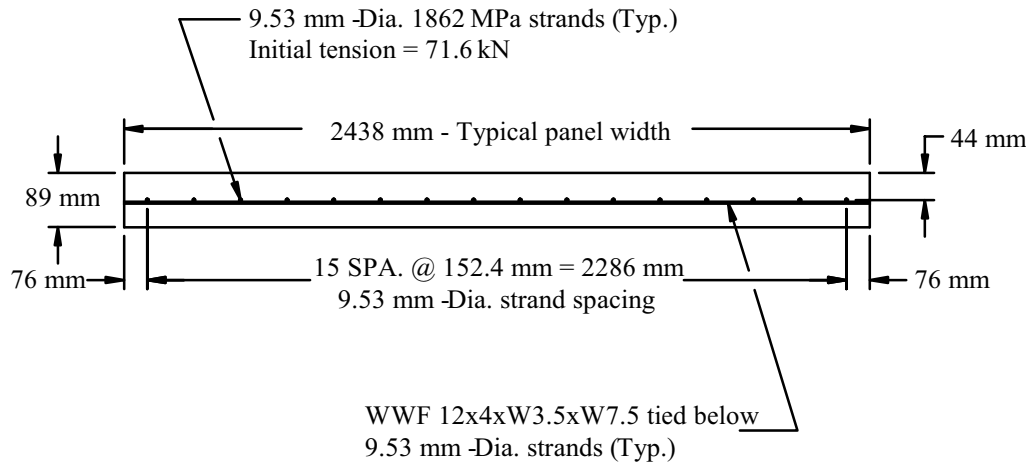


Figure 3.6 Composite U-beam cross-section details

The beams in the Louetta Road Overpass were designed as simply supported members. The typical support conditions for the U-beam can be seen in Figure 3.8. One end of the beam rested on a single bearing pad while the other end of the beam rested on two bearing pads. The bearing pad material was 50 durometer steel laminated neoprene. The pads were of varying thickness and were beveled to allow the beam to conform to the grade of the bridge.

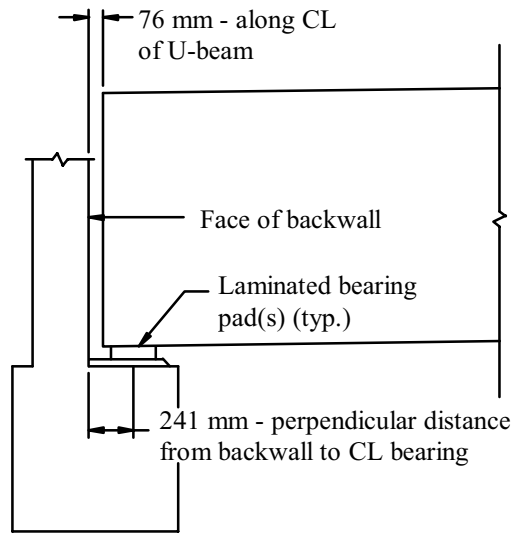


Plan

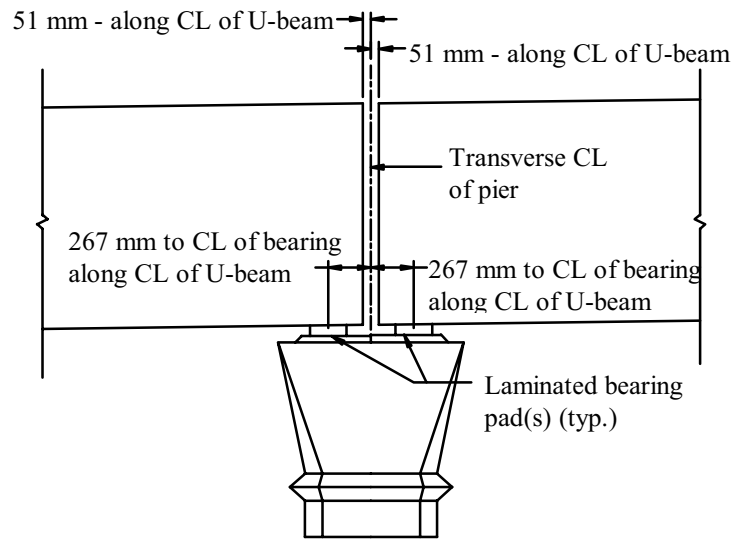


Elevation

Figure 3.7 Precast deck panel details



At Abutments (Typical)



Elevation

Figure 3.8 Typical bearing details for instrumented beams in both bridges

3.2.4 Instrumented Beams

Twelve Texas U54 beams were instrumented in the field for the purpose of measuring camber and deflection, internal strains, and temperatures gradients over time through the various stages of fabrication and construction. The locations of the instrumented beams were

chosen to reflect the goals of the instrumentation plan. One of the goals of the project was to determine the live load distribution factors for adjacent interior and exterior beams within the same span. Another consideration was that the number of data acquisition systems used to read the instrumentation needed to be minimized. To satisfy these requirements, four groups of three beams were chosen to be instrumented as shown in Figures 3.2 and 3.3. By grouping the beams together in this manner, only two data acquisition boxes were needed to read all of the beam and deck gages.

An exterior beam was included in each of the four instrumented groups because the exterior beam typically had the most prestressing strands, and it would also have thermal gradients that were different from the interior beams.

The geometric and material properties of the instrumented beams are summarized in Table 3.3. There were four different strand patterns among the twelve instrumented U-beams. The number of 15.2 mm-diameter low relaxation prestressing strands in a particular beam varied from a minimum of 64 to a maximum of 87, depending on where the beam was located in the bridge. The different strand patterns for the instrumented beams are shown in Figures 3.9 through 3.12. Both the U54A and U54B cross sections of the Texas U-beam were included in the group of instrumented beams. The U54B section, which has a higher strand capacity than the U54A section, was used for the exterior beams because those beams required the most prestressing force.

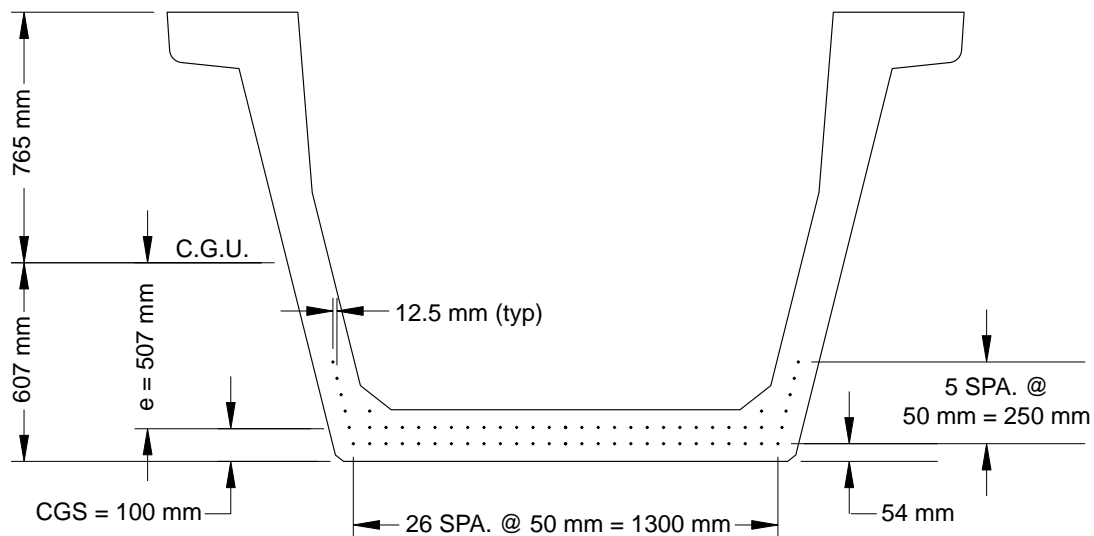


Figure 3.9 Instrumented U-beam strand pattern – 64 strands

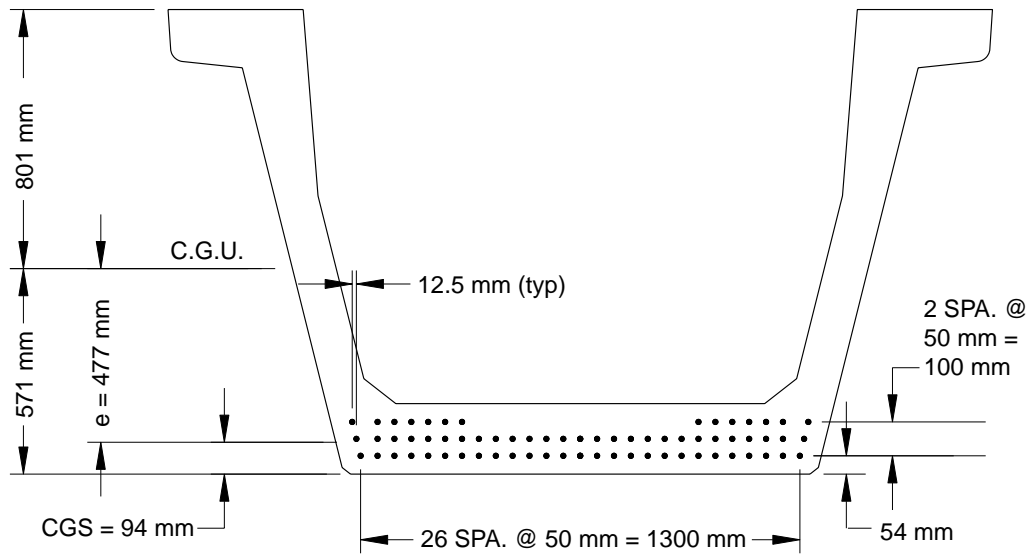


Figure 3.10 Instrumented U-beam strand pattern – 68 strands

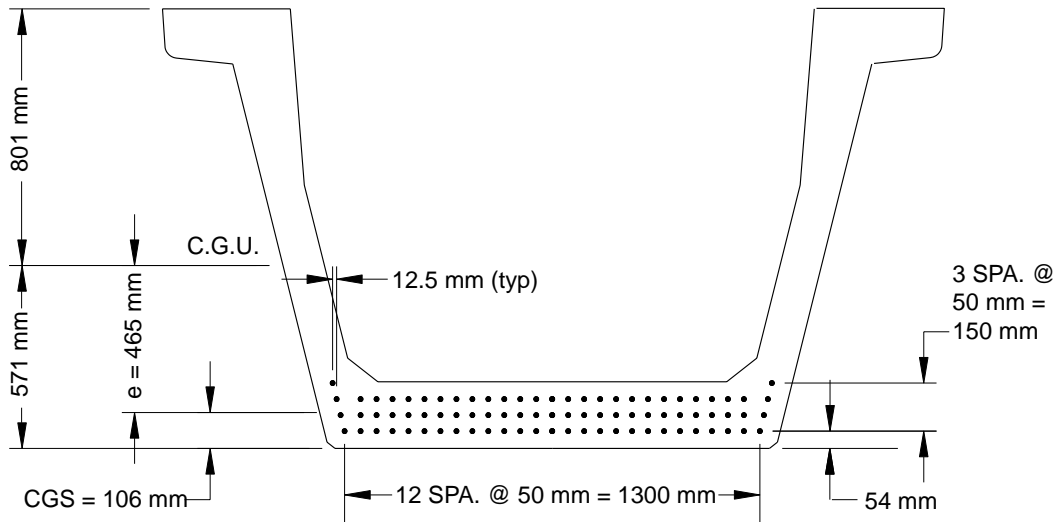


Figure 3.11 Instrumented U-beam strand pattern – 83 strands

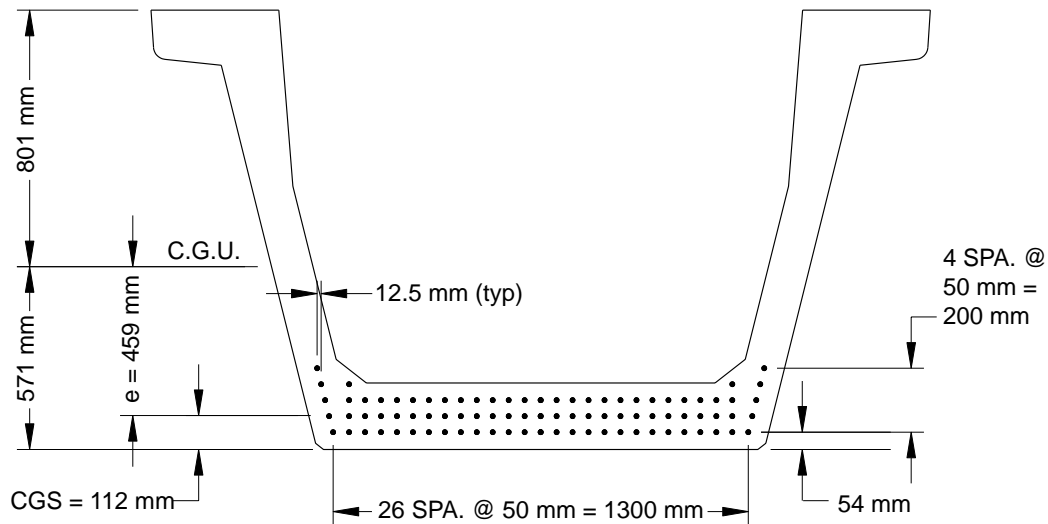


Figure 3.12 Instrumented U-beam strand pattern – 87 strands

The design beam lengths, which are the lengths of the beams from end to end, varied from 35.94 meters for Beam S14 to 41.58 meters for Beam N23. In this study the length of interest was the span length, which was taken as the center-to-center of bearing length. This length was used for calculating camber and deflection predictions, which were used to compare to the measured values. The center-to-center of bearing lengths varied from 35.55 meters (S14) to 41.25 meters (N23).

The casting dates shown in Table 3.3 indicate that the first eight instrumented beams were cast between September and November of 1994, while the remaining four beams were cast in February of 1996. This created an age difference of as much as 521 days between beams in the first group and beams in the second group. The difference in age was important when comparing the measured growth of camber during storage. Additionally, there were four pairs of beams that were cast at the same time on the same stressing bed. This was important for making comparisons of long-term behavior between the companion beams. It was also important because the internal temperature data from one beam could be used to correct the camber readings for thermally induced camber and deflection for both beams in the pair.

3.3 INSTRUMENTATION

3.3.1 Selection of Instrumentation

The purpose of this study was to monitor the time-dependent behavior of a full-scale highway bridge structure. To learn about the long-term behavior of high performance concrete in these bridges, three types of measurements needed to be obtained over a period of several years.

Table 3.3 Beam geometry, design, and fabrication data for instrumented beams

Beam	Casting Date	Section Type	Number of 15.2 mm-Diameter Strands	Design Length (m)	CL to CL of Bearing Length (m)	Specified Release Strength (MPa)	Specified 56 day Compressive Strength (MPa)
S14	2-26-96	U54A	64	35.94	35.55	53.1	80.0
S15	2-26-96	U54A	64	36.41	36.01	53.1	80.0
S16	9-30-94	U54B	68	36.89	36.49	53.1	80.0
S24	11-10-94	U54B	68	40.16	39.83	53.1	80.0
S25	11-10-94	U54B	68	40.66	40.33	53.1	80.0
S26	10-7-94	U54B	87	41.18	40.84	60.7	90.3
N21	10-28-94	U54B	87	41.23	40.90	60.7	90.3
N22	9-30-94	U54B	68	41.40	41.07	53.1	80.0
N23	9-23-94	U54B	68	41.58	41.25	53.1	80.0
N31	10-28-94	U54B	83	40.74	40.35	60.7	90.3
N32	2-15-96	U54A	64	40.90	40.50	53.1	80.0
N33	2-15-96	U54A	64	41.06	40.66	53.1	80.0

The first type of measurement was long-term strains. Long-term strains were necessary for determining the prestress losses for the high performance concrete beams. The results could be compared to prestress losses for normal strength concrete beams and could improve design procedures for prestress losses when using high performance concrete. Strains were also important for verifying the behavior of the beam cross section at midspan throughout construction and into service life.

The second type of measurement was camber and deflection. This measurement was important for determining the time-dependent changes in camber caused by creep, the fluctuations in camber owing to temperature gradients in the beam that vary throughout the day and throughout the year, and instantaneous deflection resulting from the applied deck loads.

The third type of measurement was concrete temperatures. Temperature gradients in the beams were necessary information for making corrections to the camber measurements. Temperature gradients in the finished bridge were also important for design purposes.

Because this was a field study and not a laboratory study, several additional factors needed to be considered during the development of the instrumentation plan. These factors affected the types of instrumentation used to obtain the necessary measurements and the implementation of the instrumentation plan in the field. The following conditions were considered as part of this study:

1. Because twelve beams were monitored in this study, the instrumentation needed to be simple and easy to install with repetition from beam to beam. This was essential to reduce the complexity of the instrumentation plan and to minimize the time needed for preparation and installation.

2. The instrumentation needed to be durable because the field monitoring program was going to begin at the time of fabrication of the beams and last several years into the service life of the bridge. Another reason for durability was that any exposed portions of the instrumentation would be subjected to harsh weather conditions and possible damage during handling and transportation of the beams.
3. Since there would be involvement with contractors throughout the entire study, it would be important to establish a good working relationship between the researchers and the contractors. This relationship would require frequent communication so that the researchers could install and monitor the instrumentation without significantly disrupting the fabrication and construction processes.
4. Because the locations of the precast plants and project site were several hours of travel from the laboratory in Austin, consideration was given to the amount of time that would be lost during trips to and from these places. The extended travel time would take away from the time needed for preparation, planning and building of the instrumentation systems. Also, the distance from these sites would become very important during coordination with the contractors for installation and monitoring of the instrumentation.

With these considerations in mind, along with the goals for this study, the instrumentation systems were chosen and developed for the beams, deck panels and cast-in-place deck. The following sections describe exactly what types of instrumentation were used to monitor the behavior of the structural components of the bridges and where they were placed in the various structural components.

3.3.2 Concrete Surface Strain Measurement

Concrete surface strain measurements were obtained through the use of a Demec mechanical strain gage. The gage consists of a dial mounted on a steel bar that has conical shaped tips at each end underneath the gage. The tips of the gage fit neatly into the Demec points, which are specially fabricated stainless steel disks with conical holes in the center. One tip is allowed to move so that the distance between points can be translated into a reading on the dial. The initial and final reading on the Demec gage for a set of points determines the change in length and consequently the strain between the points. A conversion to strain needed to be made since the dial gage did not measure strain directly. The difference in gage readings multiplied by the strain per division for the gage gave the total strain between the set of points. For the gage used in this study, each division on the dial gage was equal to 8.1 microstrain. Figure 3.13 shows the Demec mechanical strain gage and stainless steel disks.



Figure 3.13 Demec surface strain measuring system

The procedure for using this system began with the placement of Demec points on the surface of interest. Points were placed by using a spacer bar that was approximately 200 millimeters in length, which corresponded to the gage length. The Demec points were fixed to the concrete surface with standard five-minute epoxy gel. Although this type of epoxy did not have extremely long-term durability, its use was necessary to minimize the time loss for the fabricator.

Initial readings were taken before the release of the prestressing force and subsequent readings were taken after release. The total strain measured between the points included the thermally induced strains from the beam. The effects of temperature on the Demec gage could be accounted for by measuring the standard invar bar for each set of readings. Surface temperatures needed to be measured to account for the thermally induced strain between readings.

Previous research by Kelly et al. (26) showed that the five-minute epoxy had reliability and durability problems when used to affix the mechanical strain gages to concrete surfaces. As a result, the use of mechanical strain gages were limited to transfer length readings and backup readings for other internal instrumentation. The measurements of interest for this study were the strain measurements at the midspan to determine the sectional behavior after transfer of the prestressing force and the strain measurements at the CGS along the beam length. This type of instrumentation was fairly easy to install with little preparation time and these measurements were taken in a short time period after transfer. Table 3.4 summarizes the locations of the concrete surface strain instrumentation, and Figures 3.14 and 3.15 show typical locations for instrumentation.

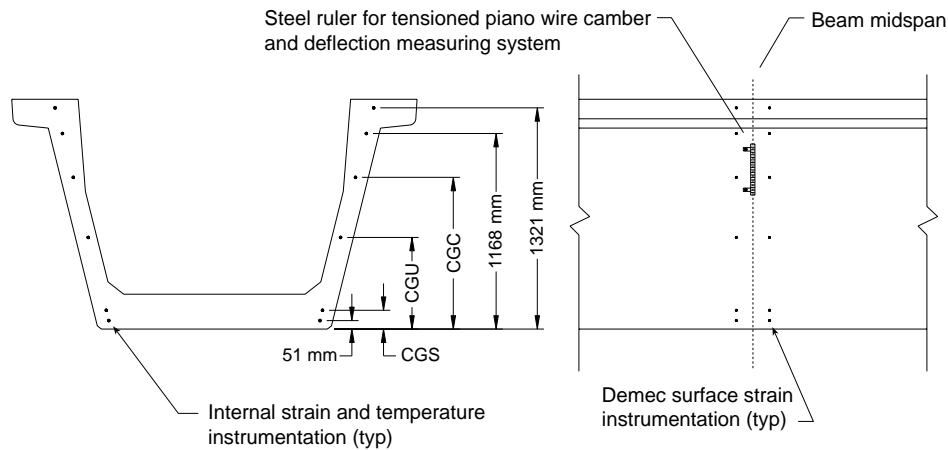


Figure 3.14 Vertical locations for beam instrumentation at midspan

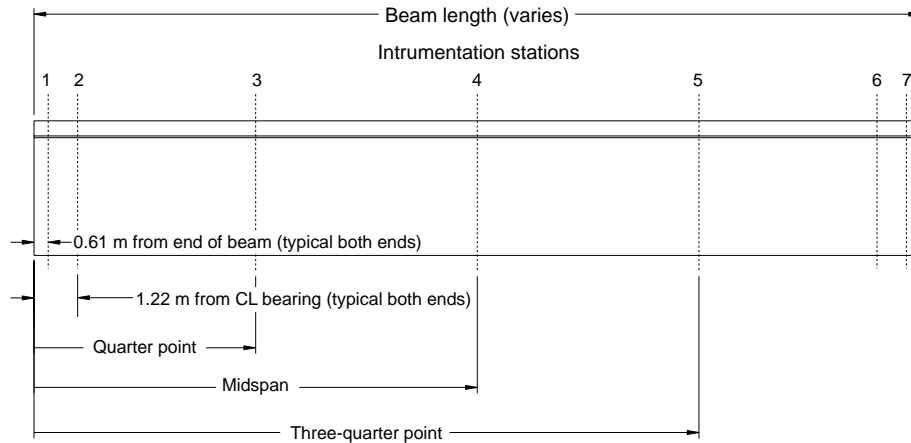


Figure 3.15 Horizontal locations for beam instrumentation

3.3.3 Internal Strain Measurement

Two types of internal strain measuring instrumentation were utilized to monitor the behavior of the prestressed beams. The first type of instrumentation was the electrical resistance strain gage (ERSG). The ERSG measures strain based on a change in resistance. The change in resistance occurs as the small wires in the gage change length, or strain. Because this is a resistance-based measurement, the reliability of the readings can be questionable owing to unwanted resistance. Resistance is added into the system as connections are made to the lead wires and as various connections are made to the data acquisition equipment.

Preparation of an ERSG for use consisted of bonding the gage to a piece of #3 rebar (approximately 1 meter long) that was specially prepared by grinding, sanding, and cleaning an area for the gage. Once the gage was bonded to the rebar, it was necessary to apply

waterproofing to the gage and lead connections to prevent moisture penetration. By bonding the gage to the rebar, a simple and effective means of inserting the gage into the beam at the desired location was established. The ERSG was an inexpensive alternative for gathering short-term strain measurements. The reliability and durability characteristics for this type of gage limited the usefulness of its readings to approximately one year.

The ERSGs used in the cast-in-place decks were prepared differently than the ones used in the beams. Instead of bonding the gages to #3 rebar, they were bonded to 9.5 mm-diameter threaded rods that were 150 mm long. Using a grinder, flat surfaces were made in the center of the rods. Large washers were mechanically fastened to the ends of the rods to provide anchorage in the concrete. Then, the gages were bonded onto the flat surfaces and protected with weather-proofing agents.

Table 3.4 Summary of external instrumentation for beams

Beam	Demec Surface Strain Gages ¹	Tensioned Piano Wire Camber and Deflection Measuring System ¹
S14	midspan/both/all	midspan/both
S15	midspan/both/all	midspan/both
S16	midspan/both/all along length/both/CGS	midspan/both
S24		midspan/both
S25	midspan/both/all along length/both/CGS	midspan/both
S26	midspan/both/all along length/both/CGS	midspan/both
N21	midspan/both/all along length/both/CGS	midspan/both
N22	midspan/both/all along length/both/CGS	midspan/both
N23	midspan/both/all along length/both/CGS	midspan/both
N31	midspan/both/all along length/both/CGS	midspan/both
N32		midspan/both
N33		midspan/both
Notes:		
1. Descriptions of instrumentation locations consist of three parts. The first part gives the station along the beam (<i>along length</i> refers to all of the stations shown in Fig. 3.15.). The second part gives the side(s) of the beam (east, west, or both). The third part tells the vertical location (<i>CGS</i> refers to the center of gravity of the prestressing strands and <i>all</i> means every vertical positions shown in Fig. 3.14.).		

The second type of internal strain measuring instrumentation utilized in this study was the vibrating wire (VW) gage manufactured by Roc-test, Inc. The model EM-5 strain gage is 168 mm in length and is composed of two circular end pieces joined by a stainless steel tube that contains a high tensile strength steel wire. The end pieces allow for the gage

to anchor into the concrete and transfer concrete deformation to the wire. Voltage pulses that cause the wire to oscillate are sent to the wire from the coil/magnet assembly in the gage. Strain that develops in the concrete changes the tension of the wire, which changes its resonant frequency. Thus, the change in resonant frequency of the wire is used to determine the change in strain in the concrete.

There was very little preparation needed for the VW gages. Each gage was tied to a piece of #3 rebar (approximately 1 meter long) for later placement in the beam. The VW gages used in the precast deck panels and cast-in-place decks were not attached to a piece of rebar, but simply tied directly onto the reinforcement in the field. Because of their strong and durable outer shells, these gages were expected to last nearly three years. An additional benefit to the VW gage was that it had a thermistor for temperature measurement inside of a coil/magnet assembly. This was beneficial for determining thermal gradients within the beam, which contributed to the camber of the beam. The one drawback to the VW gage was that it cost approximately 10 times that of an ERSG, which meant that a tradeoff in quantity and reliability needed to be determined.

The VW gages were utilized in the places where reliable long-term data were the most critical for this study. Since the prestress losses of the strands in the beams throughout the stages of construction was of great interest, six of the instrumented beams had a VW gage at the CGS on at least one side of the beam. In addition, there was an interest in the strains on the cross section at midspan throughout construction. Four of the instrumented beams had VW gages throughout the depth of the cross section at midspan on at least one side of the beam. To complete the vertical strain profile at midspan for two of the instrumented beams, VW gages were placed in the cast-in-place deck. Additional gages were placed in the precast deck panels for determination of live load distribution factors for the completed bridge. The ERSGs were utilized mainly for strains immediately after transfer of prestressing force and to provide redundancy at critical locations in the instrumented beams. Table 3.5 includes a summary of the internal strain measuring instrumentation for the twelve U-beams. Figures 3.14 and 3.15 show the instrumentation locations in the beams. A summary of the internal strain instrumentation for the precast deck panels is given in Table 3.6. Instrumentation placed in the cast-in-place decks is summarized in Tables 3.7 and 3.8.

3.3.4 Internal Temperature Measurement

As mentioned in Sec. 3.3.3, one method of measuring the internal concrete temperature was with thermistors located inside the vibrating wire gages. The other method employed in this study was the use of thermocouples that were prepared by the researchers. The thermocouples were created by twisting a copper wire and a constantin wire together and covering the connection with electrical tape. The wire and connectors were manufactured by Omega Engineering, Inc.

Table 3.5 Summary of internal instrumentation for beams

Beam	Electrical Resistance Strain Gauges (ERSG) ²	Vibrating Wire Gauges (VW) ²	Internal Temperature ²
S14	midspan/east/all		midspan/east/all
S15		midspan/both/all	
S16	midspan/east/all along length/both/CGS	midspan/west/CGS	midspan/east/all diaphragm/NE/all
S24			
S25	along length/both/CGS ¹	midspan/east/all midspan/west/CGS	along length/east/CGS
S26	along length/east/CGS	along length/west/CGS	
N21	midspan/west/all along length/both/CGS		midspan/both/all
N22	along length/both/CGS		
N23	midspan/both/CGS		
N31	along length/both/CGS		
N32	midspan/east/all	midspan/west/all midspan/east/CGS	
N33	midspan/east/all	midspan/west/all midspan/east/CGS	

Notes:

- Gages are placed along beam length at every station shown in Fig. 3.15 except midspan.
- Descriptions of instrumentation locations consist of three parts. The first part gives the station along the beam (*along length* refers to all of the stations shown in Fig. 3.15.). The second part gives the side(s) of the beam (east, west, or both). The third part tells the vertical location (*CGS* refers to the center of gravity of the prestressing strands and *all* means every vertical positions shown in Figure 3.14.).

The thermocouples were placed in locations that corresponded to strain gage locations for simplicity of installation and for uniformity in the instrumentation plan. The thermocouples were installed in the field on the #3 rebars used for the strain gages and tied in place with electrical tape. Additional thermocouples were placed in the cast-in-place deck and precast panels. These locations were needed to complete the temperature profile from the bottom flange of the beam to the top of the slab. Tables 3.5 through 3.8 summarize the locations of the thermocouples in the beams, panels, and decks and Figure 3.14 shows their locations on the beam cross section.

Table 3.6 Instrumented precast deck panels in southbound main lanes bridge

Panel Designation	Location in SB Main Lanes Bridge	Instrumentation	
		Vibrating Wire Gages ¹	Thermocouples ²
NS-19	Between Beams S14 and S15 at midspan	two (2) at center of panel	two (2), one at center of panel and one 76 mm from edge of panel
NS-32	Between Beams S15 and S16 at midspan	two (2) at 305 mm from transverse edge ³	two (2) at center of panel
NS-215	On top of Beam S15 at midspan	two (2) at center of panel	two (2) at center of panel

Notes:

- Vibrating wire gages were tied across the strands at 38 mm above the bottom of the panel and parallel to the strands at 51 mm above the bottom of the panel.
- Thermocouples were prepared on a small piece of #2 bar to be able to position them at the vertical locations of 25 mm and 76 mm above the bottom of the panel.
- These gages were positioned off the wrong edge of the panel. Section 4.5.1 discusses this in detail.

Table 3.7 CIP deck instrumentation for the southbound main lanes bridge

Transverse Section ¹	Beam ²	Location ³	Gage Type	Distance Below Panel Surface (mm) ⁴	Orientation ⁵	
Midspan of Beam S14	S14	E	TC	-44	---	
			TC	44	---	
Midspan of Beam S15	S14	E	ERSG	32	T	
			W	VW	-38	L
				VW	44	L
	S15	P	ERSG	38	T	
			VW	64	L	
			VW	38	T	
			TC	51	---	
	E	P	TC	13	---	
			VW	-32	T	
			VW	57	L	
	S14/S15	P	ERSG	38	T	
	S15/S16	P	VW	38	T	
			TC	51	---	
TC			13	---		
S16	W	ERSG	25	T		
Midspan of Beam S16	S16	E	TC	-44	---	
			TC	44	---	
Midspan of Beam S25	S25	W	VW	44	L	
		E	VW	51	L	
			VW	-38	L	
Abut. No. 1	S15	W	VW	51	L	
		E	VW	57	L	
Bent No. 2	S15	W	VW	44	L	
		E	VW	51	L	
Bent No. 3	S25	W	VW	51	L	
		E	VW	44	L	

(Notes on following page.)

Notes:

1. A transverse section extends perpendicular to the specified beam. When a support location is given, the section is only at the beam given in the next column.
2. S14/S15 and S15/S16 signify that the instrumentation is between beams.
3. Locations are the West (W) and East (E) top flange of the beam and over the panel (P).
4. Distances were measured in the field after gage installation.
5. Orientations of the gages were either longitudinal (L) or transverse (T) to the beams.
6. TC = Thermocouple; VW = Vibrating Wire Gage; ERSG = Electrical resistance strain gage.

Table 3.8 CIP deck instrumentation for the northbound main lanes bridge

Transverse Section ¹	Beam ²	Location ³	Gage Type	Distance Below CIP Deck Surface (mm) ⁴	Orientation ⁵
Midspan of Beam N33	N32	W	ERSG	50	L
		P	ERSG	50	L
			ERSG	50	T
		E	ERSG	50	L
	N32/N33	P	ERSG	50	L
			ERSG	50	T
	N33	W	ERSG	50	L
			VW	50	L
			VW	139	L
		P	ERSG	50	L
ERSG			50	T	
ERSG			50	L	
Midspan of Beam N32	N32	W	ERSG	50	L
			ERSG	50	T
		P	ERSG	50	L
			ERSG	50	T
		E	ERSG	50	L
			ERSG	50	T
	N32/N33	P	ERSG	50	L
			ERSG	50	T
	N32	W	ERSG	50	L
			ERSG	50	T
		P	ERSG	50	L
			ERSG	50	T
		E	ERSG	50	L
			ERSG	50	T
Midspan of Beam N21	N21	W	TC	50	---
			TC	139	---
		E	TC	50	---
			TC	139	---

Notes:

1. A transverse section extends perpendicular to the specified beam.
2. N32/N33 signifies that the instrumentation is between beams.
3. Locations are the West (W) and East (E) top flange of the beam and over the panel (P).
4. Distances were not measured in the field but approximated based on deck reinforcement.
5. Orientations of the gages were either longitudinal (L) or transverse (T) to the beams.
6. TC = Thermocouple; VW = Vibrating Wire Gage; ERSG = Electrical resistance strain gage.

3.3.5 Long-Term Camber and Deflection Measuring System

The initial measurement of the elastic and time-dependent camber of the beams was accomplished with a tensioned piano wire and ruler system. This system was utilized from the fabrication of the beams until the transportation of the beams to the job site. A sketch of the piano wire system is shown in Figure 3.16.

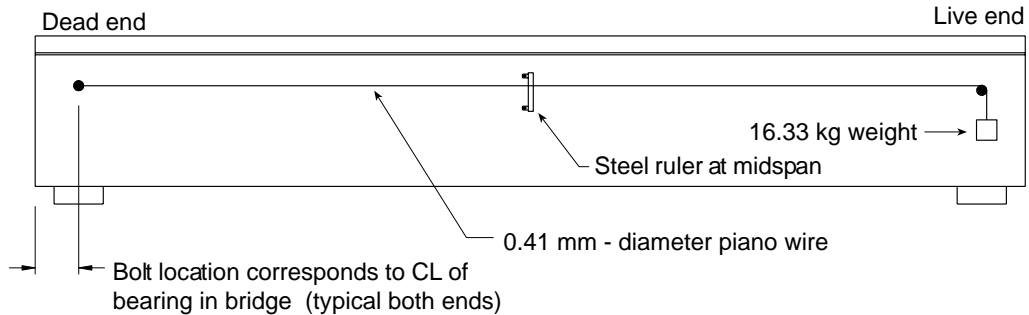


Figure 3.16 Schematic of tensioned piano wire camber and deflection measuring system

In this system, a steel ruler was fixed at midspan on both sides of each instrumented beam by retrofitting two bolts into the web. Small aluminum plates with holes in them were mechanically fastened on the bolts, and the ruler was fixed onto the plates using five-minute epoxy. Small C-clamps were used to apply pressure and to help hold the ruler in place. During positioning of the plates and ruler, care was taken to ensure that the ruler would be plumb once it was fastened in place.

To allow for tensioning of the piano wire, bolts were also retrofitted at each end of the beam. Each bolt was positioned approximately 250 mm from the end of the beam, which corresponded to the bearing locations in the bridge, and approximately 450 mm from the top of the beam. During positioning of the ruler and end bolts, it was important to have an initial reading that would be at the top part of the ruler. This would allow for the beam to gain camber without exceeding the length of the ruler (approximately 300 mm). One of the end bolts had a small hole drilled through the exposed end. This end was designated the “dead end” and would have the piano wire threaded through the hole and tied to a small washer. The bolt on the opposite end was machined so that a grooved roller bearing could fit onto the bolt and rotate freely. This end was designated the “live end” where the tension would be applied to the piano wire.

Since the piano wire was attached to the beam at the ends and the ruler was attached at the midspan, any change in camber could be determined by the relative movement of the ruler with respect to the tensioned piano wire. To obtain a reading, tension was applied by attaching a portable 16.33 kg weight to the free end of the wire. This weight was determined to be sufficient to create the necessary tension in the size six (0.41 mm-diameter) piano wire

that was used for this system. A loop tied at the free end of the wire was hooked onto the weight, and the piano wire was placed in the machined groove on the outside surface of the bearing. The weight was slowly lowered until the piano wire and weight reached equilibrium. Finally, a reading was taken on the ruler at midspan. A small mirror was placed behind the ruler and wire to eliminate parallax during the reading. To determine the camber of the beam, the reading needed to be compared to the initial reading that was taken just before release of the prestressing force. The accuracy of the rulers in this system were 0.01 inches. This accuracy is equivalent to approximately 0.25 mm.

Once the beams were transported to the job site, the tensioned piano wire system could no longer be utilized. Section 4.3.1 describes several reasons why the system failed at that point. A precise surveying system was employed in which beam elevations were measured at the supports and at the midspan of each beam using a level and rod.

Figure 3.17 shows a picture of the researchers measuring beam elevations with this system. To obtain accurate readings, the level needed to be very close to the rod and the rulers used in the original system needed to be fastened to the rod. Paint markings were placed on the underside of the beams to locate the surveying points. Readings under this system were read to 0.02 inch accuracy on the ruler, which is equivalent to approximately 0.51 mm. This system worked well and had acceptable repeatability. Some of the difficulties encountered while using this system are described in Sec. 4.5.



Figure 3.17 Precise surveying system for measuring beam camber

3.4 DATA ACQUISITION

3.4.1 General

The method of data acquisition chosen for this study was an automated system that could handle the readings from dozens of gages at frequent time intervals. This was a necessary aspect of the data acquisition system because of the complexity and size of the instrumentation plan. Although the automated system was more costly and required significant time and labor in preparation, the savings in work in the field and during data

reduction and analysis were beneficial. The following sections describe the data acquisition system that was implemented in this study and the data reduction required to make the readings usable for analysis.

3.4.2 Data Acquisition System

The primary requirements for the data acquisition system (DAS) were that it must be able to read all three types of internal instrumentation, and that it must be self-contained, transportable, and able to be positioned onto the bridge once construction was completed. Two complete data acquisition systems were necessary to read all of the instrumentation in the beams, deck panels, and cast-in-place decks of both bridges. Figure 3.18 shows a picture of a typical data acquisition system box.



Figure 3.18 Data acquisition system (DAS) box

The box, which served as a protective shell and as a mounting board for the electronic equipment, was constructed using 19 mm-thick plywood for the base and top and 50 mm by 200 mm wood pieces for the sides. Each box measured approximately 690 mm long, 610 mm wide and 250 mm tall. One side of the box was fabricated with pre-drilled holes to accommodate the Amphenol connectors that were used to interface the instrumentation with the data acquisition equipment. The opposite side of the box was used to mount a thermocouple connector board that was used to interface with male thermocouple connectors. The exterior of each box was fashioned with hinges, handles and a latch. A complete box, including the equipment inside, weighed approximately 15 kg.

Inside the box, the data acquisition equipment was positioned as shown in Figure 3.18 to minimize wiring clutter. All of the components needed for reading the instrumentation were manufactured by Campbell Scientific, Inc. Each box was equipped with a CR10 datalogger and 12 volt power supply. The datalogger read the instrumentation by interfacing

with AM416 relay multiplexers. The multiplexers were wired into the Amphenol connectors on the side of the box. The number of multiplexers in a box depended upon the amounts of each type of instrumentation in the particular bridge. Storage modules were used to hold the programming for the CR10 and to hold the data from the instrumentation. A keypad was used as an interface with the CR10 and was connected in series with the datalogger and storage module. The storage modules could be connected to a personal computer for downloading data as well as further programming.

3.4.3 Data Reduction

The raw measurements from the instrumentation and the date and time data were all in voltages. The program in the storage module was only set up to change the temperature instrumentation readings from voltages to temperatures and the rest of the data was converted using a short program written for use on an IBM compatible personal computer. To convert the strain instrumentation data, the initial readings of the instrumentation were needed. Data was downloaded from the storage module into the personal computer and input into the program. The program also sorted the raw data files and arranged new data files so that they could be inserted into a spreadsheet.

An option for data transfer which was not employed by the researchers was the use of a modem to send the data directly from the DAS boxes to the personal computer. Since the DAS box was being moved to several locations before construction of the bridges, the independent power supply and storage modules were a good system. The advantage of the modem would be realized once the DAS boxes were fixed permanently on the bridges. However, changing systems would not have been efficient, and the periodic switching of storage modules and batteries in the boxes was not difficult.

Once the data was put into a useful form, additional factors needed to be considered before that data could be compared to analytical predictions. Thermal gradients within the beam are created as a result of changes in external temperature conditions throughout the day and throughout the year. The thermal gradients induce differential strain on the cross section of the beam and cause additional curvature in the beam, which affects the camber readings. This needed to be taken into account to calculate the actual camber of the beam. The internal temperature instrumentation provided the information to make this correction.

The support conditions of the beams needed to be carefully recorded when taking measurements otherwise the data would have little meaning. After the beams were lifted off the prestressing bed, they were stored in the yard on wooden railroad ties. The support locations were usually 0.5 to 1.0 meters in from the beam ends and did not correspond to the bearing locations in the bridge. Many of the beams cast in 1994 were moved in the yard several times and the support locations moved as well. The data needed to be adjusted for these varying support conditions so that an accurate comparison of beam camber could be made based upon the span length from bearing to bearing in the bridge.

3.5 MATERIALS

3.5.1 Precast U-Beams

All of the beams in this study were cast using the high performance concrete mix design that was developed as part of this research program. Table 3.9 shows the details of the mix design used for the U-beams. The required compressive strengths at transfer and at 56 days for this concrete are summarized in Table 3.3.

The prestressing steel used in all of the instrumented beams was 15.2 mm-diameter, grade M203, low relaxation, seven wire strand. The strands were manufactured by Shinko Wire America, Inc. The elastic modulus for the strand was assumed to be 193 GPa for calculation purposes. All nonprestressing steel used in the beams was AASHTO M31M, Grade 400 reinforcement.

Table 3.9 Concrete mix design for the instrumented U-beams

Component	Quantity	Unit	Description	Source
Coarse Aggregate	1,138	kg/m ³	Crushed Dolomitic Limestone, 1-1/4 cm max	Pioneer Concrete Co.
Fine Aggregate	644	kg/m ³	Sand	The Fordyce Co.
Water	113	kg/m ³	Potable	City of Victoria
Cement	398	kg/m ³	Type III	Capitol Cement Co.
Fly Ash	187	kg/m ³	Deely Type B	Deely Fly Ash Co.
Retarder	1.04	L/m ³	Pozzolith 300R	Master Builders
Superplasticizer	6.89	L/m ³	Rheobuild 1000	Master Builders

3.5.2 Precast Deck Panels

Table 3.10 summarizes the mix design for the precast prestressed deck panels. The material properties of the deck panels in the northbound bridge were not studied because they were not included in the instrumentation plan. The deck panels in the southbound bridge were cast using this high performance concrete mix design. The specified compressive strengths at release and at 28 days was 41.4 and 55.2 MPa, respectively.

Table 3.10 Concrete mix design for the precast deck panels

Component	Quantity	Unit	Description	Source
Coarse Aggregate	1176	kg/m ³	Crushed River Gravel, 19 mm max.	
Fine Aggregate	659	kg/m ³	Sand	The Fordyce Co.
Water	135	kg/m ³	Potable	City of Houston
Cement	335	kg/m ³	Alamo Type III	Capitol Cement Co.
Fly Ash	97	kg/m ³	Class C	JTM
Retarder	0.85	L/m ³	Pozzolith 300R	Master Builders
Superplasticizer	6.24	L/m ³	Rheobuild 1000	Master Builders

3.5.3 Cast-in-Place Deck Slabs

The deck slab for the southbound bridge was cast with a high strength, high performance concrete mix. The specified 28-day design strength for cast-in-place decks for the southbound bridge was 55.2 MPa. Table 3.11 summarizes the concrete mix design for the cast-in-place deck in the southbound bridge.

The deck slab for the northbound bridge was cast with a normal-strength high performance concrete mix that had a specified 28-day design strength of 27.6 MPa. Table 3.12 summarizes the concrete mix design for the cast-in-place deck in the northbound bridge.

3.6 COMPANION TESTS

3.6.1 General

Several laboratory tests were performed on concrete cylinders made from the concrete used to cast the instrumented beams, panels and cast-in-place deck. These tests determined the properties of the high performance concretes that were necessary for making analytical predictions of the long-term behavior of the prestressed concrete U-beams and of the composite bridge section. Most of the concrete cylinders used for the tests were the smaller 100 mm diameter by 200 mm tall specimens. The main reason for the smaller specimens was to reduce the compressive force necessary to test the high strength concrete mixes. The specimens were cured under varying conditions, including match-cured using the internal temperatures of the members, member-cured, and moist-cured following ASTM specifications.

Table 3.11 Concrete mix design for the southbound main lanes bridge CIP deck

Component	Quantity	Unit	Description	Source
Coarse Aggregate	1074	kg/m ³	Southwest Texas Limestone, 19 mm max.	
Fine Aggregate	772	kg/m ³	Sand	The Fordyce Co.
Water	146	kg/m ³	Potable	City of Houston
Cement	281	kg/m ³	Hunter Type I	
Fly Ash	131	kg/m ³	Class C	JTM
Retarder	0.85	L/m ³	Pozzolith 300R	Master Builders
Superplasticizer	16.15	L/m ³	Rheobuild 1000	Master Builders

Table 3.12 Concrete mix design for the northbound main lanes bridge CIP deck

Component	Quantity	Unit	Description	Source
Coarse Aggregate	1101	kg/m ³	Southwest Texas Limestone, 19 mm max.	
Fine Aggregate	737	kg/m ³	Sand	The Fordyce Co.
Water	136	kg/m ³	Potable	City of Houston
Cement	230	kg/m ³	Hunter Type I	
Fly Ash	89	kg/m ³	Class C	JTM
Retarder	0.85	L/m ³	Masterpave 'R'	Master Builders

3.6.2 Modulus of Elasticity

Concrete stress-strain tests were performed in accordance with ASTM C469-81 (50) on 100 mm by 200 mm specimens. A compressometer which satisfied ASTM C469-81 requirements and which fit onto the smaller specimens was used to measure the strain. Concrete elastic moduli were found based upon the results of the tests. Specimens from all of the relevant beam, panel, and deck pours were tested at 1 day and at 28 days. The specimens from the two beam pours in 1996 were also tested at 7 days and 56 days.

3.6.3 Compressive Strength

Compressive strength tests were performed in accordance with ASTM C39-83b (51) on 100 mm by 200 mm specimens. The specimens were tested at the same ages as the elastic modulus specimens. Results from these tests were used to construct age-strength gain curves for the different concrete mixes. This type of curve was of special interest for the prestressed beams because of the very high release strengths that were required in the beam designs.

3.6.4 Creep and Shrinkage

Creep and shrinkage tests were performed on 100 mm by 600 mm specimens specially fabricated using PVC pipe sections sealed on one end with aluminum disks. The creep tests conform to the specifications of ASTM C512 (52). All of the tests were performed in the Austin, Texas laboratory in a room without temperature or humidity control. This was the best attempt at simulating the actual environment of the beam, panel, and deck concretes.

Figure 3.19 shows a picture of a typical creep test frame. Load was applied to a cylinder by means of a hydraulic ram and a load cell. The springs and plates in the system lock the applied load onto the specimen. Periodic re-application of the desired level of load was required as the specimen deformed over time. Indication of when to re-apply the load was obtained by monitoring the deformation of the springs. Strains in the concrete were measured using the Demec mechanical strain gage. Strains in several unloaded specimens were also measured to determine the shrinkage portion of the deformation in the creep specimens. Records were kept for the cylinder temperature, ambient temperature, and humidity so that the data could be thermally compensated. A detailed description of the steps for specimen preparation and testing can be found in a report by Farrington et al. (8).

Farrington et al. (8) performed much of the testing on the beam mix design. His work included variables such as age of loading, magnitude of loading, and temperature of curing. Since Farrington only monitored the specimens up to an age of 120 days, the researchers of this study continued monitoring the specimens through the beginning of service life of the bridge. Additional tests were performed by the researchers on the precast panel mix design and both cast-in-place deck mix designs. The testing procedures were the same as those used for the beam specimens. The panel and deck creep specimens were loaded at 2 days to 20 percent and 40 percent of the specified 28-day compressive strength. Readings were taken on shrinkage specimens at the same time as the creep specimens.



Figure 3.19 Creep test specimens sustaining applied load

3.6.5 Coefficient of Thermal Expansion

Coefficient of thermal expansion tests were performed on the concrete mixes used to cast the instrumented beams, panels, and decks in the bridge. The specimens used for these tests were 100 mm by 600 mm cylinders. Specimens for the beams were over 180 days old when tested and were cycled between 4 °C and 71 °C in an environmental chamber. The resulting coefficient of thermal expansion for the precast beam mix was 11.0×10^{-6} per degree Celsius. This value was close to the coefficient of thermal expansion for normal strength concrete. Specimens for the precast deck panels and cast-in-place decks were at least 56 days old when tested. The resulting coefficient of thermal expansion for the precast deck panel mix was 13.1×10^{-6} strain per degree Celsius. Results for the northbound and southbound CIP deck mixes were 7.2×10^{-6} and 7.6×10^{-6} strain per degree Celsius, respectively.

CHAPTER 4. FIELD WORK

4.1 INTRODUCTION

4.1.1 Coordination with Contractors

While proper preparation of the instrumentation plan was necessary to obtain the required data for long-term prestress loss, section behavior, and camber and deflection, an equally necessary and challenging aspect of this study was coordination with the contractors during the implementation of the instrumentation plan. One of the challenges was to convey the importance of the research to the contractors while keeping in mind that their primary interest was in operating profitable businesses. Additional challenges included time management for traveling and instrumentation preparation, dealing with unforeseen problems in the field, and being flexible enough to adapt to the contractors' schedules as much as possible. The latter aspect helped to establish a favorable working relationship between the researchers and the contractors.

Cooperation and coordination with Texas Concrete Company, which fabricated the precast U-beams, was not a problem. Being one of the first prestressing plants to deal with high performance concrete for beam production, Texas Concrete was very helpful to the researchers during all stages of the beam fabrication, instrumentation, and monitoring. Further work with Houston Prestress Products, Inc., during instrumentation of the precast deck panels was satisfactory as well. Williams Brothers, Inc., was helpful at the job site, providing a man lift for use during installation of the data acquisition system (DAS) boxes in the bridge, during connection of the gages to the DAS boxes, and during further accession of the DAS boxes to retrieve data.

4.1.2 Chapter Format

This chapter's organization reflects the chronological order of the fabrication and construction of the bridges. It summarizes the field operations that were an important part of this research study. Initial comments are given on the procedures used to prepare the instrumentation for installation in the field. Fabrication and instrumentation procedures for the beams, deck panels, and cast-in-place decks are described. The chapter concludes with a section describing some of the problems encountered during the instrumentation installation and monitoring activities.

4.2 PREPARATION OF INSTRUMENTATION

When specific dates were established for a beam, panel, or deck slab pour, it was immediately necessary to review the instrumentation plan and prepare the gages that would be installed. The typical preparation included the following:

1. Prepare the various gages as described in Sec. 3.3.
2. Prepare lead wire for the gages. This step included spooling out, cutting, and bundling lead wire for groups of gages. The grouping of gages to a specific

connector was done in the instrumentation plan. The length of lead wire was important because the connectors needed to reach the DAS box location on the bridge.

3. Attach the gages to the bundled lead wires.
4. Attach the connector to the bundled lead wires.
5. Gather the necessary equipment for the tensioned piano wire system (beams only).

During the instrumentation of the beams that were cast in 1994, the lead wires were simply bundled together for transportation. Problems were encountered as the wires, which sometimes exceeded 30 meters in length, became tangled, making installation cumbersome. Experience with those pours indicated that a more efficient means of gathering the massive amounts of lead wire was needed to speed up installation and minimize delays to the contractor. A spooling system for lead wires for transportation to the site was developed in 1996 in response to that problem. Figure 4.1 shows a picture of the spooling system.



Figure 4.1 Spooling system used to gather gage lead wires

The spools were constructed from plywood and used to gather up the lead wire after it was measured out, cut, and bundled. A wooden A-frame with steel hooks on the top was used to operate the spooling system. A broomstick was used to spin the spool on the stand. The gages were connected to the appropriate wire ends so that the spools could be unwound again at the site. This system saved time during preparation, transportation, and installation.

4.3 PRECAST OPERATIONS

4.3.1 Precast Beams

All twelve of the instrumented beams were cast at the Texas Concrete Company prestressing plant in Victoria, Texas. Eight of the beams were cast in late 1994 while the remaining four beams were cast in early 1996. The beam pours were arranged so that no more than two of the instrumented beams were cast during the same pour. This reduced delays for the fabricator and also eased the burden on the researchers. Nine pours were needed to fabricate all of the beams that were part of this study. The histories for all of the instrumented beams are shown in Tables 4.1 and 4.2.

Table 4.1 Southbound main lanes bridge beam histories

Event	Time from Casting (Days)					
	S14	S15	S16	S24	S25	S26
Casting completed	0	0	0	0	0	0
Initial instrumentation measurement taken	1.19	1.19	1.12	1.14	1.10	7.05
Transfer of prestressing force	1.30	1.30	1.18	1.19	1.15	7.11
Beam moved to storage location	1.32	1.32	2.96	1.22	1.17	7.19
Beam shipped to and placed in bridge	150	150	664	623	623	657
Panels placed on beam	211	211	725	684	684	718
Casting of deck slab	256	256	770	729	729	763

Table 4.2 Northbound main lanes bridge beam histories

Event	Time from Casting (Days)					
	N21	N22	N23	N31	N32	N33
Casting completed	0	0	0	0	0	0
Initial instrumentation measurement taken	1.16	1.03	0.99	1.20	1.29	1.29
Transfer of prestressing force	1.22	1.09	1.03	1.28	1.35	1.35
Beam moved to storage location	2.90	2.88	2.86	3.04	1.38	1.38
Beam shipped to and placed in bridge	636	664	671	636	161	161
Panels placed on beam	697	727	734	712	245	245
Casting of deck slab	734	762	769	734	259	259

All of the U-beams were cast on the same bed. The bed was sufficiently long to cast three beams in one pour. This casting bed needed to be upgraded to a capacity of nearly 17.8 MN to handle the design prestressing force for the U-beams. In addition, the stressing hardware needed to be retooled to handle this capacity.

The stressing operation was typically done two to three days before casting. The strands were pulled down the bed from the fixed end abutment to the stressing end with a fork lift and were hand-threaded through the steel header forms, which were located at both ends of each beam. The strands were then hand-threaded through the stressing plate at the “live” or stressing end. The stressing end consisted of a stressing plate attached to a reaction plate with large diameter rods. Because the larger 15.2-mm diameter strands were used, special chuck placement was needed for the stressing operation. Spacers were placed between the stressing plate and the chucks so that they would fit in the 50 mm grid spacing of the strands. After the chucks were secured, the multi-strand stressing commenced. The stressing plate was pulled forward as the hydraulic jacks pushed against the abutments and reaction plate. The stressing ended when the proper elongation of the strands was reached. This was determined based on the initial design stress of 1396 MPa, which is seventy-five percent of the specified strand strength.

Once the strand pattern was in place and stressed, strand debonding was applied with split plastic tubing. Where debonding was specified by design, the tubing was cut to proper length before being slipped over the strands and sealed with tape to prevent intrusion of the concrete paste during casting. Appendix A contains the debonding details for the instrumented beams.

After completing the stressing and debonding of the strands, the reinforcing steel was placed and tied. Much of the mild reinforcement consisted of welded-wire fabric and pre-tied cages. Once the steel was tied in place, the internal strain gages and thermocouples were attached to the strands or the stirrups at the required vertical and horizontal locations using rebar ties. Figure 4.2 shows an internal strain gages installed in a beam. Once all of the gages were tied in on one side of the beam, the lead wire was secured to the reinforcement with nylon cable ties. In an attempt to avoid damage from mechanical vibration of the concrete during casting, the lead wires were run up to the top flange at their horizontal location and tied along the top flange to the end of the beam.



Figure 4.2 Internal instrumentation placed at midspan of a beam

Next, the forms were placed in preparation for casting. Fork lifts with spreader bars were used to position the multiple side-form sections. These sections were bolted together and attached to the header forms that were placed before the stressing operation. Opposing side forms were connected with collars at the diaphragms to add rigidity. Finally, adjustable-length steel “tubs” were positioned as the internal void forms for the U-beams. These tubs were held in place by additional steel collars connected to the side forms.

Concrete placement followed shortly after the forms were positioned and secured. All of the high performance concrete was batched at the mixing plant and transported to the casting bed in an auger bucket using a fork lift. The concrete was placed in the forms using a dispensing unit coming from the auger bucket. It was imperative that the formation of voids in the bottom flange was avoided during casting. To do this, the concrete, with a slump of approximately 200 mm, needed to be placed on one side of the beam and forced across the bottom flange and partially up the opposite web. Then, concrete was placed on the other side of the beam to complete the casting. To ensure consolidation, external and internal vibration was used. This procedure was successful for all of the instrumented beams except Beam S26. After the forms were removed from Beam S26, voids were found in the bottom flange around the strands and patching was necessary to cover up the exposed strands. This delayed the transfer of prestress force for one week.

Once casting was completed, the beams were covered with tarps and allowed to cure to achieve the required release strength. Usually, it took only 24 to 27 hours to obtain the design release strength. After removal of the forms, the tensioned piano wire camber measurement system was installed on both sides of the beam. Also, researchers placed the mechanical strain gages (Demec points) in their locations. The typical external instrumentation that was installed at midspan is shown in Figure 4.3. Just before transfer of the prestress force, an initial measurement was taken for all of the instrumentation. After the initial measurements were gathered, the tension in each of the strands was released simultaneously.

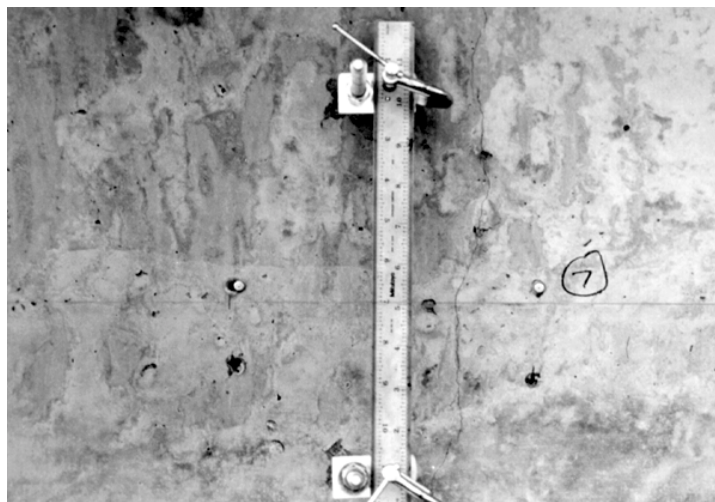


Figure 4.3 External instrumentation placed at midspan of a beam

Upon release of the tension, the excess strands were flame cut and removed. The researchers reconnected the DAS box to read the internal gages and measured the camber and surface strains. Figure 4.4 shows measurements being gathered with the DAS box. The beams were moved to storage locations within one or two days after transfer using large fork lifts. The bearing locations for storage were measured and recorded for future analytical use. Figure 4.5 shows a typical beam in storage at the prestressing plant.

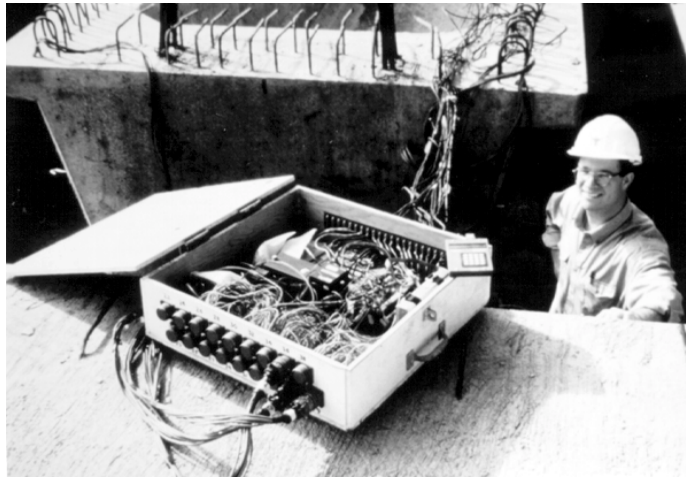


Figure 4.4 Measurements being gathered with the data acquisition system (DAS) box



Figure 4.5 Typical instrumented beam in storage at the prestressing plant

After the casting and release sequence, measurements were taken at appropriate time intervals to monitor the increase in camber resulting from creep effects. Once the beams were two to three months old, measurements were taken every few months until the beams were erected in the bridge. When the bearing conditions changed for a beam while it was in

storage, an additional reading was taken as soon as possible. Also, measurements were taken at several times during a particular day to monitor how thermal gradients that developed in the beams affected their camber. Tables 4.3 and 4.4 summarize the bearing locations for the instrumented beams.

The beams were transported to the job site and erected in the bridge on July 25, 1996. Final storage measurements were taken for all of the instrumented beams before this was done. A modification to the typical hauling system for the AASHTO Type IV beams was made to account for the heavier load of the U-beam. The longest truck was approximately 52 meters long and had extra spread axles in both the front and back to carry the load. Figure 4.6 shows the hauling system used to transport the beams. When the beams arrived at the job site, two large cranes were used to lift the beams off of the trucks and place them in the bridge. Figure 4.7 shows a beam being placed in the bridge.

Table 4.3 Support locations and span lengths for the southbound main lanes bridge beams

Beam	Time from Casting (Days)	Average Distances from Ends (m)		Span length (m)
		North End	South End	
S14	2	0.48	0.79	34.67
	150	0.17	0.22	35.55
S15	2	0.50	0.73	35.18
	150	0.17	0.23	36.01
S16	3	0.36	0.99	35.54
	21	0.52	0.86	35.51
	263	0.34	0.62	35.93
	664	0.17	0.23	36.89
S24	1.2	0.34	0.37	39.45
	8	0.45	0.38	39.33
	623	0.17	0.17	39.83
S25	1.2	0.42	0.39	39.85
	488	0.42	0.33	39.91
	620	0.53	0.36	39.77
	623	0.17	0.17	40.33
S26	7	0.43	0.46	40.29
	53	0.41	0.34	40.43
	657	0.17	0.17	40.84

Table 4.4 Support locations and span lengths for the northbound main lanes bridge beams

Beam	Time from Casting (Days)	Average Distances from Ends (m)		Span length (m)
		North End	South End	
N21	3	0.30	0.30	40.63
	20	0.39	0.39	40.45
	636	0.17	0.17	40.90
N22	3	0.23	0.57	40.60
	21	0.38	0.56	40.46

Beam	Time from Casting (Days)	Average Distances from Ends (m)		Span length (m)
		North End	South End	
	263	0.53	0.29	40.58
	347	0.53	0.36	40.51
	664	0.17	0.17	41.07
N23	3	0.70	0.39	40.49
	28	0.38	0.37	40.83
	671	0.17	0.17	41.25
N31	3	0.98	0.31	39.45
	20	0.89	0.48	39.37
	235	0.59	0.48	39.67
	636	0.22	0.17	40.35
N32	2	0.60	0.42	39.88
	161	0.23	0.17	40.50
N33	2	0.55	0.43	40.08
	161	0.23	0.17	40.66



Figure 4.6 U-beam being transported to the job site



Figure 4.7 U-beam being erected in the bridge

Approximately two weeks after the beams were erected in the bridge, measurements were taken for all of the instrumentation. Since most of the beams were almost two years old, the delay in getting that reading was not critical. At that point, the precise surveying system was developed and implemented to measure camber and deflection for the beams. This was done because many components of the piano wire systems, particularly the rulers, were damaged or missing. In addition, it was determined that restringing the piano wire, hanging the weight, and reading the ruler at midspan would be very difficult and time consuming for the beams in their elevated final positions. The precise surveying system proved to be a time-saving method of measuring camber after the beams were erected in the bridge. A complete set of camber measurements generally took one hour to complete.

4.3.2 Precast Deck Panels

Three high performance concrete deck panels were instrumented as part the deck instrumentation plan in the southbound bridge. The panels were cast in September of 1996 at the Houston Prestress Products, Inc., precast plant in Houston, Texas.

A new bulkhead for the stressing bed had to be manufactured to accommodate the 89 mm thick panels because the typical panel thickness used in Texas bridges is 102 mm. The 9.5-mm diameter strands were placed on the bed and stressed individually to 1862 MPa, and the welded wire fabric was placed underneath the strands and tied to the strands. Wood spacer blocks were used to form the ends of the panels, and in some cases, the sides of the panels that were less than the width of the bed.

Once the steel was in place, the deck panel instrumentation was tied in place. The lead wires for these gages were simply wound manually during preparation because there were only four gages per group. During installation, the lead wires were unraveled five to eight meters so that only the wire necessary to clear the casting bed was available. The remainder of the lead wires were left bundled so that they could be easily transported with the panels to the bridge. The internal strain gages and thermocouples were fastened in place with nylon cable ties and electrical tape, and the lead wires were carefully run along the strands and reinforcement to the edges of the panels. Just before casting, all of the gages were connected to the DAS box to get an initial measurement and one of the instrumented panels was monitored throughout casting.

Once the instrumentation was in place, the fabricator was ready to cast the panels. The concrete mixer came on the side of the bed and workers directed the flow of concrete onto the bed. After the concrete was poured onto the bed and spread out, the screed was guided along the side forms of the bed by two workers. The screed was equipped with a vibrator so that simultaneous vibrating and screeding could be done. Typical procedures for finishing the concrete were utilized. Workers followed after the screed to finish the concrete and to roughen the top surface of the panels with a large brush.

Throughout the casting, the workers were very conscientious about concrete placement in the instrumentation locations. The instrumentation could have sustained damage from shovels, boots, and the screed. However, no damage was observed as the panels were fabricated.

After the casting was completed, a tarp was placed over the entire bed. This tarp was supported by four strands tensioned above the bed to hold it above the panels. The panels were cured under the tarps without steam. The DAS box was connected to one set of panel gages to get measurements through transfer of the prestressing force the following morning.

Once the design strength was reached, the panels were transported to the bridge on flatbed trucks. The panels for the southbound main lanes bridge were erected beginning on September 24, 1996. The panels for spans one and two of the northbound main lanes bridge were erected beginning on September 26, 1996. Panels for span three were erected on October 17, 1996. A set of instrumentation measurements was obtained to record the strains and cambers in the beams just before placement of the panels. Before the panels were placed in the bridges, strips of fiberboard needed to be glued on the inside and outside edges of each flange of each beam. The typical dimensions of the fiberboard were 25.4 mm wide by 12.7 mm thick. A crane was used to lift the panels and place them on the beams. Figure 4.8 shows the placement of a panel and the fiberboard glued on the beam.



Figure 4.8 Precast deck panel being placed in the bridge

Complete erection of the panels occurred over the course of approximately two to three weeks. Measurements were taken when some of the beams had only a fraction of the panels on them. Table 4.5 summarizes the loads on the beams when these measurements were taken. Measurements corresponding to post-placement of the deck panels were taken just before casting of the northbound CIP deck.

Table 4.5 Conditions when measurement were taken after precast deck panel erection

Bridge	Span	Conditions During Measurements
Southbound	1	S14 - gap on the west side of beam had no panels. S14 and S15 - Additional load of two to four piles of lumber. S15 and S16 - all panels erected.
Southbound	2	S24 and S25 - all panels erected. S26 - south 40 percent of panels erected.
Northbound	2	N21 - south end to midspan panels erected, south end panel missing. N21/N22 gap - south end to north quarter point panels erected. N22 - south end to south third span panels erected, south end panel missing. Two stacks of plywood at midspan. N22/N23 gap - all panels erected. Four stacked panels and one stack of plywood along gap. N23 - south end to south quarter point panels erected.
Northbound	3	N31, N32, and N33 - All panels erected..

4.4 CAST-IN-PLACE DECKS

4.4.1 Preparation

To accommodate the instrumentation placed in the deck, most of the ERSGs in the beams cast in 1994 were disconnected by cutting off the lead wires.

These gages were not yielding useful data at that time, so their removal was not a problem. Also, several of the thermocouples used for match-curing were removed. Owing to the addition and subtraction of gages, some rewiring needed to be done in the DAS boxes.

Before casting the decks, the DAS boxes needed to be placed on the bridge. To accomplish this, a mounting board and enclosure were devised to facilitate placement of each box vertically onto the side of a beam. Figure 4.9 shows a DAS box positioned in the bridge.



Figure 4.9 Data acquisition system (DAS) box mounted in the bridge

The construction of the mounting board and enclosure was done in the lab. The board was a 1220 mm wide by 1070 mm deep by 18.3 mm thick piece of plywood that was covered with a 3.2 mm thick piece of Plexiglas for protection. Large holes were cut in each end of the board to enable the gages to be hooked up to the box once the cover was on. A bracket was made to account for the side slope of the beam and was placed on the bottom of the board. The enclosure was constructed of 3.2 mm thick Plexiglas with 25.4 mm by 50.8 mm wood pieces used as framing. The enclosure was sealed with silicone and the entire assembly was painted black.

At the site, anchor bolts were retrofitted into the beam, and the mounting board and bracket piece were placed onto the bolts and fastened mechanically. Next, the DAS box was fixed onto the mounting board using steel brackets. Finally, the enclosure was fixed onto the board over the DAS box using hinges and a latch. The boxes were positioned at the southeast quadrant of Beam N31 for the northbound main lanes bridge and at the southwest quadrant of Beam S26 for the southbound main lanes bridge.

4.4.2 Instrumentation

Before the deck instrumentation could be installed, the longitudinal and transverse reinforcement for the deck had to be completely tied into place by the workers. The VW gages and ERSGs were tied to the rebar using nylon cable ties. This proved to be a questionable method of fixing the gages in place because the ties did not resist rotation of the gage around the rebar very well. Thermocouples were fixed into place with electrical tape. The lead wires were unspooled and tied along the top of the reinforcement and run to the ends of the beams. Figure 4.10 shows a strain gage tied into the deck steel.

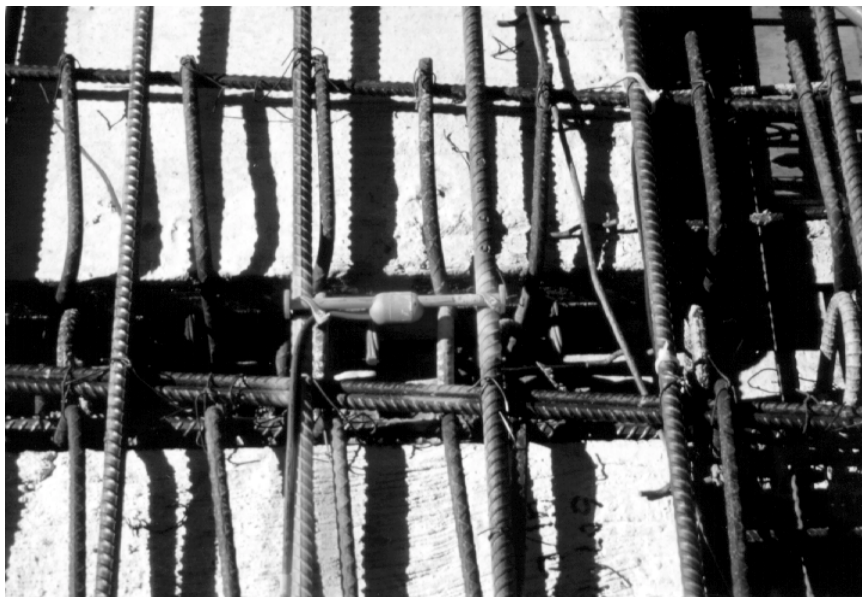


Figure 4.10 Instrumentation tied into cast-in-place deck reinforcement

At the joint between the spans, full depth cast-in-place concrete was required and the contractor had to create forms for these sections. This provided an opportunity to run the lead wires through the deck to be hooked up to the DAS box. Several holes were drilled into the formwork closest to the position of the DAS box. Then, all of the beam and deck connectors were fed through the holes and connected to the DAS box.

4.4.3 Casting

The northbound main lanes bridge deck was cast on October 31, 1996 and the southbound main lanes bridge was cast on November 8, 1996. Concrete for the cast-in-place decks was provided by Lopez-Gloria Construction Services, Inc. of Houston, Texas. Before casting, the screed assembly was set up. The assembly moved longitudinally on steel tubes placed on the side forms and was advanced by workers pushing it. The screed moved along the bridge and was mechanically driven. Because the widths of the decks were variable, the screed assembly needed to have the ability to shorten as the width decreased. On the day prior to casting, the screed elevations were set so that the deck thickness would meet the design tolerances.

Before casting began, the DAS box for the appropriate bridge was turned on to get measurements just prior to and during casting of the deck. Camber measurements were also taken on the instrumented beams before the casting began and immediately after the casting was finished.

Figure 4.11 shows the typical casting operations for both bridge decks. Casting began early in the morning and lasted until after dark because each deck was done in one pour. Concrete was delivered from the batch plant, located a few miles away, to the bridge using mixers. A pump truck was used to transport the concrete from the mixers to the deck for placement. Workers used shovels to spread the concrete and mechanical vibrators to consolidate the concrete. The instrumentation was exposed to damage from shovels, vibrators, and boots as the concrete was poured over them. In addition, the force of the concrete as it poured out of the tube was enough to possibly move the gages out of position. On several occasions, the gages needed to be repositioned after the concrete was poured over them. The weather condition during casting was very windy, so the concrete was fogged to keep moisture from escaping the mix. Next, the screed passed through and leveled out the concrete. Behind the screed assembly, a finishing bridge was used by workers to trowel the deck surface and apply curing compound. Once the surface showed signs of setting, it was tined using a rake. Finally, the deck was covered with blankets for curing. During the casting, the field engineers measured the deck thickness at the ends and midspan longitudinally and at the ends and one-third points transverse to the span. Table 4.6 summarizes the measured deck thickness for both bridges.

After the decks were cast, internal instrumentation measurements were taken at one-hour time intervals. Camber measurements were taken several times in the month following the completion of the decks and then approximately once every two months after that time.



Figure 4.11 Casting operations for the bridge decks

Table 4.6 Average measured deck thickness

Northbound Main Lanes Bridge		Southbound Main Lanes Bridge	
Beam	Average Thickness (mm)	Beam	Average Thickness (mm)
N21	190	S14	190
N22	190	S15	195
N23	185	S16	195
N31	190	S24	215
N32	185	S25	205
N33	185	S26	205

Notes:
 1. Average thickness includes deck panel thickness

4.5 PROBLEMS ENCOUNTERED IN THE FIELD

4.5.1 Difficulties with Instrumentation Placement

The main problem relating to beam instrumentation arose when the gages were being permanently connected to the DAS box in the northbound main lanes bridge. Three groups of lead wires from Beams N22 and N33 were not long enough to reach the DAS box location. The wires coming from Beam N33 were too short because the gages for Beam N32 were mistakenly put into Beam N33 during instrumentation at the precast plant. The switching of gages didn't matter because they were identical for both beams. Several other groups of gages were just long enough to reach the DAS boxes, which showed that the estimations for excess lead wire were not conservative enough. This oversight was corrected in time for the

instrumentation of the beams in 1996. The wires coming from Beam N22 were too short because the locations of the DAS boxes in the bridges were not finalized until after the beams were erected. The solution to this problem was simply to make extension pieces of lead wire to allow those groups of gages to be connected to the DAS box.

Another problem occurred while installing the instrumentation in one of the precast deck panels. In panel NS-32 that was placed between Beams S15 and S16 at midspan, the gages were positioned on the wrong side of the panel. These gages needed to be positioned off a side of the panel that was parallel to the strands so that they would coincide with the midspan of Beam S15. Instead, the instrumentation was placed off a side of the panel that was transverse to the strands. The result was that the gages were out of alignment with the rest of the deck and panel gages.

The remainder of the instrumentation problems occurred in the cast-in-place decks. In the deck for the northbound main lanes bridge, the exact vertical distances of the gages above the beams and panels were not measured. An assumption was made based upon the locations of the reinforcement. This oversight was corrected while instrumenting the deck for the southbound main lanes bridge. Another problem was that the nylon cable ties used to tie the gages to the reinforcement didn't fix the gages in place as well as desired. The gages had a tendency to move if they were disturbed at all. Since the deck casting operation had many opportunities for disturbances, keeping the gages in their desired locations became a problem. A more secure method for fixing the deck gages in place should have been used.

4.5.2 Damaged Instrumentation

Since most of the lead wires were embedded in the beams, the main opportunity for damage was from the mechanical vibrator used to consolidate the concrete. However, a few of the lead wires were damaged while the beams were being transported to the site and erected in the bridge. The exact cause of the damage was not determined, but one possibility was that the wires were inadvertently damaged by a heavy chain or a piece of equipment. These wires were spliced back together before being permanently connected to the DAS box. Subsequent measurements taken with the corresponding gages yielded good results.

The tensioned piano wire system was damaged in the field several times and ultimately rendered unusable after the beams were transported to the site. During storage of the beams at the precast plant, C-clamps were routinely removed from the rulers leaving only the epoxy to hold the rulers in place. Since the five minute epoxy gel did not have long-term durability, there was a chance that the ruler would fall off the aluminum plates. The ruler was reattached to the plates using the impression of the plates on the old epoxy to reposition it. At other times, the rulers were missing and a new ruler had to be re-epoxied to the aluminum plates. Each camber measurement using a new ruler was adjusted based on the known measurement on the other side of the beam. This adjustment assumed that both sides of the beam experienced the same change in camber from the previous reading. Table 4.7 describes which beams had rulers replaced while in storage and what adjustments were made to subsequent camber measurements.

After the beams were transported to the job site, 17 of the 24 rulers were completely gone and many of the anchor bolts were sheared off. Since the camber system relied upon the initial reading to be able to measure future cambers, it would have been very difficult to correlate new readings to the previous ones. The only way this could have been done was to assume an offset between the two sets of readings. Instead, the precise surveying system was established at the job site.

Table 4.7 Adjustments to the tensioned piano wire camber and deflection system

Beam	Side	Time from Casting (Days)	Operation	Adjustment To Future Measurements
N22	east	424	re-epoxied ruler	none
S16	east	152	placed new ruler	6.86 mm lower
S16	west	424	re-epoxied ruler	none
S25	west	287	placed new ruler	1.53 mm lower
S26	east	256	placed new ruler	4.83 mm lower
S26	east	321	placed new ruler	1.53 mm higher

The final incidence of damage to instrumentation occurred while the cast-in-place decks were being poured. Several of the deck gages were stepped on and moved out of position during placement of the concrete. It would have been very difficult to avoid all possible damage to the gages, considering the deck pouring procedures. However, a better system of tying gages to the reinforcement would have reduced the magnitude of the damage.

4.5.3 Measurements

There were very few problems while taking measurements of the internal strain gages and thermocouples with the DAS boxes. The post-transfer measurement for Beam N33 was not obtained because the DAS box was not turned on after the gage connectors were hooked up. However, this was not discovered until several days after the measurement and there was no way to correct the problem. Since twelve beams were instrumented, this mistake was not critical to the study. Also, the initial reading for Beam N23 was not taken prior to transfer. Since the baseline measurement was not obtained, the data from the strain gages was useless. However, the loss of that data was not critical because Beam N23 only had two ERSGs at midspan.

Strain gage measurements were taken before the deck panels were placed on the beams, but most of these measurements did not yield valid strains. The cause for this problem was probably due to an error with the DAS box or because of bad connections when the gage connectors were hooked up to the box. Since the beams were quite old, the previous measurements were used to represent the strain just before placement of the panels. In addition, the data gathered just before casting of the northbound bridge deck was not found

on the data storage module. Fortunately, several of the strain gages were working after the decks were cast.

Measurement of camber seemed to present the greatest variety of problems. Both of the camber measuring systems were very sensitive to gusts of wind. For the tensioned piano wire system, wind caused the wire to vibrate causing the reading on the ruler to vary by as much as 3 mm. It was usually possible to get the wire to remain still long enough so that a precise reading could be obtained. For the precise surveying system, wind caused the rod to move, which made reading the rulers through the level very difficult.

Another problem with the tensioned piano wire system was that the lower bolt that supported the ruler began to interfere with the piano wire on Beam N23. Fortunately, this problem did not occur until the beam was 335 days old. In addition, the piano wires frequently broke, which meant that a lot of time was spent restringing the piano wire.

When the beams were ready for shipment to the job site, a communication breakdown between the researchers and the contractor resulted in some of the instrumented beams being loaded onto the trucks before a final storage reading could be taken. Camber measurements were obtained for all but one of the beams before shipment to the job site. This was not a significant problem since the beams were very old at that time.

While taking camber measurements just before casting the southbound main lanes bridge deck, part of the screed assembly was being supported by the instrumented beams in span one. This happened because of the skew of the bridge and because the casting began in span one. While taking camber measurements after the deck panels were in the bridge, additional loads were introduced due to stacks of lumber and various pieces of equipment used to construct the side forms for the deck. Also, some of the panels were not in place when camber and other measurements were taken because they hadn't been shipped to the site. Most of these problems were caused by the nature of construction and could not be controlled. Camber measurements were taken just before the decks were cast to be used in determining the deflection caused by the deck panels.

CHAPTER 5. OBSERVED BEHAVIOR

5.1 INTRODUCTION

Data obtained from the field instrumentation and from the companion tests are presented in this chapter. Camber and deflection data are shown for all twelve instrumented U-beams for a time period beginning with transfer and ending approximately five months after completion of the composite bridge deck. Strains at midspan at the center of gravity of the prestressing strands are presented for the same periods of time as the camber and deflection data. In addition, midspan strain profiles are presented at release and through erection of the beams. This chapter also presents the internal temperatures that developed in the beams while they were in storage and that developed in the composite sections after the bridge deck was completed.

5.2 COMPANION TEST RESULTS

5.2.1 Concrete Compressive Strength

Concrete compressive strength test results for the seven pours corresponding to the instrumented beams at release, 28 days, and 56 days are summarized in Figures 5.1 to 5.3, respectively. Strength data were obtained from specimens cured under four different regimens to compare how the strength gain with time varied with the curing environment. The TxDOT specimens were cured with the beams before release and then moist cured in saturated lime water at 23 °C after release. The ASTM specimens were cured in a room kept at 23 °C before release and then moist cured similarly to the TxDOT specimens after release. Member cured specimens were kept with the beams both before and after release. SureCure specimens were cured based on the temperature of the bottom flange of the beam before release and kept with the beams after release.

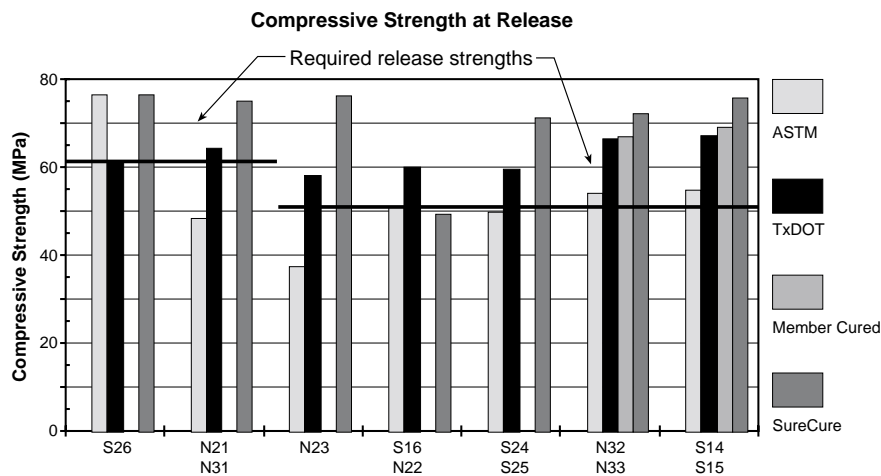


Figure 5.1 Compressive strength at release for HPC U-beams

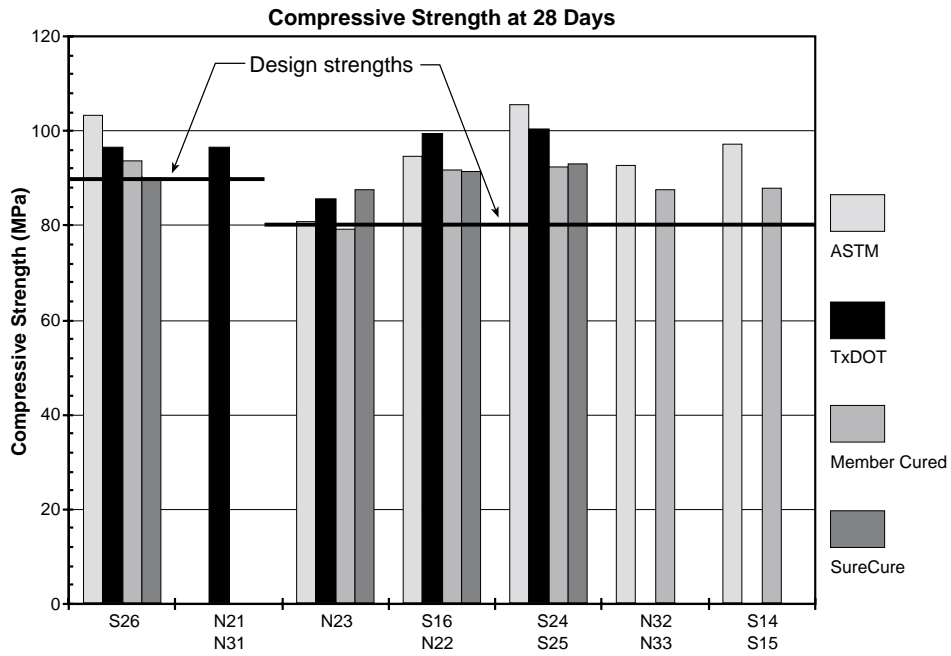


Figure 5.2 Compressive strength at 28 days for HPC U-beams

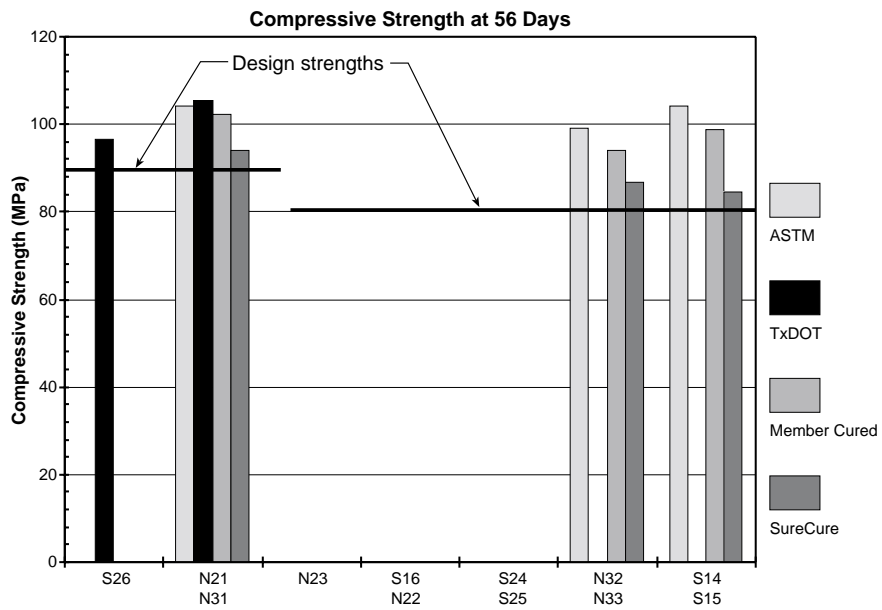


Figure 5.3 Compressive strength at 56 days for HPC U-beams

The required compressive strengths at release were 60.7 MPa for Beams N21, N31, and S26, and 53.1 MPa for the other beams. Figure 5.1 shows that the ASTM specimens,

with the exception of Beam S26, failed to reach the required release strength in four of the seven pours. Beam S26 was higher for all curing regimens because transfer of the prestressing force was at 7 days after casting. The SureCure specimens exhibited higher strength than the other curing regimens in all but one of the pours. For that pour, the SureCure system was not working properly. The higher early strength of the SureCure specimens can be attributed to the higher curing temperatures that the specimens experienced while being match cured with the temperature of the bottom flange of the beam.

The 56-day design compressive strengths were 90.3 MPa for Beams N21, N31, and S26, and 80.0 MPa for the other beams. The compressive strengths at 28 and 56 days are shown in Figures 5.2 and 5.3, respectively. For some of the beams, the required strength had already been reached at 28 days and thus the 56 day strength was not measured. These figures show the data that was available. At the ages of 28 and 56 days, the ASTM specimens that were cured at lower temperatures showed higher strengths than the SureCure specimens that were cured at higher initial temperatures. Furthermore, the SureCure and member cured specimens that were stored near the beams in an uncontrolled environment showed lower strengths than the ASTM and TxDOT specimens that were kept in a controlled environment. The average strengths at release, 28 days, and 56 days for each curing regime are summarized in Table 5.1.

Table 5.1 Average compressive strengths of HPC beam specimens under various curing regimens

Curing Regimen	Average Compressive Strength (MPa)		
	Release	28 days	56 days
ASTM	53.2	95.7	102.6
TxDOT	62.4	95.7	100.9
Member Cured	68.0	88.7	98.3
SureCure	70.9	90.6	88.4

Table 5.2 Average elastic moduli of HPC beam specimens

Pour	Beam(s)	Average Elastic Modulus (GPa) ¹		
		Release ²	28 days ³	56 days ³
1	N23	44.3	43.9 ⁴	N/A
2	S16, N22	35.2	47.8	N/A
3	S26	44.0	51.7	N/A
5	N21, N31	40.0	N/A	46.3
7	S24, S25	37.8	44.5	N/A
8	N32, N33	43.4	45.1	46.6
9	S14, S15	41.5	42.9 ⁴	46.1

Notes:

1. Minimum specified elastic modulus was 41.4 GPa.
2. Data from tests of SureCure specimens.
3. Data from tests on member cured specimens.
4. Data from tests on ASTM cured specimens

To get the best representation of the compressive strength and deformation properties of the concrete at a specific age, the environment to which the concrete was subjected must be considered when choosing the appropriate curing regime. Before release, the SureCure specimens provided the best representation of the beam concrete because the specimens were being cured at the same temperatures as the beams. After release, the member cured specimens gave the best representation of the beam concrete because the specimens were subjected to the same uncontrolled environment that the beams experienced.

An age-strength gain equation (Eq. 5.1) for the HPC beam mix was developed using the member cured specimens at all ages and the TxDOT cured specimens at release. A linear regression analysis was used to obtain a best fit curve for this data (correlation factor = 0.95). The data and the best fit curve are shown in Figure 5.4. Equation 5.1 was used in Chapter 6 with an analytical time-step method for predicting prestress losses, camber, and deflection in the instrumented beams.

$$\left(f'_c\right)_t = \frac{t^{0.4}}{0.58 + 0.85t^{0.4}}(90.5) \quad (\text{MPa}) \quad (5.1)$$

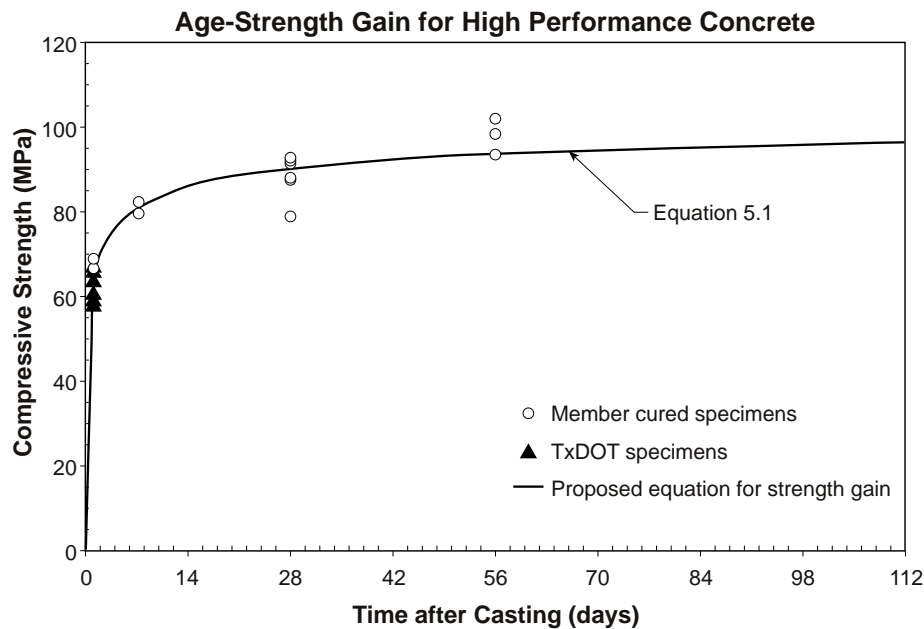


Figure 5.4 Age-strength gain for HPC beam mix based on member cured specimens

5.2.2 Elastic Modulus of Concrete

The average elastic moduli of the beam concrete for all of the pours corresponding to instrumented beams are summarized in Table 5.2. A minimum elastic modulus of 41.4 GPa

was specified in the beam design to limit deflections under superimposed dead load and live load. Data are shown for match cured specimens at release and member cured specimens at later ages, since these regimens were the most representative of the instrumented beams.

The measured elastic modulus data corresponding to the compressive strength of the cylinders cast with the high performance concrete (HPC) used for the instrumented beams are shown in Figure 5.5. There was enough scatter in the data for cylinders cured under similar conditions to conclude that curing conditions had little or no effect on the elastic modulus versus compressive strength data. The AASHTO Specifications (16) equation for calculating modulus of elasticity based on compressive strength is also shown in this figure. This curve was calculated using the unit weight of the high performance concrete, which was 2481 kg/m^3 . Based upon the data shown, the AASHTO equation clearly overestimated the elastic modulus of HPC cylinders with compressive strengths greater than 60 MPa.

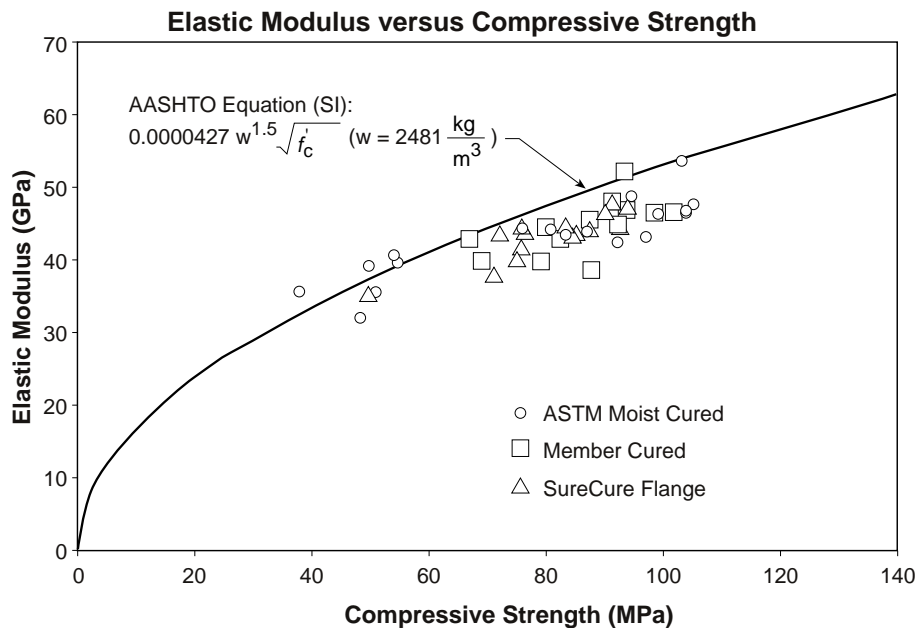


Figure 5.5 Elastic modulus versus compressive strength for HPC U-beam mix

A better formula for calculating the elastic modulus of concrete with high compressive strengths was required for making predictions of long-term deformation behavior. Figure 5.6 shows the ACI Committee 363 (13) recommended equation for concrete with compressive strength greater than 41.4 MPa plotted along with the measured data. Carrasquillo et al. (12) developed this formula based on tests of concrete mixes having gravel and crushed limestone aggregates and having compressive strengths between 20.7 and 82.7 MPa. Carrasquillo found that for cylinders with equivalent compressive strengths, the ones with crushed limestone aggregate had elastic moduli that were consistently higher than those with gravel aggregate. Since most of the data used to develop the ACI Committee 363 equation was based on cylinders with gravel aggregates, it tended to underestimate the elastic

moduli for the beams in this study, which were cast from a concrete mix having crushed limestone aggregate.

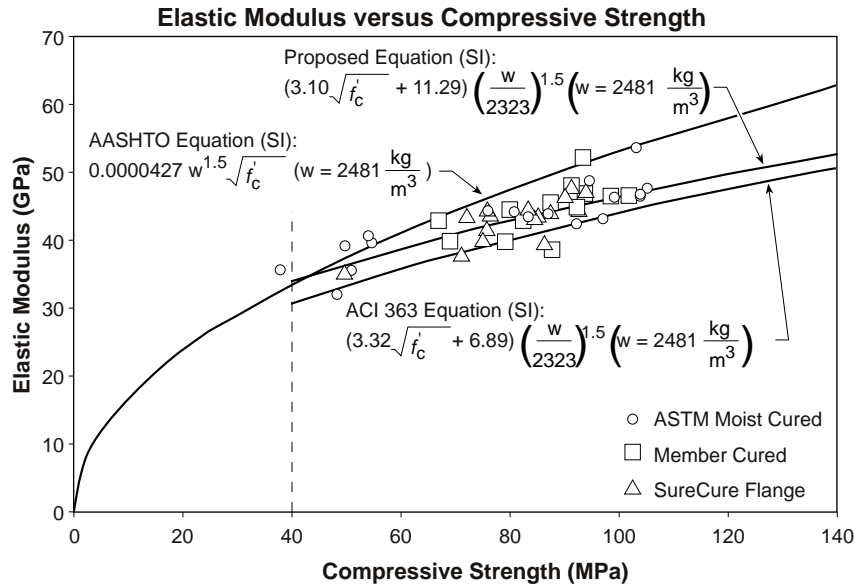


Figure 5.6 Proposed equation for elastic modulus for HPC U-beams

A more accurate equation for calculating the elastic modulus (GPa) for the high performance concrete used to cast the beams in this study was developed by adopting the form of the ACI Committee 363 equation and fitting a new curve to the measured data. The proposed equation for elastic modulus is as follows:

$$E_c = (3.10\sqrt{f'_c} + 11.29) \left(\frac{w}{2323}\right)^{1.5} \quad (5.2)$$

This equation is shown graphically in Figure 5.6 along with the AASHTO and the ACI Committee 363 equations. The proposed equation is valid for the high performance concrete mix used for the beams in this study and for the range of compressive strengths represented by the test data.

5.2.3 Creep and Shrinkage Properties of Concrete

As mentioned in Sec. 3.6.4, Farrington (8) tested eighteen creep specimens cast from the high performance concrete used to make the beams in this study. The effects of curing temperature, age of loading, and level of loading were examined as part of that study. The creep data used in this study were taken from the specimens loaded at one day under all three

stress levels, cured next to the beams, and cured with a peak internal temperature of 63 °C. Unloaded specimens were used to determine the shrinkage and thermal portions of the strains measured for the loaded specimen.

The shrinkage specimens were cured under conditions similar to the creep specimens and were stored in the same room as the creep specimens during testing. Since the creep and shrinkage tests were performed in the laboratory in Austin, the test specimens and the beams were subjected to different environments. The average relative humidity in Victoria was estimated to be 75 percent while the average relative humidity in the laboratory was approximately 55 percent. Because the testing room was not a controlled environment, corrections for relative humidity were not made on the shrinkage data.

The measured strains for the creep and shrinkage tests are shown in Figure 5.7. The creep strain is the difference between the measured strain for the creep specimen and the measured strain for the shrinkage specimen. The measurements were adjusted to remove the thermal strain from the creep and shrinkage strains. The internal temperature in the shrinkage specimen was recorded during each measurement and compared to the temperature of the specimen at loading. By using the measured coefficient of thermal expansion of the beam concrete, which was 11.0 microstrain/°C, a thermal strain was determined for the temperature differential and used to correct the measurements.

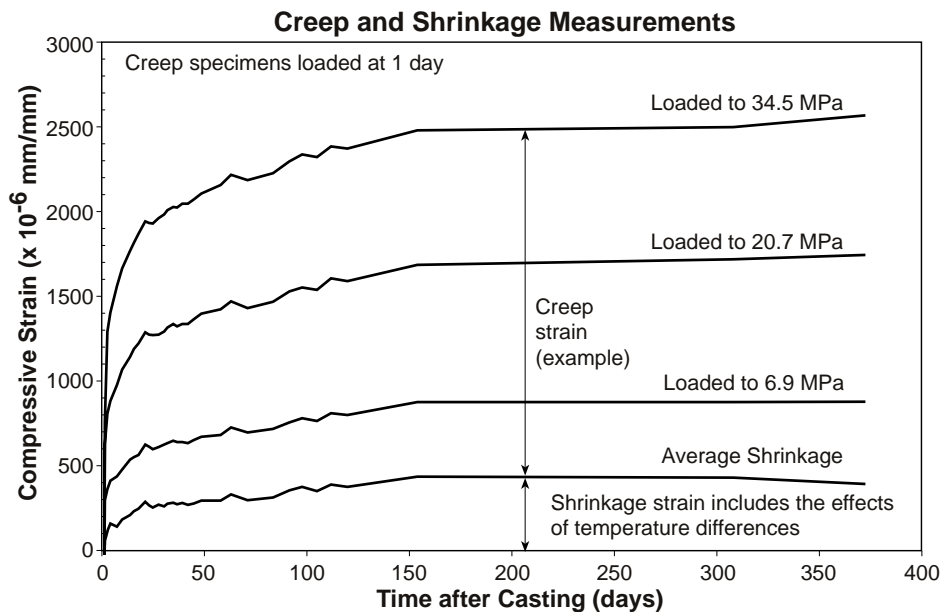


Figure 5.7 Raw measurements used to determine creep and shrinkage curves for the HPC U-beams

The measured creep coefficient, which is defined as the ratio of strain resulting from creep and the initial elastic strain, is shown in Figure 5.8. The measured creep coefficient represented an average of the creep coefficients for the three specimens. Measurements from

all three specimens could be used because the level of loading did not influence the ultimate creep coefficient (8). Averaging the creep coefficients for the three specimens allowed more data to be used for determining a best fit creep equation.

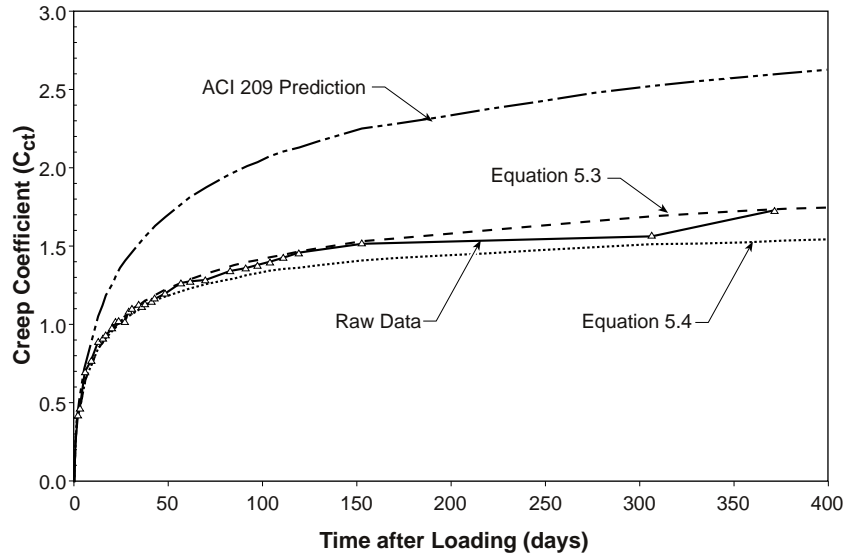


Figure 5.8 ACI prediction and proposed equations for creep coefficient

Two best fit curves were developed for the measured creep data as shown in Figure 5.8. The creep curves, given in Eqs. 5.3 and 5.4, were based on different time functions. These curves are based on data for 372 days of loading on the test specimens. The correlation factors for these curves were very close (0.997 for Eq. 5.3 and 0.996 for Eq. 5.4), but the ultimate creep coefficients were quite different. The ultimate creep coefficients for the HPC beam mix were 2.28 in Eq. 5.3 and 1.76 in Eq. 5.4. Equation 5.3 is used in Sec. 6.4 for analytical predictions of prestress losses, camber, and deflection. Both of these equations are used in Chapter 6 for developing camber and deflection multipliers.

$$C_{ct} = (2.28) \left(\frac{t^{0.5}}{6 + t^{0.5}} \right) \quad (5.3)$$

$$C_{ct} = (1.76) \left(\frac{t^{0.6}}{5 + t^{0.6}} \right) \quad (5.4)$$

The ACI Committee 209 prediction (19) of creep coefficient for this specimen was included in Figure 5.8 as a comparison to the measured creep coefficient. A detailed description of the ACI Committee 209 procedures for determining creep coefficient is presented in the report

by Farrington (8). The form of the ACI creep function is different than the forms of the best fit curves. The ultimate creep coefficient for the ACI Committee 209 curve was 3.35. The ACI prediction of ultimate creep overestimated the measured ultimate creep coefficients shown in Eqs. 5.3 and 5.4 by 47 and 90 percent, respectively.

The average measured shrinkage strain for the high-temperature cured specimens is shown in Figure 5.9. These measurements were sensitive to the relative humidity and ambient temperature fluctuations in the uncontrolled environment in the room where the tests were performed. Increases in the relative humidity would cause moisture in the air to be absorbed by the concrete resulting in swelling of the concrete. This caused the measured shrinkage strain to be distorted.

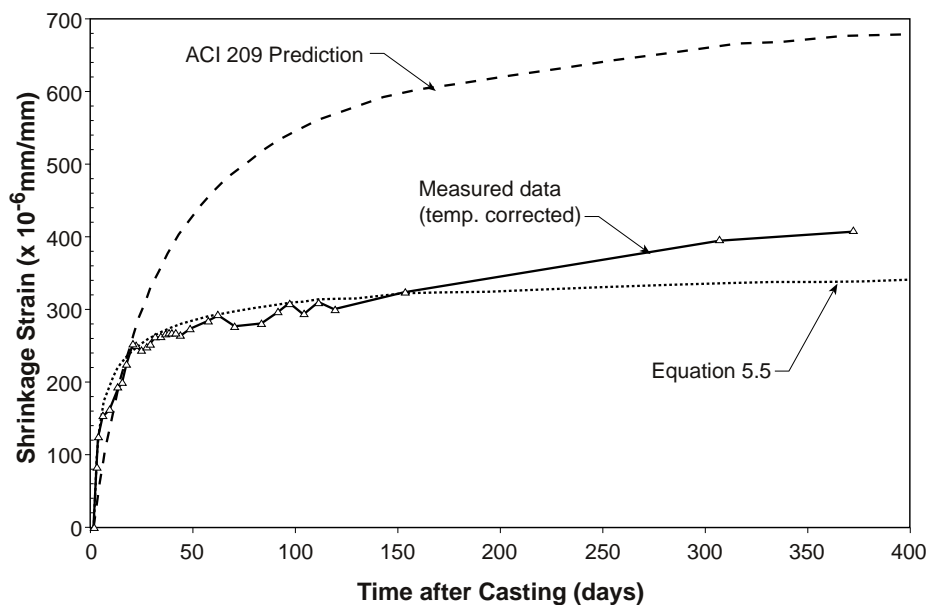


Figure 5.9 ACI prediction and proposed equation for shrinkage strain

The ACI Committee 209 prediction (19) of shrinkage for these specimens is included in Figure 5.9 as a comparison to the measured data. Equation 5.5 represents the best fit curve through the data shown in Figure 5.9. However, the measured data needed to be corrected for the shrinkage strain that occurred between stripping of the cylinders and the baseline Demec readings. The amount of time that occurred between those two events was approximately 12 hours. An approximation of the additional shrinkage strain was made by shifting the best fit curve (Eq. 5.5) up by 12 hours and then determining a correction based upon the slope of the best fit curve at that point. A new best fit curve, given in Eq. 5.6, was developed after this correction in which the ultimate shrinkage strain was 456 microstrain.

$$(\epsilon_{sh})_t = (.000368) \left(\frac{t^{0.6}}{3 + t^{0.6}} \right) \quad (5.5)$$

$$(\epsilon_{sh})_t = (.000456) \left(\frac{t^{0.6}}{2 + t^{0.6}} \right) \quad (5.6)$$

The ACI prediction of ultimate shrinkage, which was 738 microstrain, overestimated the measured ultimate shrinkage of the high performance concrete by 62 percent. Equation 5.6 was developed to provide an accurate means of predicting the long-term shrinkage of the beams cast with this HPC mix. This equation is used in Chapter 6 for analytical predictions of prestress losses.

5.3 FIELD MEASUREMENTS

5.3.1 Camber and Deflection

The measured time-dependent camber and deflection responses at midspan of the twelve instrumented U-beams are shown in Figures 5.10 to 5.21. The camber and deflection response history for each beam was monitored from the time just before transfer to the time five months after the cast-in-place decks were completed. Significant events are noted along the time axis of Figures 5.10 to 5.21, reflecting the important stages of construction of the composite prestressed concrete bridge.

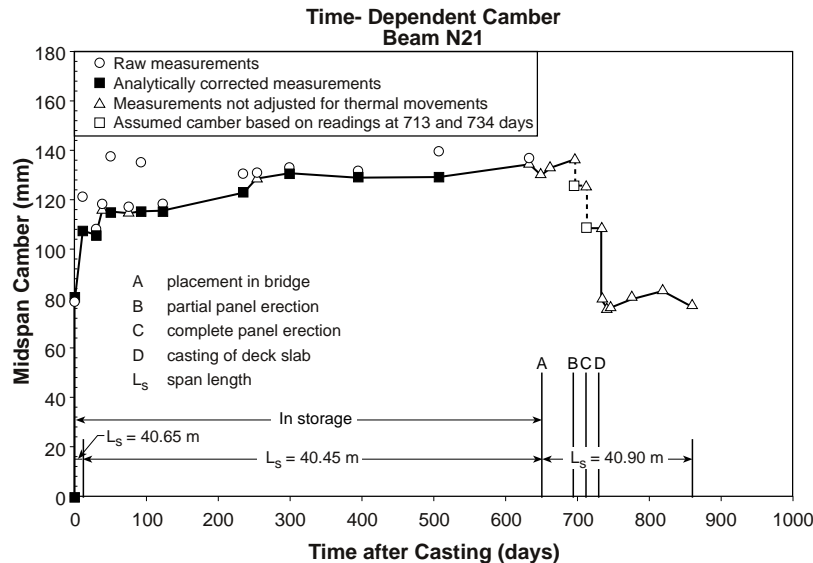


Figure 5.10 Measured midspan camber and deflection response for Beam N21

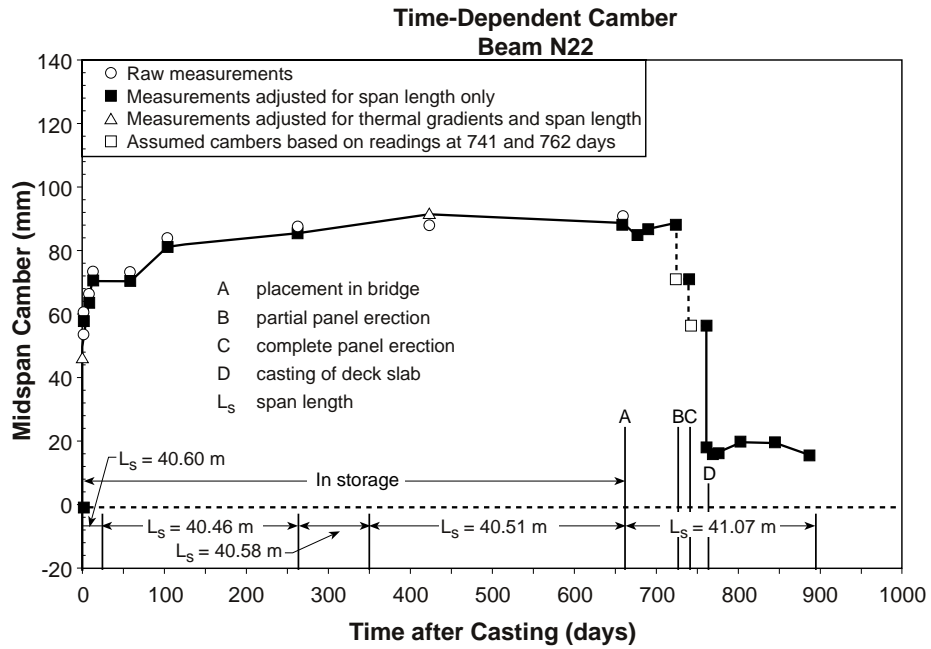


Figure 5.11 Measured midspan camber and deflection response for Beam N22

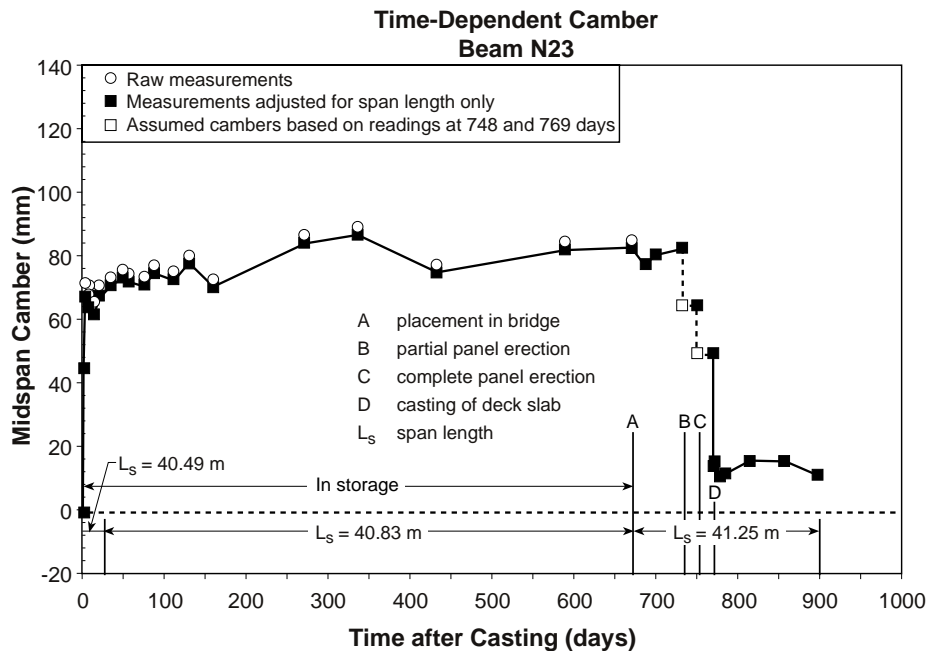


Figure 5.12 Measured midspan camber and deflection response for Beam N23

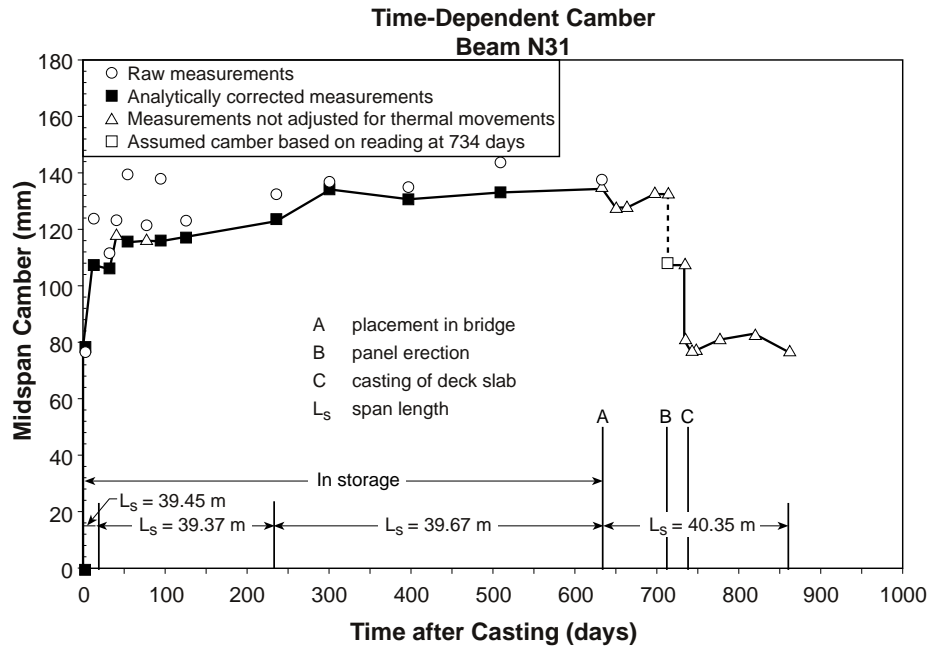


Figure 5.13 Measured midspan camber and deflection response for Beam N31

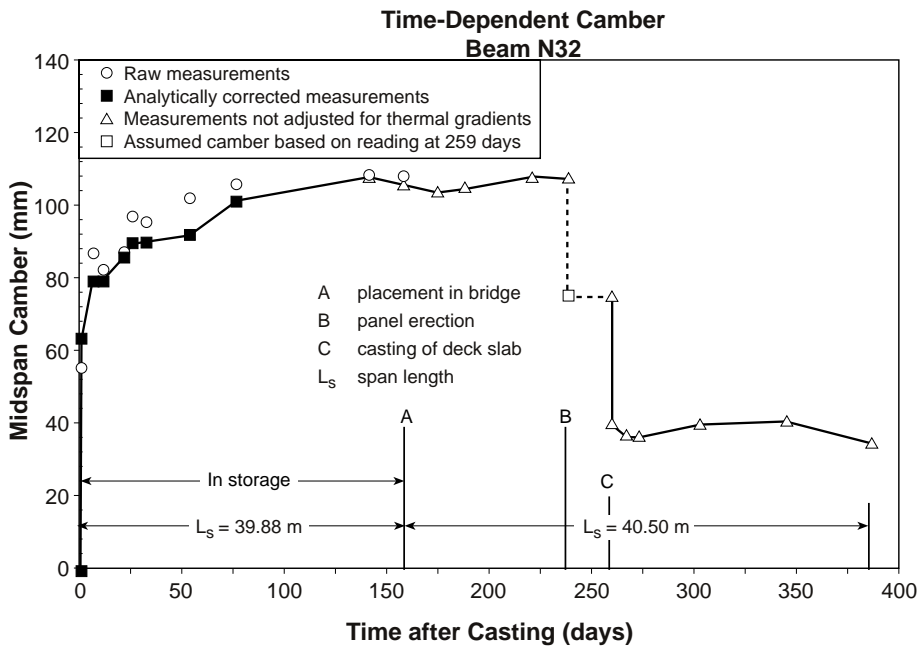


Figure 5.14 Measured midspan camber and deflection response for Beam N32

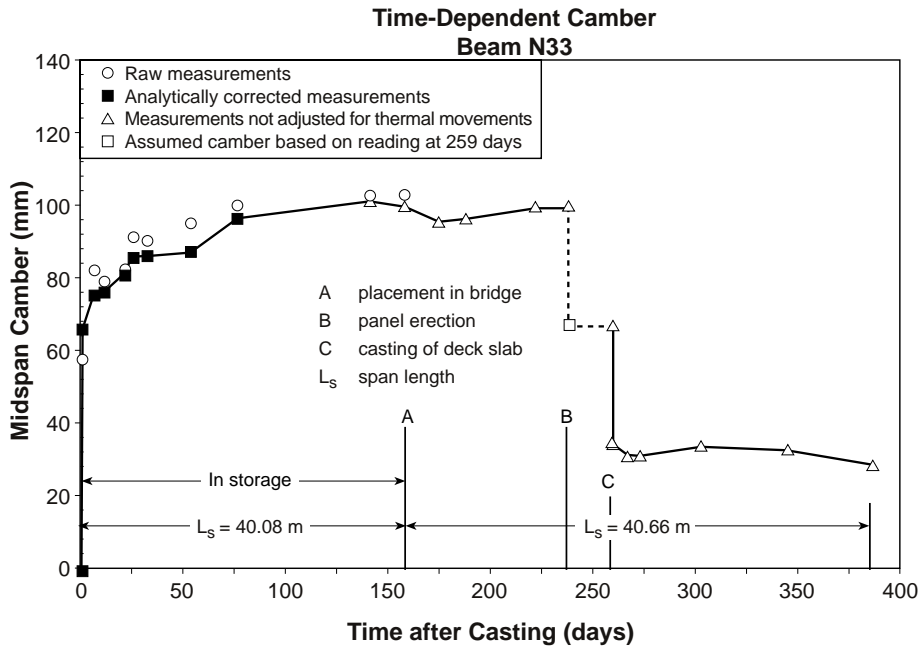


Figure 5.15 Measured midspan camber and deflection response for Beam N33

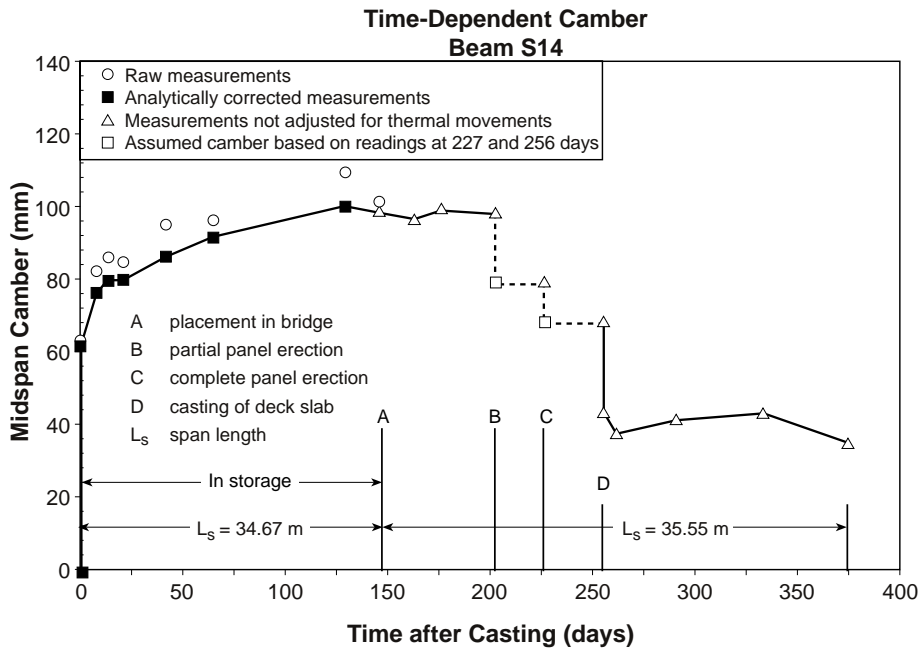


Figure 5.16 Measured midspan camber and deflection response for Beam S14

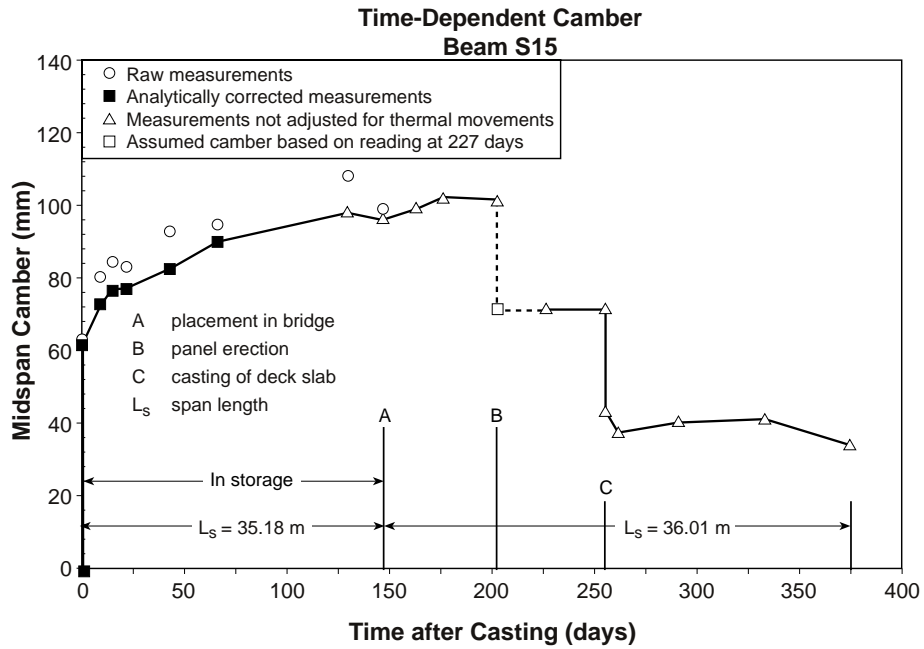


Figure 5.17 Measured midspan camber and deflection response for Beam S15

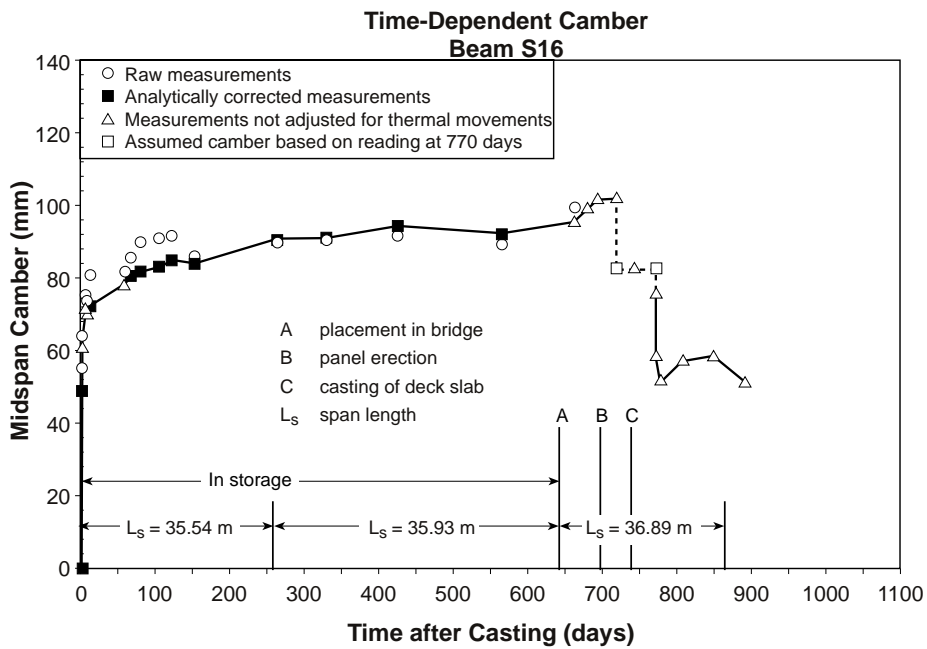


Figure 5.18 Measured midspan camber and deflection response for Beam S16

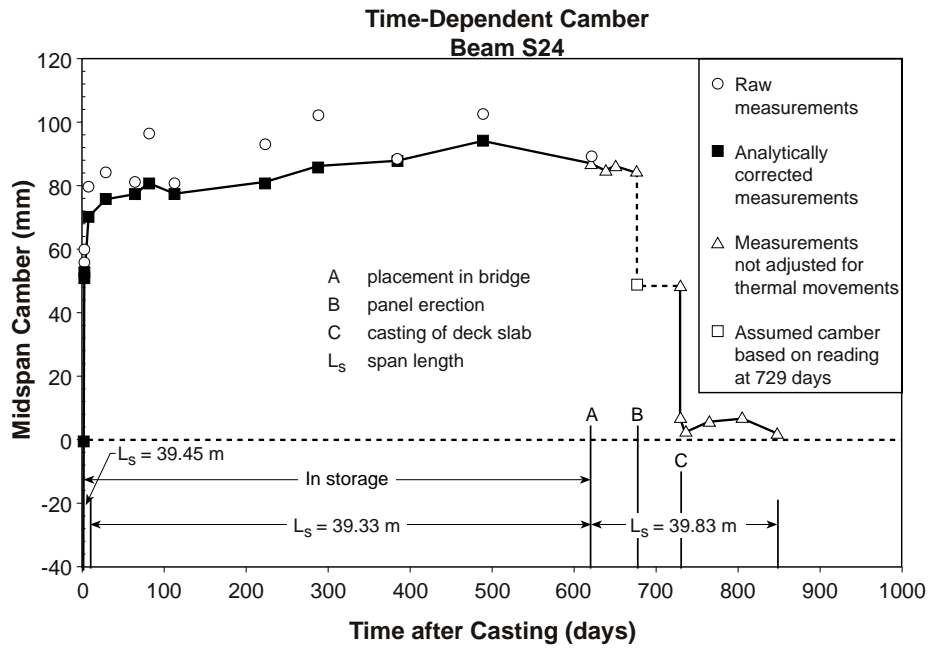


Figure 5.19 Measured midspan camber and deflection response for Beam S24

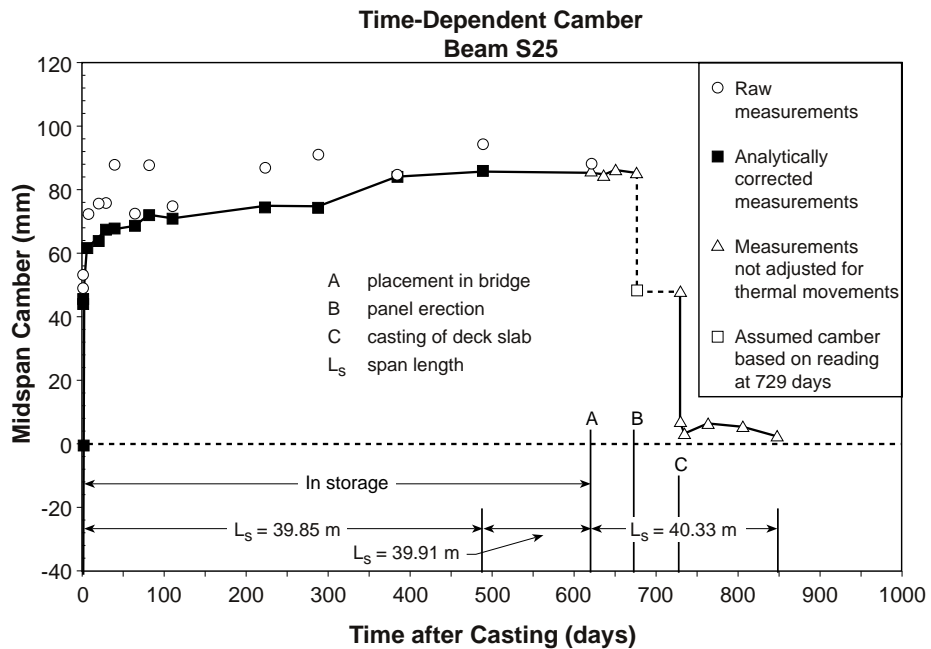


Figure 5.20 Measured midspan camber and deflection response for Beam S25

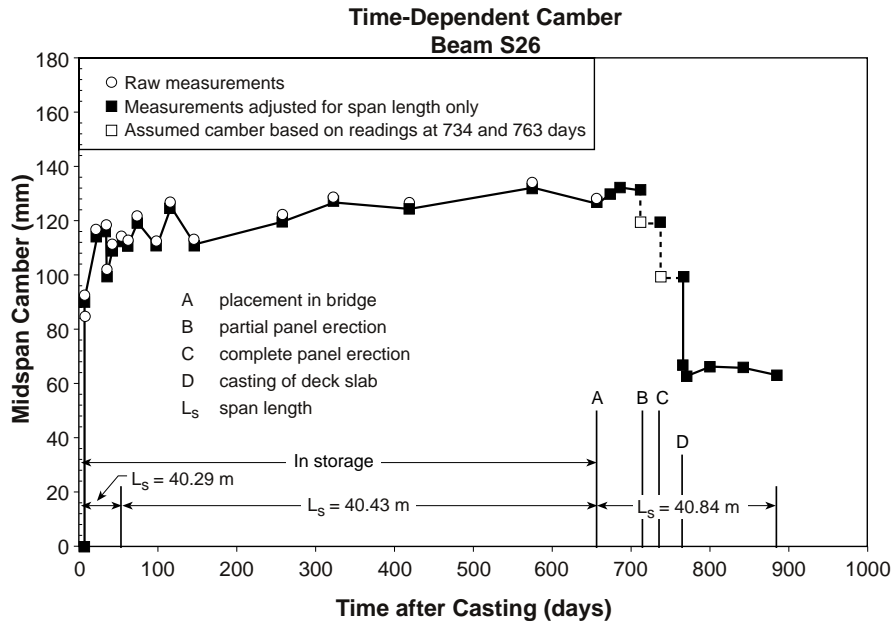


Figure 5.21 Measured midspan camber and deflection response for Beam S26

Raw midspan camber measurements are shown in each figure to represent the beam camber under the conditions at the time of the measurement. This means that large thermal gradients could have been present at the time of the reading and the bearing locations could have been different from the design bearing locations for that beam in the completed bridge. For all of the beams, the span length during storage was smaller than the design span length in the bridge. The measured span lengths during storage and their applicable time periods are shown at the bottom of each figure. In addition, most of the camber readings were taken in the afternoon when large thermal gradients were present in the beams. As a result of all of these varying span and temperature conditions, the raw camber measurements tended to be erratic.

The analytically corrected camber measurements are of more interest for identifying the shape of the camber response over time and for making comparisons of camber growth for similar beams. The analytical correction for span length was a correction on the self-weight deflection of the beam. It adjusted the measured camber to the value it would have been if the beam's bearing locations were the same as in the bridge. After the beams were erected in the bridge, this correction was no longer necessary. Using the second area-moment theorem for determining relative deflections, Eqs. 5.7 and 5.8 were derived to calculate the dead load deflections at midspan under the actual support conditions and under the bridge support conditions, respectively. Note that in Eq. 5.8, the portions of the beam that cantilevered past the bearings were considered negligible. Equation 5.9 represents the correction to the camber measurement. Also note that Eqs. 5.1 and 5.2 were used for determining the compressive strength and modulus of elasticity at the time of the change in support conditions in storage the elastic modulus. At late ages, the small changes in modulus

of elasticity did not affect the magnitude of the beam self-weight correction. The magnitude of this correction ranged from two to five millimeters.

$$\Delta_{\text{storage}} = \frac{w}{EI} \left(\frac{5}{384} L_s^4 + \frac{1}{24} L_s^3 L_o - \frac{1}{16} L_s^2 L_o^2 - \frac{1}{4} L_s L_o^3 - \frac{1}{8} L_o^4 \right) \quad (5.7)$$

$$\Delta_{\text{bridge}} = \frac{5wL_b^4}{384EI} \quad (5.8)$$

$$\Delta_{\text{measurement}} = \Delta_{\text{storage}} - \Delta_{\text{bridge}} \quad (5.9)$$

where

w = distributed weight of the beam (N/m)

E = elastic modulus of concrete as determined by Eq. 5.2 (GPa)

I = moment of inertia of beam (m^4)

L_s = measured span length in storage (m)

L_o = average measured overhang from the center line of bearing (m)

L_b = design span length in the bridge (m)

Δ_{storage} = deflection resulting from beam weight under storage support conditions

Δ_{bridge} = deflection resulting from beam weight under bridge support conditions

$\Delta_{\text{measurement}}$ = correction to measured camber for varying support conditions

In determining the analytical correction for camber resulting from a thermal gradient in a beam, the strain distribution resulting from changes in temperature with reference to a uniform temperature profile of 20 °C was determined. The uniform temperature profile corresponded to zero thermally induced movement of the beam at 20 °C. The strain distribution was usually nonlinear, corresponding to the nonlinear temperature gradients observed in the beams, which are shown in Sec. 5.3.5. No axial or bending stresses were assumed to be induced in the beam since the support conditions were modeled as a pin and a roller for simple span supports. As a result, self-equilibrating stresses were assumed to be developed in the beam from the strains induced in the member that countered the distortion of the section resulting from the nonlinear thermal strain profile (53). A constant curvature along the beam length was assumed based on the resultant strain profile and was used to calculate a theoretical camber resulting from a temperature gradient.

Details about measured thermal movements can be found in Sec. 5.3.6. Equation 5.10 represents the theoretical camber or deflection at midspan resulting from a thermal gradient. The theoretical camber resulting from thermal gradients was as large as 20 millimeters for some of the beams during storage.

$$\Delta_{\text{thermal}} = \phi_t \left(\frac{L_s^2}{8} \right) \quad (5.10)$$

where

ϕ_t = curvature caused by the internal self-equilibrating forces

L_s = measured span length (m)

The plots shown in Figures 5.10 to 5.21 represent the time-dependent camber behavior of the beams after all possible analytical corrections were applied to the raw camber measurements. As shown in those graphs, a majority of the camber growth for all of the beams occurred in the first 80 to 100 days of storage. After that point, the camber response flattened out.

For some of the measurements, a correction for thermal movements was not possible because the internal temperatures in that beam or its companion beam were not taken at that time. The measurements not corrected for thermal movements are shown as an open triangle, as can be seen in Figure 5.10. After the beams were erected in the bridge, corrections were not made for thermal movements because many of the internal instrumentation readings were not valid. In addition, the corrections became very sensitive to the deck temperatures when the sections became composite. Since nearly all of the camber readings after erection were taken in the morning, the magnitudes of the thermal movements were probably small.

For Beams N22, N23, and S26, corrections for thermal movements were not possible. Figure 5.21 shows the time-dependent camber response for Beam S26. Since most of the readings were in the afternoon, it was not possible to remove the thermal effects from the camber plot. The measurements up to 150 days demonstrated the influence that thermal gradients had on the camber readings. The shape of the response curve shows the large early-age camber growth before the curve assumed the characteristic flattened shape where the measurements were farther apart. The fluctuations in the response curve for Beam S26 were due to uncorrected temperature gradient effects.

Figure 5.12 shows the time-dependent camber response for Beam N23. For this beam, several morning readings were taken which were used to eliminate the thermal effects. In contrast to the camber plot for Beam S26 shown in Figure 5.21, the response shown in Figure 5.12 was smoother in the first 150 days of measurements and the time-dependent camber response was similar in shape to the beams whose measurements were corrected for thermal movements.

Figure 5.20 shows the time-dependent camber for Beam S25, which was cast on November 10, 1994. This beam represents the typical camber response for the group of beams that were stored at the prestressing plant for almost two years before being erected in the bridge.

An initial camber of 49.4 mm was measured immediately after release at 1.15 days while the beam was still on the prestressing bed. After determining a thermal correction, the adjusted camber was 44.1 mm. For this measurement, the span length (L_s) was approximately 40.20 meters, which was 0.46 meters less than the length of the beam. The support conditions on the prestressing bed were similar for all of the instrumented beams and were quite close to the support conditions in the bridge.

After release, the beam was moved into storage and supported with wooden blocks positioned in from the ends of the beam. The measured camber increased to 53.5 mm due to shortening of the span length. After applying the analytical corrections for support conditions and thermal movements, the camber became 45.2 mm, which was reasonably close to the camber immediately after release. The measured span length during storage was

39.85 meters, as shown above the time axis in Figure 5.20. The final span length shown was the design span length in the bridge to which all of the camber measurements were adjusted.

During the first 80 days in storage, the beam camber grew to 75.2 mm. Beam S25 was kept in storage for 620 days and was moved one time during storage. As shown in Figure 5.20, the camber grew to 86.1 mm during that period of time.

At 620 days, the beam was transported to Houston and placed in the bridge. This is shown in Figure 5.20 as event A in the response history of the beam. At that time, camber was no longer measured using the piano wire system and the precise surveying system was implemented. For most of the beams, the surveyed camber agreed closely with the last piano wire camber measurement. However, Beams N31, S16, S24, and S26 displayed positive or negative differentials of approximately four to six millimeters. The reason for this relatively small differential was probably due to error in determining the exact bearing elevations. Another possible source of error was in the thickness of the plywood pads that were placed under the beams before transfer. The pad thickness was needed to adjust the baseline piano wire readings for some of the beams. Variation in the actual pad thickness would shift the camber response curve up or down slightly relative to the surveyed cambers.

At 676 days, the placement of the precast deck panels began. This is shown as event B in Figure 5.20. The measured camber at 676 days was 85.9 mm. The measured camber at 700 days of 58.2 mm was assumed to be a reasonable approximation to the camber after placement of the panels. The elastic deflection resulting from the weight of the panels was approximately 27.7 mm.

The cast-in-place deck for the southbound bridge was poured 729 days after Beam S25 was cast. This is shown as event C in Figure 5.20. The measured camber before casting the deck was 47.8 mm. Immediately after the deck was poured, the measured camber was 7.1 mm. The elastic deflection resulting from the weight of the deck slab was 40.7 mm. Camber measurements were taken as late as 848 days after casting, where the camber had decreased slightly to 2.5 mm. At that time, guardrails had not been placed on the bridge.

The time-dependent camber responses for the other beams were similar to that of Beam S25. The main difference was that the group of beams cast in February of 1996 were stored at the prestressing plant 460 to 520 days less than the other beams.

Measurements for the elastic deflection resulting from the superimposed loading of the deck panels were not obtained immediately after placement because, for most of the beams, only a fraction of the panels were erected at the times of measurement. All of the camber response diagrams show a dashed line and symbols representing the assumed instantaneous response of the beams based upon measurements taken within several days of the measurements before the panels were erected. Section 4.3.2 summarizes the conditions during the panel measurements.

The camber responses shown in Figures 5.10 to 5.12, 5.16, and 5.21 have an intermediate stage where only part of the panels were erected on each beam during the measurement. The elastic deflection resulting from the panels for these beams was assumed to be the sum of the deflections from the two stages of panel placement. This assumption was made knowing that the camber probably changed a very small amount owing to the

additional time-dependent effects caused by creep of the concrete resulting from applied loads.

In examining the elastic responses for the exterior beams shown in Figures 5.10, 5.13, 5.18, and 5.21, the deflections caused by the weights of the precast deck panels and cast-in-place deck were smaller than those measured for the interior beams in the same span. This demonstrated how the interior beams carried a larger volume of concrete than the exterior beams, as was assumed in design. Comparison of the measured elastic responses resulting from superimposed loads for all of the beams is presented in Sec. 5.4.1.4.

5.3.2 Surface Strain at the Center of Gravity of the Prestressing Strands

Concrete surface strains were measured at the CGS along the beam length and at several vertical locations at midspan. For many of the beams, surface strain measurements were only taken for a short period of time. This limited the usefulness of the measurements for determining long-term behavior. In addition, temperatures of the concrete surface were not measured, which made it difficult to adjust the readings for strain resulting from temperature differences. For some of the beams, internal temperature data from thermocouples or vibrating wire gages were used to approximate this correction. Because of these factors, nearly all of the concrete surface strain measurements were of little use. Measurements from both sides of Beam S26 are presented in this section to show typical results for the surface strain instrumentation and to illustrate the necessity of thermal corrections.

The measured concrete surface strain at CGS for the west side of Beam S26 is shown in Figure 5.22. In this plot, the CGS strain at the quarter points and midspan are shown for a time period of 34 days after release. These measurements were adjusted for thermal strains based on the temperatures that were measured using the vibrating wire gages in the beam. The measured strains at release were 13 to 22 percent higher than the predicted strains at release. These differences can be attributed to not knowing the actual modulus of elasticity in the beam and to the approximate correction for thermal strain.

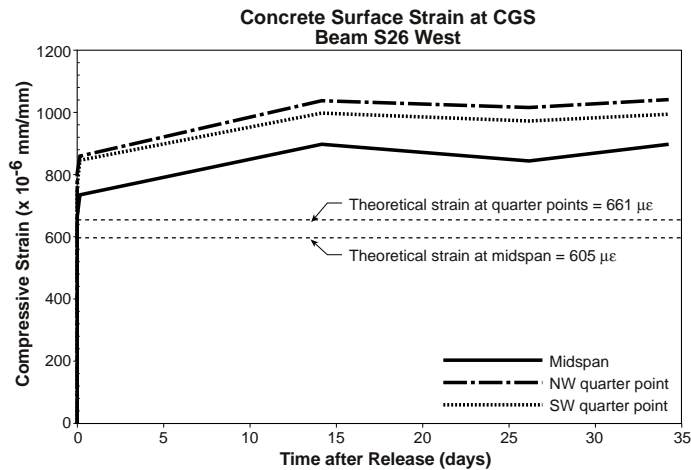


Figure 5.22 Measured surface strain at the CGS on the west side of Beam S26

As expected, the strains at midspan remained less than the strains at the quarter points owing to the larger dead load moment at midspan. The measured surface strains for this beam over 34 days were in close agreement with the measured internal strains for Beam S26 that are shown in Figure 5.27. The measured strains from the two sources are within 6 percent of each other at release and are within 4 percent of each other at 34 days. Unfortunately, surface strain readings for this beam were not taken past 34 days, which was typical for all of the beams.

Figure 5.23 illustrates the importance of correct temperature data for the concrete surface strain measurements. In this plot, the CGS strains at the quarter points and midspan of the east side of Beam S26 are shown. These measurements were adjusted for temperature differences using the internal temperatures from the vibrating wire gages on the west side of the beam. One problem with the data was that the measured strains at midspan were higher than the strains at the southeast quarter point. Also, the measured strains at release for the midspan and southwest quarter point locations were approximately 44 percent higher than the measured internal strains on the west side shown in Figure 5.27. At 34 days, the measured strains at release for the midspan and southwest quarter point locations were approximately 31 percent higher than the strains shown in Figure 5.27. Obviously, the surface strain measurements for the east side of the beam should not be relied upon to represent the strain behavior of Beam S26.

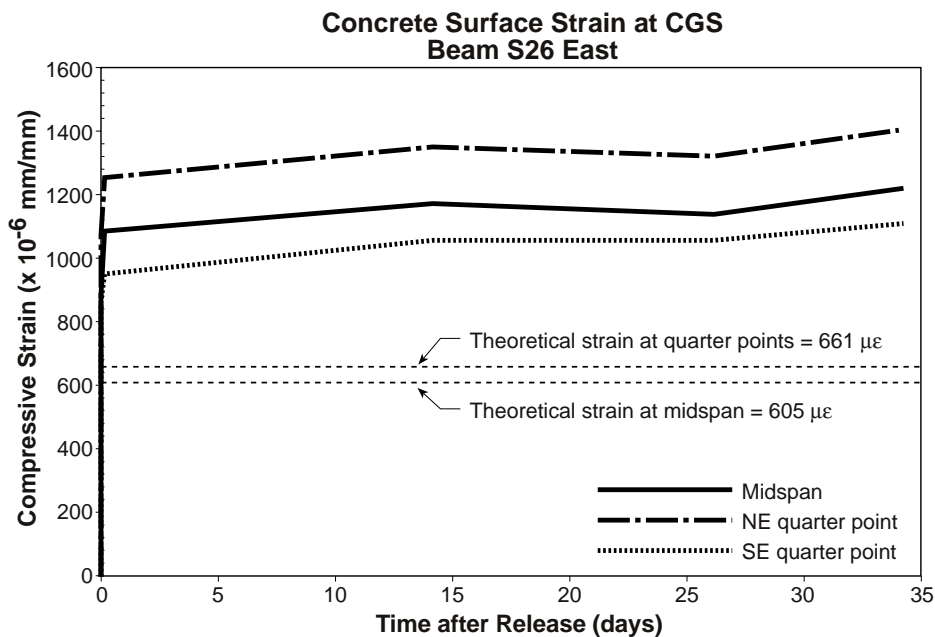


Figure 5.23 Measured surface strain at the CGS on the east side of Beam S26

5.3.3 Internally Measured Strain at the Center of Gravity of the Prestressing Strands

Strain measurements from the embedded gages provided the most useful long-term strain data. The data shown in this section focus on measured strain at the center of gravity of the prestressing strands (CGS). The measured strains at CGS were of interest for determining immediate and long-term prestress losses.

Both the electrical resistance strain gages (ERSG) and the vibrating wire (VW) gages were thermally compensated so that the effect of differences in uniform temperature changes between readings was eliminated. Strain corrections were not made for changes in support conditions, as was done for the camber measurements. Since the initial strain measurements, or baseline readings, were not taken until just before release, the effects of strand relaxation, shrinkage, and changes in temperature of the strand were not part of the strain measurements. The predicted strains at release included prestress losses of 2 percent for relaxation and 2 percent for shrinkage and temperature effects in addition to the prestress loss resulting from elastic shortening. Transformed section properties and the measured modulus of elasticity at release were used to compute the theoretical release strains.

The measured strains at the CGS at midspan for several beams are shown in Figures 5.24 to 5.28. The strains shown in these figures were measured with vibrating wire gages. Measured strains at release were generally quite close to the theoretical release strains. Measured release strains were within 4 percent of the predicted strains for the beams shown in Figures 5.24 and 5.25, while the measured release strains for the beams shown in Figures 5.26 to 5.28 varied from the predicted values by 10 to 29 percent. Error between the measured and predicted release strains could have been caused by differences in the actual elastic modulus of the beam and the elastic modulus used in the predictions, variation between the actual location of the VW gages during placement and the theoretical CGS, movement of the VW gages during placement of the concrete, and restraint offered by the prestressing bed while shrinkage and cooling of the beams occurred.

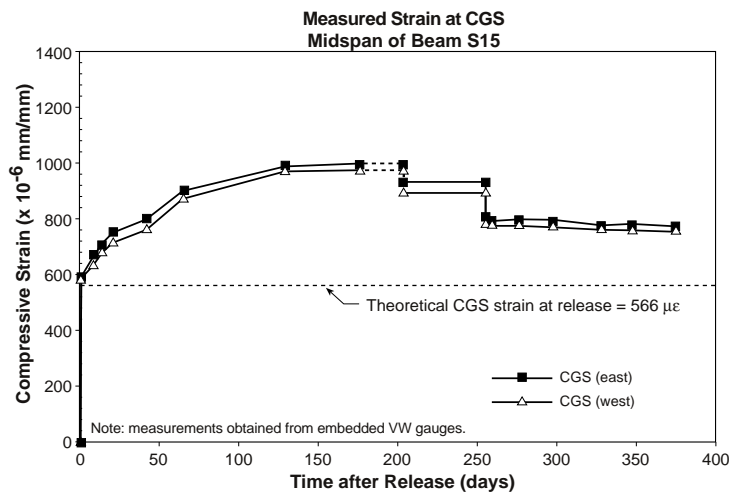


Figure 5.24 Measured prestressing strand strain at the midspan of Beam S15

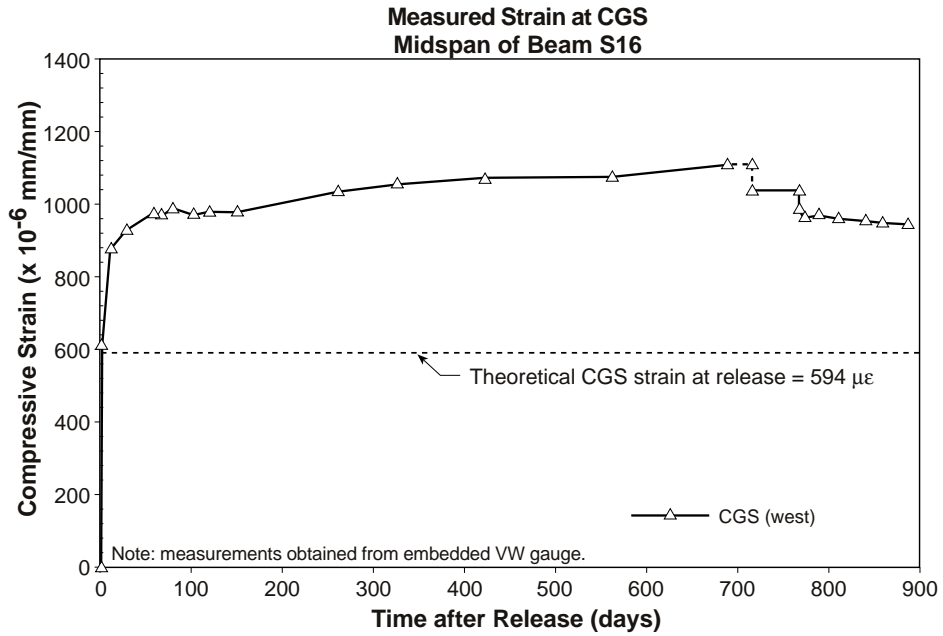


Figure 5.25 Measured prestressing strand strain at the midspan of Beam S16

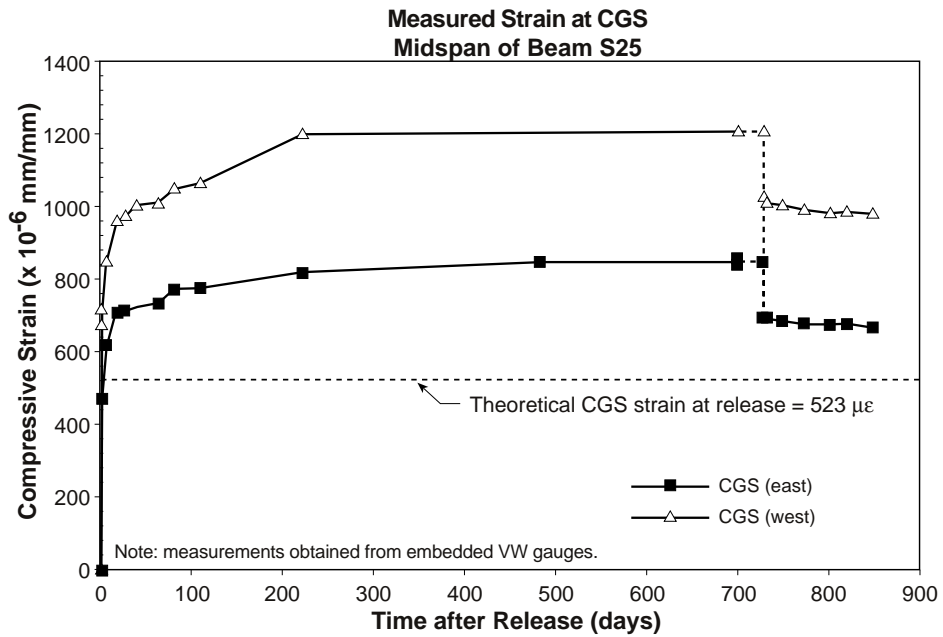


Figure 5.26 Measured prestressing strand strain at the midspan of Beam S25

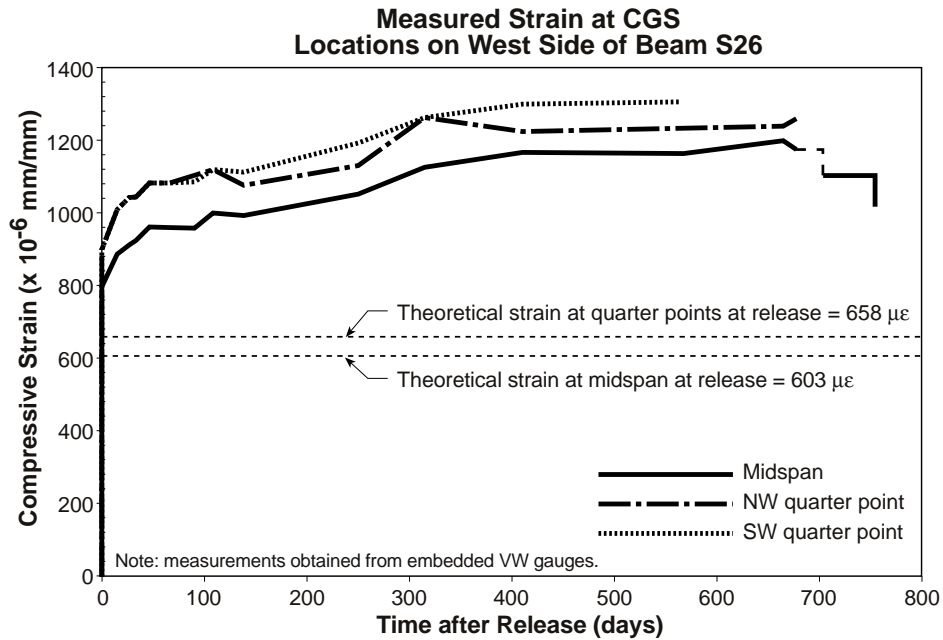


Figure 5.27 Measured prestressing strand strain at the midspan and quarter points of Beam S26

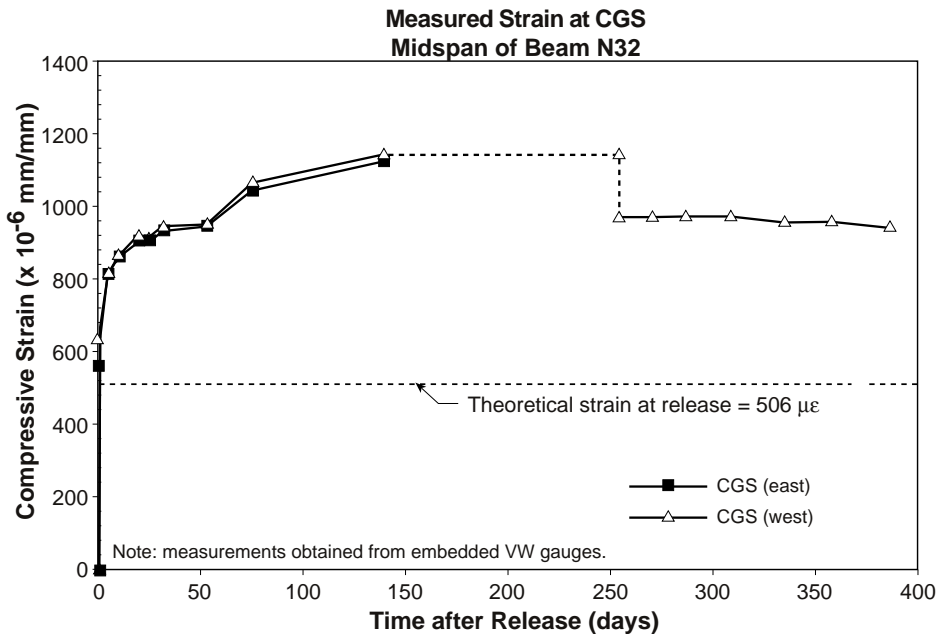


Figure 5.28 Measured prestressing strand strain at the midspan of Beam N32

From the point just after release to just before placement of the deck panels, the time-dependent strain response represented the increase in compressive strain at the CGS resulting from creep and shrinkage of the concrete. The measured strains did not include the additional relaxation of the prestressing strands after release. The increase in compressive strain also could be used to determine the loss of prestress during that time period. For Beam S15 shown in Figure 5.24, the increase in strain over time was well distributed over the 180 day time period. This did not agree with the results from the rest of the beams, where the increase in strain was dramatic during the first 50 days (similar to Figure 5.28) and then flattened out asymptotically. Most of the time-dependent strain was gained in the first 100 days for all of the beams shown in Figures 5.24 to 5.28.

The results of the measured strain at CGS for Beam S16, which is shown in Figure 5.25, were very dependable. The measured release strain was within 3 percent of the predicted strain. The long-term behavior was stable through the construction of the bridge. The compressive strain continued to grow through 700 days of storage due to creep and shrinkage. These results represented the typical behavior of all of the beams that were kept in storage for 600 to 700 days.

Figure 5.26 shows the measured CGS strains for the east and west sides of Beam S25. The difference between the strains was 209 microstrain at release and that difference continued to grow throughout storage. It was not clear what caused this disagreement in measured strains at midspan. Upon averaging the measured release strains at midspan, the resulting strain became 569 microstrain, which was within 9 percent of the predicted release strain. This was probably a better representation of the CGS strain at midspan than what was given by either the east or the west side measurements individually.

The measured CGS strains for both sides of Beam N32 are shown in Figure 5.28. Unlike Beam S25, the correlation between the strain measurements was almost exact through 80 days in storage. The only difference occurred at release, where the strain differential between sides was 74 microstrain. This may have been caused by restraint from the prestressing bed.

Except for Beam S26, all of the beams with VW gages at CGS, as shown in Figures 5.24 to 5.28, were yielding valid strain measurements after the cast-in-place decks were completed. The change in strain after the beam section became composite was very small. Since the ages of the beams were quite high, very little creep and shrinkage was occurring at that time. In addition, the composite U-beam section was approximately three times as stiff as the non-composite section. Therefore, the changes in strain were expected to be quite small which was confirmed by the measurements shown in Figures 5.24 to 5.28.

Figures 5.29 to 5.34 summarize the CGS strain measurements obtained with electrical resistance strain gages (ERSGs). For most of the beams, results were reliable for the first 200 days, after which the integrity of the resistance-based measuring system broke down.

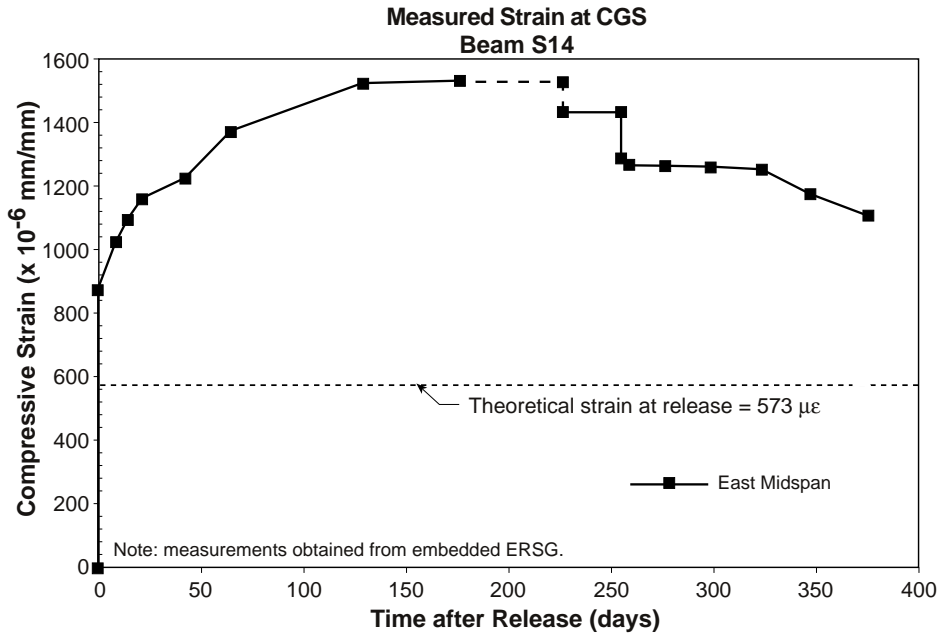


Figure 5.29 Measured prestressing strand strain at the midspan of Beam S14

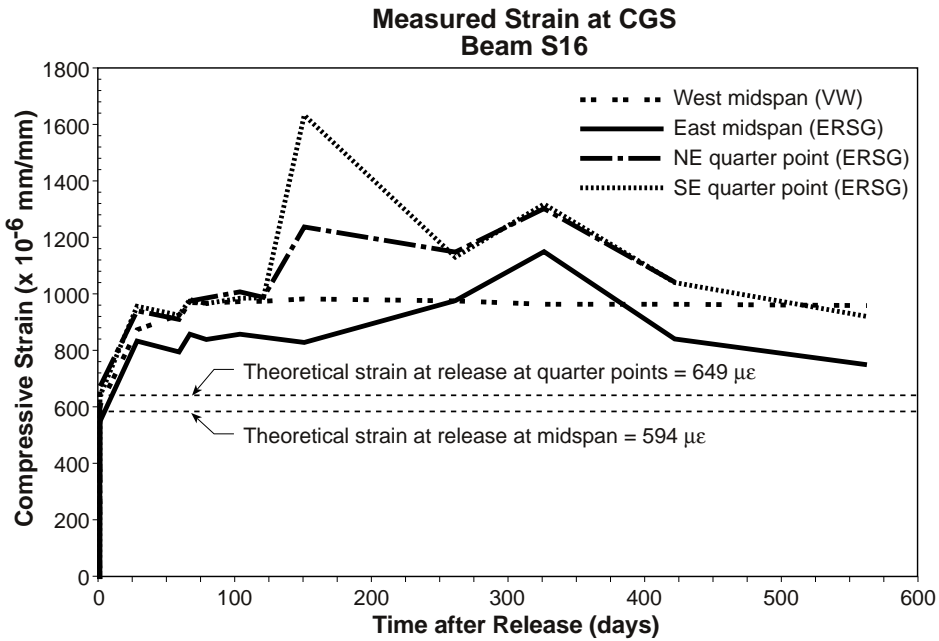


Figure 5.30 Measured prestressing strand strain at the midspan and quarter points of Beam S16

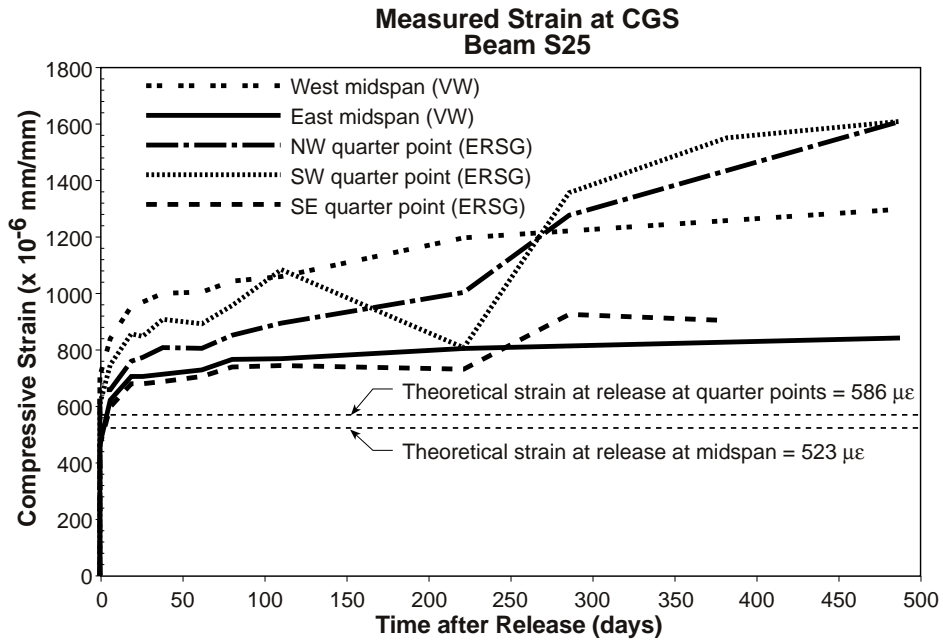


Figure 5.31 Measured prestressing strand strain at midspan and quarter points of Beam S25

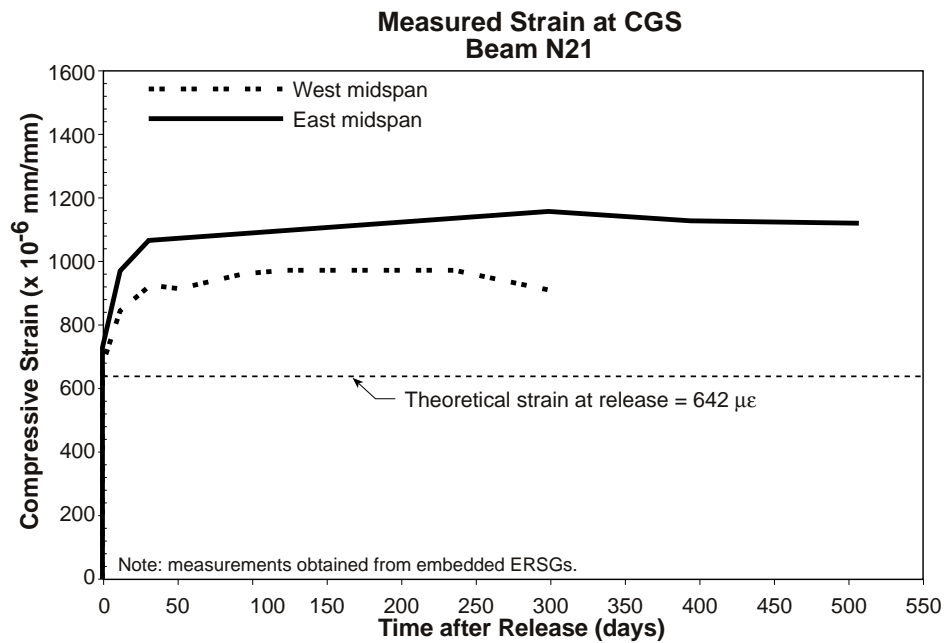


Figure 5.32 Measured prestressing strand strain at the midspan of Beam N21

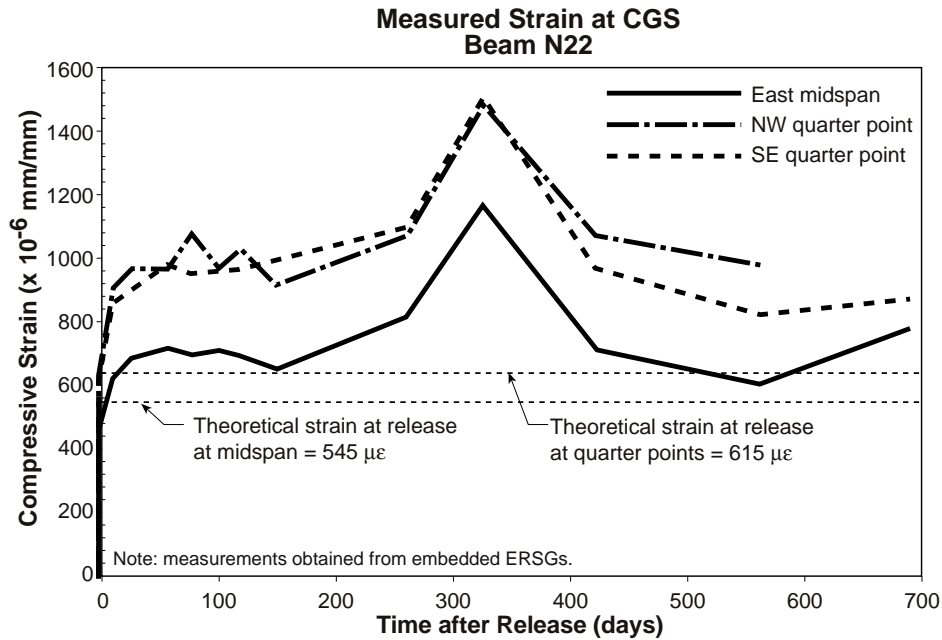


Figure 5.33 Measured prestressing strand strain at midspan and quarter points of Beam N22

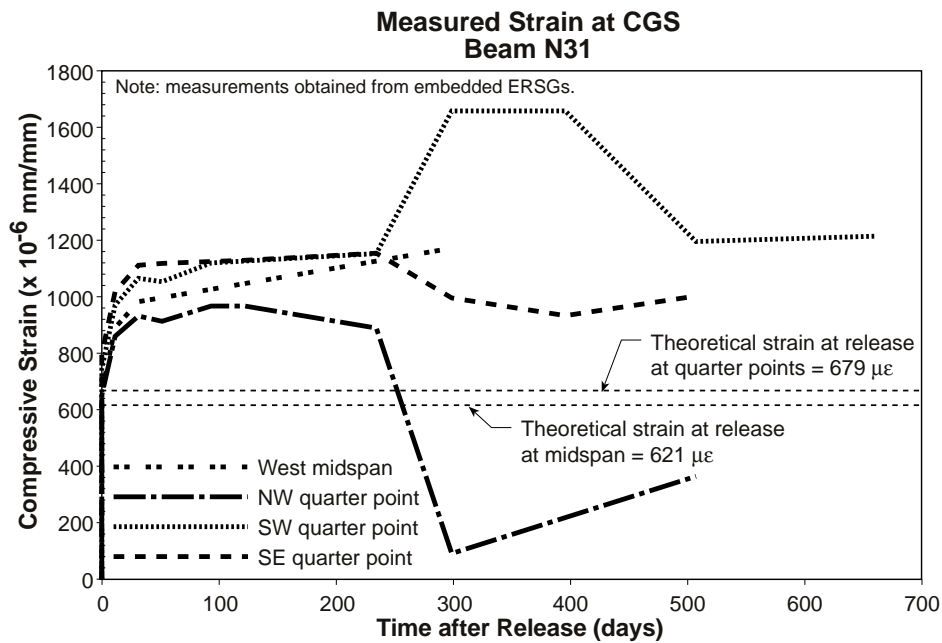


Figure 5.34 Measured prestressing strand strain at the midspan and quarter points of Beam N31

The strain response at midspan for Beam S14, shown in Figure 5.29, was reliable through completion of the deck even though the strain at release was significantly higher than the predicted value. At approximately 325 days, the ERSG at midspan of Beam S14 began to show signs of breakdown. The total strain throughout storage for Beam S14 was abnormally higher than all of the other beams, especially when compared to the results for Beam S15, shown in Figure 5.24, which was the companion beam for Beam S14. Theoretically, the strain responses for these beams should have been similar. Differences between Beams S14 and S15 can be attributed to the type of gage used to obtain strain measurements.

The strain response at midspan of Beam N21, shown Figure 5.32, was very reliable at release and throughout most of the time in storage. The measured and predicted release strains were within 1 percent of each other. The compressive strain increased throughout the first 250 days of storage and then decreased slightly at 300 days. After 300 days, no further measurements were provided by that gage.

The measured strains at CGS for Beam N22 are shown in Figure 5.33. The strain behavior was stable up to 100 days, after which the strain measurements became very erratic. The strain responses that were measured with ERSGs for Beams S16 and N31, which are shown in Figures 5.30 and 5.34, respectively, showed behavior that was similar to the results for Beam N22. The strain measurements obtained with ERSGs were not reliable past 200 days for almost all of the beams.

Figure 5.30 compares the measured CGS strains using a VW gage at midspan to the measured strains using ERSGs at midspan and the quarter points for Beam S16. The strain behavior at most locations along the beam was reliable through 150 days for Beam S16. The quarter point strains were higher than the midspan strains and the strain increase during that time was similar for both types of gages. However, the quarter point and midspan strain measurements made with ERSGs past 150 days became erratic. Similar patterns of erratic response from ERSGs are illustrated in Beams S25, N22, and N31, shown in Figures 5.31, 5.33, and 5.34, respectively. These comparisons illustrated that the VW gages yielded far more reliable long-term strain measurements. The ERSGs consistently yielded reliable results for much shorter periods of time and then generally became unstable.

5.3.4 Measured Strain Profiles at Midspan

Strain profiles at midspan were measured for nine of the twelve instrumented beams using internal strain gages, Demec surface strain gages, or a combination of both types of gages. The measured strain profiles at midspan were of interest for determining the immediate midspan curvatures at release as well as the time-dependent increases in curvature throughout storage. The curvatures at release could be compared to the measured cambers at release to determine whether a correlation existed between the two sets of measurements.

The measured strain profiles at release are shown in Figures 5.35 to 5.43. The predicted strain profiles at release were included in these figures for comparison purposes. The predicted profiles were calculated based on the same assumptions that were used to calculate the theoretical strains at the CGS in Sec. 5.3.3.

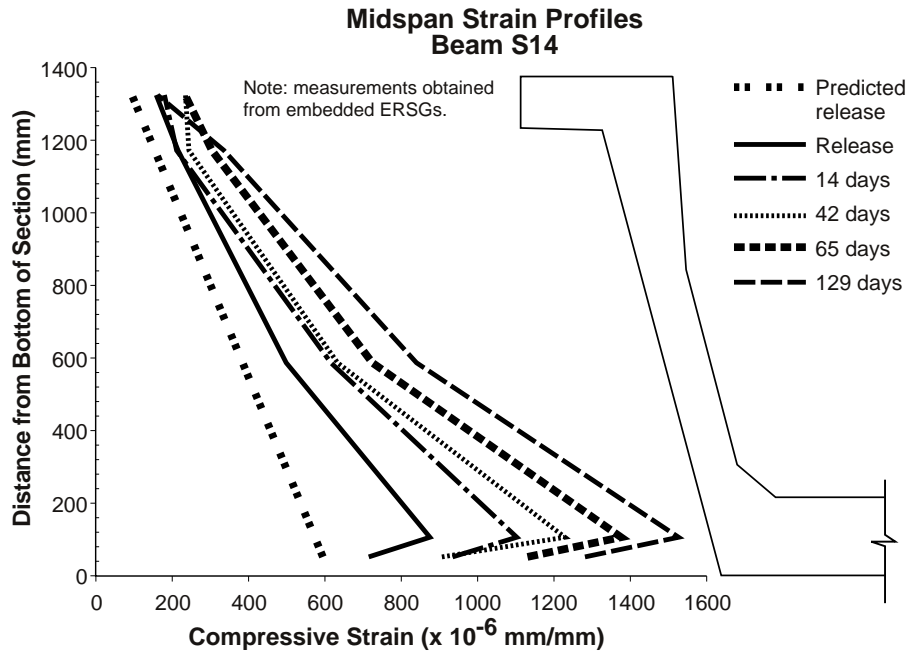


Figure 5.35 Measured strain profiles at midspan for Beam S14

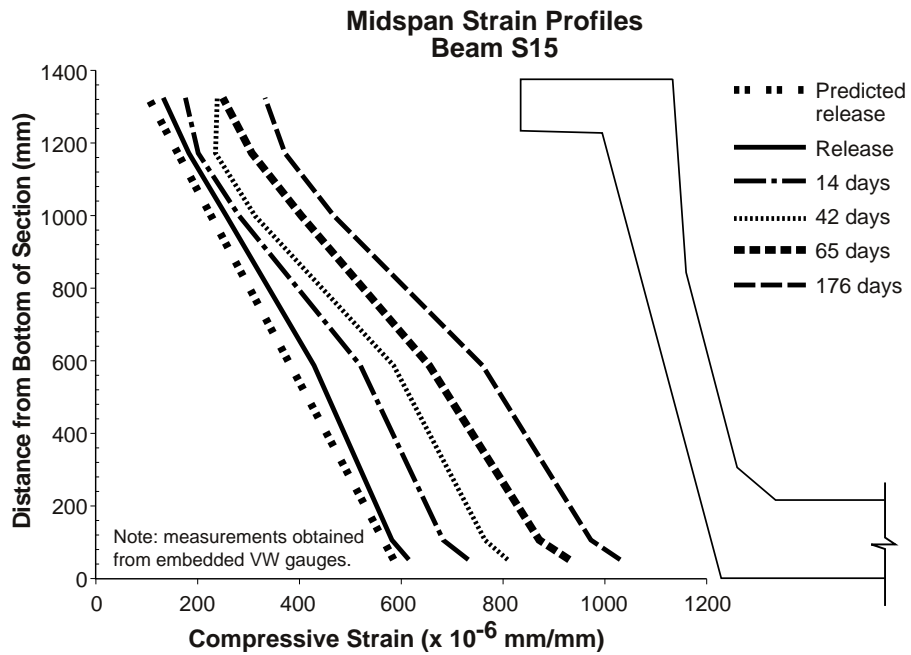


Figure 5.36 Measured strain profiles at midspan for Beam S15

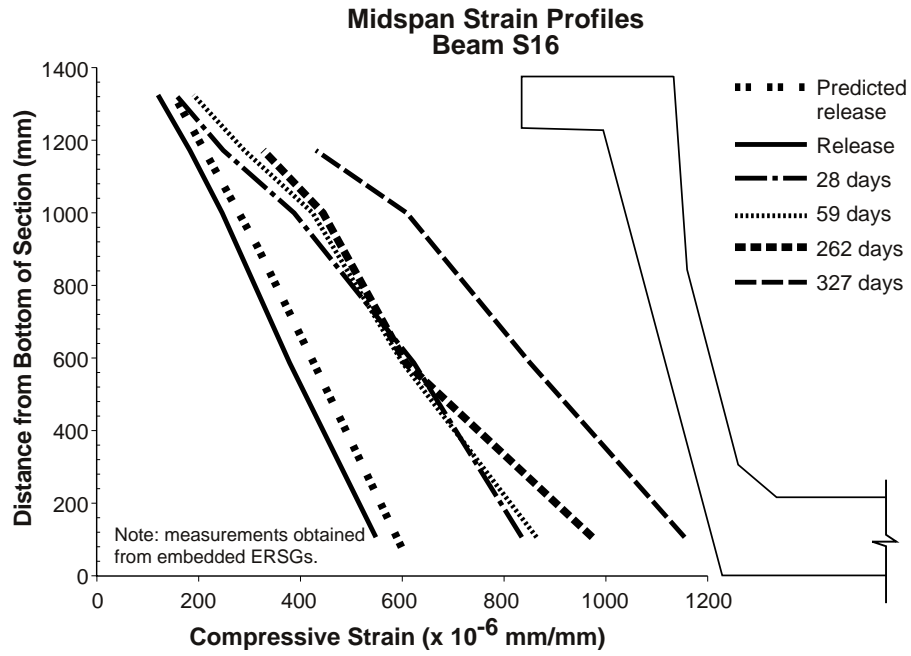


Figure 5.37 Measured strain profiles at midspan for Beam S16

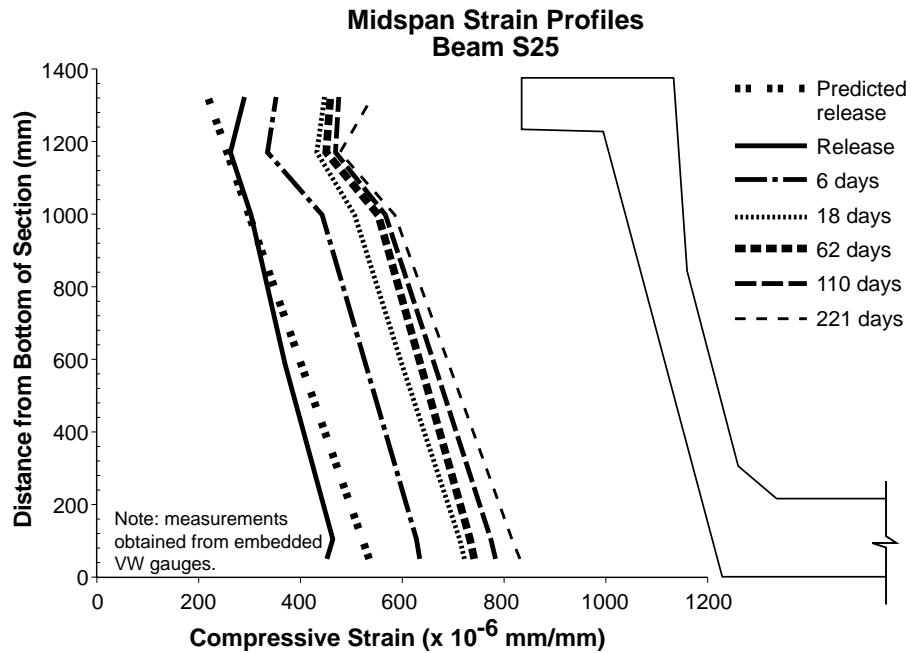


Figure 5.38 Measured strain profiles at midspan for Beam S25

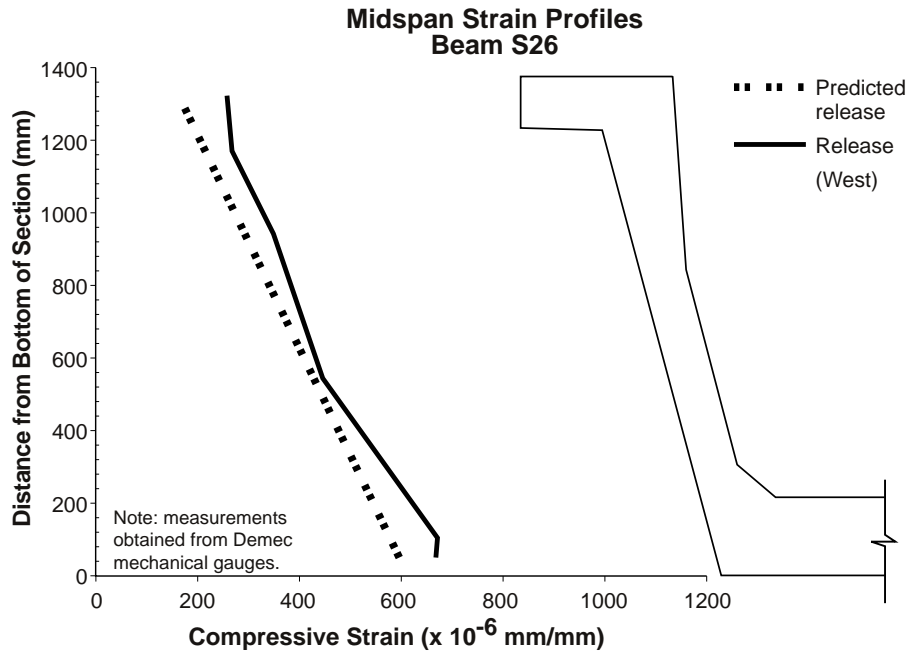


Figure 5.39 Measured strain profiles at midspan for Beam S26

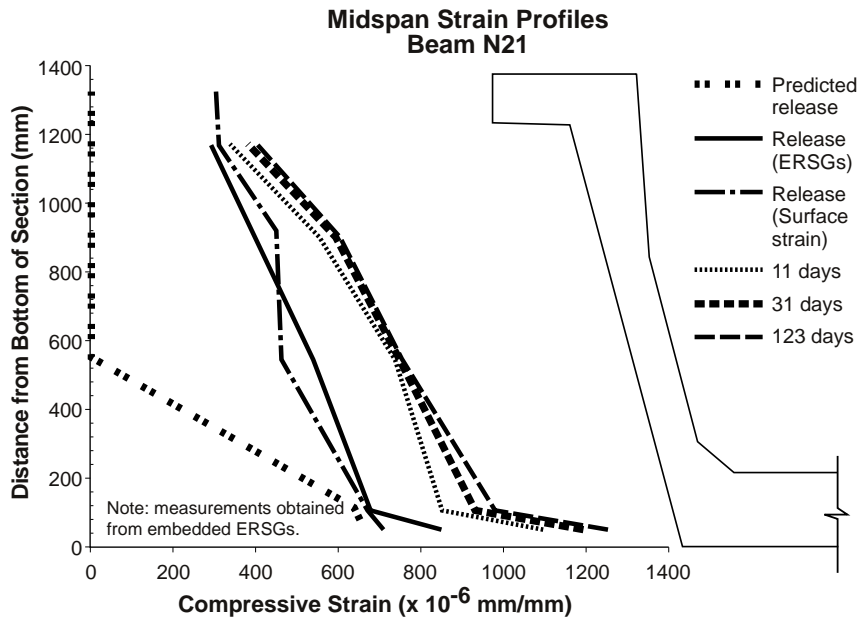


Figure 5.40 Measured strain profiles at midspan for Beam N21

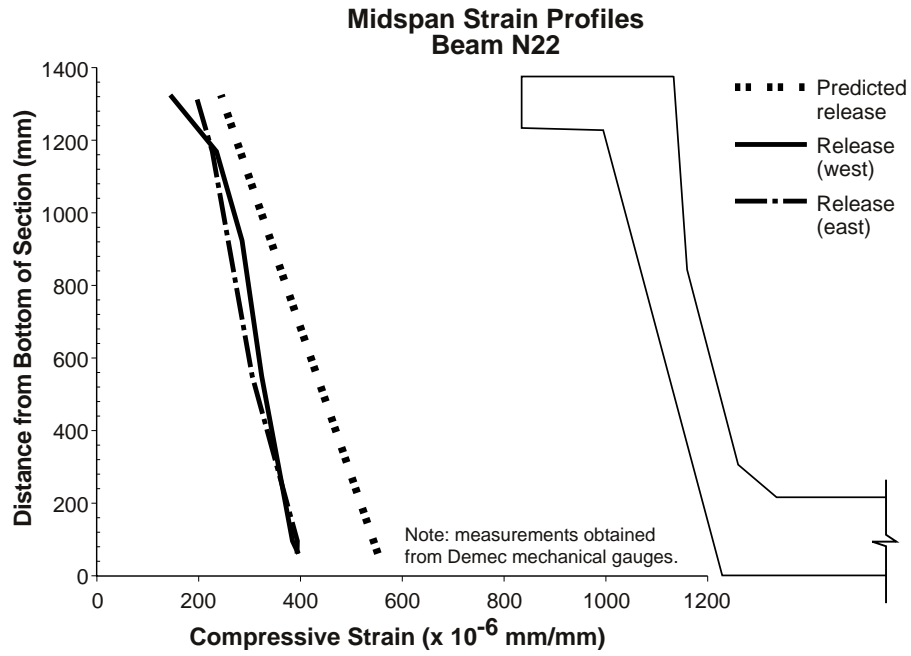


Figure 5.41 Measured strain profiles at midspan for Beam N22

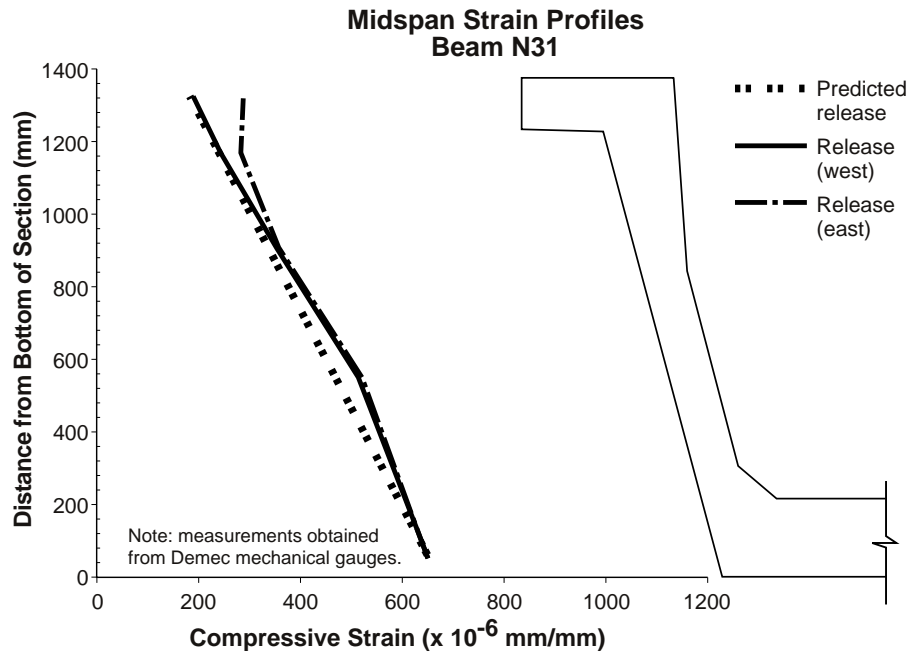


Figure 5.42 Measured strain profiles at midspan for Beam N31

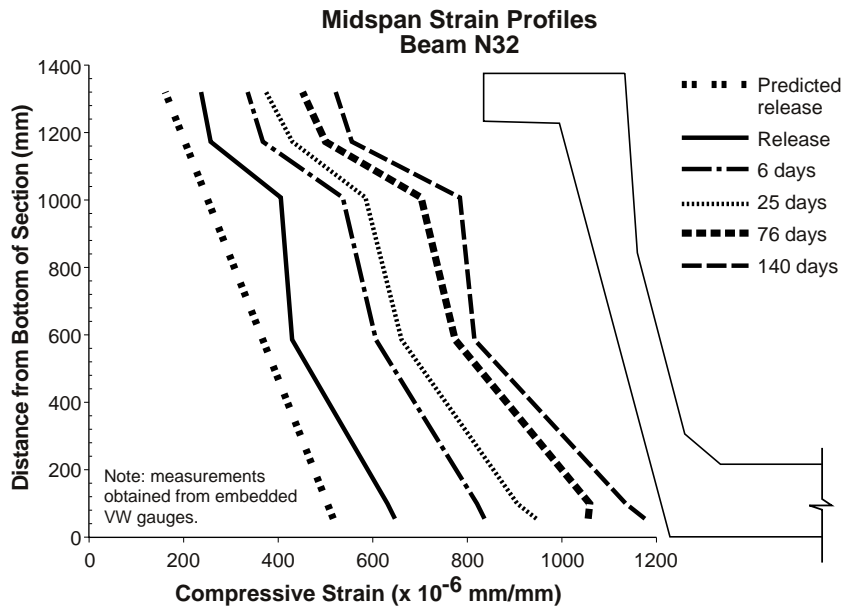


Figure 5.43 Measured strain profiles at the midspan of Beam N32

The measured midspan strain profiles at release generally supported the theory of plane sections remaining plane. For Beams S15, S16, S26, and N31, there was very good correlation between the measured and predicted strain profiles at release. For Beams S25, N22, and N32, differences in the slope of the strain profile (curvature), magnitudes of the strains, or a combination of both were observed between the measured and predicted strain profiles. For Beams S14 and N21, the measured curvatures were erratic because of one strain measurement that did not correlate with the other strains in the profile.

For all of the beams, error between the measured and predicted strain profiles was probably caused by differences between the assumed and actual prestressing force and elastic modulus of the beam. In addition, higher strains in the profiles could have been caused by restraint of the beam offered by the prestressing bed while shrinkage and cooling of the beam occurred before release. For the beams with strain profiles measured using surface strain instrumentation, some of the error was caused by the lack of temperature data for making corrections to the strain readings. For several of the beams shown in Figures 5.35 to 5.43, the measured strain profile was on one side of the beam. Since differences in the measured strain at the CGS on both sides of the beam were observed in Sec. 5.3.3, there probably were some differences in the strain profiles on both sides of the beam.

The measured time-dependent strain profiles for six of the nine beams are shown in Figures 5.35 to 5.43. The most reliable time-dependent strain profiles were observed in Beams S15 and N32, shown in Figures 5.36 and 5.43, respectively. The time-dependent strain profiles for Beams S14, S16, and N21 showed less reliability because the ERSGs were not as durable as the VW gages. Time-dependent strain profiles were not shown for Beams S26, N22, and N31 because the results from the surface strain instrumentation became highly erratic.

Beams S15, shown in Figure 5.36, was a good example of how the strain profile at midspan changed with time owing to creep and shrinkage. The effects of creep and shrinkage on the strain profile were shown by variable increases in the magnitudes of the strains in the cross section. Shrinkage caused a uniform increase in all of the strains while creep caused the strain at each location in the profile to increase in proportion to its magnitude at release. At 176 days, all of the strains had increased in magnitude and the slope of the strain profile, or curvature, had increased with respect to the curvature at release. The measured increase in curvature for Beam S15 was expected to be accompanied by a measured increase in camber. The time-dependent camber response for Beam S15, shown in Figure 5.17, verified the measured curvature response shown in Figure 5.36. Beam N32 displayed behavior that was similar to Beam S15.

5.3.5 Temperature Gradients

Temperature gradients are nonuniform vertical distributions of temperature that develop as a result of uneven heating and cooling. Heat energy is provided to a beam or a bridge superstructure by means of solar radiation. Additional heat may be gained or lost owing to convection to or from the surrounding atmosphere. The amount of temperature change created by these heat sources depends upon wind speed, ambient temperature, relative humidity, weather conditions (clear or cloudy), material properties of the bridge, surface characteristics, the time of day, and the time of year (53,54,55). Maximum temperature gradients can be expected during times of very high solar radiation and very low wind speed (54). Conditions such as these would most likely occur in the summer. At that time of the year, the distance of the sun from the earth is the smallest and the angle of the sun relative to the earth is the largest.

Temperatures distributions in the beams and composite bridge were measured to determine the temperature gradient variation throughout the day and year as well as the maximum gradient that could be expected in the bridge. The magnitude of a temperature gradient was taken as the temperature difference between the top and bottom flanges. The measured temperature gradients were also used to correlate predicted and observed thermally induced movements in the beams. This will be discussed in Sec. 5.3.6.

Temperature gradients in the beams varied significantly while they were in storage. The temperature gradients in storage were primarily used for making analytical corrections to the camber measurements, which is discussed in Sec. 5.3.1. It is important to note that all temperature data presented for the U-beams corresponds to typical weather patterns that exist in the southeast region of Texas.

Figures 5.44 and 5.45 show typical variations in temperature distribution in the beams during the day while they were in storage at the prestressing plant. Temperature gradients were typically uniform or slightly negative during the morning hours just before sunrise. A negative temperature gradient was characterized by a temperature decrease from bottom to top of the section. In general, temperature gradients were nonlinear during sunny afternoons with temperature differences between the top and bottom flanges ranging from 7 to 10 °C. The nonlinear shape of the temperature gradient, as shown in Figure 5.45, was due to shading

of the web by the top flange. This shading caused the upper part of the web to remain slightly cooler than the lower part of the web. The lower flange heated and cooled more slowly than the rest of the beam because of its large mass.

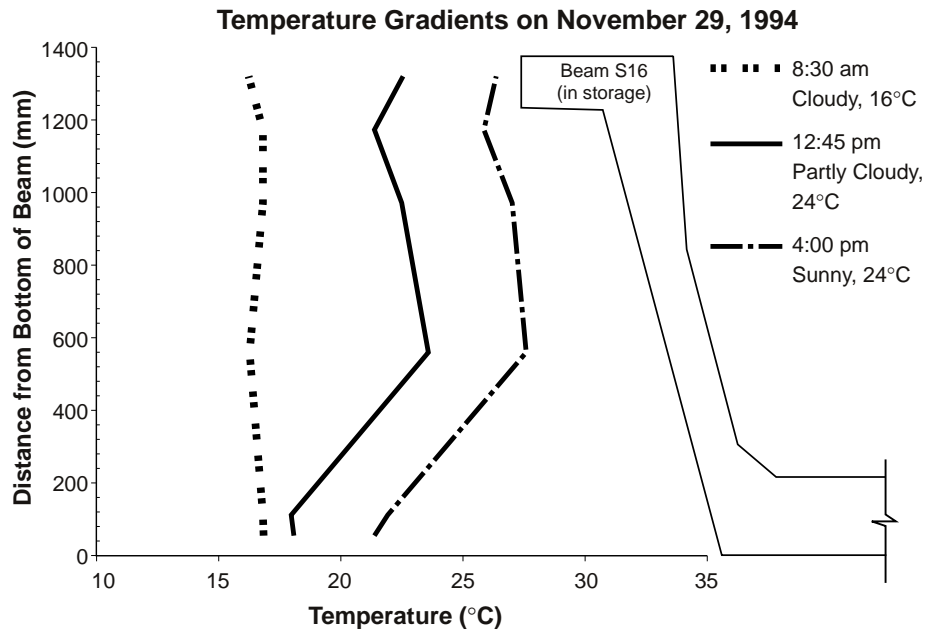


Figure 5.44 Temperature distributions at midspan on a mostly cloudy fall day

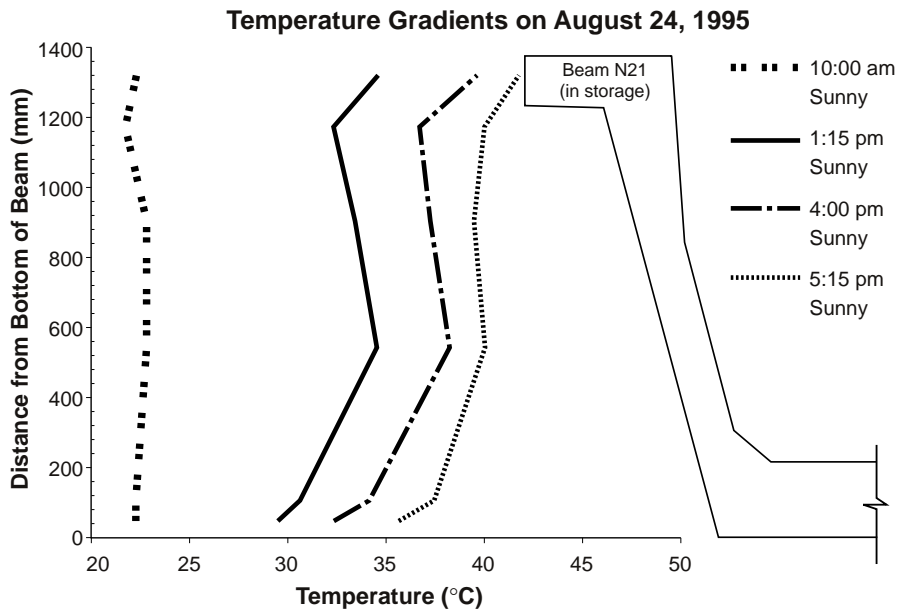


Figure 5.45 Temperature distributions at midspan on a hot summer day

Figure 5.44 shows how temperature distributions changed on November 29, 1994, which was a mostly cloudy fall day. The temperature gradient changed from $-1\text{ }^{\circ}\text{C}$ at 8:30 a.m. to $5\text{ }^{\circ}\text{C}$ by 4:00 p.m. The shape of the temperature gradient became highly nonlinear in the afternoon as the weather conditions changed from cloudy to sunny.

Figure 5.45 shows the variation in temperature distribution in Beam N21 on August 24, 1995, which was a hot sunny summer day. At 10:00 a.m., the measured temperature distribution was nearly uniform. By 1:15 p.m., the beam had heated up considerably with the top flange and lower web experiencing a larger increase in temperature than the upper web and lower flange. The temperature distribution had assumed the characteristic nonlinear shape by that time. The temperature gradient reached a maximum of $7\text{ }^{\circ}\text{C}$ by 4:00 p.m. This large temperature gradient lasted all afternoon with the peak beam temperatures occurring between 5 p.m. and 6 p.m.

Temperature distributions in the composite bridge were of more interest than those measured while the beams were in storage. The measurement of temperatures in the composite bridge were important for determining variations in temperature gradients throughout the day and the year, and for determining the maximum gradient that could be expected in the composite section. The maximum temperature gradients observed in the composite section between November of 1996 and March of 1997 was $12\text{ }^{\circ}\text{C}$. The maximum change in temperature in the deck during a single day was $19\text{ }^{\circ}\text{C}$.

Figures 5.46 through 5.49 show the large nonlinear temperature gradients that were measured in the composite U-beam sections. Figures 5.46 and 5.48 show the variation of temperature gradients in Beam N21, which was an exterior beam. Figures 5.47 and 5.49 show the variation of temperature gradients for Beam N33, which was an interior beam. These beams were used to represent typical temperature distributions in exterior and interior composite U-beams. The positions of these beams in the bridge are shown in Sec. 3.2.1. There will be some variation among similar beams based on their position in the bridge and based on the thickness of the deck slab.

Figures 5.46 and 5.47 show the temperature gradients that developed in Beams N21 and N33, respectively, on March 10, 1997, which appeared to be a hot and sunny day. The temperature distributions early in the morning were generally uniform or slightly negative for both beams with the deck being cooler than the bottom flange. From 8:00 a.m. to 12:00 p.m., the temperature in the deck had increased by $7\text{ }^{\circ}\text{C}$ and $9\text{ }^{\circ}\text{C}$ for Beams N21 and N33, respectively. During the same period of time, the lower part of Beam N21 had increased uniformly by $3\text{ }^{\circ}\text{C}$ while the lower part of Beam N33 remained almost the same temperature. By 3:00 p.m., the temperature gradient in Beam N21 was $6\text{ }^{\circ}\text{C}$ ($13\text{ }^{\circ}\text{C}$ increase at the top and $7\text{ }^{\circ}\text{C}$ increase at the bottom flange) while the temperature gradient in Beam N33 was $9\text{ }^{\circ}\text{C}$ ($13\text{ }^{\circ}\text{C}$ increase at the top and $4\text{ }^{\circ}\text{C}$ increase at the bottom flange). The portion of Beam N33 below the top flange increased uniformly by a smaller amount than Beam N21 because of the complete shading of the interior beam from the sun.

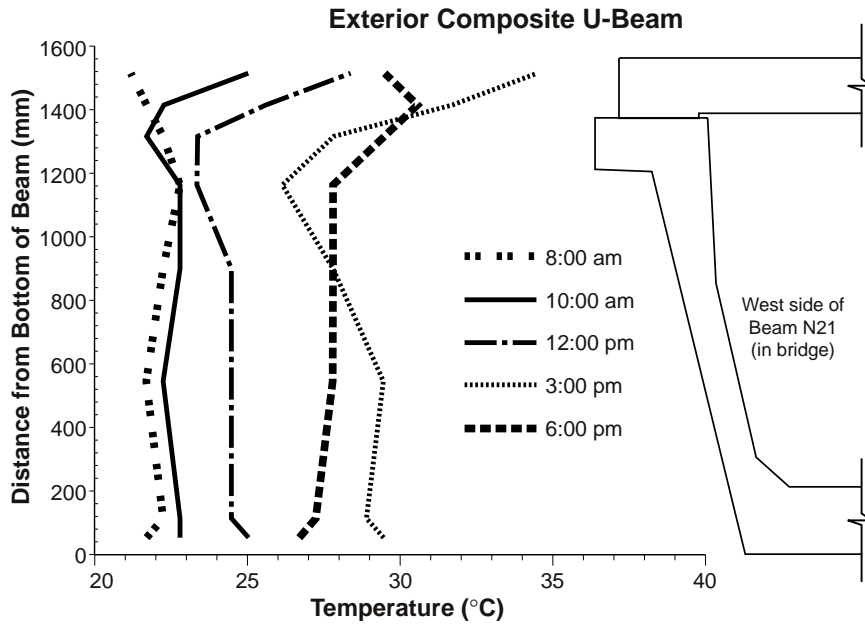


Figure 5.46 Temperature distributions at midspan for an exterior composite U-beam on March 10, 1997

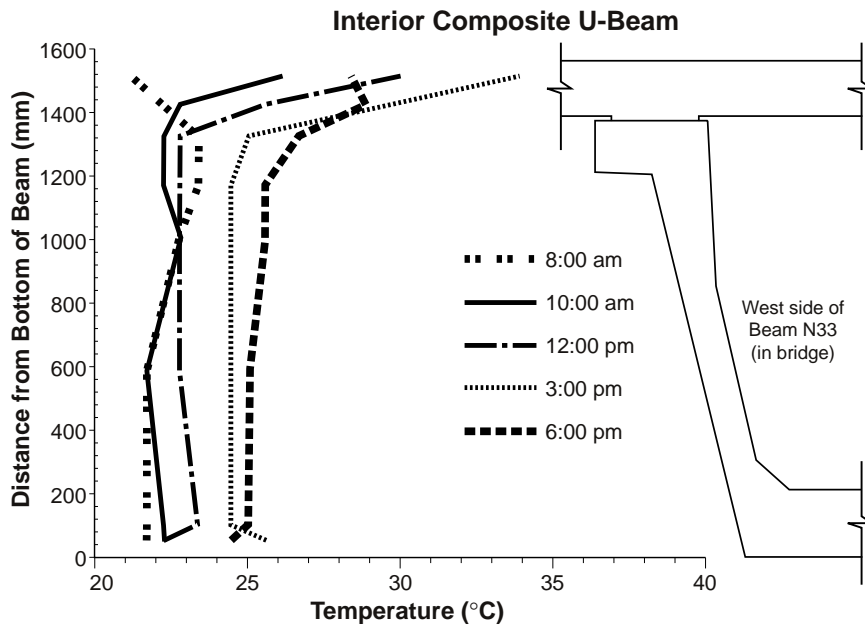


Figure 5.47 Temperature distributions at midspan for an interior composite U-beam on March 10, 1997

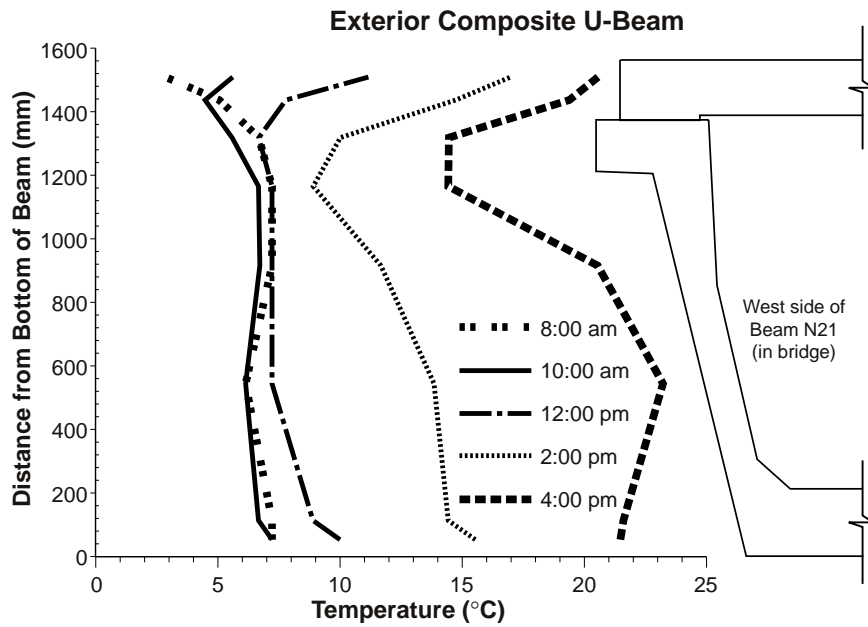


Figure 5.48 Temperature distributions at midspan for an exterior composite U-beam on January 30, 1997

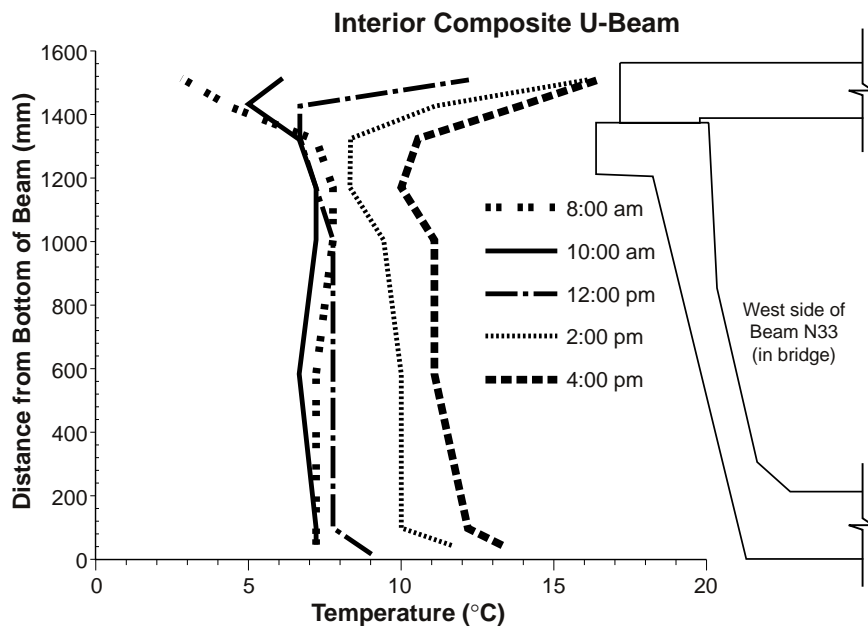


Figure 5.49 Temperature distributions at midspan for an interior composite U-beam on January 30, 1997

In addition, the shape of the afternoon temperature gradient for Beam N21 differed from that of Beam N33 because its exterior web was exposed to the sun. As shown in Figure 5.46, the temperatures in the lower portion of the web increased more than that of the top portion of the web, because of the shading offered by the top flange.

Figures 5.48 and 5.49 show the temperature gradients that developed in Beams N21 and N33, respectively, on January 30, 1997, which appeared to be a cold and sunny day. The temperature distributions early in the morning were $-4\text{ }^{\circ}\text{C}$ for both beams. By 4:00 p.m., the temperature in the deck had increased $18\text{ }^{\circ}\text{C}$ for Beam N21 and $14\text{ }^{\circ}\text{C}$ for Beam N33. However, a temperature gradient of $4\text{ }^{\circ}\text{C}$ had developed in Beam N33 but there was very little difference between the deck and bottom flange for Beam N21. The center part of the web was hotter than the top and bottom flanges because of the exposure of the web to the sun in the afternoon hours. In contrast, the lower portion of Beam N33 heated fairly uniformly.

Figures 5.50 and 5.51 show typical temperature distributions in both sides of the same beam in the morning and in the afternoon on March 10, 1997. For Beam N21, shown in Figure 5.50, the temperature distributions were very similar at 8:00 a.m. but by 3:00 p.m. the temperatures in the west side, which was exposed to the sun, had increased more than the temperatures in the east side. However, the temperature gradient in the east side ($7\text{ }^{\circ}\text{C}$) was larger than the temperature gradient in the west side ($5\text{ }^{\circ}\text{C}$) because of the complete shading of the east side from the sun.

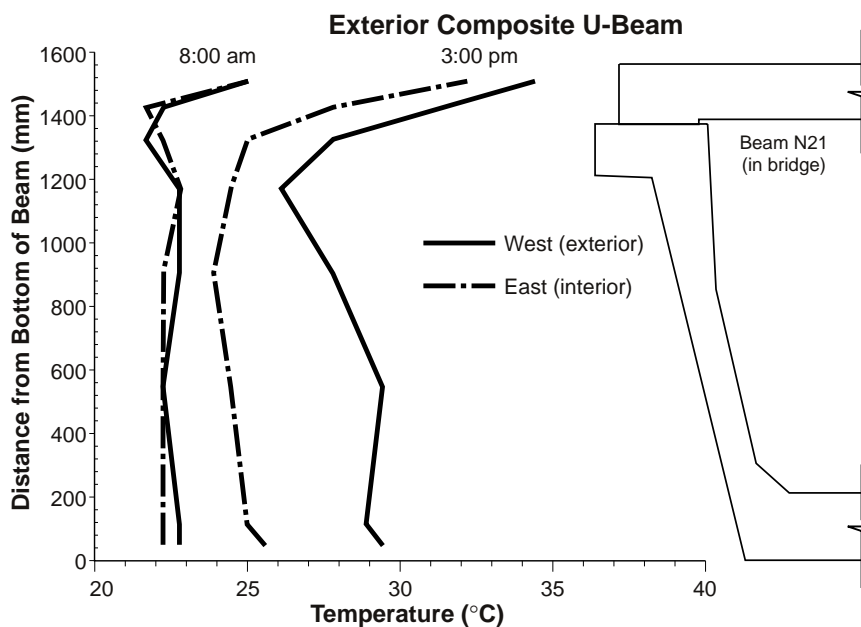


Figure 5.50 Comparison of temperature distributions at midspan for both sides of an exterior composite U-beam on March 10, 1997

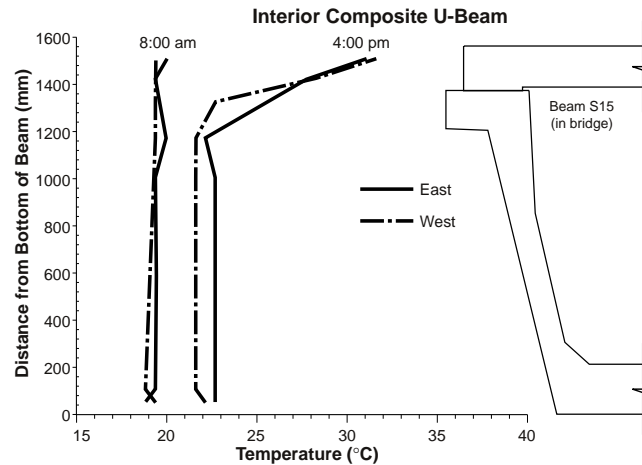


Figure 5.51 Comparison of temperature distributions at midspan for both sides of an interior composite U-beam on March 9, 1997

Figure 5.51 shows a similar comparison for Beam S15, which was an interior beam. The temperature data shown was from March 9, 1997. The temperature distributions in both sides of Beam S15 were nearly identical at 8:00 a.m. By 4:00 p.m., both temperature distributions became highly nonlinear but there was very little difference between the temperature gradients that developed in both sides of the beam. Since both sides were completely shaded from the sun, there was no influence that caused the temperature distributions to vary between the two sides of the beams.

5.3.6 Thermally Induced Camber and Deflection

Thermal movements in prestressed concrete beams occur as both axial and flexural deformations. Axial lengthening or shortening occurs when a beam is uniformly heated or cooled, respectively. If a beam is allowed to expand or contract freely, camber or deflection will not be induced in the beam by this type of deformation. Flexural deformations are caused by nonuniform temperature distributions throughout the depth of the beam cross section. When a simply supported beam is subjected to nonuniform temperature distributions, a resulting thermally induced camber or deflection will occur in the beam (53).

Changes in camber resulting from temperature gradients were measured for Beams N21 and S16 during storage and for the beams in spans two and three of the northbound main lanes bridge after the composite deck was completed. The locations of these beams in the bridge are shown in Figures 3.2 and 3.3 in Section 3.2.1. These measurements are summarized in Tables 5.3 to 5.6. Camber measurements were taken throughout the day to observe the increase in camber resulting from temperature gradients in the beam. The first camber measurements were taken in the morning and were used as the baseline reading. Thermal movements were determined by subtracting the initial camber measurement from the measurement later in the day. It was assumed that no time-dependent changes in camber occurred during the times that the measurements were taken.

Table 5.3 shows the measured thermal movements for Beam N21 on August 24, 1995. The maximum measured increase in camber was 8.6 mm at 2:45 p.m. Several of the measured temperature gradients for Beam N21 on that day are shown in Figure 5.45. Predicted changes in camber based on these gradients were calculated and included in Table 5.3 for comparison with the measured changes in camber. The predicted thermal movements were calculated as described in Section 5.3.1. The maximum theoretical increase in camber was 10.7 mm at 3:50 p.m. The predictions tended to overestimate the measured thermal movements throughout the afternoon. Incorrect assumptions in the theoretical model, unequal heating of the two sides of the beam, and variation of the temperature gradient along the length of the beam could have been possible causes for the overestimations of camber resulting from thermal movements. The theoretical model was very sensitive to the temperature of the bottom flange since it had such a large mass relative to the whole section. Small errors in the bottom flange temperature caused large variations in the estimated thermal movement.

Table 5.3 Measured thermal movements on August 24, 1995 for Beam N21 in storage

Time	Weather Conditions	Measured Change in Camber (mm)	Predicted Change in Camber (mm)²
10:10 a.m. ¹	Sunny	0.0	0.0
11:00 a.m.	Sunny	3.6	0.3
1:05 p.m.	Sunny	7.1	7.6
2:45 p.m.	Sunny	8.6	9.7
3:50 p.m.	Sunny	8.4	10.7
5:10 p.m.	Sunny	6.6	9.9

Notes:

1. The measurement taken at this time was considered the baseline reading.
2. Predicted changes in camber were calculated based on the measured temperature gradients for Beam N21 as shown in Fig. 5.45.

Table 5.4 shows the measured thermal movements for Beam S16 on November 29, 1994. The measured camber grew 11.4 mm by 4:00 p.m. as the day turned from cloudy to sunny. The measured temperature gradients for Beam S16 on that day are shown in Figure 5.44. For this beam, the measured changes in camber were larger than the predicted changes in camber. The probable causes for these differences are the same as those identified for the results of Beam N21.

These two days were the only times that thermal movements were measured throughout the course of a day for beams in storage. Because of the limited amount of data, the maximum camber caused by temperature gradients for 40-meter long U-beams in storage cannot be determined. Based on the data available, as summarized above, the expected thermally induced camber should be at least 11.4 mm.

Table 5.4 Measured thermal movements on November 29, 1994 for Beam S16 in storage

Time	Temperature (°C)	Weather Conditions	Measured Change in Camber (mm)	Predicted Change in Camber (mm) ²
8:25 a.m. ¹	16	Cloudy	0.0	0.0
9:50 a.m.	18	Partly Cloudy	1.5	N/A
11:05 a.m.	21	Sunny	5.6	2.8
12:40 p.m.	24	Partly Cloudy	9.9	7.9
2:30 p.m.	24	Partly Cloudy	10.4	N/A
4:00 p.m.	24	Sunny	11.4	8.9

Notes:

1. The measurement taken at this time was considered the baseline reading.
2. Predicted changes in camber were calculated based on the measured temperature gradients for Beam S16 as shown in Fig. 5.44.

Tables 5.5 and 5.6 summarize the measured thermal movements for the composite bridge deck on November 8, 1996. The maximum observed changes in camber caused by temperature gradients occurred in the exterior girders of spans two and three between 2 p.m. and 3 p.m. The maximum thermal movements were 7.4 mm for Beam N31 and 5.3 mm for Beam N21. The thermal movements decreased going from west to east across the bridge deck. This was probably a result of more intense heating of the exterior beam as the sun moved across the sky in the afternoon. Thermal gradients for Beams in the northbound main lanes bridge on November 8, 1996 were not available because of a malfunction in the storage of the data during that time.

Table 5.5 Measured thermal movements on November 8, 1996 for span three of the northbound main lanes bridge

Time	Weather Conditions	Measured Change in Camber (mm)				
		N31	N32	N33	N34 ²	N35 ²
8:30 a.m. ¹	Sunny	0.0	0.0	0.0	0.0	0.0
12:25 p.m.	Sunny	5.1	5.1	4.3	3.8	4.1
2:20 p.m.	Sunny	7.4	6.6	6.4	4.6	5.8
5:00 p.m.	Sunny	5.6	4.6	4.6	4.1	4.6

Notes:

1. The measurements taken at this time were considered the baseline readings.
2. Camber measurements for Beams N34 and N35 were only taken after erection in the bridge.

Measurements of thermal movements in the composite bridge were not obtained during other times of the year. Consequently, maximum expected camber resulting from temperature gradients in the composite deck cannot be identified based on the limited data

presented here. The maximum thermal movements for this composite bridge can be expected to be at least 7.4 mm.

Table 5.6 Measured thermal movements on November 8, 1996 for span two of the northbound main lanes bridge

Time	Weather Conditions	Measured Change in Camber (mm)		
		N21	N22	N23
8:20 a.m. ¹	Sunny	0.0	0.0	0.0
12:10 p.m.	Sunny	4.1	3.6	3.3
2:40 p.m.	Sunny	5.3	5.1	5.1
5:20 p.m.	Sunny	4.8	3.6	3.8

Notes: 1. The measurements taken at this time were considered the baseline readings.

5.4 COMPARISON OF MEASURED BEHAVIOR

5.4.1 Camber and Deflection

Measured camber and deflection responses for the twelve instrumented beams were compared to identify similarities and differences in behavior among the beams. Comparison of time-dependent camber responses were made between sets of companion beams that had nearly identical properties. Further comparisons were made among all of the beams to examine differences between measured and predicted elastic cambers at release, growth in camber from release to just before placement of the deck panels, and correlation of measured elastic responses to superimposed loads among beams in the same span.

5.4.1.1 Camber Responses for Companion Beams

The time-dependent camber plots shown in Sec. 5.3.1 can be compared to one another because many of the beams shared similar casting dates, section types, span lengths, and strand patterns. The camber responses for four pairs of beams are shown in Figures 5.52 to 5.55 to examine whether the companion beams behaved similarly.

Figure 5.52 shows the time-dependent camber responses for Beams N32 and N33, which were cast on February 15, 1996. Both beams were U54A cross sections having 64 prestressing strands. The span length during storage for Beam N32 was only 0.20 meters less than the span length of Beam N33. The beams were positioned next to one another in span three of the northbound bridge. The span length in the bridge for Beam N32 was only 0.16 meters less than the span length for Beam N33. The camber responses for both of the beams were adjusted for thermally induced camber and support conditions during storage.

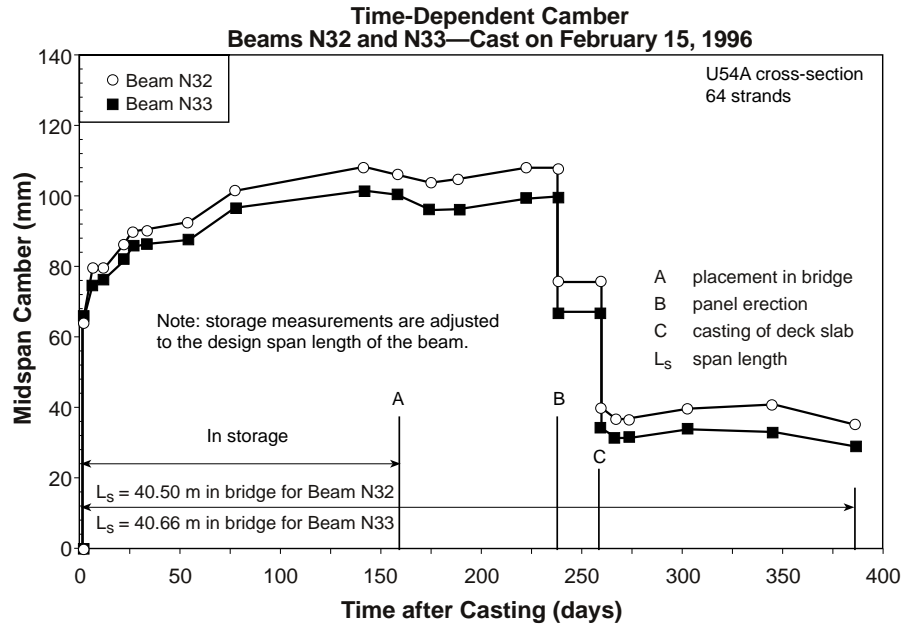


Figure 5.52 Comparison of the measured camber and deflection responses of Beams N32 and N33

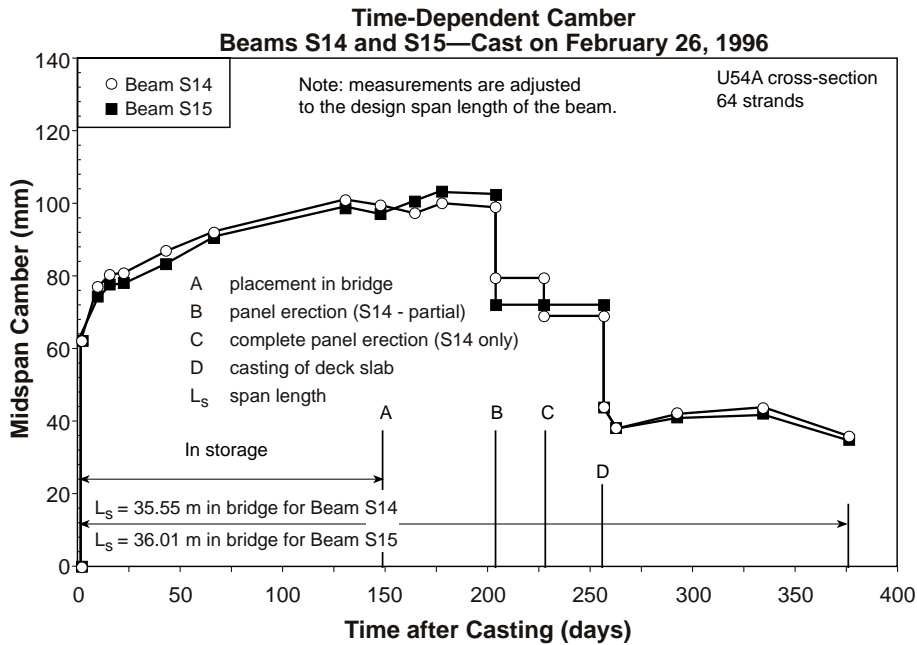


Figure 5.53 Comparison of the measured camber and deflection responses of Beams S14 and S15

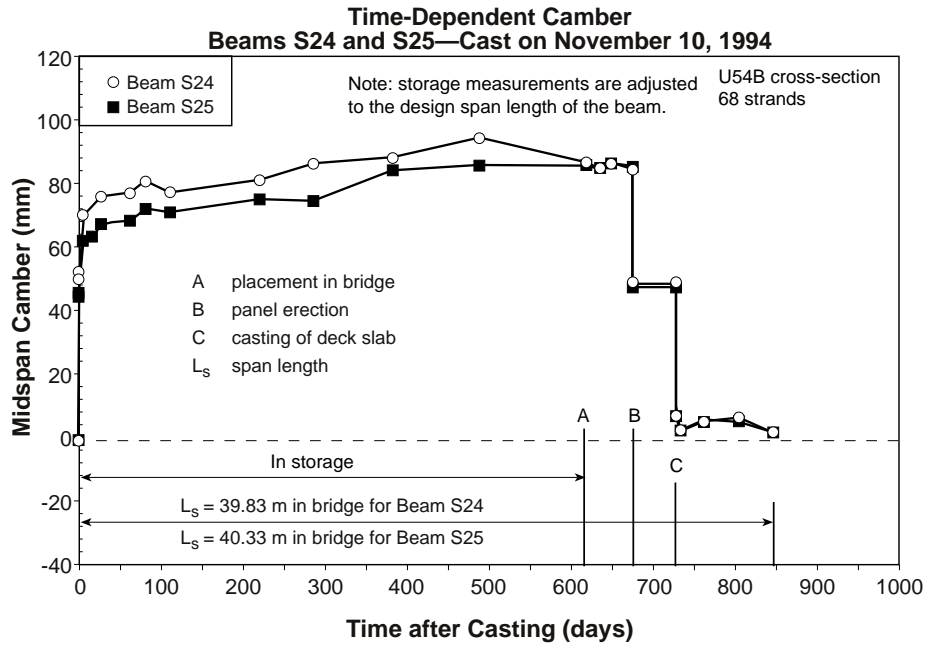


Figure 5.54 Comparison of the measured camber and deflection responses of Beams S24 and S25

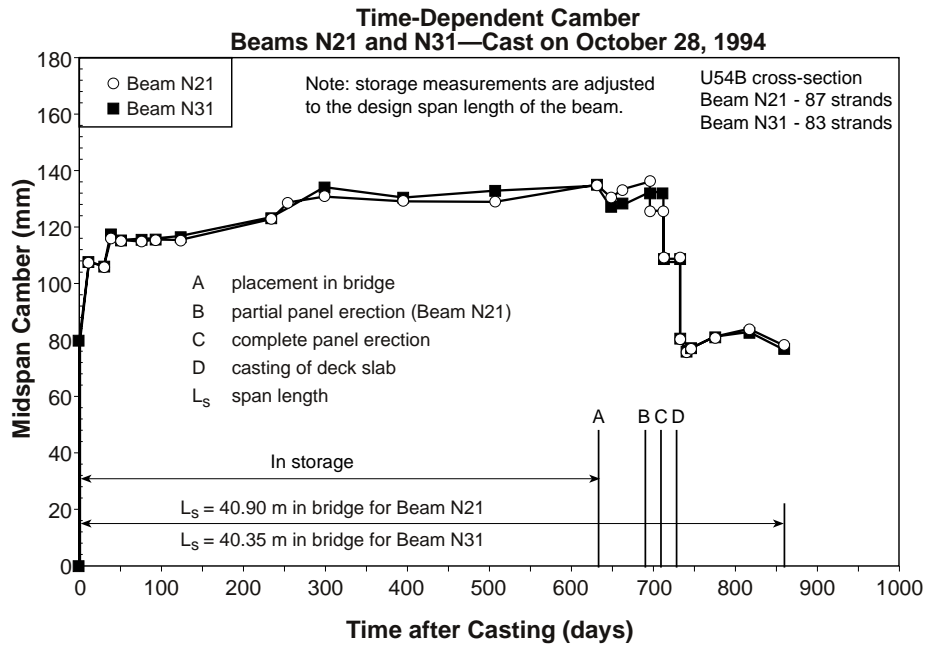


Figure 5.55 Comparison of the measured camber and deflection responses of Beams N21 and N31

The initial cambers at release were 63.8 mm and 65.9 mm for Beams N32 and N33, respectively. The camber for Beam N32 increased faster than for Beam N33, even though the support conditions were almost identical for these two beams. The plots of the midspan camber versus time shown in Figure 5.52 have the same shape. The cambers for Beams N32 and N33 just before the precast deck panels were erected were 107.7 mm and 99.8 mm, respectively. The camber in Beam N32 increased 10.0 mm more than Beam N33 over a period of 238 days.

Elastic responses to superimposed loads were very similar for the two beams. When the precast panels were erected, Beam N32 deflected 32.0 mm while Beam N33 deflected 32.7 mm. After the cast-in-place deck was poured, Beam N32 deflected 35.3 mm and Beam N33 deflected 32.0 mm. The difference between the last two measurements can be attributed to variations in the deck thickness. At 386 days after casting, a camber differential of only 6.1 mm remained between the two beams. The measured camber and deflection values for all three sets of companion beams are summarized in Table 5.7.

Figure 5.53 shows the camber response histories for Beams S14 and S15. These beams were also U54A cross sections with 64 prestressing strands. The design span length of Beam S14 was 0.47 meters shorter than the design span length of Beam S15, and its span length in storage was 0.50 meters shorter as well. The camber responses for these beams were much closer than for Beams N32 and N33 even though the difference in supported length was larger. There was virtually no camber differential between Beams S14 and S15 at release, after casting of the deck, and at 375 days after casting. At 375 days, the camber in Beam S14 was only 1.3 mm larger than that of Beam S15. Table 5.7 summarizes the camber and deflection values for Beams S14 and S15.

Figure 5.54 shows the camber response histories for Beams S24 and S25. These beams were U54B cross sections with 68 prestressing strands. The design span length of Beam S24 was 0.50 meters shorter than the design span length of Beam S25, and its span length in storage was 0.52 to 0.60 meters shorter as well. Measured camber and deflection values for these beams are summarized in Table 5.7. The camber at release for Beam S24 was 6.7 mm higher than for Beam S25. The camber for Beam S24 remained higher until placement of the deck panels. At that time, the cambers of the two beams were nearly identical and stayed that way through 848 days after casting. At 848 days, the camber in Beam S24 was only 0.2 mm larger than that of Beam S25.

Table 5.7 Comparison of camber and deflection responses for companion beams

Time or Event	Measured Camber or Deflection (mm)							
	N21	N31	N32	N33	S14	S15	S24	S25
Initial camber at release	80.5	78.1	63.8	65.9	61.8	62.4	50.8	44.1
Camber before deck panels	136.4	132.6	107.7	99.8	98.3	101.9	84.8	85.9
Deflection resulting from deck panels	27.7	24.9	32.0	32.7	29.7	30.3	36.0	38.1
Deflection resulting from CIP deck	29.5	26.7	35.3	32.0	24.9	28.7	41.4	40.7
Long-term camber	77.7	76.7	35.1	29.0	35.6	34.3	2.3	2.5

Figure 5.55 shows the camber response histories for Beams N21 and N31. These beams were U54B cross sections with similar span lengths but their strand patterns were slightly different. The strand patterns for Beams N21 and N31 contained 87 and 83 strands, respectively. Since these beams were in the same pour, four of the strands needed to be debonded for the entire length of Beam N31.

The design span length of Beam N21 was 0.55 meters longer than that of Beam N31, and its span length in storage was 0.78 to 1.08 meters longer as well. Measured camber and deflection values for these beams are summarized in Table 5.7. The camber at release for Beam N21 was only 2.4 mm higher than for Beam N31. The camber responses for these beams remained nearly identical up to placement of the deck panels, at which time the camber for Beam N21 was only 3.8 mm larger. The agreement in camber for these beams was probably due to the slightly shorter span length of Beam N31 offsetting the slightly higher prestressing force of Beam N21.

The elastic deflections resulting from the deck panels and cast-in-place (CIP) deck were very similar. The deflections observed in Beam N31 were slightly lower than those of Beam N21 because of a shorter span length, smaller beam spacing, and possible variation in the actual thickness of the CIP deck. At 861 days after casting, the camber in Beam N21 was only 1.0 mm larger than that of Beam N31. The smaller deck load deflections for Beam N31 offset the slightly larger increase in camber during storage for Beam N21.

5.4.1.2 Comparison of Measured and Predicted Cambers at Release

The measured and predicted elastic cambers at release are summarized in Table 5.8. Predicted cambers at release were calculated based on the second area-moment theorem for calculating deflections, which can be found in any mechanics of materials text. The elastic camber response at release was comprised of a component resulting from the prestress force (upward deflection) and a component resulting from the weight of the beam (downward deflection). Strand debonding was considered when calculating the upward deflection caused by the prestress force. The prestress losses assumed for this calculation were 2 percent for strand relaxation, 2 percent for temperature losses, and the immediate losses resulting from elastic shortening. The beam diaphragms were included in the calculation of downward deflection resulting from the beam weight. The elastic modulus for the concrete used in these calculations was the measured elastic modulus at release for each beam, which is shown in Sec. 5.2.2. Transformed section properties, which were calculated by transforming the strand steel to an equivalent area of concrete, were also used for the predicted camber calculations.

Differences between measured and predicted camber at release varied considerably. All of the measured release cambers were lower than the predicted cambers. The measured cambers ranged from 2.4 to 25.0 mm lower than the predicted values. Ratios of measured camber to predicted camber varied between 0.646 and 0.972. The initial cambers were reasonably well estimated, considering that the net camber was the small difference between two large components of deflection, namely the upward prestress component and the downward beam weight component.

For the beams that had ratios of measured camber to predicted camber greater than 0.868, the lack of camber was probably resulting from some combination of the following:

1. The measured elastic modulus was lower than the actual elastic modulus in the beam.
2. The actual prestress force transferred to the beam was lower than the assumed prestress force.
3. The actual beam weight was slightly larger owing to the volume of steel embedded in the concrete.
4. The calculation for thermally induced camber or deflection in the beams was not correct.

Table 5.8 Comparison of measured and predicted cambers at release

Beam	Measured Camber (mm)	Predicted Camber (mm)	Measured - Predicted (mm)	Ratio of Measured to Predicted Camber
S14	61.8	69.9	-8.1	0.884
S15	62.4	69.9	-7.5	0.893
S16	49.1	71.9	-22.8	0.683
S24	50.8	69.3	-18.5	0.733
S25	44.1	68.3	-24.2	0.646
S26	84.5 ¹	86.9	-2.4	0.972
N21	80.5	92.7	-12.2	0.868
N22	46.4	71.4	-25.0	0.650
N23	45.0 ¹	61.2	-16.2	0.735
N31	78.1	89.2	-11.1	0.876
N32	63.8	71.1	-7.3	0.897
N33	65.9	71.1	-5.2	0.927
Notes:				
1. These measurements were not adjusted for thermally induced movement.				

An increase in the modulus of elasticity by 10 percent lowered the predicted cambers by 5.1 to 7.6 mm. An increase in the estimated losses before release by 2 percent lowered the predicted cambers by 2.5 to 3.8 mm. An increase in the weight of the beam by 2 percent lowered the predicted cambers by an additional 1.3 to 2.0 mm. A combination of these conditions could possibly change the predicted cambers by as much as 13.4 mm.

The analytical correction for thermally induced movement was very sensitive to the temperature assigned to the bottom flange because of its large mass. In addition, the temperatures measured at the bottom flange and CGS were assumed not to vary across the section. Thus, small errors in the measured temperatures could have resulted in sizeable variations in the thermal camber.

Also, the analytical correction for thermally induced movement was made based on a uniform temperature gradient, as described in Sec. 5.3.1. However, temperature gradients of

9 °C were observed during casting for Beams S16 and N32. From that temperature gradient, a beam would cool down to a uniform temperature gradient, implying that cooling of the section would be uneven. Since the top would cool down, or shorten, more than the bottom, a negative curvature would be induced in the beam that would cause a component of deflection. This component of deflection would not be observable until after release. Corrections for uneven cooling were not made because of lack of data. However, sample calculations for Beams S16 and N32 showed that the magnitude of this component could be as large as 12 mm.

While seven of the beams had camber that was low by 12.2 mm or less, the other five beams had camber that was low by as much as 25.0 mm. Differences that large were not caused by variations in elastic modulus and prestress force alone. One possible cause for these large differences was that there were errors in the baseline camber reading for some of these beams. For the beams cast in 1994, which includes all five of the beams with very low initial camber, the baseline piano wire camber reading was taken after the plywood pads were placed under the ends of the beam. Therefore, corrections needed to be made to account for the thickness of the pads. This problem was not realized until the last pour in 1994 and estimations needed to be made for the pad thickness. Corrections for the pad thickness were made although there could have been a variation of as much as 6.4 mm between the assumed and actual pad thickness.

The baseline camber reading for the beams cast in 1996 was taken before the pads were in place. The cambers for those beams were much closer to the predicted cambers, as shown in Table 5.8.

5.4.1.3 Camber Growth During Storage

The midspan camber growth during storage for all of the instrumented beams is summarized in Table 5.9. The measured camber just before placement of the deck panels was used to determine a ratio of long-term camber to camber at release. This was a convenient way of comparing the camber growth for all of the beams. Shrinkage and creep of the concrete was essentially complete for all of the beams at the time of placement of the deck panels.

The camber growth ratios were between 1.51 and 1.70 for eight of the twelve beams. The average growth ratio was 1.74. Beam S16 had the largest growth ratio at 2.08, which was probably a result of low initial camber. The initial camber for Beam S16 was approximately 12 mm lower than Beams S14 and S15 despite having four more prestressing strands. All three beams had essentially the same span.

Out of the four sets of companion beams, only Beams S14 and S15 and Beams N21 and N31 had growth ratios that were close to each other. The other two sets of companion beams had significantly different growth ratios.

The growth ratio for Beam S26 was only 1.55 because transfer occurred at 7 days. The later age for transfer (compressive loading of the concrete owing to prestress) significantly affected the time-dependent camber growth resulting from creep. The four

beams that were kept in storage the least amount of time generally had lower growth ratios than the other beams.

Some of the observed differences in long-term camber growth between similar beams was due to variations in support conditions. However, the differences in support conditions were generally less than 0.5 meters.

Table 5.9 Comparison of midspan camber growth during storage for all of the instrumented beams

Beam	Time (days)	Camber at Release (mm)	Camber Before Panels (mm)	Increase in Camber (mm)	Camber Growth Ratio
N21	697	80.5	136.4	55.9	1.69
N22	725	46.4	88.6	42.2	1.91
N23	732	45.0 ¹	83.1 ¹	38.1	1.85
N31	713	78.1	132.6	54.5	1.70
N32	238	63.8	107.7	43.9	1.69
N33	238	65.9	99.8	33.9	1.51
S14	203	61.8	98.3	36.5	1.59
S15	203	62.4	101.9	39.5	1.63
S16	717	49.1	102.1	53.0	2.08
S24	676	50.8	84.8	34.0	1.67
S25	676	44.1	85.9	41.8	1.95
S26 ²	710	84.5 ¹	131.1 ¹	46.6	1.55

Notes:

1. Measurements not adjusted for thermally induced movement.
2. Release occurred at 7 days after casting.

Figures 5.56 to 5.63 show the time-dependent growth of midspan camber in the form of a multiple of the measured release camber. These plots were developed using the time-dependent camber and deflection responses presented in Sec. 5.3.1. Multiples of the initial camber were calculated for several beams up to panel erection and plotted as functions of time.

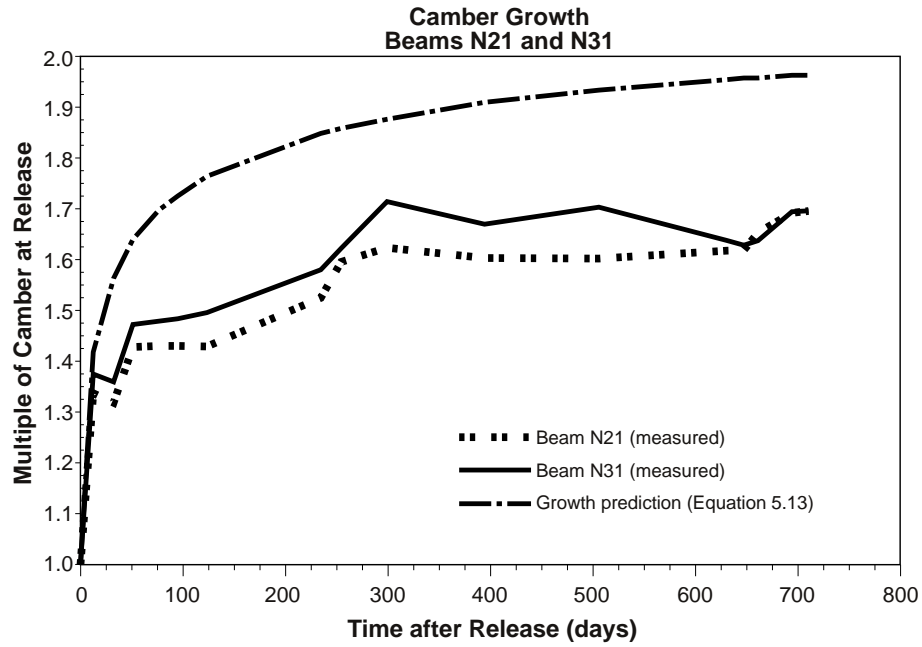


Figure 5.56 Camber growth ratios up to panel erection for Beams N21 and N31

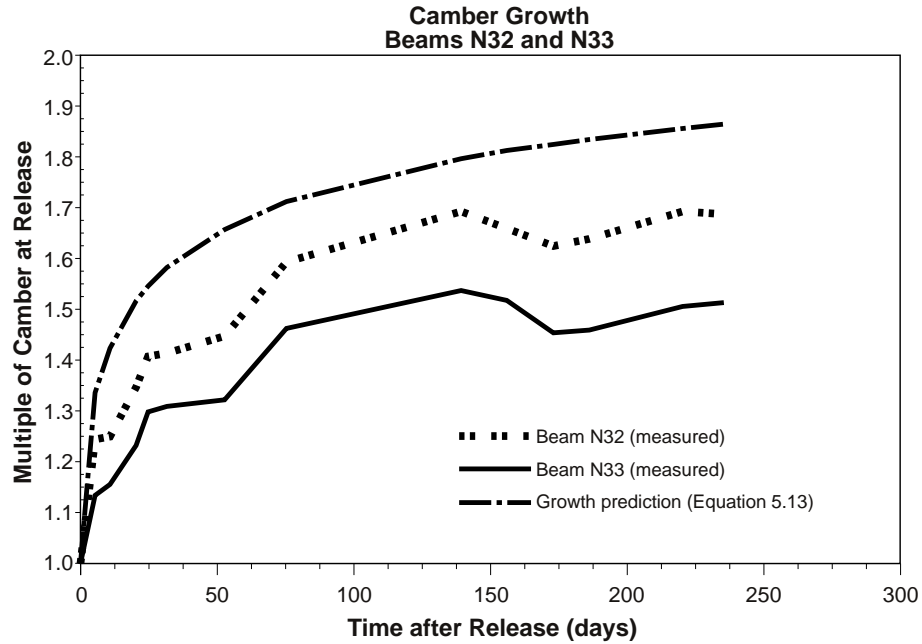


Figure 5.57 Camber growth ratios up to panel erection for Beams N32 and N33

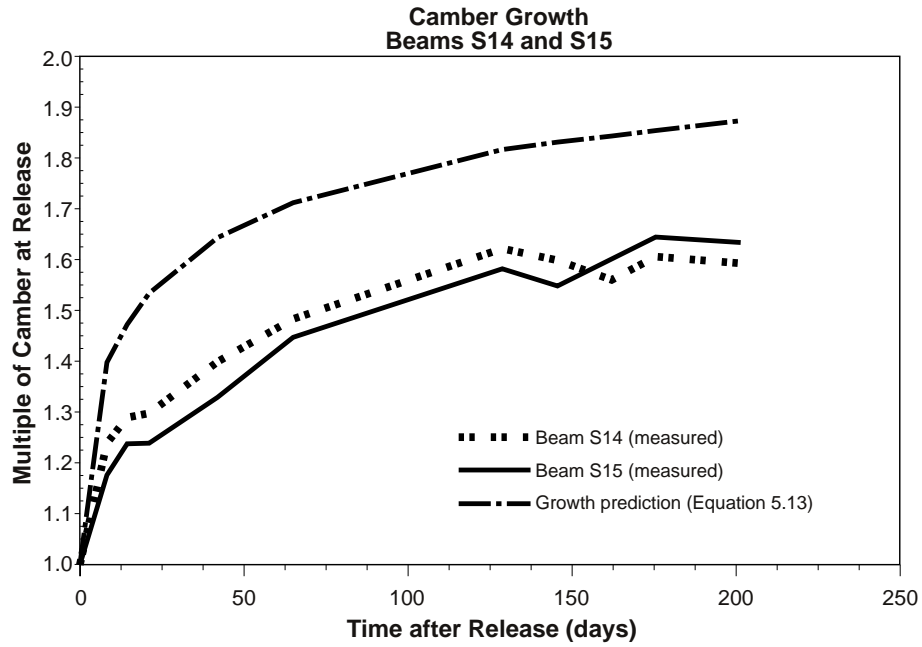


Figure 5.58 Camber growth ratios up to panel erection for Beams S14 and S15

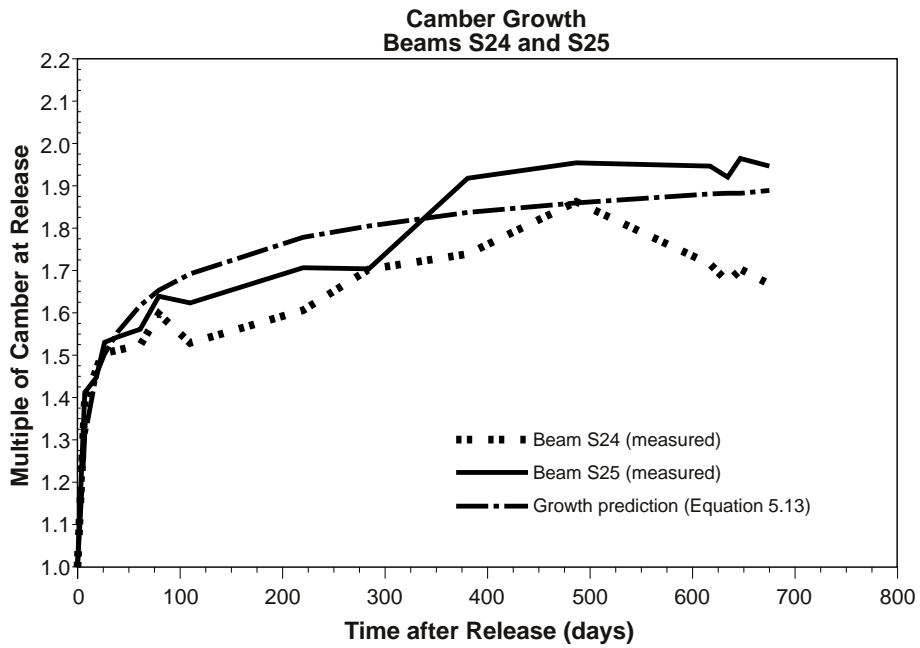


Figure 5.59 Camber growth ratios up to panel erection for Beams S24 and S25

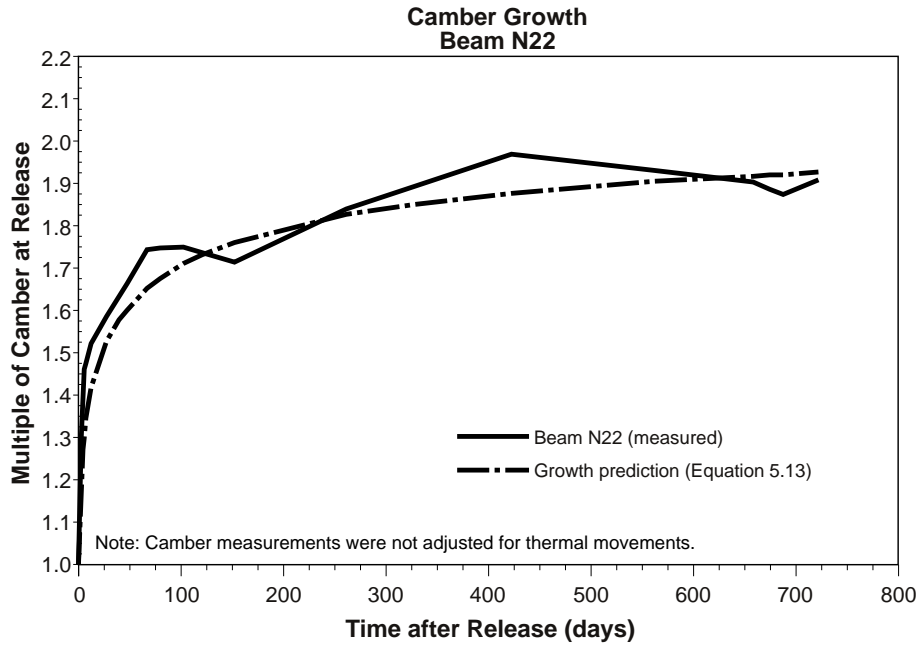


Figure 5.60 Camber growth ratios up to panel erection for Beam N22

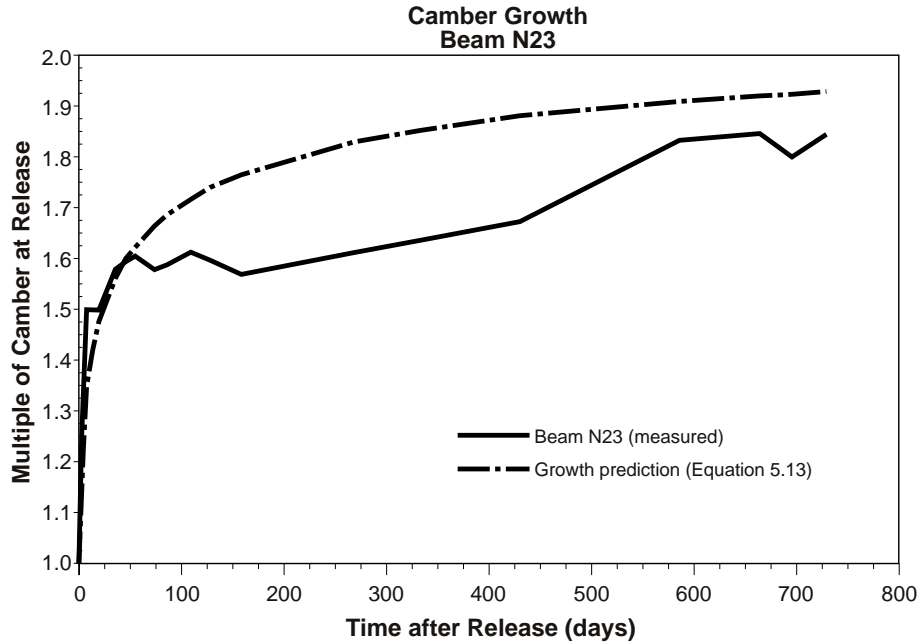


Figure 5.61 Camber growth ratios up to panel erection for Beam N23

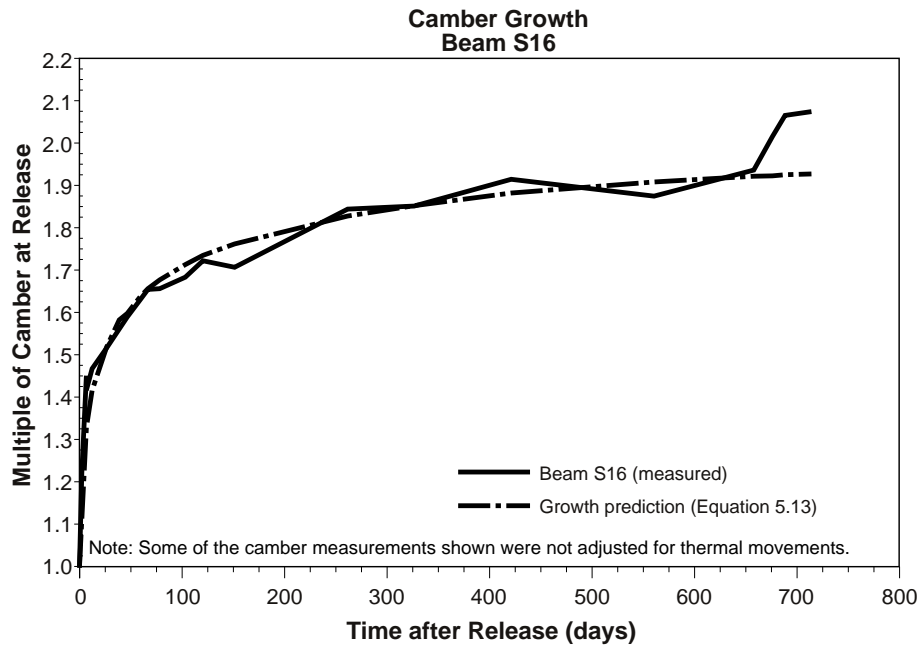


Figure 5.62 Camber growth ratios up to panel erection for Beam S16

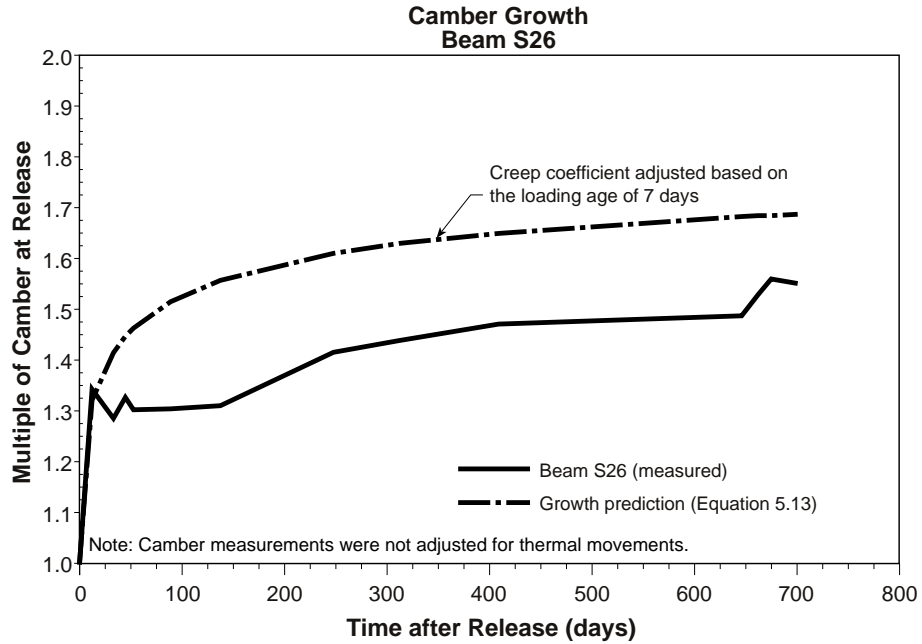


Figure 5.63 Camber growth ratios up to panel erection for Beam S26

The time-dependent camber growth curves were compared to the measured creep coefficient for the beam concrete, which was given in Eq. 5.3. This equation needed to be modified to account for the difference in volume-to-surface ratio and relative humidity between the creep specimens and the U-beams. The ultimate creep coefficient was modified based on a relative humidity of 75 percent and volume to surface ratios of 73.4 mm and 81.0 mm for the U54A and U54B cross sections, respectively. For the creep specimens, the relative humidity was 55 percent and the volume-to-surface ratio was 25.4 mm. The adjustments were made using correction factors suggested by ACI Committee 209 procedures (19). The creep coefficient at any time for the U-beams are given in Eqs. 5.11 and 5.12. For Beam S26, C_{cu} (the ultimate creep coefficient) was 1.05 because transfer occurred at 7 days.

$$C_{ct} = (1.45) \left(\frac{t^{0.5}}{6 + t^{0.5}} \right) \quad (\text{U54A sections}) \quad (5.11)$$

$$C_{ct} = (1.41) \left(\frac{t^{0.5}}{6 + t^{0.5}} \right) \quad (\text{U54B sections}) \quad (5.12)$$

The theoretical camber growth during storage can be expressed as a function of the time-dependent creep coefficient (C_{ct}), the ratio of initial prestress camber to initial beam weight deflection (μ_1) corresponding to the camber predictions in Sec. 5.4.1.2, and a modification factor that estimates the average loss of prestress during storage (μ_2). The theoretical growth function, which is only an approximation to the actual behavior, is given by Eq. 5.13. In this expression, the creep coefficient is slightly reduced by the effects of prestress loss. This expression was fairly sensitive to the value of μ_2 but was not sensitive to the deflection component ratio (μ_1).

$$\eta_t = \frac{(\mu_1 \mu_2 - 1)}{(\mu_1 - 1)} C_{ct} + 1 \quad (5.13)$$

where

η_t = predicted camber growth ratio during storage

$\mu_1 = \Delta_{\text{prestressed}} / \Delta_{\text{beam}}$ at release based on predictions given in Sec. 5.4.1.2
(varied from 1.7 to 2.3 for instrumented U-beams)

μ_2 = approximate average loss of prestress (taken as 0.92)

The camber growth curves for most of the beams were much lower than the growth curve predicted using Eq. 5.13. For example, Beams N21 and N31 shown in Figure 5.56 show the extreme case where the shape of the camber growth curve was very flat during the first 150 days compared to the creep coefficient curve. Other beams, such as N23, N33, S14, and S15, exhibited camber growth over time that was similar to Beams N21 and N31. Much

of the expected camber resulting from creep in the first 100 to 150 days was not achieved by these beams and the growth thereafter was very small.

A few of the beams exhibited camber growth that agreed with the camber growth prediction based on Eq. 5.13. Beam S25, shown in Figure 5.59, had an erratic growth curve but was close to the predicted creep curve for the 300-day period just before erection. At the time of erection, Beam S25 was only 3 percent over the predicted camber growth ratio. The camber growth of Beams N22 and S16, shown in Figures 5.60 and 5.62, respectively, also showed good agreement with the predicted growth curves.

Figures 5.56 to 5.59 show the camber growth curves for the companion beams discussed in Sec. 5.4.1.1. Beam N32, shown in Figure 5.57, displayed growth that was reasonably close to the predicted growth, while its companion beam (N33) displayed much lower growth. The difference in camber throughout storage for Beams N32 and N33 was magnified when the camber growth ratio was used as a comparison. Both growth curves showed similar shapes, which was expected based on the camber response curves shown in Figure 5.52. Beams S14 and S15 exhibited camber growth ratios that were very close throughout storage, while Beams S24 and S25 tended to separate at 200 days before erection of the panels. Beams N21 and N31 also had very similar camber growth ratios during storage.

The camber growth ratio curves tended to exaggerate measured differences in camber, errors in the measuring systems, and analytical corrections because the quantities being compared were much smaller than the actual cambers. The general shape of each growth curve was more important than examining differences between beams. However, the growth curves shown for the beams in this study generally indicated that rate of camber growth in the first 100 to 200 days and the total camber resulting from creep were considerably less than what was predicted with the camber growth equation shown in Eq. 5.13.

5.4.1.4 Comparison of Elastic Responses to Superimposed Loads

The measured deflections of the beams resulting from the deck panels and cast-in-place deck are shown in Table 5.10. The deflections of the interior beams were generally larger than the deflections of the exterior beams because they carried a larger volume of concrete. The ratios of deflections of the interior beams and the exterior beam for each span should have been approximately equal to the ratio of concrete volumes carried by each beam.

The interior beams of spans two and three of the northbound bridge carried 30 and 27 percent more deck panel load, respectively, than the exterior beam. The interior beams of spans one and two of the southbound bridge carried 44 and 38 percent more load, respectively, than the exterior beam. The ratio of loading depended upon the average beam spacing for the particular span. The ratios of measured deflections for span three of the northbound bridge and span one of the southbound bridge were very close to the approximate ratios of load carried. The ratios of measured deflections for the other spans were lower than the load ratios.

Similar ratios of measured deflections were expected after the cast-in-place deck was poured on the beams. The overhangs on the exterior beams were not cast because future

plans called for widening each bridge. This meant that the load ratios resulting from the CIP deck were nearly identical to the load ratios due the deck panels for all of the spans. The load ratios depended upon the actual deck thicknesses that were poured, which are shown in Sec. 4.4.3. The measured deflections resulting from the CIP deck generally exhibited similar behavior to the deflections caused by the deck panels.

Table 5.10 Summary of elastic responses resulting from superimposed loads for interior and exterior beams

Beam Group	Measured Deflection (mm)					
	Deck Panels ²			Cast-in-Place Deck		
	Interior ¹	Exterior	Ratio ³	Interior ¹	Exterior	Ratio ³
N21, N22, N23	32.8	27.7	1.18	36.7	29.7	1.24
N31, N32, N33	32.4	24.9	1.30	33.7	26.7	1.26
S14, S15, S16	29.9	19.8	1.51	26.8	24.1	1.11
S24, S25, S26	37.1	32.5	1.14	41.1	32.1	1.28

Notes:

1. Deflections represent an average of the two interior beams.
2. Measurements were not taken immediately after placement of the panels. There is a small amount of time-dependent deflection in these values. Measurements also were not adjusted for thermal movements.
3. Represents the ratio of deflection of interior beams to deflection of exterior beam.

The deflection ratios for the interior and exterior beams are much more complicated than simply the ratio of loads carried by the beams. Differences in span lengths and stiffnesses that existed among the beams affected the measured ratio of deflections. Also, the beam spacings were not constant, which meant that the superimposed load varied linearly along the length of the beam. The relative deflections between beams varied with the ratio of span lengths raised to the fourth power. Therefore, small differences in span length had a measurable effect on the deflection. As mentioned previously, the load ratios are good approximations of the expected deflection responses for the beams.

For the measured deflections resulting from the deck panels, corrections for thermal movements were not made on camber readings both prior to and after placement. Also, the reading after placement was taken several days after the actual placement. Some small additional time-dependent deflection probably occurred in between those readings. Both of these circumstances contributed to the variation in the measured deflection ratios shown in Table 5.10.

5.4.2 Prestressing Strand Strain

The measured strain at the center of gravity of the prestressing strands (CGS) was equivalent to the change in prestressing strand strain in the beams. The increase in the measured compressive strain at the CGS represented the loss of prestress with time in the

beams, not including the loss resulting from relaxation of the strands after release. Comparisons of the measured initial CGS strains and the measured time-dependent CGS strain responses were made for several of the instrumented beams. Additional comparisons were made between the time-dependent strain responses and the measured creep and shrinkage strains obtained from the companion tests.

5.4.2.1 Measured and Predicted Concrete Strain at CGS at Release

The measured and predicted strains at CGS immediately after transfer of the prestressing force are summarized in Table 5.11. The predicted strains at release were calculated assuming prestress losses of 2 percent resulting from relaxation and 2 percent resulting from shrinkage and strand temperature changes that occurred before transfer. Transformed section properties and the measured modulus of elasticity at release were used for the predictions as well.

Table 5.11 Measured and predicted compressive strain at midspan at CGS immediately after transfer

Beam	Side	Measured CGS Strain ($\mu\epsilon$)	Predicted CGS Strain ($\mu\epsilon$) ³	Difference ($\mu\epsilon$)	Ratio ⁴
S14 ¹	E	875	573	302	1.53
S15 ²	W	582	566	16	1.03
S15 ²	E	588	566	22	1.04
S16 ²	W	613	594	19	1.03
S16 ¹	E	552	594	-42	0.93
S25 ²	W	674	523	151	1.29
S25 ²	E	463	523	-60	0.89
S26 ²	W	727	603	124	1.21
N21 ¹	W	677	642	35	1.05
N21 ¹	E	731	642	89	1.14
N22 ¹	E	454	545	-91	0.83
N31 ¹	W	670	621	49	1.08
N32 ²	W	634	506	128	1.25
N32 ²	E	560	506	54	1.11
N32 ¹	E	629	506	123	1.24

Notes:

1. These measurements were obtained from electrical resistance strain (ERSG) gages.
2. These measurements were obtained from vibrating wire (VW) gages.
3. Predicted strains at transfer were calculated using transformed section properties, 2 percent loss for relaxation, 2 percent loss for temperature changes, and the measured elastic modulus at release for the specific beam pour.
4. Ratios were calculated as the measured strain divided by the predicted strain.

For many of the beams, the measured strains were within 10 percent of the predicted strains. Several of the measured strains varied with the predicted strains by only 3 to 5 percent. The strain measurements were generally higher than the predicted strains, which contradicted the low initial camber measurements that were observed for all of the beams. Based on the results found for initial camber, the measured strains were expected to be lower than the predictions, indicating a stiffer beam and/or an increase in the prestress losses before release.

The post-release measurements were taken an average of one hour after transfer began, so the possibility that creep and shrinkage had caused the strains to be higher was eliminated. The performances of the gages probably affected some of the measurements. However, the strains were consistently high for all of the beams and the errors between the predicted and measured strains were fairly low for most of the beams. In addition, most of the gages remained stable for several days past release, as shown in Sec. 5.3.3.

Voids in the concrete around the vibrating wire gages also may have contributed to some of the high strain measurements. The presence of voids would reduce the effective modulus of the concrete over the gage length. This would cause the strain readings to be higher than the actual strain at that section.

A more likely cause for the high measured strains at release may have been due to uneven cooling through the depth of the beam prior to release. Hydration temperatures of up to 60 °C were observed in Beams S16 and N32 during casting. In addition, temperature gradients as large as 9 °C between the top and bottom flanges were observed in these beams. Once the side forms were removed, these beams began to rapidly cool to a uniform temperature. However, the prestressing bed probably offered some degree of restraint to the beam as the beam began to shorten as a result of cooling and shrinkage. Evidence of this restraint was seen in the form of a regular pattern of cracks located at the stirrups and extending from the top of the beam to the lower part of the web.

The combination of uneven cooling and restraint of the bed may have caused a nonlinear distribution of strain to develop in the beam. The tendency of the uneven cooling was to induce a curvature in the beam, similar to the curvatures discussed in Sec. 5.3.1. However, if the bed were offering restraint at the bottom of the beam, that curvature would not be fully developed. The strain distribution in the beam was most likely linear down to the bottom flange, where the distribution became highly nonlinear owing to the restraint.

The strains that developed in the beams from uneven shortening prior to release probably affected the strain measurements just after release. The baseline measurement for the strain gages was taken immediately before transfer, when the effects of restraint were present in the beam. Upon transfer of the prestressing force, the restraint offered by the bed was removed, allowing the thermal curvature induced by uneven cooling of the section to fully develop.

The release of restraint at the bottom flange would be evident in the strain measurements at the CGS after release. The CGS strain gage would be measuring the net compressive strain resulting from the prestressing force and beam weight and an additional compressive strain that occurred once the restraint was removed and the thermal curvature was allowed to develop.

The thermal effects that occurred during casting and after the forms were removed were very complex. The magnitude of the strains that developed as a result of uneven shortening of the beam were difficult to determine. The purpose in this study was not to quantify these strains but to recognize the possible effects that uneven shortening prior to release had on the measured strains at the CGS.

It was also possible that the uneven thermal cooling had an adverse effect upon the measured camber at release. This was a valid assumption since the uneven cooling tended to induce a negative curvature, which would have caused a component of deflection in the beams. This is discussed further in Sec. 5.4.3.

Beams S16, S25, N21, and N32 showed differences in measured strains on each side. One possible cause for this was that the prestress force transferred to the section was not centered about the vertical axis. This would have resulted in a horizontally eccentric loading causing the beam to deflect, or sweep, in the horizontal plane. Unfortunately, measurements of sweep were not taken for these beams. The U-beams are twice as stiff in bending about the vertical axis as they are in bending about the horizontal axis. The required effective eccentricity to produce a strain differential between sides of 60 microstrain for these beams was approximately 63 mm. There were probably other factors related to the strain gages that caused these apparent differences in concrete strains between sides. As shown in Table 5.11, there was good correlation between sides for Beam S15 and for two of the three measurements for Beam N32.

5.4.2.2 Measured Immediate and Long-Term Prestress Losses

The measured immediate and long-term prestress losses are summarized in Table 5.12. Since the measured strain at CGS represented the change in strain of the prestressing strands, the change in stress was determined based on the elastic modulus of the strand given in Section 3.5.1 and the percent loss was calculated with reference to an initial stress of $0.75f_{pu}$.

The measured immediate prestress losses varied between 6.28 and 12.09 percent for the beams with internal strain instrumentation. The predicted immediate prestress losses resulting from elastic shortening for these beams were between 7.29 and 8.93 percent. The measured prestress losses at release were generally higher than predicted losses because they were directly related to the measured CGS strains. The possible reasons that the measured CGS strains were higher than the predicted strains are discussed in Sec. 5.4.2.1.

The measured long-term prestress losses varied between 11.24 and 21.17 percent. Long-term losses were based on strain measurements in the beams before the panels were erected in the bridge. Beam N21 had the lowest immediate and long-term losses while Beam S14 had the highest immediate and long-term losses. A majority of the strain measurements were taken between 140 and 690 days after release. The length of time depended upon when the beam was cast and the reliability of the strain gage. For Beams N32, N33, S14, and S15, the measured prestress losses were based on strains measured 140 to 176 days after release because they were cast in 1996. Beams S16 and S26 had strain measurements that were

taken 690 and 664 days after release. Beam S26 displayed relatively large prestress loss even though transfer was 7 days after casting for that beam.

Table 5.12 Immediate and long-term prestress losses based on measured compressive strains at beam midspan at CGS

Beam	Side	Measured Release Strain ($\mu\epsilon$)	Measured Long-Term Strain ($\mu\epsilon$) ³	Immediate Prestress Losses (% of $0.75f_{pm}$)	Long-Term Prestress Losses (% of $0.75f_{pm}$)
S14 ¹	E	875	1532	12.09	21.17
S15 ²	W	582	975	8.04	13.47
S15 ²	E	588	998	8.13	13.79
S16 ²	W	613	1113	8.48	15.38
S16 ¹	E	552	1158	7.63	16.00
S25 ²	W	674	1201	9.31	16.60
S25 ²	E	463	849	6.40	11.73
S26 ²	W	727	1198	10.05	16.56
N21 ¹	W	677	975	9.36	13.47
N21 ¹	E	731	1126	10.11	15.56
N22 ¹	E	454	813	6.28	11.24
N31 ¹	W	670	1174	9.26	16.22
N32 ²	W	634	1139	8.77	15.74
N32 ²	E	560	1121	7.74	15.49
N32 ^{1,4}	E	629	1233	8.69	17.04
N33 ^{2,5}	W	N/A	1147	N/A	15.85

Notes:

1. These measurements were obtained from electrical resistance strain (ERSG) gages.
2. These measurements were obtained from vibrating wire (VW) gages.
3. The long-term strain measurements used for these gages were at several days before placement of the superimposed loads because the gages failed to give reliable readings.
4. Measurement taken at 25 days, after which the gage became unreliable.
5. Release measurement was missed for Beam N33.
6. Release occurred 7 days after casting for Beam S26

Most of the beams experienced 5 to 7 percent of additional losses after release. These losses were directly related to the time-dependent creep and shrinkage of the beams and indirectly related to the relaxation of the steel during storage. The additional strain at release attributed to uneven thermal cooling, which was discussed in Sec. 5.4.2.1, would affect both the immediate and long-term measured prestress losses because it created an offset to the measured compressive strain. The time-dependent prestress losses, defined as the difference between the long-term and initial losses, would not be affected by uneven thermal cooling. The long-term losses were small for the U-beams, even with the effects of uneven thermal cooling present in the prestress losses.

5.4.2.3 Growth of Compressive Strain at CGS During Storage

Figures 5.64 to 5.69 show the time-dependent growth of compressive strain at CGS as plots of the time-varying multiple of the measured strain at release. These plots were developed using the time-dependent strain responses for the beams, which are presented in Sec. 5.3.3. Multiples of the compressive strain at release were calculated for several beams up to a time approximately equal to the time of panel erection.

The time-dependent strain growth curves were compared to the predicted strain growth curves based on the measured creep and shrinkage data for the companion specimens. The modified time-dependent creep coefficients for the U54A and U54B sections are given by Eqs. 5.11 and 5.12. The ultimate shrinkage coefficient, shown in Eq. 5.6, was modified using correction factors suggested by ACI Committee 209 procedures (19). The relative humidities and volume-to-surface ratios used to calculate corrections are given in Sec. 5.4.1.3. Equations 5.14 and 5.15 were used to calculate shrinkage strain for the U-beams. The ultimate shrinkage strain for Beam S26 was 224 microstrain to account for 7 days of steam curing.

$$(\varepsilon_{sh})_t = (.000279) \left(\frac{t^{0.6}}{2 + t^{0.6}} \right) \quad (\text{U54A sections}) \quad (5.14)$$

$$(\varepsilon_{sh})_t = (.000269) \left(\frac{t^{0.6}}{2 + t^{0.6}} \right) \quad (\text{U54B sections}) \quad (5.15)$$

The theoretical growth of the compressive strain at the CGS during storage can be expressed as a function of the time-dependent creep coefficient (C_{ct}), the ratio of initial prestress strain to initial beam strain (α_1) corresponding to the strain predictions in Sec. 5.4.2.1, a modification factor that estimates the average loss of prestress during storage (α_2), and the ratio of time-dependent shrinkage strain to initial strain owing to beam weight (α_{shr}). The theoretical strain growth function, which is only an approximation to the actual behavior, is given by Eq. 5.16. In this expression, the creep coefficient is slightly reduced by the effects of prestress loss. This expression was fairly sensitive to the values of α_2 and α_{shr} but was not sensitive to the strain component ratio (α_1).

$$\xi_t = \frac{(\alpha_1 \alpha_2 - 1) C_{ct} + (\alpha_{shr})_t}{(\alpha_1 - 1)} + 1 \quad (5.16)$$

where

ξ_t = predicted strain growth ratio during storage

$\alpha_1 = \varepsilon_{\text{prestressing}} / \varepsilon_{\text{beam}}$ at release based on predictions given in Sec. 5.4.2.1
(varied from 3.7 to 4.0 for the beams shown in Figs. 5.64 to 5.69)

α_2 = approximate average loss of prestress (taken as 0.92)

$\alpha_{shr} = (\varepsilon_{sh})_t / \varepsilon_{\text{beam}}$ which is based on Eqs. 5.14 and 5.15 for shrinkage strain and the predictions used to calculate release strain in Sec. 5.4.2.1

The measured strain growth curves were lower than the predicted growth curves for all of the beams shown in Figures 5.64 to 5.69. This was expected based upon the low measured long-term prestress losses presented in Section 5.4.2.2. The predicted strain growth ratio for the beams varied from 2.13 for Beam S26 to 2.47 for Beam S25, depending on the measured release strain and the age of the beam. The measured strain growth ratios varied from 1.61 for Beam S26 to 2.00 for Beam N32. Beam S26 was expected to be lower based on its age of 7 days at transfer, which was when compressive stress was applied to the concrete.

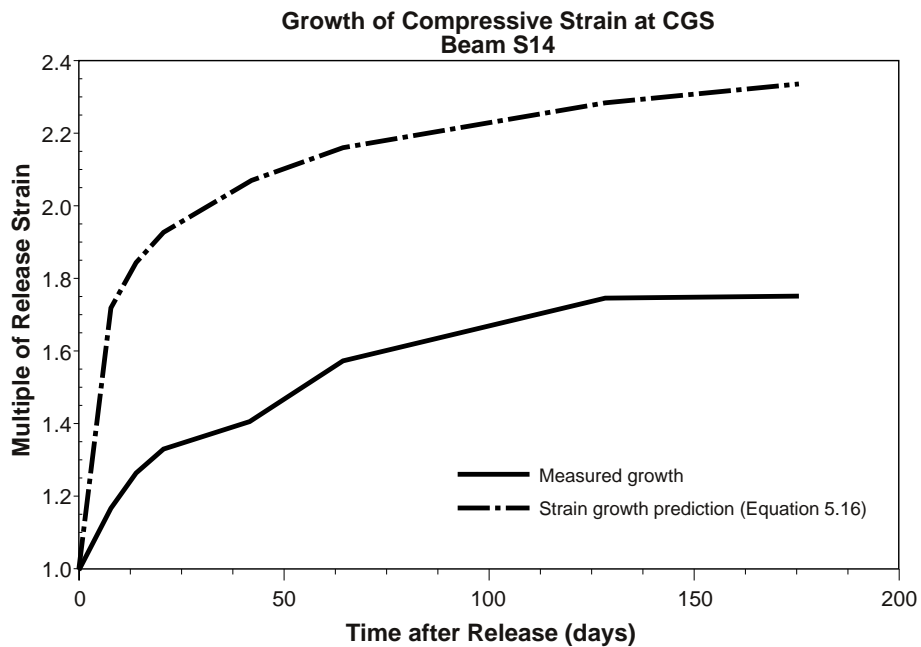


Figure 5.64 Strain growth ratio at the CGS up to panel erection for Beam S14

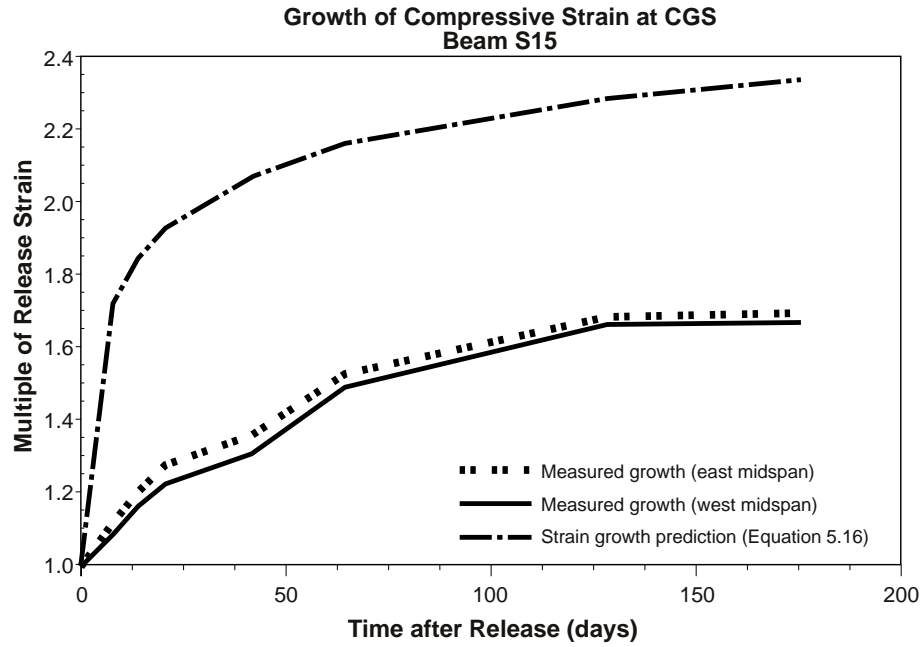


Figure 5.65 Strain growth ratio at the CGS up to panel erection for Beam S15

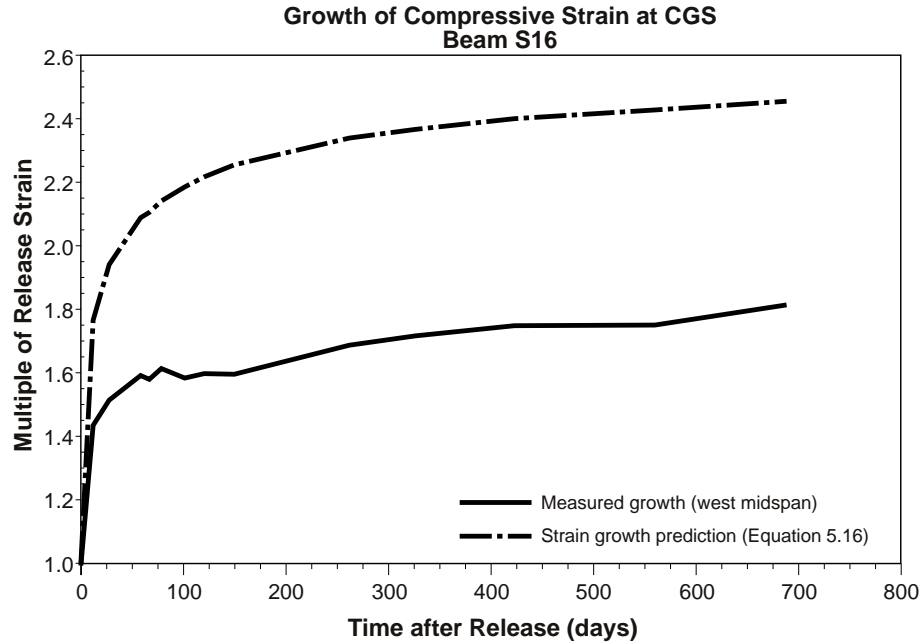


Figure 5.66 Strain growth ratio at the CGS up to panel erection for Beam S16

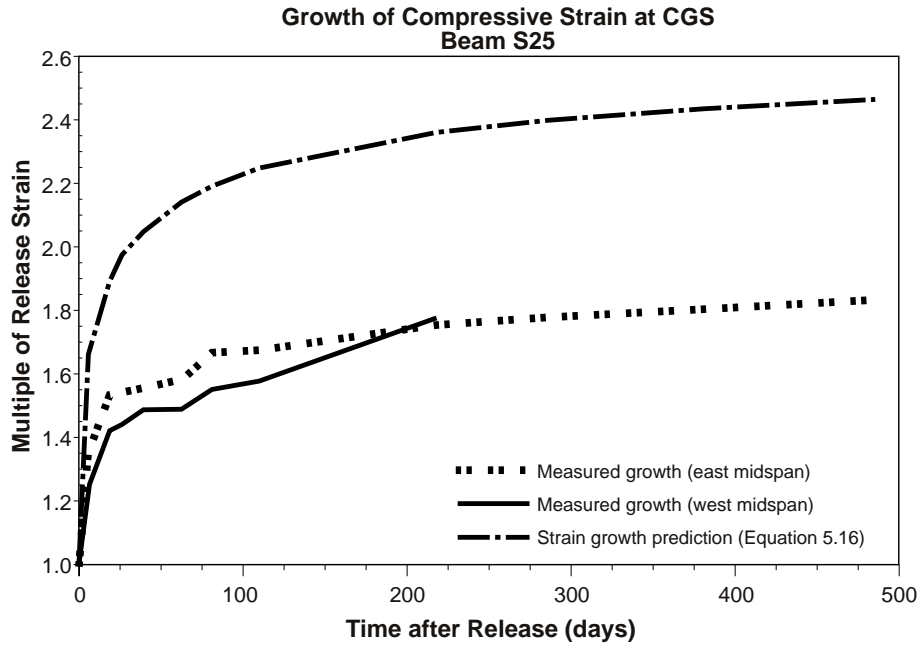


Figure 5.67 Strain growth ratio at the CGS up to panel erection for Beam S25

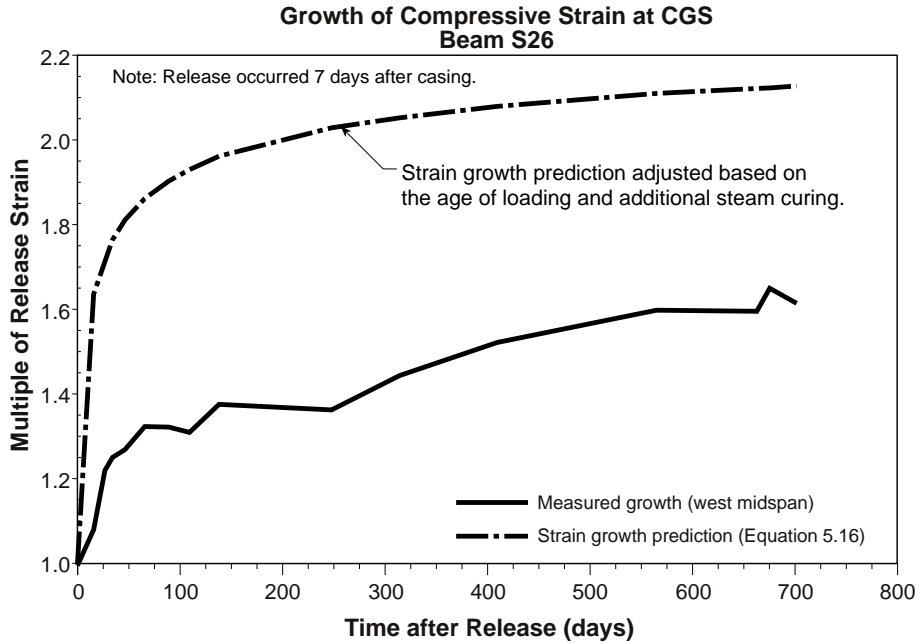


Figure 5.68 Strain growth ratio at the CGS up to panel erection for Beam S26

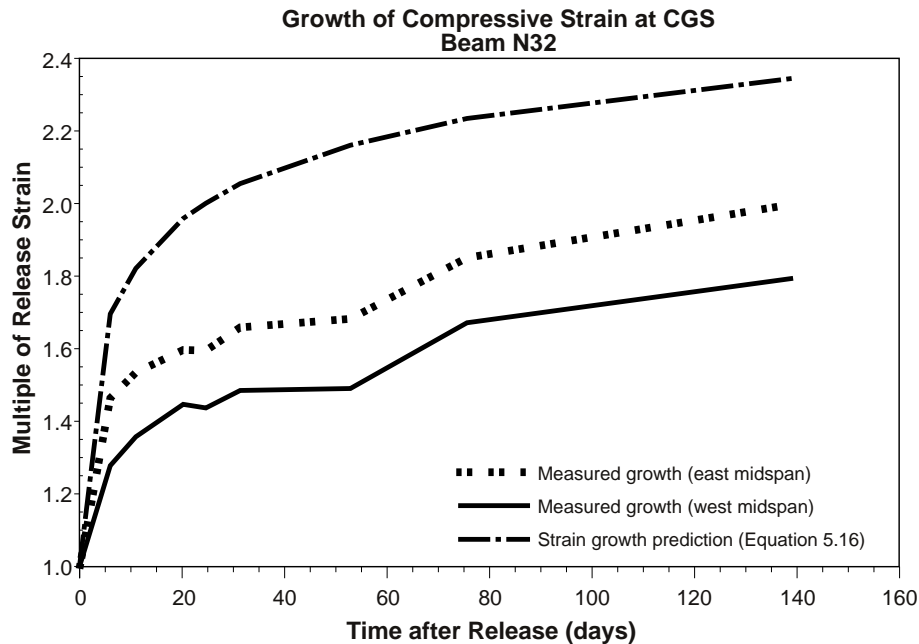


Figure 5.69 Strain growth ratio at the CGS up to panel erection for Beam N32

For all of the beams, except the east side of Beam N32, the behavior of the measured strain growth curves was similar. During the initial 100 to 150 days of storage, significantly less increase was observed in the measured growth curves than in the predicted curves. Much of the strain increase owing to creep and shrinkage during the first 100 days was not achieved by these beams and the growth thereafter was very small.

For Beam S15, shown in Figure 5.65, the strain growth curve was very flat during the first 150 days of storage compared to the predicted curve. Based on the strain growth curve for Beam S15, one would expect the camber growth to be similar. Examination of Figure 5.58 confirms that the camber growth curve for this beam had the same characteristics. Beam S15 had a strain growth ratio at CGS of 1.70 and a camber growth ratio of 1.63. The strain growth ratio should be larger because of the component of compression owing to the prestressing force that does not cause curvature in the beam (P/A).

Not all of the beams had strain and camber growth characteristics that agreed as well as was observed for Beam S15. Beams S16 and S25, shown in Figures 5.66 and 5.67 respectively, exhibited strain growth ratios of approximately 1.83. These ratios were higher when compared to the other beams, but low compared to the predictions. Figures 5.59 and 5.62 show the camber growth curves for Beams S25 and S16, respectively. The long-term camber growth ratios for these beams were higher than the long-term strain growth ratios. Furthermore, the camber growth for both beams agreed with the prediction fairly well, while the strain growth did not.

The observance of low strain growth at CGS in the beams agreed with the observance of low camber growth for most of the beams, as was shown in Sec. 5.4.1.3. With the

exception of Beams S16 and S25, the characteristics for the camber growth and strain growth curves were similar. If the growth ratios for both sides of Beam N32 were averaged, then the strain growth curve would show better agreement with the camber growth curve for Beam N32 shown in Figure 5.57.

Although it seemed that less creep and shrinkage were occurring in the beams during storage, the possible effects of uneven thermal cooling on the measured release strains were evident in the strain growth ratios. If the release strains were artificially high owing to the effects of uneven cooling, as discussed in Sec. 5.4.2.1, the strain growth ratios would be lower. The strain growth ratio is defined as the measured strain at any time divided by the measured strain at release. Since the measured strain was offset by the effects of uneven cooling, the ratio would increase as the denominator, or measured release strain, decreased. However, even if the release strains were actually lower than what was measured, the time-dependent strain growth curves would still be significantly less than the predicted curves for all of the beams.

5.4.3 Midspan Strain Profiles at Release

The measured strain profiles at midspan at release represented the curvature in the beam owing to the prestressing force and the weight of the beam. The measured midspan curvature could also be used as an indicator of the amount of camber in the beam at release. Comparisons of the measured and predicted midspan curvature at release for several of the instrumented beams are presented in this section and are compared to the measured cambers at release and the measured strains at release.

The measured and predicted midspan curvatures at release are summarized in Table 5.13. The measured midspan curvatures were determined by linear regression analysis. The predicted midspan curvatures were calculated based on the assumptions presented in Sec. 5.4.1.2 for predicting midspan camber at release. The predicted curvatures at release were positive because of the sign convention used in the calculations. A positive curvature corresponded to a moment that caused tension in the top fiber.

Differences between the measured and predicted midspan curvature varied from 1.21 to $-0.94 \text{ rad/mm (} \times 10^{-7} \text{)}$. A positive difference indicated that the measured curvature was larger than the predicted curvature. The ratios of measured to predicted midspan curvatures varied from 0.62 for Beam S25 to 1.31 for Beam S14 and the average curvature ratio was 0.95. Most of the measured curvature ratios agreed reasonably well with the predicted curvatures. Five of the nine beams had at least one ratio of measured to predicted curvature that was between 0.94 and 1.02.

Wide variations in the measured curvatures were probably due to the use of three different strain measuring systems to determine midspan curvatures. Generally the vibrating wire gages (VW) provided the most reliable data while the Demec surface strain gages were the least reliable. The Demec surface strains were less accurate because there were no corrections made for surface temperature differences between readings.

The measured curvature ratios at midspan are compared to the measured camber and CGS strain ratios in Table 5.14 for nine of the twelve instrumented beams. Whenever

possible, the data provided by the internal strain gages were used for the measured curvatures.

Table 5.13 Comparison of measured and predicted midspan curvatures at release

Beam	Source of Data	Measured Curvature¹ (x10⁻⁷ rad/mm)	Predicted Curvature² (x10⁻⁷ rad/mm)	Difference (x10⁻⁷ rad/mm)	Ratio³
S14	ERSG(East)	5.15	3.94	1.21	1.31
S15	VW ⁴	3.57	3.80	-0.23	0.94
S16	ERSG(East)	3.44	3.58	-0.14	0.96
S25	VW(East)	1.55	2.49	-0.94	0.62
S26	Demec ⁴	3.59	3.52	0.07	1.02
N21	ERSG(West)	4.45	3.72	0.73	1.20
	Demec ⁴	2.85	3.72	-0.87	0.77
N22	Demec ⁴	1.54	2.43	-0.89	0.63
N31	Demec ⁴	3.40	3.61	-0.21	0.94
N32	VW(West)	3.17	2.80	0.37	1.13
	ERSG(East)	2.70	2.80	-0.10	0.96
Notes:					
1. Measured curvatures were determined using a linear regression analysis of the data					
2. Predicted curvatures were based on the same assumptions used for predicting camber at release, which are presented in Sec. 5.4.1.2.					
3. Values represent the ratio of measured to predicted curvatures					
4. Measured curvatures for each side were averaged after the linear regression analysis					

The measured curvature ratios at release agreed with the measured camber ratios for five of the nine beams shown in Table 5.14. The differences between the measured camber and curvature ratios for Beams S15, S25, S26, N22, and N31 were less than or equal to 0.06. For the remainder of the beams, the measured curvature ratios were significantly higher than the measured camber ratios.

The curvature ratios were lower than the strain ratios for seven of the nine beams shown in Table 5.14. In addition, six of the nine beams had measured curvature ratios that

were below 1.05. A ratio less than 1.0 indicated that the measured curvature at midspan was less than the predicted curvature. Possible causes for lower curvature included a higher modulus of elasticity and a lower prestressing force than what was used in the predictions. However, these differences would have caused the measured strain at the CGS to be lower, which was not shown in the strain ratios given in Table 5.14.

Table 5.14 Comparison of the ratios of measured to predicted camber, curvature and CGS strain at midspan at release

Beam	Measured Camber Ratio¹	Measured Curvature Ratio²	Measured CGS strain Ratio³
S14	0.88	1.31	1.53
S15	0.89	0.94	1.03
S16	0.68	0.96	0.93
S25	0.65	0.62	0.89
S26	0.97	1.02	1.21
N21	0.87	1.20	1.05
N22	0.65	0.63	0.83
N31	0.88	0.94	1.08
N32	0.90	1.05 ⁴	1.24 ⁴

Notes:

1. Measured camber ratios at release taken from Table 5.8
2. Measured curvature ratios at release taken from Table 5.13
3. Measured CGS strain ratios at release taken from Table 5.11. Unless otherwise noted, the strain measurement was obtained from the same source of data as the corresponding curvature measurement.
4. Ratios were determined by averaging the west (VW) and east (ERSG) measurements.

Although an exact comparison between curvature and strain was not possible, the magnitudes of the curvature and strain ratios should have been relatively close. In addition, both of these ratios should have been fairly close to the measured camber ratio. Possible variations in the elastic modulus, beam weight, and prestressing force at release would have the same general effect on the magnitude of all three measurement ratios.

Beam S16 had measured curvature and strain ratios that were 0.96 and 0.93, respectively. However, the measured camber ratio was only 0.68. Since the strain measurements tended to agree with the predictions, the low camber may have been due to a component of deflection resulting from negative temperature gradients. This is discussed in Sec. 5.4.1.2. Another possibility is that the strain instrumentation measured additional strain resulting from restraint offered by the prestressing bed, which is discussed in Sec 5.4.2.1. Beams S14, N21, and N32 also showed similar behavior to Beam S16.

Beam N22, which was in the same pour as Beam S16, had camber and curvature ratios of 0.65 and 0.63, respectively, and a measured CGS strain ratio of 0.83. This seemed to contradict the behavior that was observed in Beam S16. However, the release curvature for Beam N22 was measured using surface strain instrumentation. It appeared that these measurements were distorted by changes in temperature since the camber ratios for both beams agreed and the strain ratios were relatively close. In addition, Beam N22 was 4.5 meters longer than Beam S16, which would magnify differences in the assumed and actual prestressing force and modulus of elasticity. Also, the deflection resulting from temperature gradients would be magnified, as shown in Eq. 5.10 (Sec. 5.3.1).

The measured curvatures were sensitive to strain measurements that did not correlate with the other readings in the strain profile. Beam S14, shown in Figure 5.35, was a perfect example of one strain reading (at CGS) not correlating with the other measurements. This was reflected in the measured strain ratio shown in Table 5.14. A better representation of the release curvature for Beam S14 may have been from the surface strain measurements. However, the curvature ratio based on surface strains, which was 1.12, was still much higher than the camber ratio of 0.88. Beam N21, shown in Figure 5.40, was another good example of how one strain measurement can significantly affect the measured curvature.

It was difficult to correlate the curvature and strain ratios shown in Table 5.14 for several reasons. First, the measured CGS strains at release include a component resulting from the prestressing force that does not induce curvature in a beam. Therefore, variations between the assumed and actual prestressing force would have affected the strain at CGS more than the curvature. Secondly, the measured curvatures shown in Table 5.13 were determined with linear regression analysis. One or two erroneous readings in the strain profile would have a large influence on the curvature, as shown for Beams S14 and N21. Thirdly, for Beams S26, N22, and N31, the strains at the CGS and the strain profiles were measured with different instrumentation. Also, the measured strains at the CGS for those beams were from one side (east or west), while the measured strain profiles represented an average of the measurements from both sides.

Based on the results presented for measured midspan camber, curvature, and CGS strain at release, it appeared that several factors accounted for the differences between the measured and predicted values. Since there most likely was a complex combination of variations between assumed and actual prestressing forces and moduli of elasticity, restraint offered by the prestressing bed during cooling of the beam, uneven cooling of the beam causing a thermally induced deflection component, and errors inherent to the camber and strain measurement systems, it was difficult to determine a pattern of behavior among these three types of measurements.

CHAPTER 6. ANALYTICAL METHODS FOR PREDICTING TIME-DEPENDENT BEHAVIOR

6.1 INTRODUCTION

There are many different methods available to the engineer for predicting long-term behavior of prestressed concrete bridge beams. These methods can range from simple hand calculation procedures to complex analytical procedures that require the use of a computer. Hand calculation methods can provide only a very general estimation of the long-term prestress loss, camber, and deflection of a prestressed beam. Computer-based analytical procedures can yield a more accurate prediction of long-term behavior, given that these methods can incorporate the time-dependent models for the properties of concrete and divide the time history of the beam into several discrete intervals. No matter which type of method is used for making predictions, it should be understood that only an estimation of behavior can be achieved and that a high degree of accuracy is not probable because of the complexity of time-dependent behavior in prestressed concrete beams.

In this chapter, three specific methods for predicting long-term prestress losses, camber, and deflection of prestressed concrete bridge beams are presented. For each method, the calculation procedures are discussed and the predicted behavior is compared to the measured behavior for the instrumented beams. Based upon the results of the analytical methods and the measured behavior, recommendations are presented for estimating prestress losses and camber for prestressed high performance concrete U-beams.

6.2 AASHTO

The AASHTO Standard Specifications for Highway Bridges (16) provides a simplified set of equations for estimating total prestress losses. This procedure takes into consideration prestress losses due to elastic shortening, creep, shrinkage, and prestressing steel relaxation. The equations for calculating prestress losses were developed based on normal weight concrete and both stress-relieved and low-relaxation prestressing strand. Assumptions for calculating each component of prestress loss based on the AASHTO procedure are outlined in this section followed by the resulting prestress loss predictions for the instrumented U-beams.

The equation for calculating the loss due to elastic shortening is based upon the modular ratio of the prestressing steel to concrete at release and the stress at the center of gravity of the prestressing steel (CGS) immediately after release. The concrete modulus of elasticity is calculated using the AASHTO equation shown below, in which f'_{ci} is the concrete compressive strength at release (MPa) and w is the unit weight of the concrete (kg/m^3).

$$E_{ci} = 4.27 \times 10^{-5} w^{1.5} \sqrt{f'_{ci}} \quad (\text{GPa}) \quad (6.1)$$

The tendon stress immediately after release is taken as $0.69 f'_s$ for low-relaxation strand. This accounts for the reduction of the initial tendon stress ($0.75 f'_s$) due to elastic shortening of the concrete and strand relaxation that occurs during placement and curing of the concrete. The resulting factor applied to the initial prestressing force is 0.92.

The equation for prestress loss due to shrinkage takes into account the mean ambient relative humidity of the surrounding environment of the beam and does not include the volume-to-surface ratio of the beam as a factor. The AASHTO Specifications provide a map identifying relative humidity for all sections of the U.S. The mean ambient relative humidity for Victoria and Houston, Texas, was taken as 75 percent. The resulting shrinkage strain for all of the instrumented beams was 205 microstrain and the loss due to shrinkage was 39.6 MPa (based on $E_s = 193$ GPa).

The equation for loss due to creep of the concrete is a function of the concrete stress at the center of gravity of the prestressing steel. The first component of the equation represents the initial stress at release due to the prestressing force and beam weight. This component of stress is multiplied by 12. If the modular ratio of steel to concrete were 6 then the theoretical creep coefficient applied to the concrete strain at release would be 2.0. The second component in this equation represents the stress due to all dead loads applied to the beam other than the beam self-weight. A smaller multiple of 7 is applied to this concrete strain to reflect the increased stiffness of the beam concrete at the later age of loading.

The last component of prestress loss is the relaxation of the prestressing steel. The equation for relaxation contains a constant loss of 34.5 MPa which is reduced based upon fractions of the calculated losses due to elastic shortening, creep, and shrinkage. This was done in an attempt to include the interdependent nature of relaxation with these other components.

Predictions of total prestress losses for the instrumented beams were calculated for two cases and compared to the measured prestress losses. The two prediction cases used different combinations of material properties, section properties, and equations for the modulus of elasticity of the concrete. These two prediction cases were also used in Sec. 6.3 and are as follows:

1. *Design Properties*: prestress losses are computed using gross cross-section properties, design concrete strengths, and the AASHTO equation for modulus of elasticity (Eq. 6.1).
2. *Measured Properties*: prestress losses are computed using transformed section properties (e.g., transforming the strands to an equivalent area of concrete), measured concrete strengths, and the proposed expression for modulus of elasticity shown in Eq. 6.2 (f'_{ci} in MPa and w in kg/m^3). This equation is the same as Eq. 5.2 based on the best fit to the measured moduli from the companion specimens.

$$E_{ci} = 3.10 \left(\sqrt{f'_{ci}} + 11.29 \right) \left(\frac{w}{2323} \right)^{1.5} \quad (\text{GPa}) \quad (6.2)$$

The case using design properties represented the typical procedure for using the AASHTO Specifications to calculate prestress losses. The case using measured properties was chosen to examine the influence of transformed sections and the proposed equation for elastic modulus on total losses. These two prediction cases will be referred to as AASHTO(des.) and AASHTO(meas.) predictions.

The design and measured properties used for calculating prestress losses are summarized in Tables 6.1 and 6.2, respectively. The transformed section properties used for calculating prestress losses for the AASHTO(meas.) predictions are shown in Table 6.3. The strengths, moduli, and transformed section properties at 28 and 56 days were not used in the either set of AASHTO predictions of prestress losses.

The span lengths and midspan moments used to calculate stresses at the CGS for both cases are summarized in Table 6.4. The internal beam diaphragms were included in the calculation of midspan moment due to the beam weight. The average measured deck thicknesses, which are given in Section 4.4.3, were used to calculate moments due to the cast-in-place deck for the case using measured properties. For both cases, the overhangs on the exterior beams (S16, S26, N21, N31) were included in the moment calculations even though they actually were not cast with the deck. Exclusion of the overhangs would have caused the creep loss to become excessively large for those beams. In determining the midspan moments due to the deck panel and CIP deck loads, a unit weight of 2403 kg/m³ was assumed for the concrete.

The results of the AASHTO predicted total prestress losses are shown in Figures 6.1 to 6.8. Predictions were made for the ten instrumented beams that had measured strains at the center of gravity of the prestressing steel at midspan. The measured prestress losses were determined by calculating the product of the measured strain and the modulus of elasticity of the prestressing steel. For the pairs of companion beams (such as S14 and S15), the predicted losses were nearly the same for each beam. Therefore, predicted losses for one of the two companion beams was used for comparison with the measured losses. The results for the companion beams are given in Figures 6.1 and 6.8.

The AASHTO(des.) predicted prestress losses varied between 26.18 and 34.11 percent. The losses for Beams N21, N31, and S26 were the largest because they had the largest products of initial prestressing force and eccentricity. As an example, the total prestress loss for Beam S26 (shown in Figure 6.4) was comprised of 10.34 percent (144.4 MPa) due to elastic shortening, 2.84 percent (39.6 MPa) due to shrinkage, 20.38 percent (284.6 MPa) due to creep, and 0.27 percent (3.8 MPa) due to relaxation. Beam S25, shown in Figure 6.3, had a slightly higher relaxation loss of 0.79 percent (11.0 MPa) but a lower elastic shortening loss of 8.19 percent (114.4 MPa) and a lower creep loss of 14.42 percent (201.3 MPa). Both beams were U54B sections with similar span lengths. The differences were mainly due to Beam S26 having 19 more strands than Beam S25. Elastic shortening and creep had the greatest effect on total losses for all of the beams.

Table 6.1 Design beam properties used for calculating prestress losses

Design Property	Beam(s)			
	S14 S15 N32 N33	S16 S24 S25 N22 N23	S26 N21	N31
Release Strength (MPa)	53.1	53.1	60.7	60.7
Design 56-day Strength (MPa)	80.0	80.0	90.3	90.3
Elastic Modulus at Release (GPa)	38.5	38.5	41.2	41.2
Elastic Modulus at 56 days (GPa)	47.3	47.3	50.3	50.3
Initial Prestressing Force (kN)	12,508	13,291	17,006	16,223
Moment of Inertia ($\times 10^{11}$ mm ⁴)	1.580	1.679	1.679	1.679
Cross-Section Area ($\times 10^5$ mm ²)	6.598	7.217	7.217	7.217
Eccentricity of Prestressing Strands (mm)	507	477	459	465
<u>Notes:</u>				
1. Modulus of elasticity calculated using the Eq. 6.1 with $w=2481$ kg/m ³ .				

Table 6.2 Measured beam properties used for calculating prestress losses and elastic camber and deflection

Measured Property	Beam(s)						
	S14 S15	S24 S25	N32 N33	S16 N22	N21 N31	S26	N23
Release Strength (MPa)	75.8	71.2	72.2	60.1	75.1	76.5	76.3
28 or 56 day Strength (MPa)	98.7 ²	92.5	94.0 ²	91.6	102.2 ²	93.5	85.6
Elastic Modulus at Release ¹ (GPa)	42.2	41.3	41.5	39.0	42.1	42.4	42.4
Elastic Modulus at 28 or 56 days ¹ (GPa)	46.5	45.4	45.6	45.2	47.1	45.5	46.0
<u>Notes:</u>							
1. Modulus of elasticity calculated using Eq. 6.2 with $w=2481$ kg/m ³ .							
2. 56 day measured compressive strength was used for these beams.							

Table 6.3 Transformed section properties used for calculating prestress losses and elastic camber and deflection

Beam(s)	At Release			At 28 or 56 days	
	Area ($\times 10^5 \text{ mm}^2$)	Moment of Inertia ($\times 10^{11} \text{ mm}^4$)	Eccentricity (mm)	Moment of Inertia ($\times 10^{11} \text{ mm}^4$)	Eccentricity (mm)
S14, S15	6.933	1.6617	483	1.6530	486
S16, N22	7.605	1.7638	453	1.7503	457
S24, S25	7.579	1.7582	455	1.7500	457
S26	7.662	1.7686	433	1.7613	435
N21	7.666	1.7693	433	1.7582	436
N23	7.568	1.7560	455	1.7488	457
N31	7.646	1.7675	439	1.7567	442
N32, N33	6.940	1.6633	483	1.6546	485

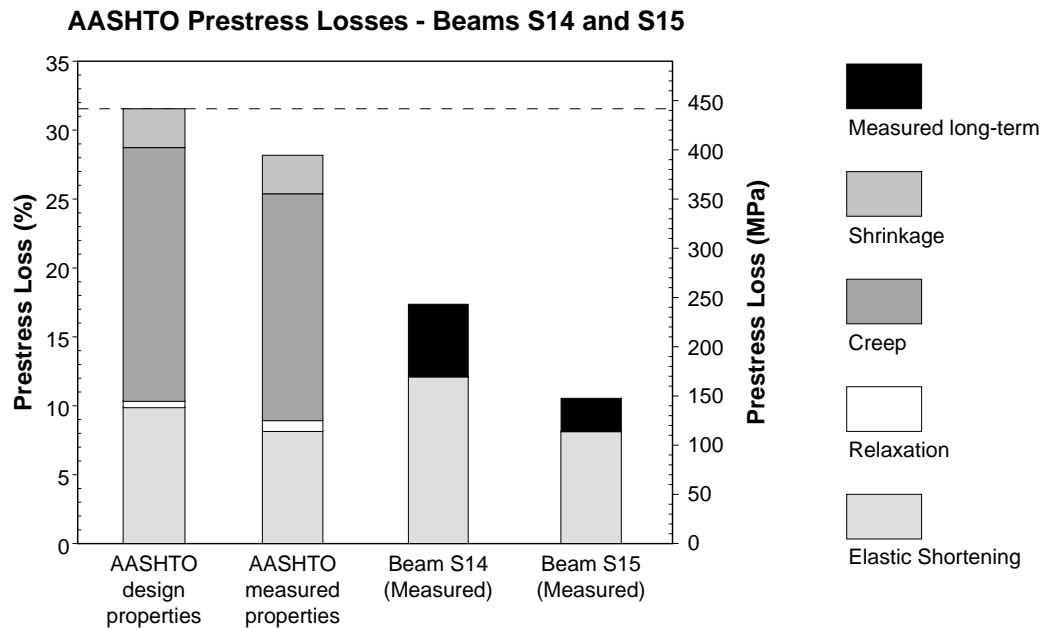


Figure 6.1 AASHTO predicted prestress losses for Beams S14 and S15

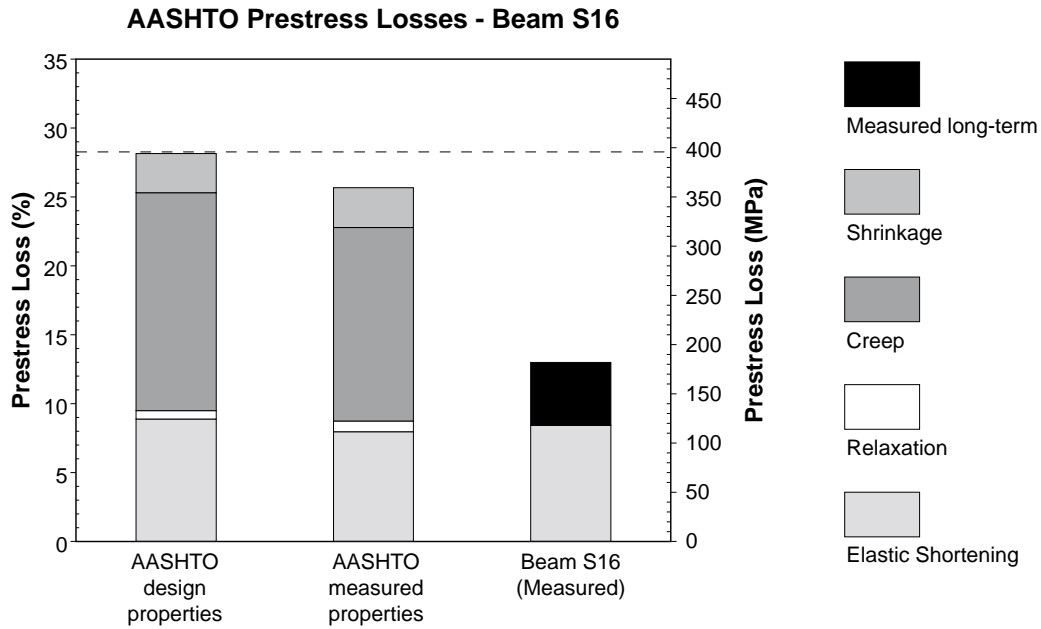


Figure 6.2 AASHTO predicted prestress losses for Beam S16

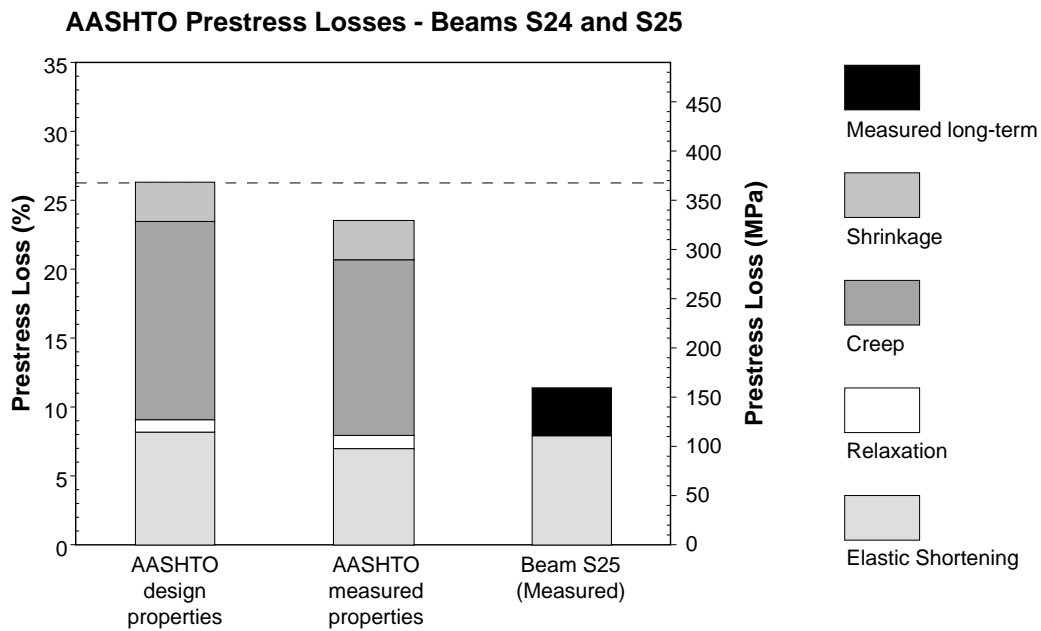


Figure 6.3 AASHTO predicted prestress losses for Beams S24 and S25

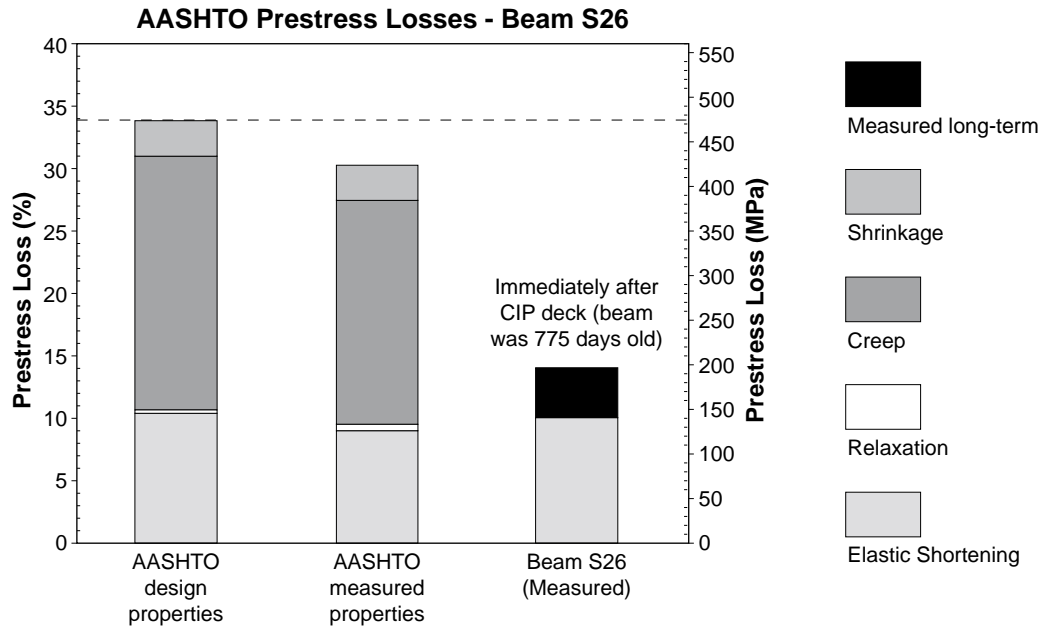


Figure 6.4 AASHTO predicted prestress losses for Beam S26

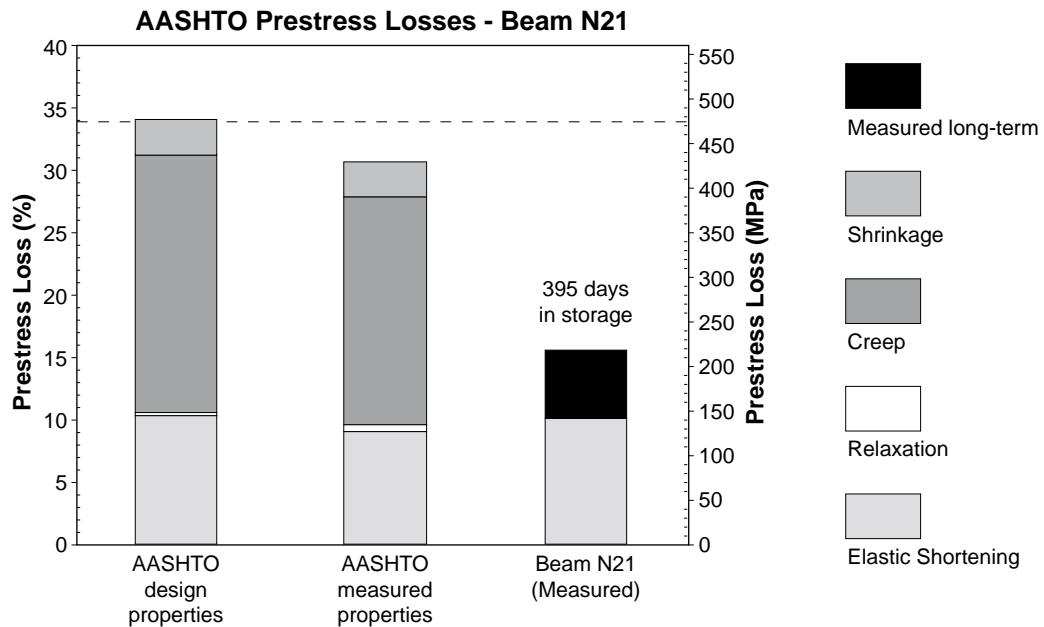


Figure 6.5 AASHTO predicted prestress losses for Beam N21

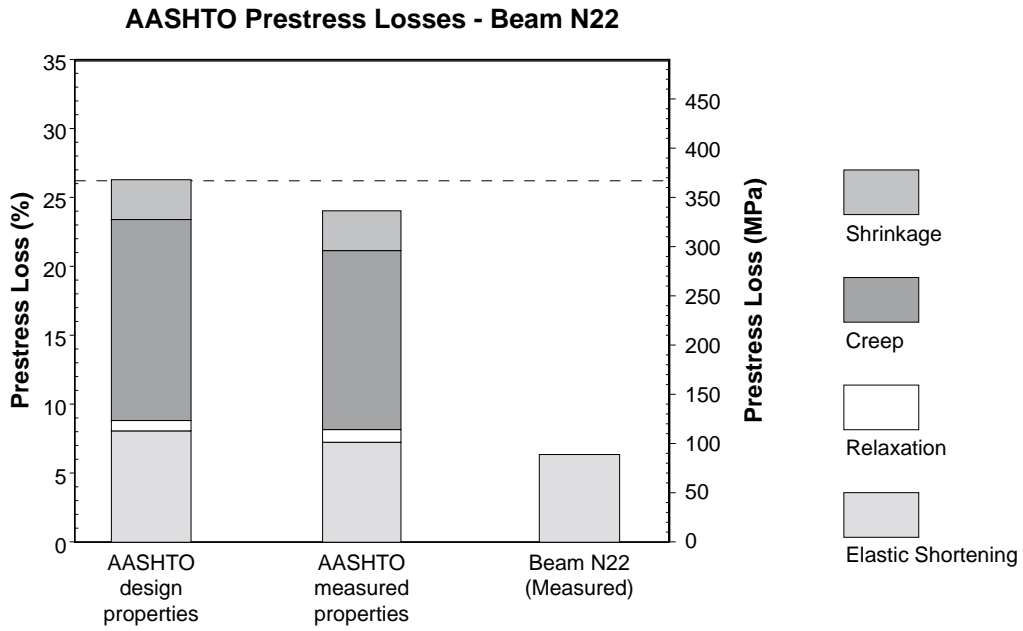


Figure 6.6 AASHTO predicted prestress losses for Beam N22

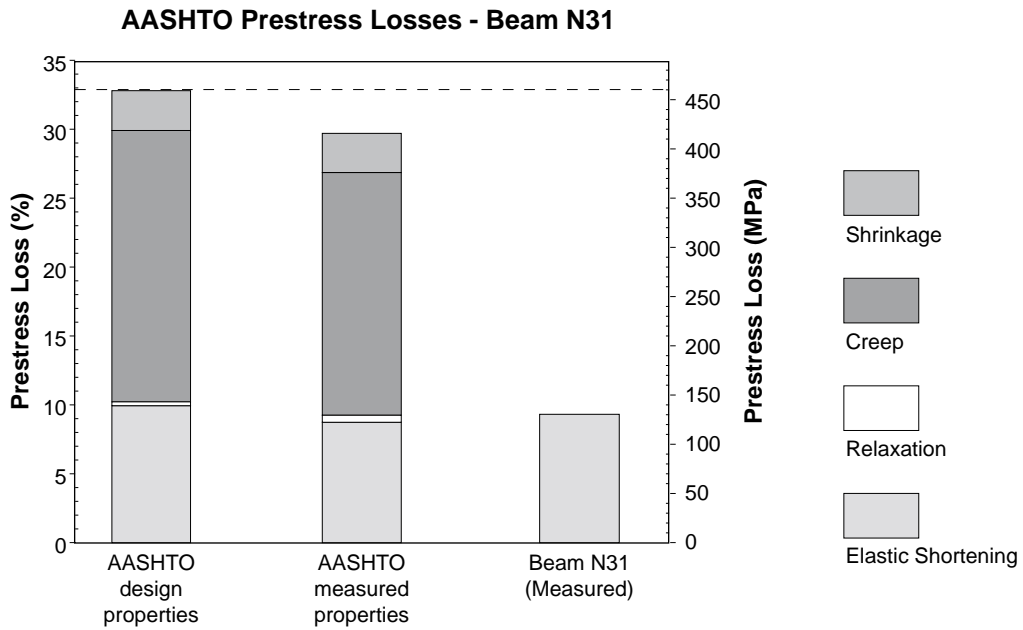


Figure 6.7 AASHTO predicted prestress losses for Beam N31

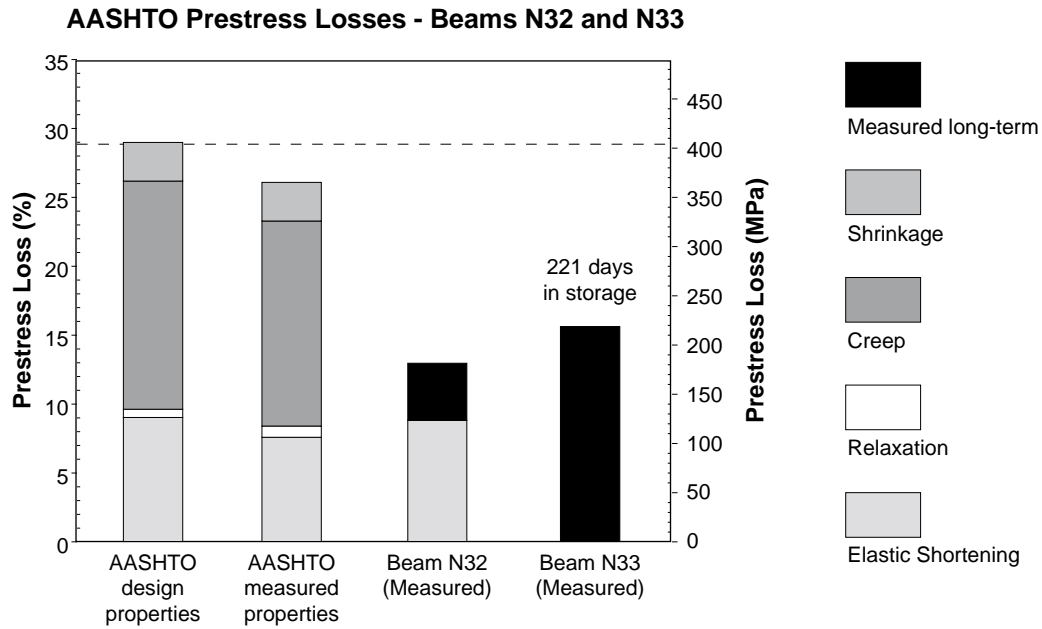


Figure 6.8 AASHTO predicted prestress losses for Beams N32 and N33

Table 6.4 Midspan moments used to calculate prestress losses based on AASHTO and PCI procedures

Beam	Span (m)	Midspan Moment (kN-m)					
		Beam Weight	Panels	Design CIP Deck	Measured CIP Deck	Total Deck (Design)	Total Deck (Measured)
S14	35.55	2640	1514	1814	1922	3328	3436
S15	36.01	2741	1533	1839	2058	3372	3591
S16	36.49	3063	1098	2689	2846	3787	3944
S24	39.83	3611	1633	1989	2339	3622	3972
S25	40.33	3738	1651	2015	2369	3666	4020
S26	40.84	3819	1237	3222	3487	4459	4724
N21	40.90	3814	1140	3122	3203	4262	4343
N22	41.07	3840	1493	1855	1962	3348	3455
N23	41.25	3884	1499	1864	1971	3363	3470
N31	40.35	3706	1067	2993	3069	4060	4136
N32	40.50	3427	1366	1712	1810	3078	3176
N33	40.66	3464	1370	1718	1816	3088	3186

Differences in the magnitude of creep loss were also a function of the span lengths of the beams. For Beams S14 and S15, shown in Figure 6.1, the loss due to elastic shortening

was 9.91 percent (138.3 MPa) and the loss due to creep was 18.39 percent (256.7 MPa). For Beams N32 and N33, shown in Figure 6.8, the loss due to elastic shortening was 9.00 percent (125.7 MPa) and the loss due to creep was 16.62 percent (232.1 MPa). These beams were all U54A sections having 68 strands but Beams N32 and N33 had spans approximately five meters longer than the spans for Beams S14 and S15.

The large elastic shortening and creep losses for some of the beams caused the loss due to strand relaxation to be underestimated. The form of the equation in the AASHTO Specifications for calculating relaxation loss is not appropriate for high prestressing forces such as those applied to the U-beams. Despite this underestimation, the loss due to relaxation still remains insignificant because of the use of low-relaxation strands.

The AASHTO(meas.) predicted prestress losses ranged from 23.46 to 30.78 percent. Examining Beam S26 (Figure 6.4) once again, the loss due to shrinkage remained the same and the loss due to relaxation was nearly the same. However, the loss due to elastic shortening was reduced to 9.02 percent (125.9 MPa) and the loss due to creep was reduced to 17.92 percent (250.2 MPa). This was a result of using transformed section properties, a different modulus of elasticity, and different deck moments.

Since the U-beams contained a large number of strands, using transformed section properties resulted in a measurable increase in the area and moment of inertia of the section and a measurable decrease in the eccentricity of the strands for all beams. The differences in section properties can be observed by comparing Tables 6.1 and 6.3. As a result of using transformed section properties, the stress at the center of gravity of the strands at release was lower than the stress based on gross section properties. Consequently, the elastic shortening and creep losses were lower.

The modulus of elasticity at release based on measured compressive strengths and Eq. 6.2 was slightly higher than the design modulus of elasticity. This can be seen by examining Tables 6.1 and 6.2. The elastic moduli calculated with Eq. 6.2 were larger because the measured release strengths were generally much higher than the design release strengths. Since the AASHTO equation (Eq. 6.1) did not overestimate the modulus of elasticity at the design release strengths, using the proposed equation with the higher measured strengths yielded slightly higher values for elastic moduli. Figure 5.6 in Sec. 5.2.2 shows the graphs of both modulus of elasticity equations. As a result of the higher elastic moduli, the losses due to elastic shortening were lower.

The measured deck thicknesses were larger than the design deck thickness for all of the beams. As a result, the midspan moments due to the deck panels and cast-in-place (CIP) deck were larger, as shown in Table 6.4. Consequently, the stress at the CGS was increased which caused the loss due to creep to be less than the creep loss calculated using design properties.

The measured prestress losses are compared to the AASHTO predicted prestress losses in Figures 6.1 to 6.8. Measured losses varied between 10.56 and 17.38 percent. These values did not include the loss of prestress due to strand relaxation. Unless otherwise indicated in the figures, measured long-term losses corresponded to a time approximately five months after the CIP deck was completed. At that time, Beams S14, S15, and N32 were approximately 375 days old and Beams S16 and S25 were approximately 875 days old.

Based upon the measured strains after the completion of the deck, it appeared that long-term changes in strain would be small.

As can be seen in Figures 6.1 to 6.5 and Figure 6.8, the measured long-term prestress losses, which represented the effects of creep and shrinkage, were significantly less than either set of predicted long-term losses. The measured losses for Beams N21 and N33, shown in Figures 6.5 and 6.8, respectively, were significantly lower than predictions despite not including the elastic gain in prestress and reduced creep loss that the deck panels and CIP deck would have caused.

Comparisons of the measured and AASHTO predicted immediate losses due to elastic shortening are summarized in Figure 6.9. The ratios of measured to predicted elastic shortening losses are plotted for the instrumented beams shown in Figures 6.1 to 6.8. As can be seen in Figure 6.9, the AASHTO(des.) predicted losses generally overestimated the measured losses at release. The average ratio of measured losses to AASHTO(des.) predicted losses was 0.96. If the results for Beam S14, which seemed to be abnormally high, were removed from the graph, the average ratio would become 0.92. The AASHTO(des.) predicted losses were higher because of the use of gross section properties and a low modulus of elasticity.

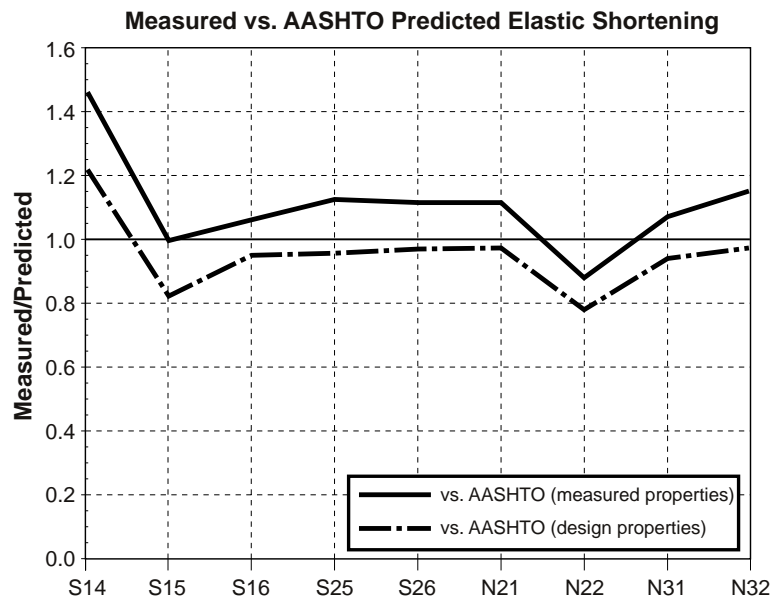


Figure 6.9 Summary of the ratios of measured to AASHTO predicted prestress losses at release

The AASHTO(meas.) predicted losses generally underestimated the measured losses at release. The average ratio of measured losses to AASHTO(meas.) predicted losses was 1.11. If the results for Beam S14 were removed from the graph, the average ratio would

become 1.07. The use of transformed section properties and a high modulus of elasticity contributed to the predictions underestimating the measured values.

Comparisons of the measured and AASHTO predicted total losses are summarized in Figure 6.10. The differences between the predicted and measured total losses are plotted for the instrumented beams shown in Figures 6.1 to 6.8. Unlike the comparisons of measured and predicted elastic shortening losses shown in Figure 6.9, the differences between measured and predicted total losses were quite large. The graph shown in Figure 6.10 represents the algebraic difference between the predicted total losses (in percent) using the AASHTO equations and the measured total losses (in percent) using the measured strains at CGS. AASHTO(des.) predicted losses and AASHTO(meas.) predicted losses overestimated the measured losses by an average of 16.5 and 13.4 percent, respectively. Differences between the two prediction values were discussed earlier in this section.

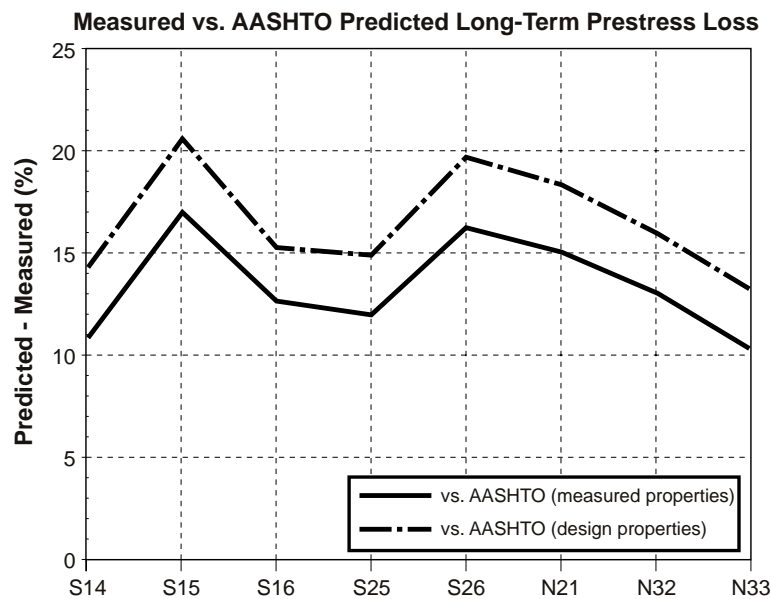


Figure 6.10 Summary of the differences in measured and AASHTO predicted long-term prestress losses

Based on the summary shown in Figure 6.10, the AASHTO procedures grossly overestimated the long-term loss due to creep. It appeared that the equation for creep loss was not applicable for the high performance concrete U-beams. The theoretical creep coefficient of 2.0 applied to the initial stress at CGS at release overestimated the actual creep coefficient measured for the HPC beam mix, which is shown in Secs. 5.2.3 and 5.4.1.3. The creep and shrinkage tests on the HPC beam mix showed smaller strains than with normal strength concrete, which indicated that less creep and shrinkage would occur in the instrumented beams. In addition, the actual modular ratio at release for the HPC mix was approximately 5.0, meaning that the AASHTO creep coefficient applied to the strains at CGS

was 2.4 rather than 2.0. Also, the large stresses at the CGS, which were due to the large prestressing forces and allowed for by very high concrete strength, contributed to the high creep loss estimations.

6.3 PCI DESIGN HANDBOOK: PRESTRESS LOSSES, CAMBER, AND DEFLECTION

6.3.1 Prestress Losses

The PCI Design Handbook (27) provides a simple method for estimating prestress losses for prestressed concrete beams. The equations for losses due to elastic shortening, creep, shrinkage, and prestressing steel relaxation were adopted from the work of Zia et al. (38). This method is very similar to the AASHTO Specifications (16) procedure for calculating prestress losses. In this section, the assumptions used in the PCI Design Handbook method are reviewed and the predicted and measured prestress losses are presented.

The equation for calculating the loss due to elastic shortening is the same as the one given in the AASHTO Specifications except that the reduction in the initial prestressing force is 0.90 instead of 0.92. In addition, the PCI method suggests using 196.5 GPa for the modulus of elasticity of the strands. However, 193 GPa was used to remain consistent with the other methods for predicting losses. The elastic moduli of the concrete were calculated using Eqs. 6.1 and 6.2.

The equation for prestress loss due to shrinkage considers the ambient relative humidity and the volume-to-surface ratio of the beam cross-section. The ambient relative humidity was assumed to be 75 percent, as in the AASHTO procedure. Since there were two slightly different cross-sections for the instrumented U-beams, two shrinkage losses were calculated. The ultimate shrinkage strains for the U54A and U54B beams were 169 and 166 microstrain, respectively. The resulting prestress losses due to shrinkage for the U54A and U54B beams were 32.7 and 32.0 MPa, respectively.

The equation for prestress loss due to creep applies a creep coefficient of 2.0 to the initial compressive strain at the CGS immediately after release and the tensile strain at the CGS due to superimposed dead loads. The 28-day modulus of elasticity is used for calculating the modular ratio of prestressing steel to concrete. This attempts to account for the age of the concrete when the superimposed dead load is placed on the beams. For some of the instrumented beams, the 56-day compressive strength was used for calculating the modulus of elasticity in the creep loss equation.

The equation for prestress loss due to relaxation of the strands is in the same form as the AASHTO equation. A constant loss of 34.5 MPa is reduced by a fraction of the losses due to elastic shortening, creep, and shrinkage. However, the coefficient applied to these losses is only 0.04. This means that the relaxation loss is less sensitive than the AASHTO equation to the magnitudes of the other losses.

Prestress loss estimations were calculated using the design and measured property cases that are described in Sec. 6.2. The design and measured properties for the beams are summarized in Tables 6.1 to 6.3. A summary of the midspan moments used to calculate

stresses at the center of gravity of the strands (CGS) is given in Table 6.4. These two cases will be referred to as PCI(des.) and PCI(meas.) predicted prestress losses in this section.

The results of the PCI predicted total prestress losses are shown in Figures 6.11 to 6.18. Predictions were made for the ten instrumented beams that had measured strains at CGS at midspan.

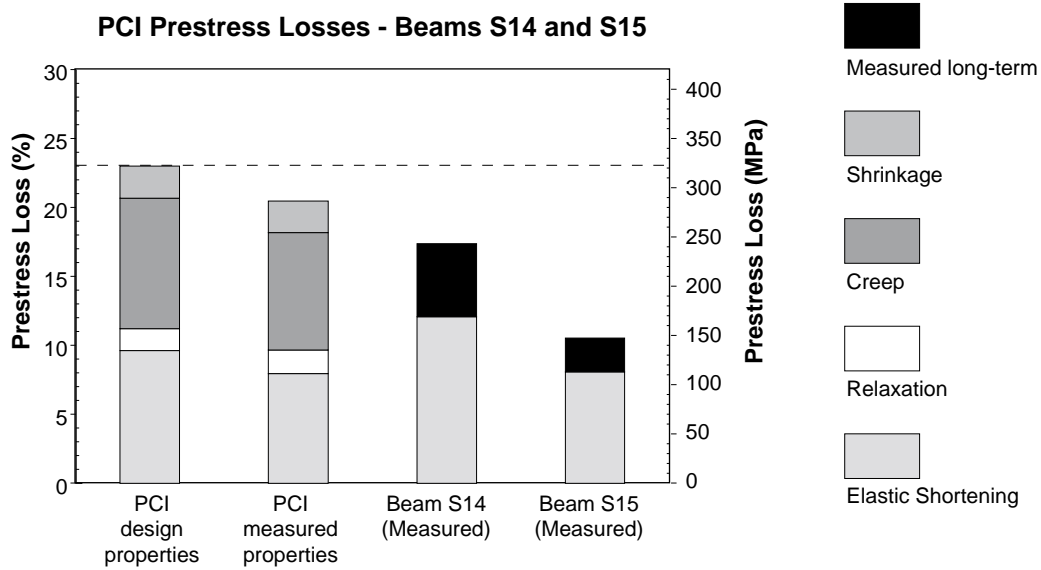


Figure 6.11 PCI predicted prestress losses for Beams S14 and S15

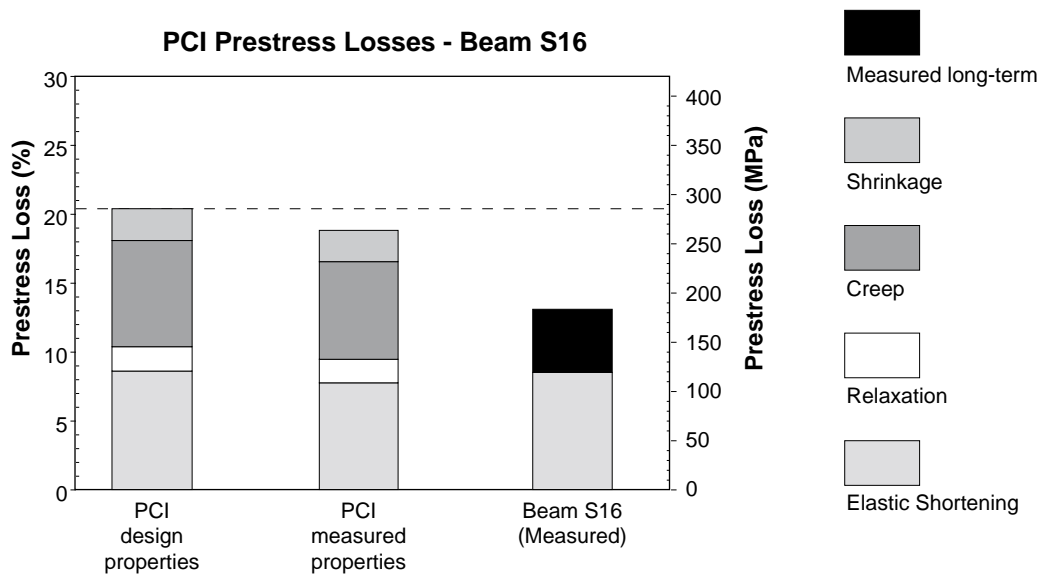


Figure 6.12 PCI predicted prestress losses for Beam S16

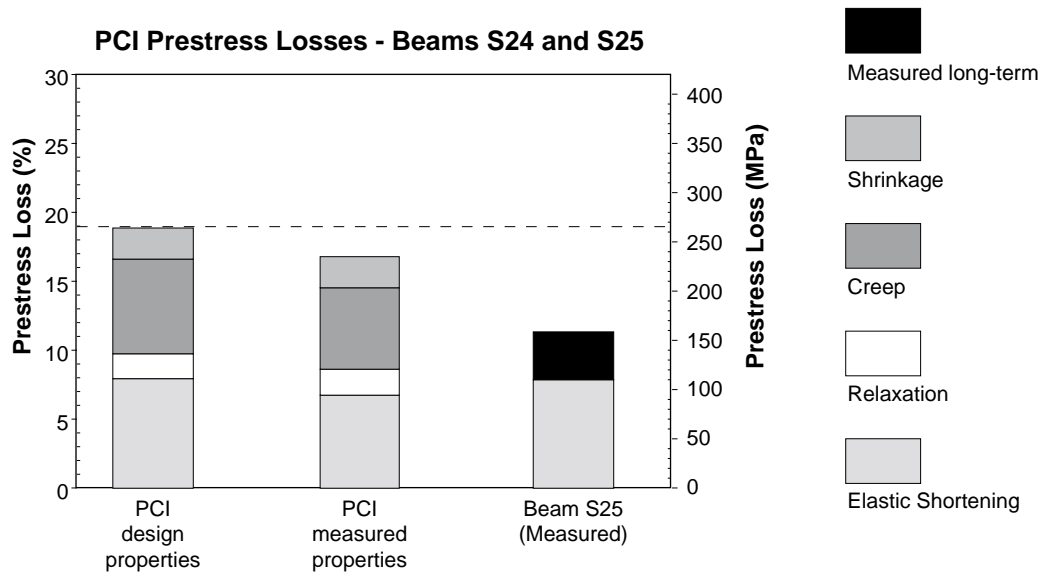


Figure 6.13 PCI predicted prestress losses for Beams S24 and S25

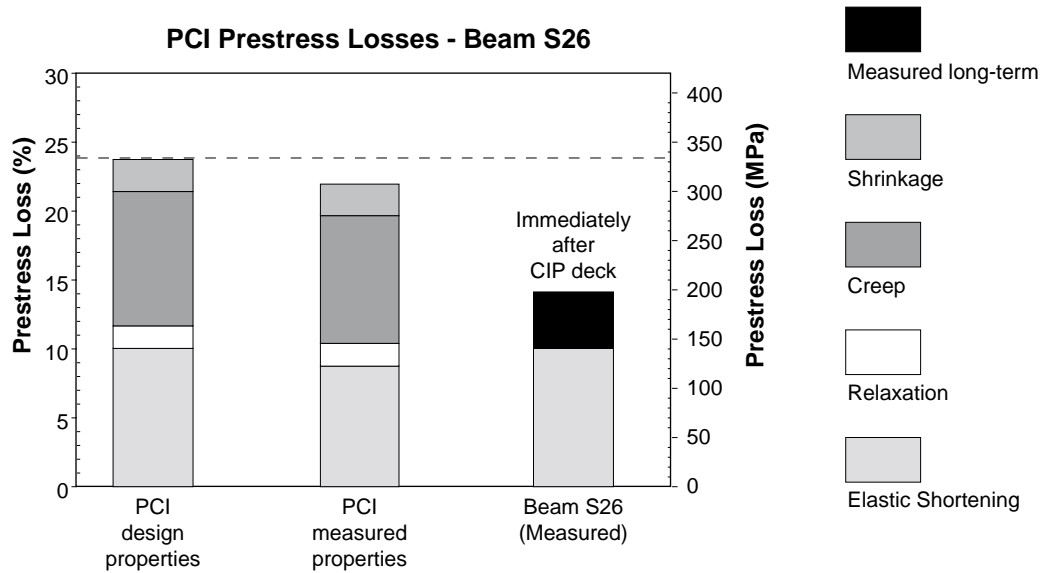


Figure 6.14 PCI predicted prestress losses for Beam S26

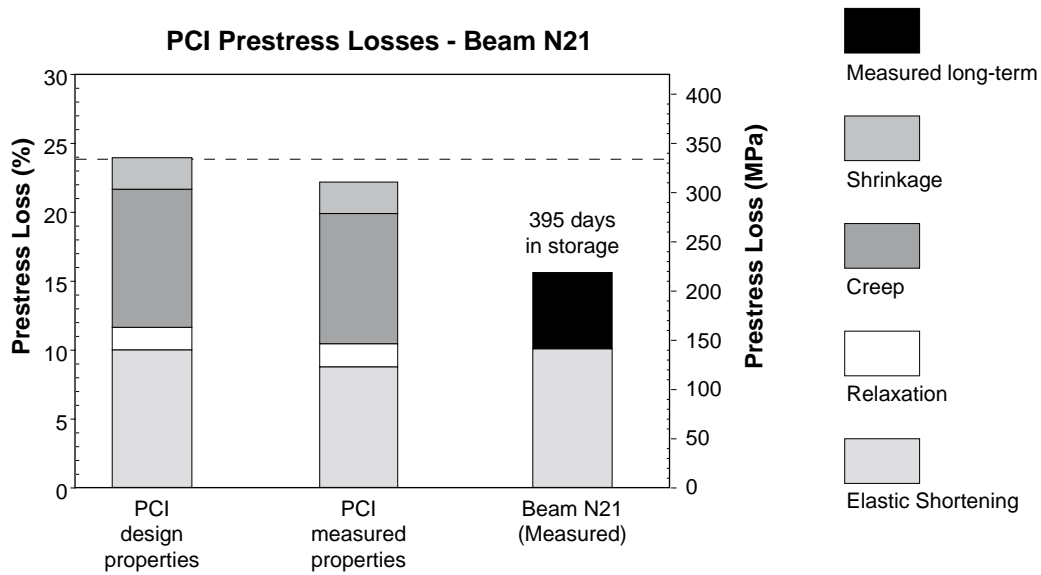


Figure 6.15 PCI predicted prestress losses for Beam N21

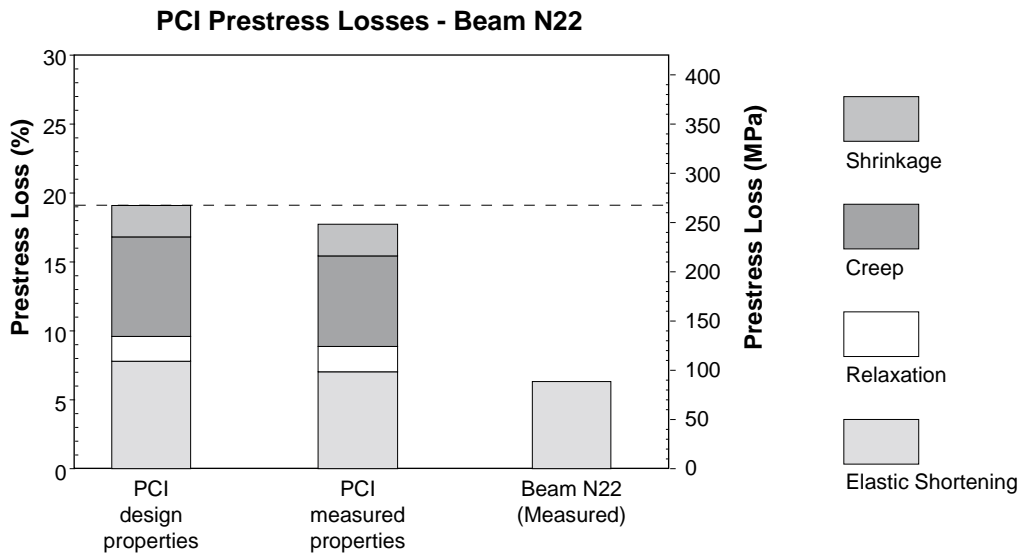


Figure 6.16 PCI predicted prestress losses for Beam N22

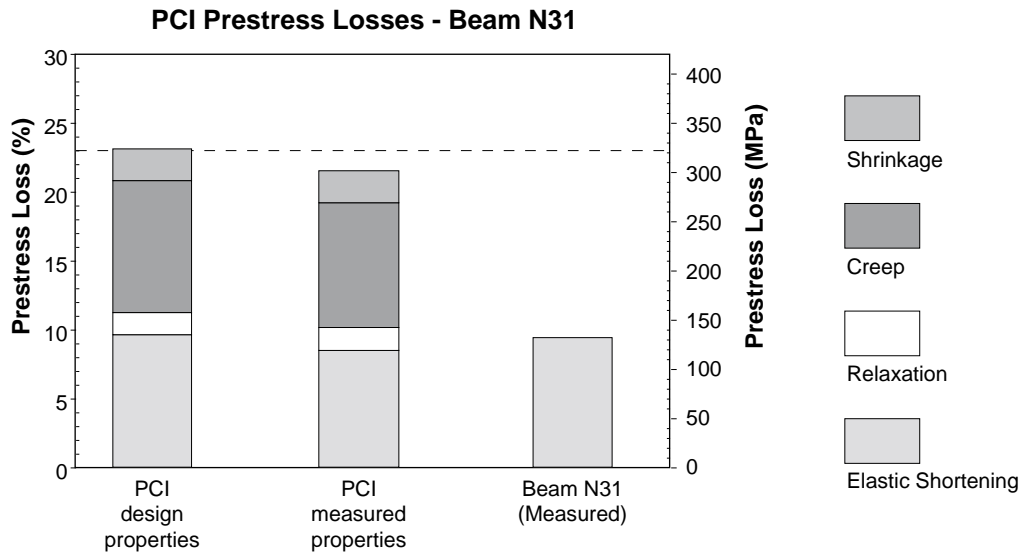


Figure 6.17 PCI predicted prestress losses for Beam N31

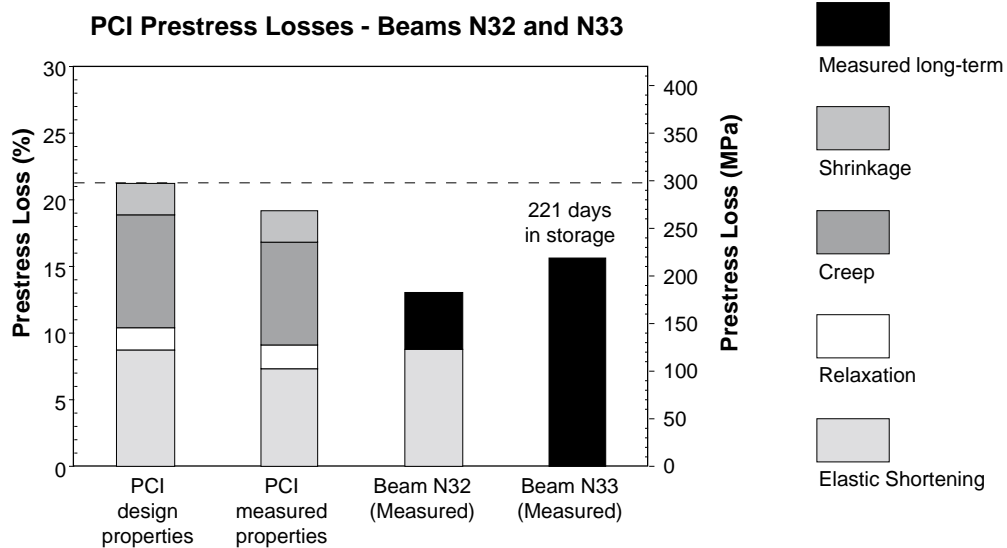


Figure 6.18 PCI predicted prestress losses for Beams N32 and N33

The PCI(des.) predicted prestress losses varied between 18.87 and 23.99 percent. The prestress losses in Beams N21, N31, and S26 were larger than the losses for the other beams. These beams had the largest initial prestressing forces, as shown in Table 6.1, which caused the predicted elastic shortening and creep losses to be larger than in the other beams. The

lowest prestress losses were in Beams S24 and S25, shown in Figure 6.13, and Beam N22, shown in Figure 6.16. These beams were similar to Beams S26 and N21 in span length, cross-section, and moment due to the beam dead load, but their initial prestressing forces were much smaller. In addition their deck moments were smaller than those of Beams S26 and N21, yet their predicted elastic shortening and creep losses were smaller.

The components of the PCI(des.) predicted total losses can be illustrated with Beam S26. The total prestress loss for Beam S26 (shown in Figure 6.14) was comprised of 10.04 percent (140.2 MPa) due to elastic shortening, 2.29 percent (32.0 MPa) due to shrinkage, 9.77 percent (136.4 MPa) due to creep, and 1.59 percent (22.1 MPa) due to relaxation.

The PCI(meas.) predicted prestress losses varied from 16.82 to 22.20 percent. Examining Beam S26 (Figure 6.14) once again, the loss due to elastic shortening was reduced to 8.76 percent (122.3 MPa) and the loss due to creep was reduced to 9.22 percent (128.7 MPa). The average difference between the two sets of predicted losses was approximately 2 percent. This was a result of using a higher moment of inertia and lower eccentricity based on transformed section properties, a higher modulus of elasticity, and a higher deck moment for the PCI(meas.) predictions. Tables 6.3 and 6.4 summarize these properties for all of the beams. Sec. 6.2 examines the effects that these variables had on creep and shrinkage losses.

The 56-day elastic moduli calculated using design properties and Eq. 6.1 tended to be higher than the elastic moduli using measured properties and Eq. 6.2. This can be seen in Tables 6.1 and 6.2. Upon examination of the PCI creep equation, it appears that the higher elastic moduli would cause the creep loss to be smaller. However, the combination of all variables, including section properties and deck moments, made the PCI(des.) predicted creep losses higher than the PCI(meas.) predicted creep losses.

The measured losses are compared to the PCI predicted losses in Figures 6.11 to 6.18. Measured losses varied between 10.56 and 17.38 percent. These measurements did not include the loss of prestress due to strand relaxation. Unless otherwise indicated in the figures, measured long-term losses corresponded to a time approximately five months after the CIP deck was completed.

As can be seen in Figures 6.11 to 6.15 and Figure 6.18, the measured long-term prestress losses, which represented the effects of creep and shrinkage, were less than either set of predicted long-term losses. The measured total losses were also lower than the predicted total losses. However, if the PCI estimated relaxation loss, which was approximately 1.5 percent, were added to the measured losses, there would be closer agreement between measured and predicted total losses.

The measured losses for Beams N21 and N33, shown in Figures 6.15 and 6.18, respectively, appeared to be close to the predicted losses. However, the measured losses did not include the elastic gain in prestress and reduced creep loss that the deck panels and CIP deck would have caused.

Comparisons of the measured and PCI predicted immediate losses due to elastic shortening are summarized in Figure 6.19. The ratios of measured to predicted elastic shortening losses are plotted for the instrumented beams shown in Figures 6.11 to 6.18. As can be seen in Figure 6.19, the PCI(des.) predicted losses generally agreed the measured

losses at release. The average ratio of measured losses to PCI(des.) predicted losses was 0.99. If the results for Beam S14, which seemed to be abnormally high, were removed from the graph, that average ratio would become 0.95. The reduced factor of 0.9 applied to the initial prestressing force caused this set of predictions to agree closely with the measurements.

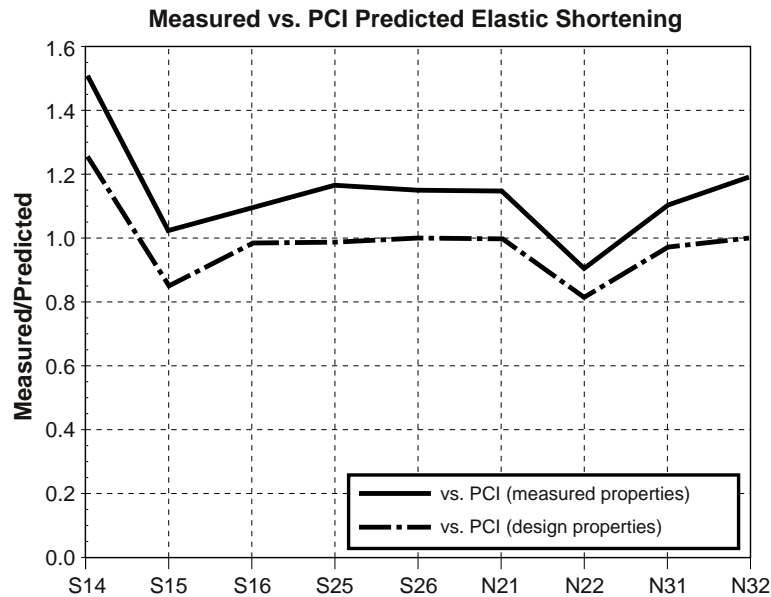


Figure 6.19 Summary of the ratios of measured to PCI predicted prestress losses due to elastic shortening

The PCI(meas.) predicted losses generally underestimated the measured losses at release. The average ratio of measured losses to PCI(meas.) predicted losses was 1.15. If the results for Beam S14 were removed from the graph, that average ratio would become 1.10. In addition to the reduced factor of 0.90 applied to the initial prestressing force, the use of transformed section properties and a high modulus of elasticity contributed to the predictions underestimating the measured values.

Comparisons of the measured and PCI predicted total losses are summarized in Figure 6.20. The differences between the predicted and measured total losses are plotted for the instrumented beams shown in Figures 6.11 to 6.18. The differences between measured and predicted total losses are large, although much less than what was found with the AASHTO predicted losses. The graph shown in Figure 6.20 represents the algebraic difference between the predicted total losses (in percent) using the PCI equations and the measured total losses (in percent) using the measured strains at the CGS. The PCI(des.) and PCI(meas.) predicted losses overestimated the measured losses by averages of 8.0 and 6.0 percent, respectively. By adding relaxation to the measured losses, these differences would

be reduced by about 1.5 percent. Differences between the two sets of predictions were attributed to differences in section properties, material properties, and midspan moments.

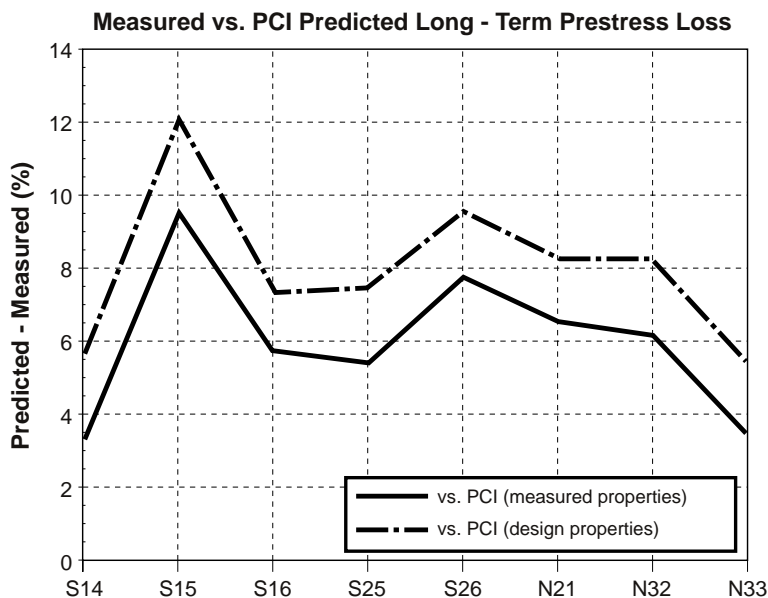


Figure 6.20 Summary of the differences in measured and PCI predicted long-term prestress losses

Based on the comparisons shown in Figures 6.19 and 6.20, the PCI method predicted the immediate losses due to elastic shortening fairly well yet overestimated the long-term losses. When PCI(meas.) predictions are used to examine both the immediate and long-term loss comparisons, a contradiction occurs. Larger measured elastic shortening losses implies that the prestressing force at transfer was larger and that the modulus of elasticity was smaller than that used in the predictions. If that were true, the measured long-term losses should have been greater than the predicted losses, assuming that the PCI creep coefficient was applicable to the HPC U-beams. However, the measured additional time-dependent losses were lower than those predicted using the PCI equations.

In addition, the PCI equation for creep loss applies a creep coefficient of 2.0 to the stress caused by the deck load. This coefficient is also applied to the initial stress at transfer. For the instrumented beams, which were as much as 734 days old when the deck panels were erected, a creep coefficient of 2.0 applied to the stress caused by the deck loads was too large. This large creep coefficient caused the total loss predicted using the PCI equations to appear fairly accurate. Measured strains in the beams after the deck was placed did not reflect the large amount of creep due to the deck load that was assumed in the PCI creep loss equation.

The adjusted creep coefficients for the HPC U-beams, which are given in Sec. 5.4.1.3, were lower than the creep coefficient used in the PCI equation for creep loss. Also, the

measured strains at release may have been artificially high due to the restraint effects of the prestressing bed which were discussed in Sec. 5.4.2.1. These two factors may explain why the predicted elastic shortening losses were accurate while the predicted long-term losses were much higher than the measured losses. In addition, the PCI equation for estimating shrinkage strain underestimated the adjusted ultimate shrinkage strains for the HPC U-beams by approximately 100 microstrain. However, this would result in an increase in the PCI shrinkage loss of only 1.4 percent (19.3 MPa).

6.3.2 Camber and Deflection

6.3.2.1 Elastic Camber and Deflection Due to Applied Loads

The PCI Design Handbook (27) provides equations for calculating elastic camber and deflection responses that are based upon second moment-area principles. The expression for midspan camber due to the prestressing force is shown in Eq. 6.3. The prestressing force (P) used in this equation was taken as 0.90 multiplied by the initial prestressing force (P_i). This equation ignores strand debonding at the ends of the beams. If strand debonding were included, it would cause the camber due to prestress to be an average of only 2 millimeters lower. The expression for the midspan deflection of a simply supported beam due to its own distributed weight is shown in Eq. 6.4. The distributed load (w) was determined using a unit weight for the concrete of 2481 kg/m³. The deflection due to symmetrical internal diaphragm loads was calculated using Eq. 6.5. The total midspan deflection of the beam at release is shown in Eq. 6.6. The initial midspan camber at release is given in Eq. 6.7.

$$\Delta_{ps} = \frac{PeL_s^2}{8E_cI} \quad (6.3)$$

$$\Delta_{\text{dist-beam}} = \frac{5wL_s^4}{384E_cI} \quad (6.4)$$

$$\Delta_{\text{diaphragm}} = \frac{P_d a}{8E_cI} \left(\frac{L_s^2}{8} - \frac{a^2}{6} \right) \quad (6.5)$$

$$\Delta_{\text{beam}} = \Delta_{\text{dist-beam}} + \Delta_{\text{diaphragm}} \quad (6.6)$$

$$\Delta_{\text{release}} = \Delta_{ps} - \Delta_{\text{beam}} \quad (6.7)$$

where

L_s = design span length (m)

a = length from centerline of bearing to the internal diaphragm (m)

P_d = internal diaphragm load (kN)

e = eccentricity of prestressing strands at midspan (mm)

Elastic camber and deflection components were calculated using design properties and measured properties. These two cases are described in Sec. 6.2 and will be referred to as PCI(des.) and PCI(meas.) elastic responses. Beam material properties and geometric properties (E_c , I , e , P_i , L_s) used to calculate the elastic components of camber and deflection at release are shown in Tables 6.1 to 6.4. The distributed deck loads, which varied between the ends of the beams summarized in Table 6.5. Elastic midspan deflections due to the superimposed loads from the deck panels and cast-in-place deck were calculated using Eq. 6.8.

$$\Delta_{\text{deck}} = \frac{5w_1L_s^4}{384E_cI} \left[\frac{1}{2} + \frac{1}{2} \left(\frac{w_2}{w_1} \right) \right] \quad (6.8)$$

The calculated elastic responses due to applied loads based on design and measured properties are summarized in Table 6.6. The measured camber at release and the deflections due to the deck panels and the CIP deck for each instrumented beam are shown in Table 6.6 for comparison.

Table 6.5 Distributed deck panel and cast-in-place deck loads based on design and measured deck thicknesses

Beam	Deck Panels ¹ (kN/m)		Design CIP Deck ¹ (kN/m)		Measured CIP Deck ^{1,2} (kN/m)	
	w_1	w_2	w_1	w_2	w_1	w_2
S14	9.02	10.16	10.87	12.10	11.51	12.82
S15	8.89	10.02	10.74	11.95	12.01	13.38
S16	6.32	6.88	15.86	16.46	8.88	9.56
S24	7.60	8.87	9.35	10.72	10.98	12.62
S25	7.49	8.75	9.23	10.59	10.84	12.47
S26	5.62	6.25	15.11	15.79	8.44	9.24
N21	5.35	5.55	14.82	15.04	7.33	7.56
N22	6.88	7.29	8.58	9.02	9.08	9.50
N23	6.85	7.25	8.55	8.98	9.04	9.50
N31	5.14	5.34	14.60	14.81	7.09	7.31
N32	6.49	6.84	8.16	8.54	8.62	9.02
N33	6.45	6.81	8.13	8.50	8.59	8.99

Notes:

- w_1 and w_2 represent the loads at each end of the beam. These loads were different because of the varying beam spacing along the span length. Equation 6.8 was used to calculate deflections for the deck loads.
- The cast-in-place deck loads for the exterior beams (S16, S26, N21, and N31) do not include the overhang that was part of the design. This overhang was not cast because future plans called for widening the bridges.

Table 6.6 Comparison of PCI predicted and measured elastic responses to applied loads

Elastic Component	Source	Camber or Deflection (mm)											
		S14	S15	S16	S24	S25	S26	N21	N22	N23	N31	N32	N33
Camber due to prestress	PCI (design)	147.6	151.5	146.3	174.3	178.8	211.4	211.9	185.4	187.0	199.2	191.7	193.2
	PCI (meas)	122.4	125.6	131.2	148.4	152.1	184.3	185.9	166.2	155.7	175.4	161.3	162.6
Deflection due to beam weight	PCI (design)	56.9	60.6	65.4	91.8	97.4	95.5	95.7	103.9	105.9	90.5	95.8	97.6
	PCI (meas)	49.4	52.7	61.7	81.9	86.9	88.3	89.0	97.9	92.3	84.3	84.6	86.2
Camber at release	PCI (design)	90.7	90.9	80.9	82.5	81.4	115.9	116.2	81.5	81.1	108.7	95.9	95.6
	PCI (meas)	73.0	72.9	69.5	66.5	65.2	96.0	96.9	68.3	63.4	91.1	76.7	76.4
	Measured	61.8	62.4	49.1	50.8	44.1	84.5	80.5	46.4	45.0	78.1	63.8	65.9
Deflection due to deck panels	PCI (design)	26.6	27.7	19.1	33.9	35.2	25.4	23.5	33.0	33.4	21.4	31.2	31.5
	PCI (meas)	26.0	27.0	19.2	34.0	35.2	26.8	24.0	33.2	33.0	21.9	30.9	31.3
	Measured	29.7	30.0	19.8	36.0	38.1	32.5	27.7	32.2	33.3	24.9	32.0	32.7
Deflection due to CIP deck	PCI (design)	31.9	33.2	46.9	41.3	42.9	66.2	64.3	41.0	41.5	60.0	39.1	39.5
	PCI (meas)	32.9	36.2	26.9	48.7	50.6	39.9	32.8	43.6	43.4	30.1	41.0	41.4
	Measured	24.9	28.7	24.1	41.4	40.7	32.1	29.5	38.1	35.3	26.7	35.3	32.0

The PCI(des.) calculated cambers at release varied from 80.9 mm (Beam S16) to 116.2 mm (Beam N21). The largest release cambers were calculated for Beams N21, N31, and S26 because these beams had the most prestressing strands. The PCI(meas.) calculated cambers at release varied between 63.4 mm (Beam N23) and 96.9 mm (Beam N21). The initial cambers calculated using measured properties were an average of 17.1 mm lower because, for all of the beams, the modulus of elasticity and moment of inertia were higher and the eccentricity of the prestressing strands was lower than the design values. Clearly, the use of measured properties had a significant effect on the prediction of camber at release.

The PCI(des.) calculated midspan deflections due to the deck panels varied between 19.1 mm (Beam S16) and 35.2 mm (Beam S25). The PCI(meas.) calculated midspan deflections were nearly identical, varying between 19.2 mm and 35.2 mm. There appeared to be no difference between the two cases because the changes in elastic modulus and moment of inertia tended to offset each other when measured properties were used rather than design properties. Careful examination of Tables 6.1 to 6.3 shows this effect.

The PCI(des.) calculated midspan deflections due to the cast-in-place (CIP) deck varied between 31.9 mm (Beam S14) and 66.2 mm (Beam S26). Large deflections were calculate for Beams N21, N31, and S26 because these beams had long spans and carried the overhang load. The PCI(meas.) calculated midspan deflections due to the CIP deck varied between 26.9 mm (Beam S16) and 50.6 mm (Beam S25). The deflections for all of the interior beams were higher because the measured deck thicknesses were larger than the design thickness. As in the deck panel deflection calculations, the effect of a lower modulus

of elasticity canceled the effect of a higher moment of inertia. Also, the deflections of Beams N21, N31, S16, and S26 were much smaller than in the design case because the overhangs were not cast with the rest of the deck.

The measured elastic responses due to applied loads are given in Table 6.6 for comparison purposes. The measured cambers at release varied between 44.1 mm (Beam S25) and 84.5 mm (Beam S26). The measured initial cambers were an average of 15.3 mm lower than the PCI(meas.) release cambers. The maximum difference was observed in Beam N22, which had a measured camber that was 21.9 mm lower than the predicted value. The measured deflections due to the deck panels were within approximately 7 mm of the predicted values. The measured deflections due to the CIP deck were within 9 mm of the PCI(meas.) predicted values.

The measured and PCI predicted elastic responses are compared in Figures 6.21 and 6.22. The ratios of measured to predicted responses for initial camber, deck panel deflection, and CIP deck deflection are plotted for each instrumented beam.

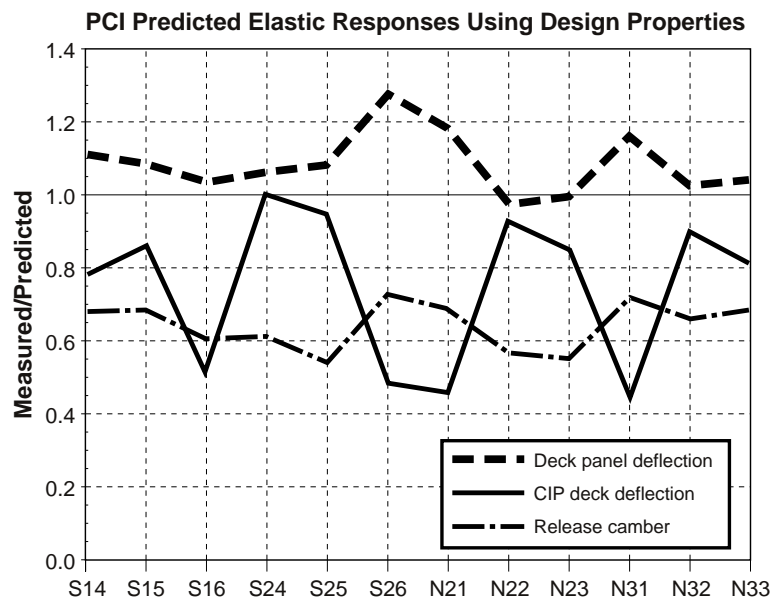


Figure 6.21 Summary of measured elastic response ratios based on PCI Design Handbook predictions using design properties

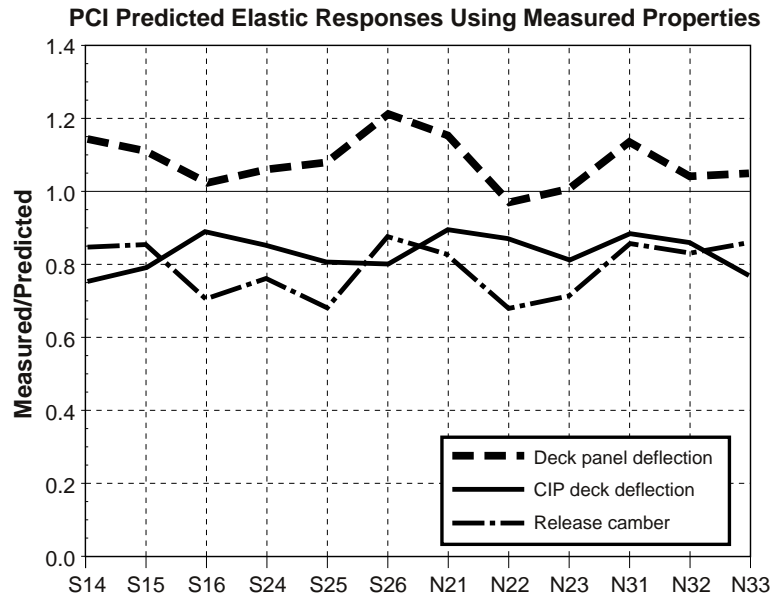


Figure 6.22 Summary of measured elastic response ratios based on PCI Design Handbook predictions using measured properties

The predictions for camber at release significantly overestimated the measured release cambers. The average ratios of measured to PCI(des.) and PCI(meas.) predicted release cambers were 0.65 and 0.79, respectively. The PCI(des.) predictions were considerably higher because of the use of gross cross-section properties. Possible causes of the overestimations included lower prestressing forces transferred to the beams, incorrect estimations of thermally induced movements at release, and a higher modulus of elasticity than was used in the predictions. A detailed discussion of these sources of error can be found in Sec. 5.4.1.2.

The predictions for deck panel deflection tended to slightly underestimate the measured deflections. The average ratio of measured to PCI(des.) and PCI(meas.) predicted deck panel deflections were 1.09 and 1.08, respectively. Errors inherent to the measurements, such as the gap of time between the measurements taken before and after the panels were placed, possible thermal movements, and flaws in the precise surveying system, probably contributed to these differences. Also, variations in material properties could have caused these differences.

The predictions for CIP deck deflection generally overestimated the measured deflections. The ratios shown in Figure 6.21 for beams with overhangs exhibited the lowest ratios because the overhangs were not cast with the deck. Excluding those beams, the average ratio of measured to PCI(des.) predicted CIP deck deflection was 0.89. The average ratio using PCI(meas.) predictions was 0.83. One possible reason that the predicted deflections overestimated the measured deflections was that shrinkage of the deck caused an increase in the prestressing force. This would have caused the measured elastic deck

deflection to appear smaller because the increased prestressing force would cause a slight upward deflection. Another possible reason for less measured deck deflection was that high temperatures in the top part of the beam as the deck concrete hydrated created positive temperature gradients. Consequently, thermally induced camber may have occurred in the beams while the post-casting measurements were being taken. Other sources of error were discussed previously.

6.3.2.2 Long-term Camber and Deflection

The PCI Design Handbook (27) procedure for estimating long-term camber and deflection consists of a set of multipliers that are applied to the elastic components of camber and deflection. These camber and deflection multipliers were developed by Martin (28). The PCI multipliers, which are shown in Table 6.7, were developed based on the following assumptions:

1. The basic creep coefficient is 2.0
2. Initial loss of prestress at release is 8.0 percent
3. Time-dependent loss of prestress is 15.0 percent
4. Percent of total camber/deflection change at erection is 50 percent
5. Ratio of non-composite to composite moment of inertia is 0.65

Table 6.7 PCI Design Handbook suggested multipliers for estimating long-term camber and deflection (27)

	PCI Multipliers	
	Without Composite Topping	With Composite Topping
At erection:		
Deflection (downward) component - apply to the elastic deflection due to the member weight at release of prestress	1.85	1.85
Camber (upward) component - apply to the elastic camber due to prestress at the time of release of prestress	1.80	1.80
Final:		
Deflection (downward) component - apply to the elastic deflection due to the member weight at release of prestress	2.70	2.40
Camber (upward) component - apply to the elastic camber due to prestress at the time of release of prestress	2.45	2.20
Deflection (downward) - apply to the elastic deflection due to superimposed dead load only	3.00	3.00
Deflection (downward) - apply to the elastic deflection caused by the composite topping	-----	2.30

The PCI multipliers are based upon a fixed construction schedule. The beams are assumed to be erected 30 to 60 days after casting and the deck is assumed to be placed immediately thereafter. There is no flexibility in the camber and deflection multipliers to accommodate different construction schedules. Even if the project schedule was known to be different during the design of the bridge, there would be no change in the multipliers used for determining long-term camber or deflection.

Long-term camber and deflection estimates were calculated for the instrumented beams using both design properties and measured properties. These two cases are described in Sec. 6.2 and will be referred to as PCI(des.) and PCI(meas.) predictions. The PCI(des.) predicted responses are shown using the PCI construction schedule. The PCI(meas.) predicted responses are shown using the actual construction schedules of the U-beams. The actual construction schedule for the Louetta Road Overpass, shown in Sec. 4.3.1, was quite different from the schedule used to develop the PCI multipliers. Many of the instrumented U-beams were over two years old before they were erected in the bridge. However, the same multipliers were used for both sets of predictions.

Long-term camber and deflection responses were calculated using the elastic components of camber and deflection shown in Sec. 6.3.2.1. A summary of the predicted and measured long-term responses are shown in Table 6.8. Figures 6.23 to 6.28 shows the measured and predicted long-term responses versus time for several representative beams. For the PCI(des.) predicted responses, 45 days was chosen as the time of erection and the time that the deck loads were placed on the beams. For the PCI(meas.) predicted responses, the actual times of the construction events for each beam were used. Figures 6.29 and 6.30 provide summaries of the comparisons between measured and predicted responses for all of the beams.

Table 6.8 Comparison of predicted and measured long-term camber and deflection responses

Time	Source	Camber or Deflection (mm)											
		S14	S15	S16	S24	S25	S26	N21	N22	N23	N31	N32	N33
At erection	PCI (design)	160.5	160.6	142.3	143.9	141.5	203.7	204.4	141.5	140.6	191.1	167.8	167.2
	PCI (meas.)	128.8	128.7	121.9	115.5	113.0	168.4	169.9	117.9	109.4	159.7	133.8	133.2
	Measured	98.3	101.9	102.1	84.8	85.9	131.1	136.4	88.6	83.1	132.6	107.7	99.8
After deck panels	PCI (design)	133.9	132.9	123.2	110.0	106.3	178.3	180.9	108.5	107.2	169.7	136.6	135.7
	PCI (meas.)	102.8	101.7	102.7	81.5	77.8	141.6	145.9	84.7	76.4	137.8	102.9	101.9
	Measured	68.6	71.9	82.3	48.8	47.8	98.6	108.7	56.4	49.8	107.7	75.7	67.1
After CIP deck	PCI (design)	102.0	99.7	76.3	68.7	63.4	112.1	116.6	67.5	65.7	109.7	97.5	96.2
	PCI (meas.)	69.9	65.5	75.8	32.8	27.2	101.7	113.1	41.1	33.0	107.7	61.9	60.5
	Measured	43.7	43.2	58.2	7.4	7.1	66.5	79.2	18.3	14.5	81.0	40.4	35.1
Long-term	PCI (design)	53.7	48.0	13.1	-9.9	-20.1	24.9	34.6	-11.5	-15.1	33.7	30.1	27.4
	PCI (meas.)	15.1	4.7	34.3	-60.4	-71.3	40.1	64.8	-45.9	-54.8	64.0	-13.6	-16.4
	Measured	35.6	34.3	51.1	2.3	2.5	62.7	77.7	16.0	11.4	76.7	35.1	29.0

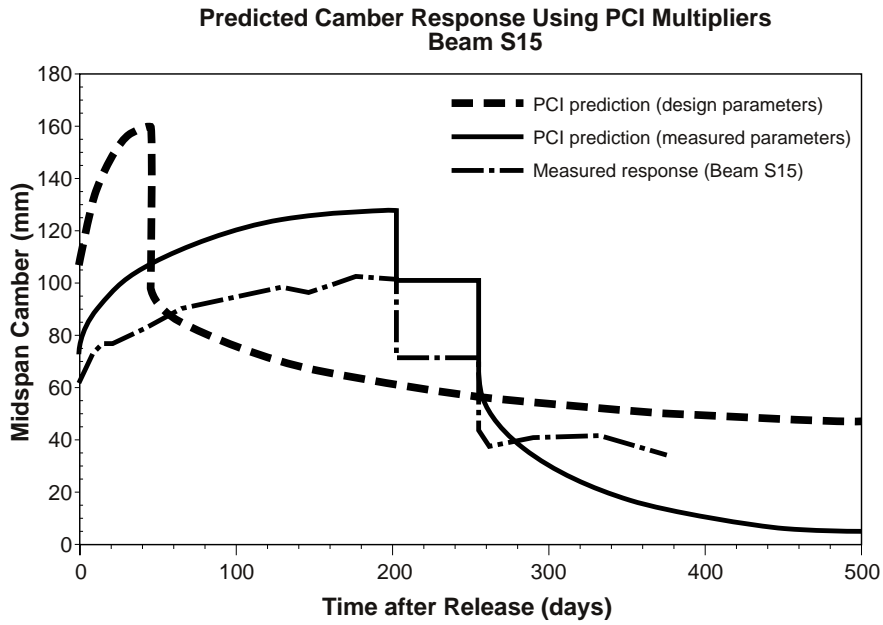


Figure 6.23 Comparison of measured and predicted camber responses for Beam S15 using the PCI Design Handbook procedures

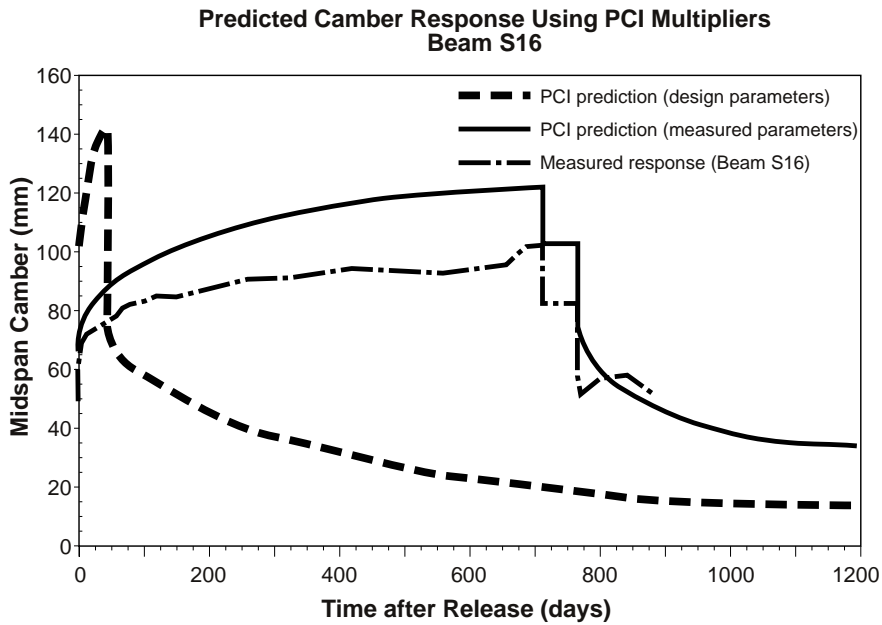


Figure 6.24 Comparison of measured and predicted camber responses for Beam S16 using the PCI Design Handbook procedures

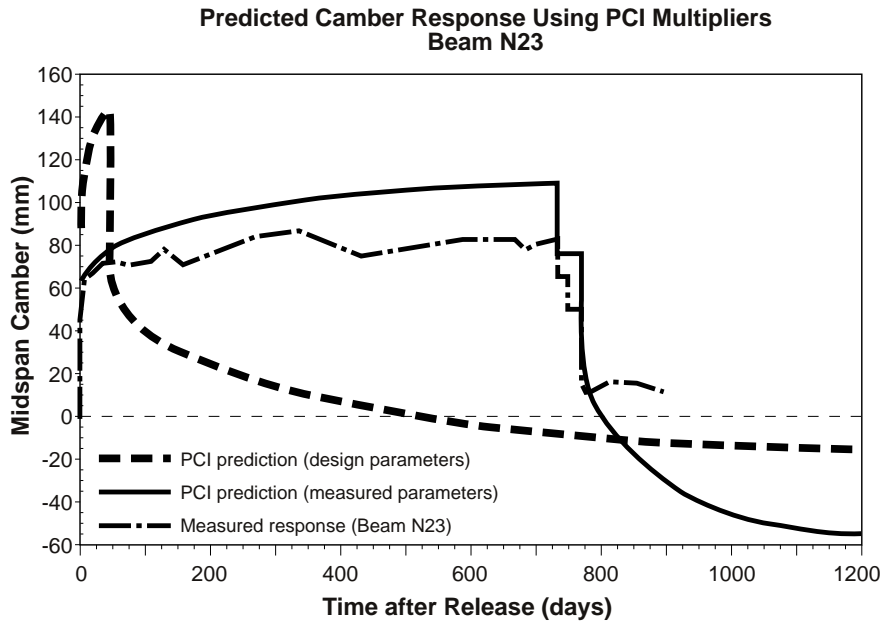


Figure 6.27 Comparison of measured and predicted camber responses for Beam N23 using the PCI Design Handbook procedures

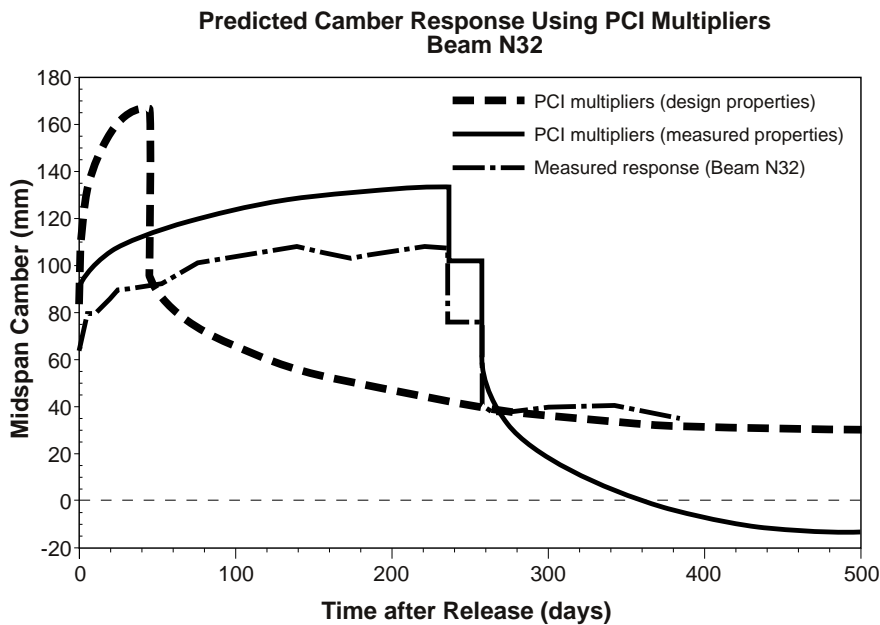


Figure 6.28 Comparison of measured and predicted camber responses for Beam N32 using the PCI Design Handbook procedures

The PCI(des.) predicted cambers at erection varied between 140.6 mm (Beam N23) and 204.4 mm (Beam N21) and the PCI(meas.) predicted cambers at erection varied between 109.4 (Beam N23) and 169.9 mm (Beam N21). The difference between these two predictions was directly related to the magnitudes of the initial components of camber and deflection shown in Table 6.6.

The differences between the PCI(des.) and PCI(meas.) predicted responses remained fairly constant through placement of the deck loads because the elastic components of deflection were quite similar, except for the exterior beams. For those beams, the differences in camber between the two predictions after placement of the deck loads were significantly smaller because the PCI(meas.) predictions excluded the weight of the overhang in the cast-in-place deck deflections.

The PCI(des.) predicted long-term responses varied between -20.1 mm (Beam S25) and 53.7 mm (Beam S14) and the PCI(meas.) predicted long-term responses varied between -71.3 mm (Beam S25) and 64.8 mm (Beam N21). The differences between predictions were a direct result of the differences in the initial components of camber and deflection at release. In addition, the PCI(meas.) predictions for the long-term responses of the exterior girders were higher because the elastic deflections from the CIP deck were smaller.

The measured long-term responses are given in Table 6.8 for comparison purposes. The measured long-term cambers varied from 2.3 mm (Beam S24) to 77.7 mm (Beam N21). The PCI(des.) predicted long-term responses grossly overestimated the measured values. The reason for this was that the differences in camber at release, which were quite large, were magnified by the multipliers. The PCI(meas.) predictions, which best represented the instrumented beams, overestimated the cambers at erection by an average of 29.0 mm. The average difference in camber at release was 15.3 mm, as given in Sec. 6.3.2.1. The larger camber growth of the PCI(meas.) predictions between release and erection is also apparent in Figures 6.23 to 6.28. Differences in measured and predicted growth were attributed to a combination of the differences in camber at release and overestimation of the creep coefficient of the HPC U-beams by the PCI multipliers.

Examination of the predicted and measured long-term responses in Table 6.8 and Figures 6.23 to 6.28 shows that the PCI multipliers overestimated the additional time-dependent deflection that occurs after the deck loads are placed on the beams. For Beams S15, S25, and N32, which are shown in Figures 6.23, 6.25, and 6.28, respectively, the PCI(des.) predictions appear to estimate the measured response fairly accurately. However, this was merely a result of the gross overestimation of release camber and camber at erection followed by the gross overestimation of the long-term deflection after placement of the deck. These two errors tended to offset each other. As can be seen in Figures 6.23 to 6.28, the measured camber growth during the first 45 days was much smaller than the PCI(des.) predicted camber growth using the PCI multipliers. For all of the beams, the PCI(des.) predictions provided a poor estimation of the camber and deflection history of the U-beams. In addition, the use of the PCI multipliers seemed to overestimate creep of the U-beams.

For all of the beams shown in Figures 6.23 to 6.28, the PCI(meas.) predicted long-term camber also overestimated the deflection after the deck loads were placed. For Beam S25, shown in Figure 6.25, the PCI(meas.) prediction overestimated the camber at erection

by 27.1 mm and then significantly overestimated the long-term deflection after placement of the deck loads by 88.1 mm. Even though the elastic components of deflection were reasonably close, as discussed in Sec. 6.3.2.1, all of the instrumented beams displayed very little additional deflection after placement of the deck. This indicated that the multipliers applied to the superimposed loads did not appropriately represent creep deflection of the composite HPC U-beam sections, especially when large differences between the actual and assumed construction schedule exist.

General trends that appeared between the PCI predicted and measured long-term camber responses are presented in Figures 6.29 and 6.30. The differences between the predicted and measured cambers at release, at erection, after the CIP deck was placed, and after a long period of time are shown for both prediction cases. Positive differences indicated that the predicted values overestimated the measured values, while negative differences indicated the opposite. The final measured camber values were considered long-term in this study even though camber measurements will continue for several more years. The measured loss of camber during the five month period after the CIP deck was cast indicated that very little change was occurring.

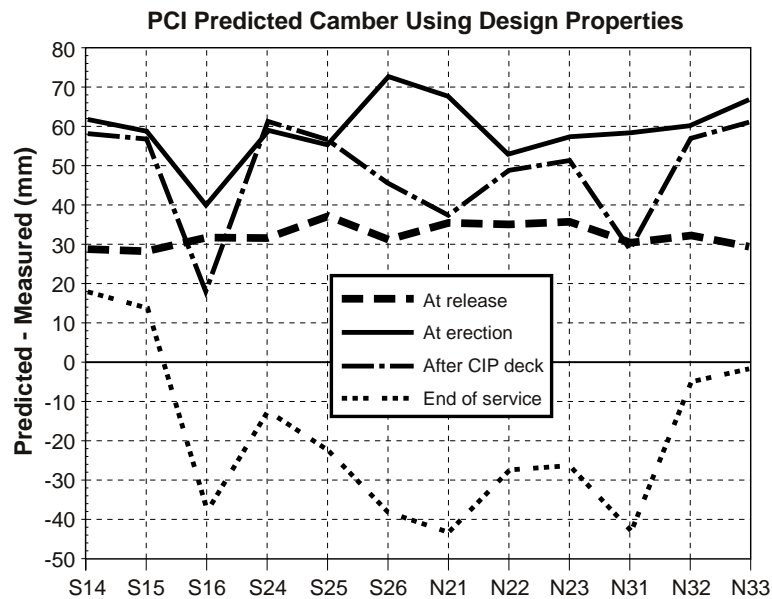


Figure 6.29 Differences in measured and predicted long-term camber and deflection (based on design parameters)

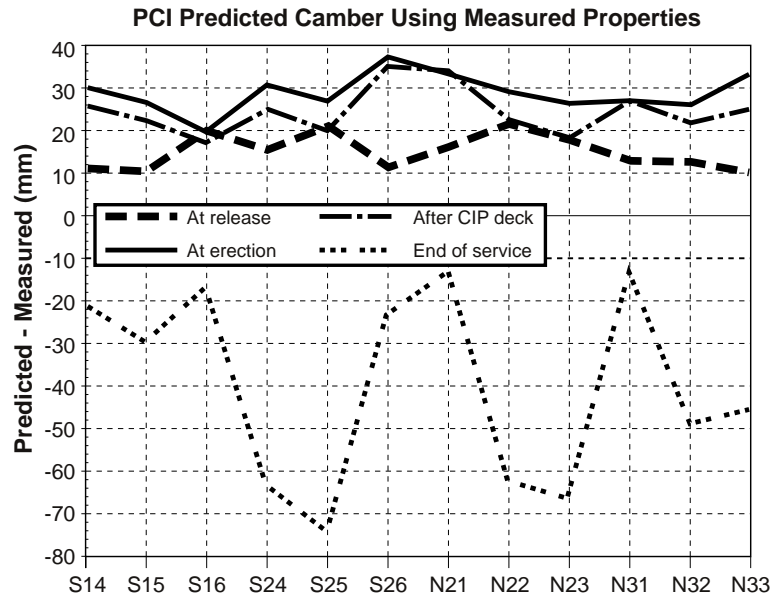


Figure 6.30 Differences in measured and predicted long-term camber and deflection (based on measured parameters)

The differences between the measured and predicted cambers at release, at erection, and after placement of the CIP deck, all remained positive for every instrumented beam. This was true for both prediction cases. The general trend was that the magnitude of the positive differences remained the same or larger than the differences that were observed at release, especially for the PCI(meas.) predictions shown in Figure 6.30. However, the long-term differences at the end of service became negative. The magnitudes of the negative differences ranged from 13 to 74 mm for the PCI(meas.) predictions. The negative differences were much less for the PCI(des.) predictions, shown in Figure 6.29, because they had much higher erection cambers. Based on the comparisons in these diagrams, it was evident that the PCI multipliers were not applicable for the HPC U-beams.

The PCI multipliers overestimated additional long-term deflection due to the deck loads because some of the assumptions made when developing the multipliers were not appropriate for the instrumented U-beams. First, the creep coefficient applied to the deck loads was assumed to be 2.0. However, the concrete will not creep as much when it is loaded at later ages. This was especially true for the beams in this study, although it would also apply to beams loaded at 45 days. Secondly, the ratio of non-composite to composite moments of inertia for the U-beams was approximately 0.35, which was much different than the assumed ratio of 0.65. Using the actual ratio would reduce the long-term multipliers for all components of camber and deflection.

6.4 ANALYTICAL TIME-STEP METHOD

6.4.1 General

An analytical time-step method was developed based on the procedure outlined by Branson and Kripanarayanan (43). This method was developed on a computer spreadsheet program and used to predict the time-dependent prestress losses, camber, and deflection for all of the instrumented beams.

The time-dependent models for creep, shrinkage, and age-strength gain that were developed from companion test data for the high performance concrete beam mix were used in time-step method. These functions were assumed to be the most accurate representation of the properties of the instrumented beams.

The equations and assumptions used for the time-step analysis are presented in the following sections. The resulting prestress loss and camber response predictions are presented and compared to the measured behavior.

6.4.2 Prestress Losses

6.4.2.1 Analytical Procedure

The analytical procedure for calculating prestress losses involved calculating the initial losses that occurred prior to release, the immediate loss during transfer of the prestressing force, the time-dependent losses due to creep, shrinkage, and relaxation over discrete time intervals, and instantaneous gains in prestress that occurred when the deck panels and cast-in-place deck were placed on the beams. The effect of differential shrinkage of the deck was also considered. The total losses at any time were determined by summing the instantaneous prestress losses (or gains) and the incremental losses that occurred during the previous time intervals.

The initial prestress losses that were assumed to occur between initial stressing of the strands and release included losses due to increases in temperature of the strands, relaxation, and shrinkage after the side forms were stripped. The initial stress to which the strands were pulled was assumed to be $0.75f_{pu}$ (1396 MPa). It was assumed that a 2 percent loss occurred due to increased temperature of the strands, three days occurred between initial stressing and release, and 12 hours occurred between stripping the side forms and release. Equation 6.9, taken from the PCI Committee Report on Prestress Losses (56), was used to calculate relaxation loss. Equation 6.10 was used to calculate shrinkage strain. The shrinkage loss was the product of the shrinkage strain and the modulus of elasticity of the prestressing steel, which was assumed to be 193 GPa.

$$RE_t = f_{si} \left(\frac{\log_{10} t}{45} \right) \left(\frac{f_{si}}{f_{py}} - 0.55 \right) \quad (6.9)$$

where

t = time after initial stressing (hours)

f_{si} = initial stress in the strands (MPa)

f_{py} = 0.1 percent offset yield strength taken as $0.9f_{pu}$ (MPa)

$$(\varepsilon_{sh})_t = (\varepsilon_{sh})_u \left(\frac{t^{0.6}}{2 + t^{0.6}} \right) \quad (6.10)$$

where

$(\varepsilon_{sh})_u$ = ultimate shrinkage strain adjusted for volume-to-surface ratio and 75 percent relative humidity (given in Table 6.9)
 t = time after stripping of the side forms (days)

Table 6.9 Ultimate creep and shrinkage coefficients for U-beams

U-beam Cross section	Ultimate shrinkage coefficient ($\mu\varepsilon$)	Ultimate creep coefficient (C_{cu})
U54A	279	1.45
U54B	269	1.41

The immediate loss at transfer due to elastic shortening was calculated using the transformed section properties, material properties calculated using Eqs. 6.11 and 6.12, beam loads based on a concrete unit weight of 2481 kg/m³ (including the diaphragms), design span lengths shown in Table 6.4, and the actual time between casting and release, which are shown in Sec. 4.3.1. Equation 6.11 was developed in Sec. 5.2.1 based on data from member-cured specimens. The elastic shortening loss was determined exactly using an iterative procedure.

$$(f'_c)_t = \frac{t^{0.4}}{0.58 + 0.85t^{0.4}} (90.5) \quad (\text{MPa}) \quad (6.11)$$

$$E_{ct} = 3.10 \left(\sqrt{(f'_c)_t} + 11.29 \right) \left(\frac{w}{2323} \right)^{1.5} \quad (\text{GPa}) \quad (6.12)$$

The time-dependent losses were calculated over very short time intervals just after release and then over larger time intervals as the changes in creep and shrinkage became less. Equation 6.13 was used to calculate the creep coefficient at any time.

$$(C_c)_t = C_{cu} \left(\frac{t^{0.5}}{6 + t^{0.5}} \right) \quad (6.13)$$

where

C_{cu} = ultimate creep coefficient adjusted for volume-to-surface ratio and 75 percent relative humidity (given in Table 6.9)
 t = time after release (days)

Time-dependent losses for each interval were determined by using Eqs. 6.10 and 6.13 to calculate shrinkage and creep coefficients, respectively, and then using Eqs. 6.14 to 6.16 to calculate incremental losses in MPa due to shrinkage, creep, and relaxation.

$$(PL_{shr})_i = [(\varepsilon_{sh})_t - (\varepsilon_{sh})_{t-\tau}] E_s \quad (6.14)$$

$$(PL_{cr})_i = (nf_c)_{t-\tau} [(C_c)_t - (C_c)_{t-\tau}] \quad (6.15)$$

$$(PL_{rel})_i = (f_s)_{t-\tau} \left(\frac{\log_{10}(t-\tau)}{45} \right) \left(\frac{(f_s)_{t-\tau}}{f_{py}} - 0.55 \right) \quad (6.16)$$

where

t = end of time interval i (will be different for each component of loss)

τ = differential length of time for interval i

n = modular ratio of steel to concrete at the beginning of interval i

f_c = stress in the concrete at CGS at the beginning of time interval i

$(f_s)_{t,\tau}$ = stress in the strands at the beginning of interval i

The loss component due to creep, given by Eq. 6.15, was modified by the ratio of non-composite to composite moments of inertia after the bridge was composite. At that time, the effects of differential shrinkage were also included. The ultimate shrinkage strains for the northbound and southbound decks, which were determined using shrinkage specimens as described in Sec. 3.6.4, were 196 and 166 microstrain, respectively. After the bridge was composite, the section properties were no longer varied with time. This was done because the composite section was extremely stiff and the beam modulus of elasticity was not changing. The elastic moduli used for calculating the composite section properties were estimated to be 44.8 GPa for the deck panels, 34.5 GPa for the northbound CIP deck, 37.9 GPa for the southbound CIP deck. Small variations in these values had no effect on the results. An expression for the total loss at any time is given in Eq. 6.17.

$$PL_t = PL_o + \sum_{i=1}^n (PL_{cr} + PL_{shr} + PL_{rel} + PL_{loads} + PL_{diff-shr}) \quad (6.17)$$

where

t = time after release in days (corresponds to the end of time interval n)

n = number of time intervals used to reach time t

PL_o = all losses that occur before release

PL_{loads} = all instantaneous losses that occur due to superimposed loads
(will be negative to represent a gain in prestress)

$PL_{diff-shr}$ = losses due to differential shrinkage (will be negative)

Calculations for a typical time interval began by calculating concrete compressive strength using Eq. 6.11, calculating the elastic modulus using Eq. 6.12, and then calculating transformed section properties. Incremental losses were calculated using Eqs. 6.14 to 6.16, summed, and added to the total prestress loss that was determined at the end of the previous time interval. This operation can be represented by Eq. 6.17. Based on the new value for prestress loss, a new strand stress was determined. This strand stress was used for calculating relaxation and creep losses in the next time interval.

6.4.2.2 Predicted Prestress Losses

The measured and predicted prestress losses at the CGS at midspan using the analytical time-step method are shown in Figures 6.31 to 6.38. Results were shown for the beams that had measured strains at midspan at the CGS for a lengthy period of time. A summary of the measured and predicted prestress losses at release, at erection, after the deck loads, and long-term are shown in Table 6.10.

Table 6.10 Summary of measured and predicted prestress losses using the analytical time-step method

Time	Source	Prestress Losses ^{1,3} (%)									
		S14	S15 ⁵	S16	S25 ⁵	S26	N21	N22	N31	N32	N33
Elastic Shortening	Time-step	8.09	8.00	7.40	6.89	8.22	8.83	6.80	8.51	7.36	----
	Measured	12.10	8.09	8.48	7.86	10.05	10.11	6.28	9.26	8.77	----
At erection	Time-step	22.32	22.15	22.69	20.83	21.50	24.02 ⁴	----	----	21.17	21.05 ⁴
	Measured	25.31	17.77	19.48	18.50	20.97	19.76 ⁴	----	----	19.88	19.81 ⁴
After CIP deck	Time-step	19.53	19.23	20.69	17.77	19.29	----	----	----	18.47	----
	Measured	21.88	15.11	17.68	15.98	18.81	----	----	----	17.50	----
Long-term ²	Time-step	19.57	19.31	20.66	17.75	----	----	----	----	18.52	----
	Measured	21.51	14.68	17.17	15.44	----	----	----	----	17.14	----

Notes:

1. Measured losses after release include approximately 4 percent for relaxation, shrinkage, and temperature effects that were assumed to occur before release in the analytical time-step model.
2. Long-term predictions correspond to the time of the last gage measurement.
3. Measured losses do not include loss due to relaxation after release.
4. Measurements were before erection because the gage stopped giving quality results.
5. Measured losses were determined using an average of the measured strains on both sides of the beam at midspan.

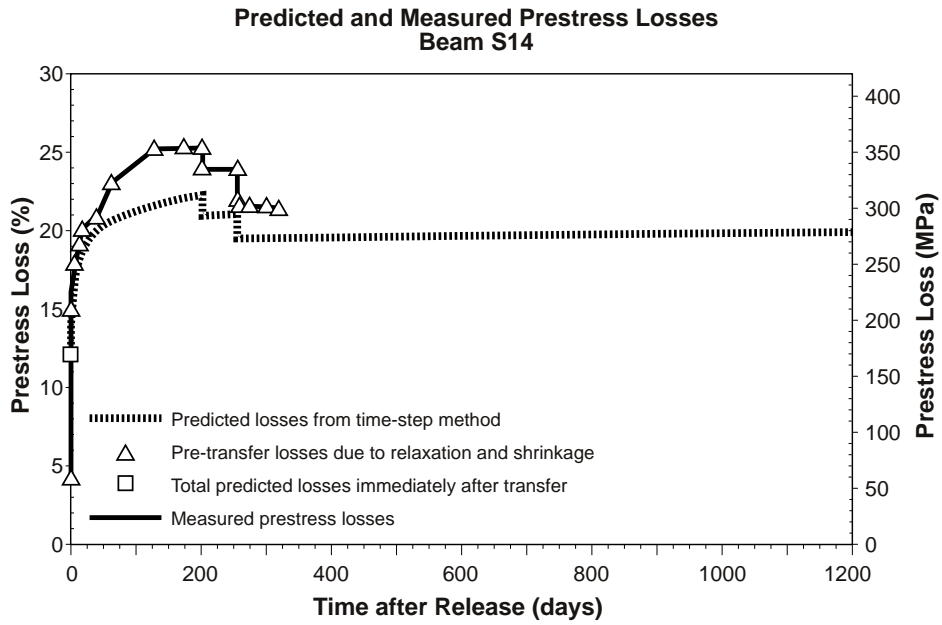


Figure 6.31 Predicted prestress losses for Beam S14 (time-step method)

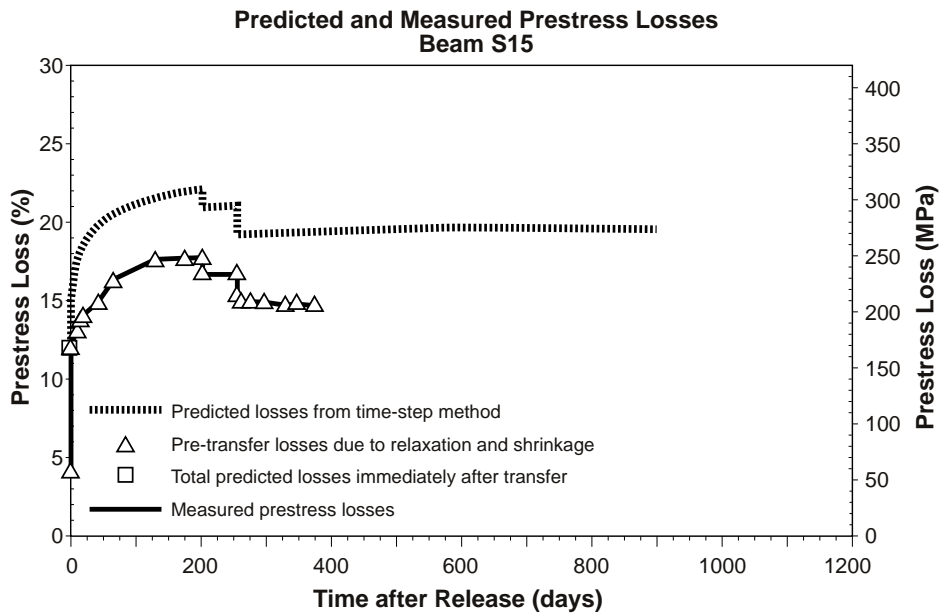


Figure 6.32 Predicted prestress losses for Beam S15 (time-step method)

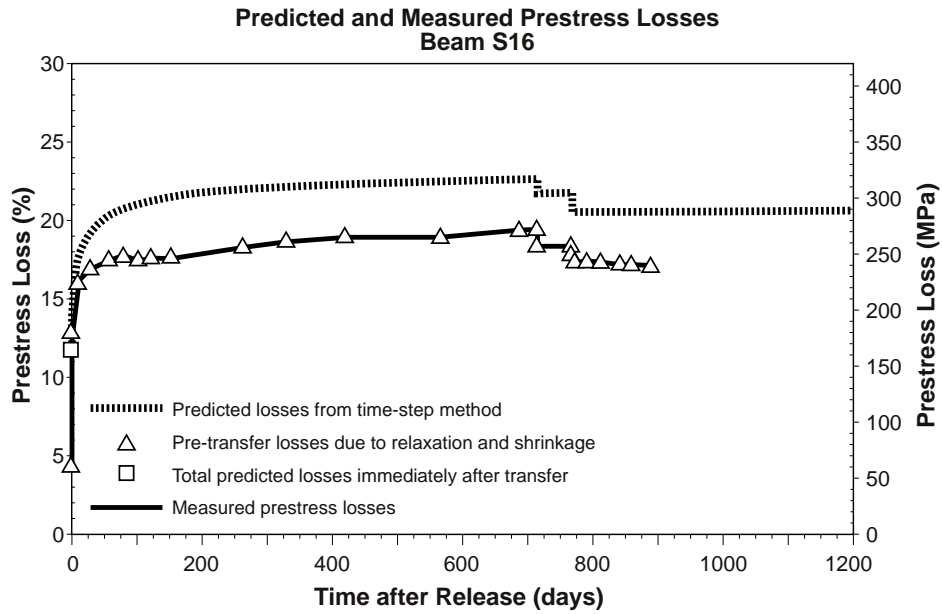


Figure 6.33 Predicted prestress losses for Beam S16 (time-step method)

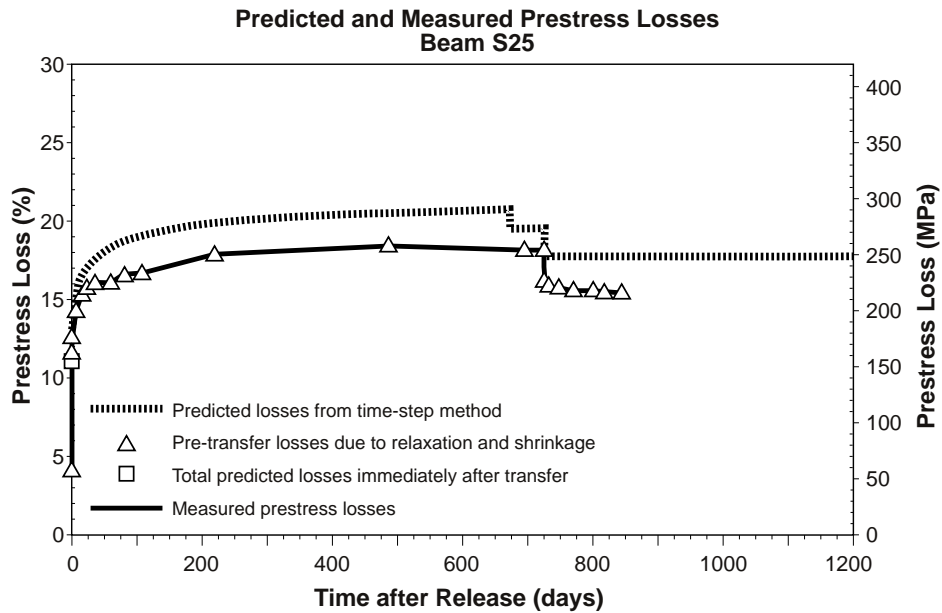


Figure 6.34 Predicted prestress losses for Beam S25 (time-step method)

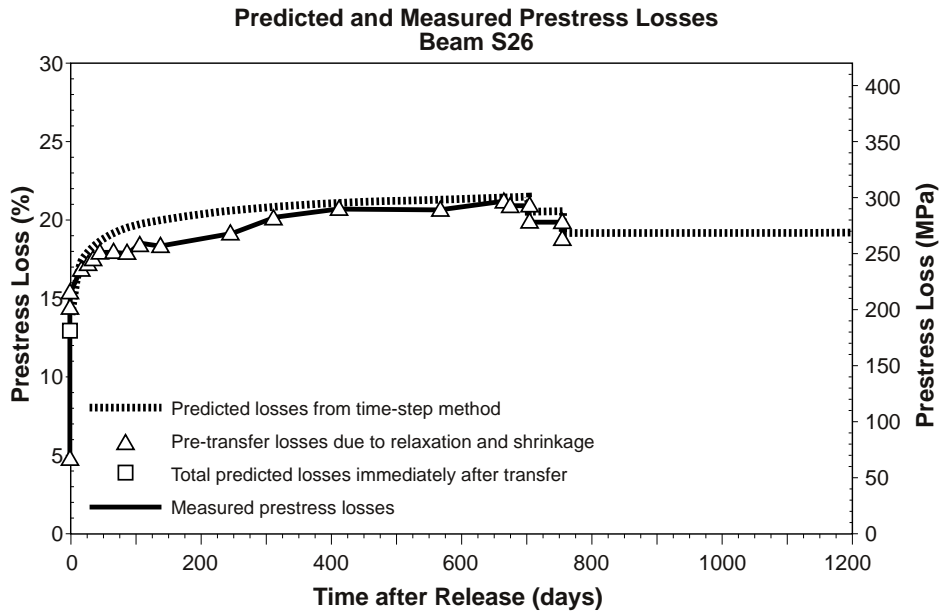


Figure 6.35 Predicted prestress losses for Beam S26 (time-step method)

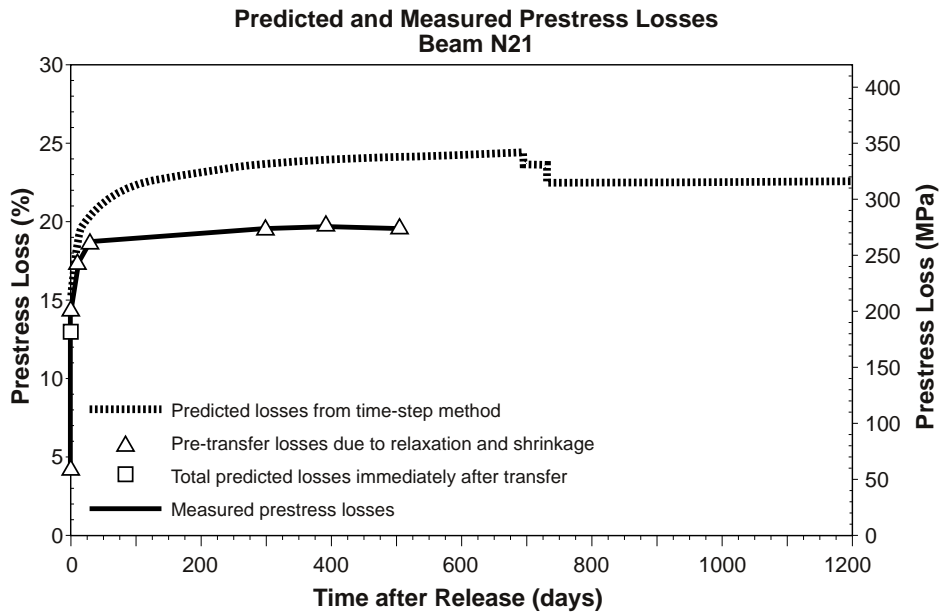


Figure 6.36 Predicted prestress losses for Beam N21 (time-step method)

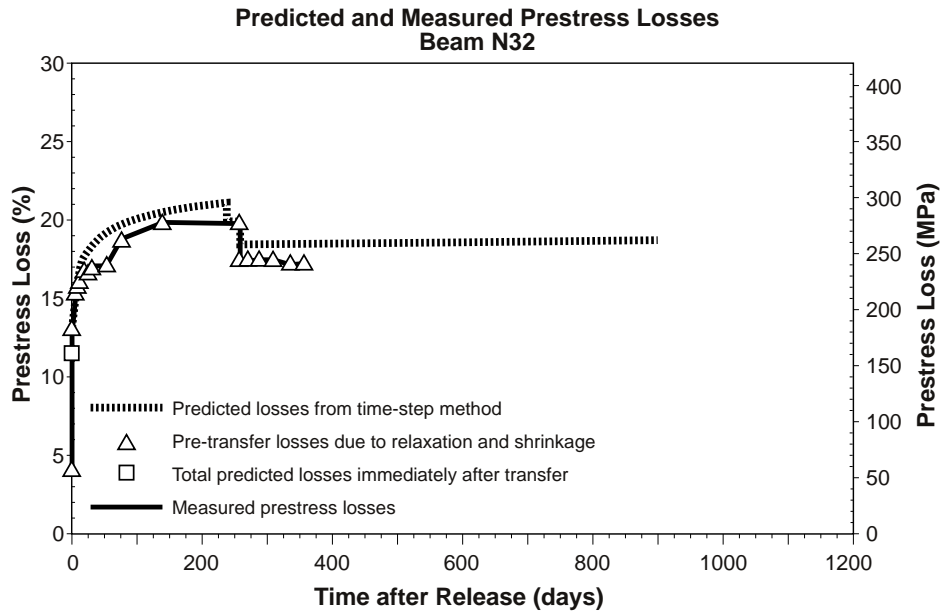


Figure 6.37 Predicted prestress losses for Beam N32 (time-step method)

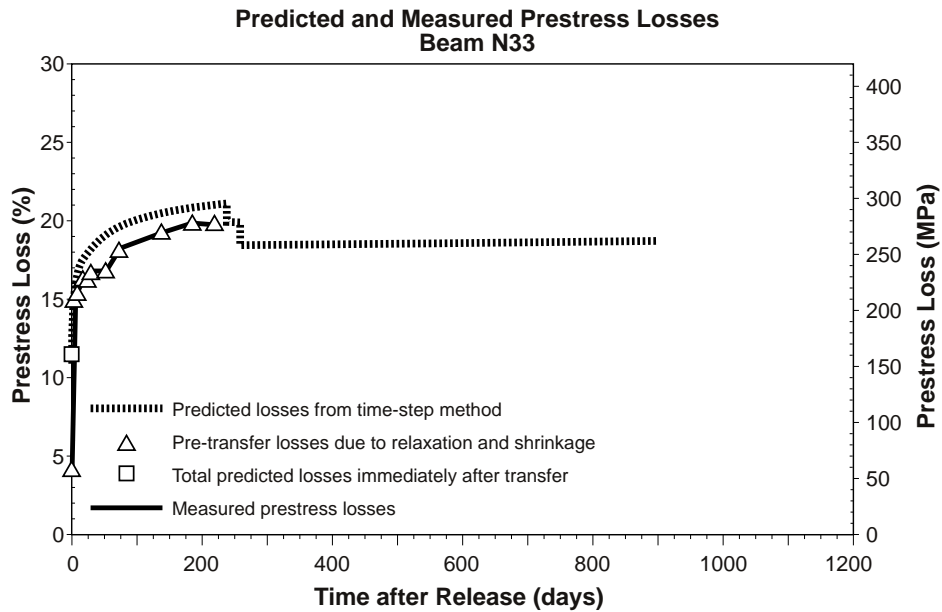


Figure 6.38 Predicted prestress losses for Beam N33 (time-step method)

The initial losses before release that were calculated in the time-step method were added to all of the measured prestress losses. This was done because the baseline readings for the strain gages were taken just before release. As a result, any relaxation, shrinkage, or

temperature losses that occurred before release were not recorded by the gages. The measured losses did not include losses due to relaxation after release and no corrections were made in Table 6.10 or in Figures 6.31 to 6.38 to account for this. The total additional predicted relaxation loss was approximately 0.5 percent.

The predicted elastic shortening losses varied between 6.80 percent (Beam N22) and 8.83 percent (Beam N21). The measured elastic shortening losses varied between 6.28 percent (Beam N22) and 12.10 percent (Beam S14). Generally, the largest measured elastic shortening losses were in Beams S26, N21, and N31, which had the largest prestressing forces. This was consistent with the predictions. Measured elastic shortening losses were higher than the predicted losses for all of the beams except for Beams S15 and N22.

Total prestress losses after release, which are shown in Figures 6.31 to 6.38, were determined by adding the additional losses that were assumed to occur before release to the elastic shortening losses. These additional losses were approximately 4 percent for all of the beams. Since the predicted losses before release were added to the measured values, comparisons between measured and predicted losses at any time were not affected.

The predicted prestress losses at erection varied between 20.83 percent (Beam S25) and 24.02 percent (Beam N21). As shown in Table 6.10, several of the instrumented beams did not have reliable long-term strain measurements. Therefore, predictions for those beams were not included in the summary. The measured prestress losses at erection varied between 17.77 percent (Beam S15) and 25.31 percent (Beam S14). With the exception of Beam S14, all of the measured prestress losses at erection were lower than the predicted losses.

Predicted increases in prestress losses from release to erection varied between 9.3 percent (Beam S26) and 11.3 percent (Beam S16). The average predicted increase in prestress losses was 10.2 percent. Beam S26 exhibited low time-dependent prestress loss because the prestressing force was transferred at 7 days. Measured increases in prestress losses varied between 6.7 percent (Beam S15) and 9.2 percent (Beam S14). The average measured increase was only 7.1 percent. When the loss due to relaxation was added to the measured values, the average difference was still nearly 2.5 percent.

For Beam S15, shown in Figure 6.32, the measured and predicted prestress losses at release were nearly the same but the predicted time-dependent increase in prestress loss was significantly larger than what was observed. Beams S16 and S25, shown in Figures 6.33 and 6.34, respectively, had higher measured initial losses at release yet displayed smaller increases in prestress losses up to erection. Similar trends were found in Beams S26 and N32, shown in Figures 6.35 and 6.37, respectively, although there was good agreement between measured and predicted losses at erection for these beams. Beam N21, shown in Figure 6.36, also exhibited higher measured losses at release followed by very little long-term growth. However, the measurements for this beam were probably unreliable after 100 days.

The only beam to exhibit a measured time-dependent increase in prestress loss equal to the predicted increase was Beam S14. For this beam, the measured increase was 9.2 percent while the predicted increase was 10.2 percent. After adding relaxation into the measured loss, the predicted and measured growths agreed well. However, the measured elastic shortening loss was much larger than the corresponding predicted loss.

Beam N33, shown in Figure 6.38, exhibited good agreement between measured and prediction prestress losses but a measurement at release was not obtained. As a result, a comparison of the measured and predicted increases in prestress loss was not possible.

The predicted long-term prestress losses varied between 17.75 (Beam S25) and 20.66 (Beam S16) percent for the beams that had working gages after the deck panels and CIP deck were added to the bridge. These predictions correspond to the times that the last measurements were taken by the gages. The measured long-term prestress losses varied between 14.68 (Beam S15) and 21.51 (Beam S14) percent. The predicted long-term prestress losses were an average of only 2 percent higher than the measured prestress losses. If the additional relaxation loss after release were added to the measured losses, the average difference would be 1.5 percent.

Differences between the measured and predicted losses remained fairly constant after erection because the instantaneous losses due to the deck loads were quite similar. Very little time-dependent losses were predicted after the decks were completed. This was attributed to the stiffness of the composite section, which was almost three times as stiff as the non-composite section, as well as the age of the concrete when the deck loads were placed. Based on the models for material behavior, given by Eqs. 6.10 and 6.13, very little creep and shrinkage were predicted to occur at late ages. Also, the effects of differential shrinkage were quite small, mainly because of the stiffness of the composite section.

Possible reasons that the measured losses at release were larger than the predicted losses at release are discussed in Sec. 5.4.2.1 and are reviewed in this section based on the results of the time-step method. Differences between the measured and predicted losses at erection were included in an attempt to explain the observed behavior.

If the actual prestressing force transferred to a beam had been larger than what was assumed in the time-step model, the measured loss due to elastic shortening would have been larger. This also would have tended to increase the loss due to creep between release and erection. However, all of the beams that had higher measured losses at release showed less time-dependent losses during that time period. In addition, Beam S15, which had similar measured and predicted losses due to elastic shortening, had lower measured time-dependent prestress losses. Based on these results, a higher transferred prestressing force was probably not the cause of differences between the measured and predicted losses at release.

If the modulus of elasticity at release had been lower than what was assumed in the time-step model, the measured loss due to elastic shortening would have been larger. The loss due to creep would have increased because the initial strain would have been larger. As a result, the increase in prestress loss should have been larger than the predicted increase using the time-step model. However, the average measured increase in prestress loss between release and erection was less than the average predicted increase.

The cause of the higher measured losses at release accompanied by lower measured losses at erection was probably a combination of several factors. Part of the difference may have been caused by variation in the actual modulus of elasticity of the concrete, problems attributable to the strain gages and data acquisition system, and errors in applying the mathematical models for time-dependent material properties, most notably creep and shrinkage, to the HPC U-beams. The other factor that may have contributed to the high

measured release losses was restraint offered by the prestressing bed during extreme thermal cooling that occurred in the beams after hydration. This concept is discussed extensively in Sec. 5.4.2.1. This effect may have made the measured strains at release artificially high due to the measurement of additional strain in the beams caused by restraint of the bed during uneven cooling of the section. This effect would not have changed the amount of time-dependent prestress losses observed in the HPC U-beams. In addition, the creep and shrinkage losses in the time-step model probably slightly overestimated the actual behavior.

6.4.3 Camber and Deflection

6.4.3.1 Analytical Procedure

The analytical procedure for predicting the time-dependent camber and deflection response for the instrumented beams involved determining elastic camber or deflection due to applied loads and then calculating time-dependent increases in the elastic responses for a finite number of time intervals. The time-dependent portion of the response was determined by applying differential creep coefficients to the elastic responses over each discrete time interval. Additional consideration was given to the loss of prestress over time and to the effect of differential shrinkage, which are outlined in Sec. 6.4.2.1.

The calculation of elastic camber due to the prestressing force included the effect of strand debonding. Since the debonding patterns, which are found in Appendix A, were quite complicated, a formula for the camber due to prestress is not shown. The values for modulus of elasticity and transformed section properties were identical to those used for calculating elastic shortening. In addition, the stress in the strands was identical to the predicted stress just after release, which included the losses that occurred before release. This was discussed in Sec. 6.4.2.1.

The elastic deflection due to the beam weight was calculated using Eqs. 6.4 and 6.5, which are given in Sec. 6.3.2.1. The material and section properties used for this calculation were the same as those used in the calculation of elastic camber due to the prestressing force.

The elastic deflections due to the deck panels and the cast-in-place (CIP) deck were calculated using Eq. 6.8, which is given in Sec. 6.3.2.1. The actual times of the events, which are given in Sec. 4.3.1, and Eqs. 6.11 and 6.12, shown in Sec. 6.4.2.1, were used to calculate the material properties. Transformed section properties were calculated based on the modular ratio of prestressing steel to concrete at the time of loading. The loads were based on the measured deck thicknesses. These loads are summarized in Table 6.5.

Time-dependent components of camber and deflection were calculated using Eqs. 6.18 and 6.19, respectively. These expressions represent changes in camber and deflection over a discrete time interval based on the incremental creep coefficient, the average loss of prestress force at that time, and the elastic components of camber and deflection. Equation 6.18 also includes the incremental reduction in the elastic prestress component due to the incremental reduction in the prestressing force over each time interval.

$$(\Delta_{ps})_i = \left[-\left(\frac{\Delta F_t - \Delta F_{t-\tau}}{F_o} \right) + \left(1 - \frac{\Delta F_t + \Delta F_{t-\tau}}{2 F_o} \right) \left((C_c)_t - (C_c)_{t-\tau} \right) \right] (\Delta_{ps}) \quad (6.18)$$

$$(\Delta_{dl})_i = (\Delta_{beam} + \Delta_{panel} + \Delta_{CIP}) \left((C_c)_t - (C_c)_{t-\tau} \right) \quad (6.19)$$

where

t = end of time interval i (time after release)

τ = differential length of time for interval i

ΔF_t = loss of prestressing force after release at time t

$\Delta F_{t-\tau}$ = loss of prestressing force after release at time $(t-\tau)$

F_o = prestressing force immediately after release

C_c = creep coefficient at times t and $(t-\tau)$ calculated using Eq. 6.13

Δ_{ps} = initial camber due to prestressing force, F_o

Δ_{beam} = initial deflection due to beam weight

Δ_{panel} = initial deflection due to deck panels

Δ_{CIP} = initial deflection due to cast-in-place deck

In Eq. 6.19, Δ_{panel} and Δ_{CIP} will be zero for all time intervals that occur before the time of placement of these loads on the beams. Once the beam section becomes composite, the incremental components of camber and deflection shown in Eqs. 6.19 and 6.20 are multiplied by the ratio of non-composite to composite moments of inertia. The assumptions made in Sec. 6.4.2.1 concerning calculation of transformed section properties for the composite section apply to the calculations presented in this section. The total camber or deflection at any time is given by Eq. 6.20.

$$\Delta_t = \Delta_{ps} - \Delta_{beam} - \Delta_{panel} - \Delta_{CIP} + \sum_{i=1}^n \left[(\Delta_{ps})_i - (\Delta_{dl})_i - (\Delta_{diffshr})_i \right] \quad (6.20)$$

where

t = time after release in days (corresponds to the end of time interval n)

n = number of time intervals used to reach time t

$\Delta_{diffshr}$ = deflection due to differential shrinkage between the deck and the beam during the time interval I

In Eq. 6.20, Δ_{panel} and Δ_{CIP} may equal zero if time t is before placement of these loads on the beam. Also, the deflection due to differential shrinkage, $\Delta_{diffshr}$, will be zero at any time before placement of the CIP deck. The equation for differential shrinkage was not included in this section but its effect was shown in Eq. 6.20. Branson and Kripanarayanan (43) provided an equation that was used in conjunction with the assumed ultimate deck shrinkages

presented in Sec. 6.4.2.1. The additional deflection due to differential shrinkage in the time-step model was fairly small.

6.4.3.2 Elastic Camber and Deflection Due to Applied Loads

The predicted and measured elastic responses due to applied loads are summarized in Table 6.11. The predicted camber due to the prestressing force and deflection due to the beam weight are included to show the magnitudes of the individual components of camber at release. Measured elastic responses are given for release camber, deck panel deflection, and CIP deck deflection. The predicted cambers at release varied between 64.3 mm (Beam N23) and 91.7 mm (Beam N21). Variation in predicted release camber among beams was attributed to differences in span length, section type, and number of prestressing strands. The measured cambers at release varied between 44.1 mm (Beam S25) and 84.5 mm (Beam S26). The average difference between the measured and predicted cambers at release was 12.2 mm. The maximum difference was 20.7 mm for Beam S25 and the minimum difference was 1.0 mm for Beam S26.

Table 6.11 Summary of measured and predicted elastic responses due to applied loads based on the analytical time-step method

Elastic Component	Source	Camber or Deflection (mm)											
		S14	S15	S16	S24	S25	S26	N21	N22	N23	N31	N32	N33
Camber due to prestress	Time-step	122.8	126.2	125.5	151.1	155.1	172.2	185.3	161.0	162.5	176.2	160.9	162.2
Deflection due to beam weight	Time-step	51.9	55.3	60.4	85.2	90.3	86.6	93.6	96.3	98.2	88.3	87.2	88.8
Camber at release	Time-step	70.9	70.9	65.1	65.9	64.8	85.6	91.7	64.7	64.3	87.9	73.7	73.4
	Measured	61.8	62.4	49.1	50.8	44.1	84.5	80.5	46.4	45.0	78.1	63.8	65.9
Deflection due to deck panels	Time-step	26.0	27.0	18.6	32.9	34.1	26.1	24.1	32.0	32.4	21.9	30.4	30.7
	Measured	29.7	30.0	19.8	36.0	38.1	32.5	27.7	32.2	33.3	24.9	32.0	32.7
Deflection due to CIP deck	Time-step	32.9	36.1	25.9	47.5	49.3	38.8	32.8	42.3	42.9	30.1	40.2	40.7
	Measured	24.9	28.7	24.1	41.4	40.7	32.1	29.5	38.1	35.3	26.7	35.3	32.0

The ratios of measured to predicted cambers at release are shown in Figure 6.39. A ratio below unity indicates that the predicted camber overestimated the measured camber. Figure 6.39 shows that all of the instrumented beams had measured release cambers that were lower than the predicted values. The maximum ratio was 0.99 (Beam S26), the minimum ratio was 0.68 (Beam S25), and the average ratio was 0.83.

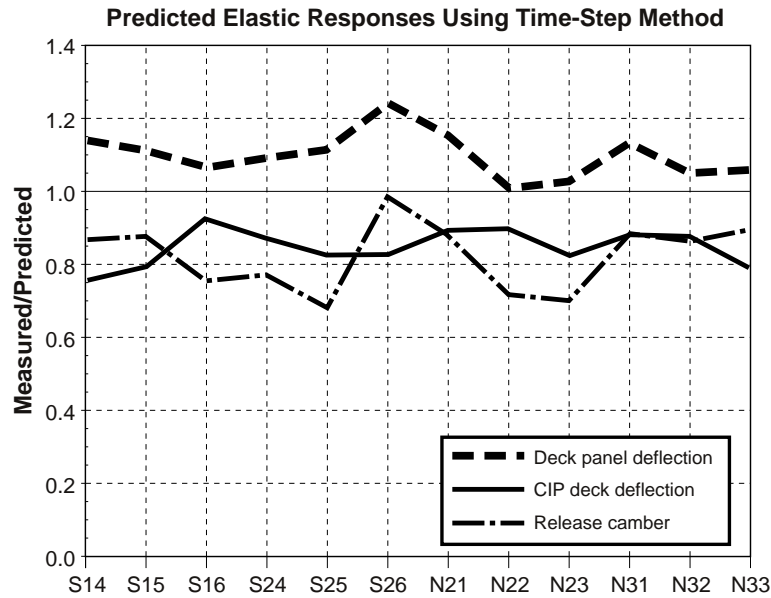


Figure 6.39 Summary of the ratios of measured to predicted elastic responses using the time-step method

Consistently low camber at release did not agree with the consistently high measured elastic shortening losses shown in Sec. 6.4.2.2. Low measured camber implied the following differences, alone or in combination, between actual conditions during the measurements and the assumptions used in the time-step method:

1. Higher modulus of elasticity
2. Lower prestressing force transferred to the beam
3. Increased beam self-weight

These differences would have caused the measured elastic shortening loss to become smaller rather than larger. This observation supports the idea that additional strain due to restraint offered by the bed during cooling of the beam was being measured at release. Since the measured elastic shortening losses appeared to be distorted in this way, it was difficult to verify the cause of low measured cambers at release.

The predicted deflections due to the deck panels varied between 18.6 mm (Beam S16) and 34.1 mm (Beam S25). The predicted deflections were the largest for beams with the largest spacing and span length. The predicted deflections were the smallest for the exterior beams. The measured deflections due to deck panels varied from 19.8 mm (Beam S16) to 38.1 mm (Beam S25). The average difference between measured and predicted deflections was only 2.7 mm. The maximum difference was 6.4 mm (Beam S26) and the minimum difference was 0.2 mm (Beam N22).

The ratios of measured to predicted deck panel deflections are shown in Figure 6.39. All of the ratios were above unity, indicating that the measured deck panel deflection exceeded the predicted deflection for all of the beams. The maximum ratio was 1.25 (Beam S26), the minimum ratio was 1.01 (Beam N22), and the average ratio was 1.10. The agreement between the measured and predicted deflections was very good, considering the possible errors due thermal gradients, variations in material properties, and the method of measurement.

The predicted deflections due to the CIP deck varied from 25.9 mm (Beam S16) to 47.5 mm (Beam S24). The predicted deflections were the largest for beams with the largest spacing, span length, and measured deck thickness. The predicted deflections were the smallest for the exterior beams because the overhangs were not cast with the deck. The measured deflections due to the CIP deck varied from 24.1 mm (Beam S16) to 41.4 mm (Beam S24). The average difference between measured and predicted deflections was only 5.9 mm. The maximum difference was 8.7 mm (Beam N33) and the minimum difference was 1.8 mm (Beam S16).

The ratios of measured to predicted CIP deck deflections are shown in Figure 6.39. All of the ratios were below unity, indicating that the measured CIP deck deflection was less than the predicted deflection for all of the beams. The maximum ratio was 0.93 (Beam S16), the minimum ratio was 0.76 (Beam S14), and the average ratio was 0.85. The agreement between the measured and predicted deflections was good, considering the magnitude of the deflection and the possible sources of error that were mentioned previously. In addition differential shrinkage and temperature gradients that developed soon after the decks were cast may have induced camber in the beams. This would have caused the measured cambers to appear low.

6.4.3.3 Long-term Camber and Deflection

The measured and predicted long-term camber and deflection responses for the instrumented beams are summarized in Table 6.12. Camber values were shown at erection, after placement of the deck panels, after placement of the CIP deck, and long-term. Camber values at release were included in Table 6.12 for convenient comparison of the measured and predicted camber growth between release and erection. Predicted and measured long-term cambers in Table 6.12 corresponded to approximately five months after the decks were completed. The predicted and measured time-dependent camber and deflection responses are also shown in Figures 6.40 to 6.51.

The predicted cambers at erection varied from 109.4 mm (Beam N23) to 156.9 mm (Beam N21). Beams N23 and N21 also had the lowest and highest predicted cambers at release, respectively. Differences in predicted camber at erection among beams were directly related to differences in the magnitudes of the components of camber and deflection at release. The measured cambers at erection varied from 83.1 mm (Beam N23) to 136.4 mm (Beam N21). These results tended to agree with the predictions, although the magnitudes of the cambers were much lower. The average difference between the predicted and measured

cambers at erection was 20.5 mm. The maximum difference was 29.2 mm (Beam S24) and the minimum difference was 3.9 mm (Beam S26).

Table 6.12 Comparison of measured and predicted long-term camber and deflection based on the analytical time-step method

Time	Source	Camber (mm)											
		S14	S15	S16	S24	S25	S26	N21	N22	N23	N31	N32	N33
At release	Time-step	70.9	70.9	65.1	65.9	64.8	85.6	91.7	64.7	64.3	87.9	73.7	73.4
	Measured	61.8	62.4	49.1	50.8	44.1	84.5	80.5	46.4	45.0	78.1	63.8	65.9
At erection	Time-step	121.3	120.9	122.2	114.0	111.1	135.0	156.9	110.5	109.4	151.8	123.2	122.4
	Measured	98.3	101.9	102.1	84.8	85.9	131.1	136.4	88.6	83.1	132.6	107.7	99.8
After deck panels	Time-step	97.2	95.9	104.8	83.2	79.2	110.8	134.6	80.6	79.1	131.5	94.9	93.9
	Measured	68.6	71.9	82.3	48.8	47.8	98.6	108.7	56.4	49.8	107.7	75.7	67.1
After CIP deck	Time-step	67.4	63.1	80.6	38.9	33.2	74.8	104.3	41.0	39.0	103.7	57.8	56.4
	Measured	43.7	43.2	58.2	7.4	7.1	66.5	79.2	18.3	14.5	81.0	40.4	35.1
Long-term	Time-step	63.2	58.4	75.4	32.2	26.1	67.9	96.1	32.3	30.2	95.6	48.3	46.7
	Measured	35.6	34.3	51.1	2.3	2.5	62.7	77.7	16.0	11.4	76.7	35.1	29.0

The differences between the predicted and measured cambers at erection for all of the beams are plotted in Figure 6.39. A positive difference indicates that the predicted camber overestimated the measured camber. This figure shows that all of the beams had camber at erection that was lower than the predicted value. With the exception of Beam S26, all of the beams showed significantly less camber at erection than what was predicted. The differences between the predicted and measured cambers at release are also shown in Figure 6.39. As mentioned previously, the measured cambers at release were lower than the predicted values for all of the beams. Based on the information provided in this graph, the differences become larger from release to erection for every beam.

Figures 6.40 to 6.51 show the predicted and measured growth of midspan camber from release to erection. For nearly all of the beams, the measured camber response did not increase as rapidly during the first 100 days as the predicted response. The shapes of the measured and predicted curves were fairly similar, despite the differences in the magnitude of camber growth. The measured camber response for Beam S26, shown in Figure 6.45, followed the predicted response almost exactly. The measured camber responses for Beams S25, N22, and N32, shown in Figures 6.44, 6.47, and 6.50, respectively, appeared to be offset from the predicted response curve by a constant amount. Beam N22 was the only beam that had low measured elastic shortening losses and low midspan camber from release to erection.

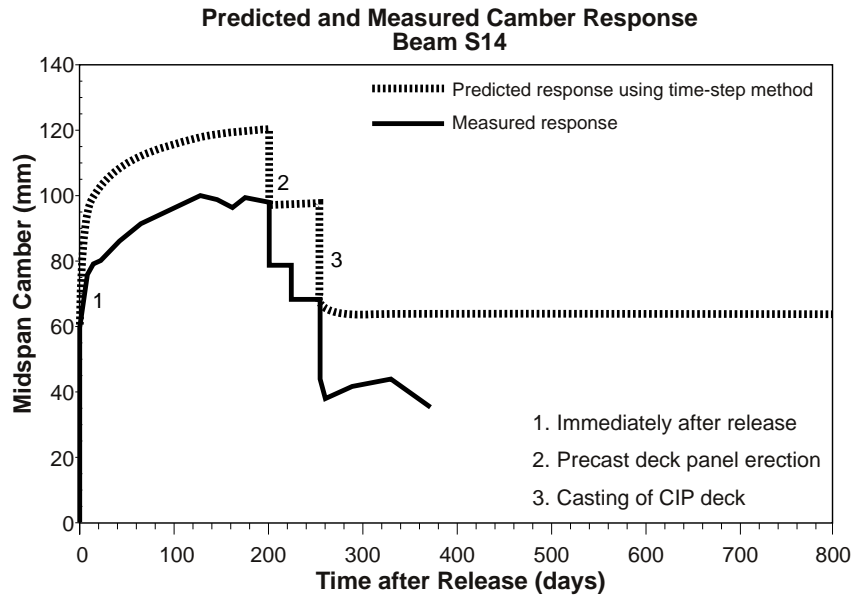


Figure 6.40 Predicted camber for Beam S14 using the time-step method

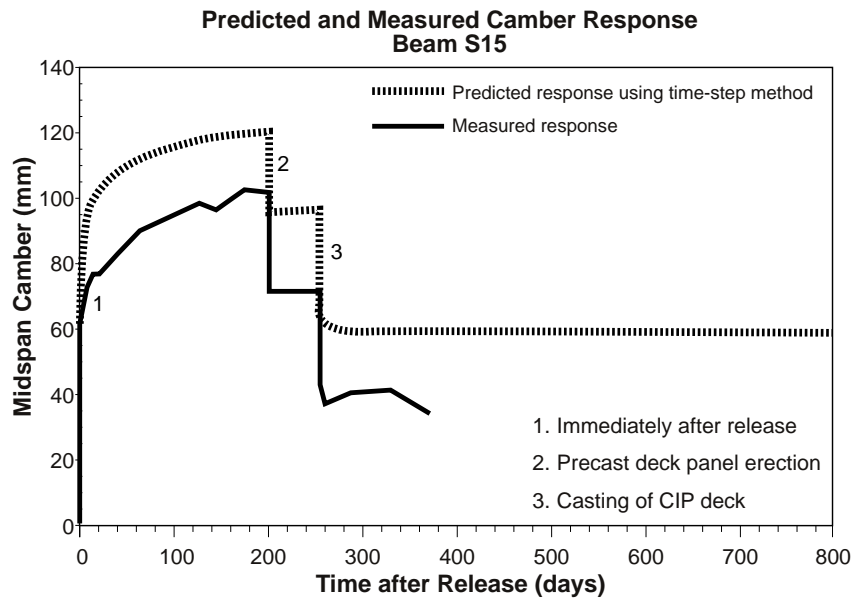


Figure 6.41 Predicted camber for Beam S15 using the time-step method

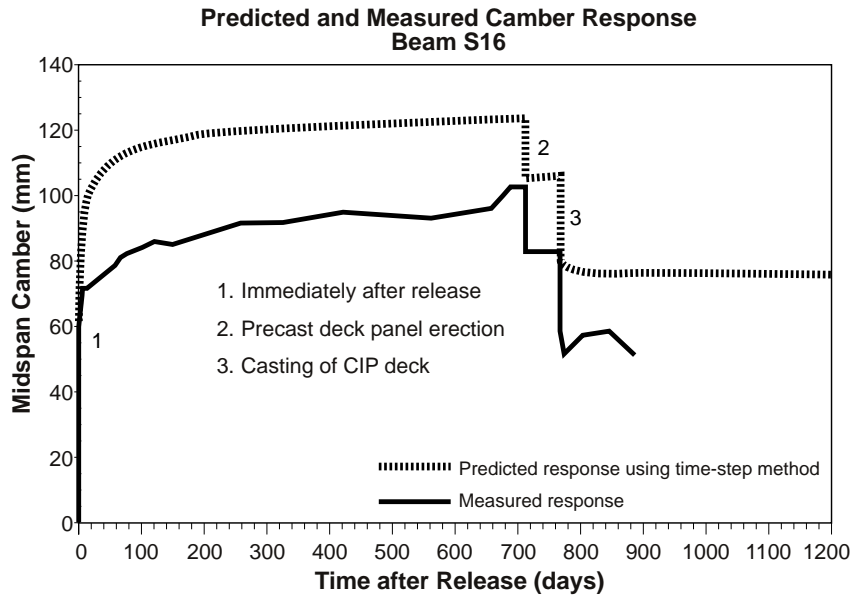


Figure 6.42 Predicted camber for Beam S16 using the time-step method

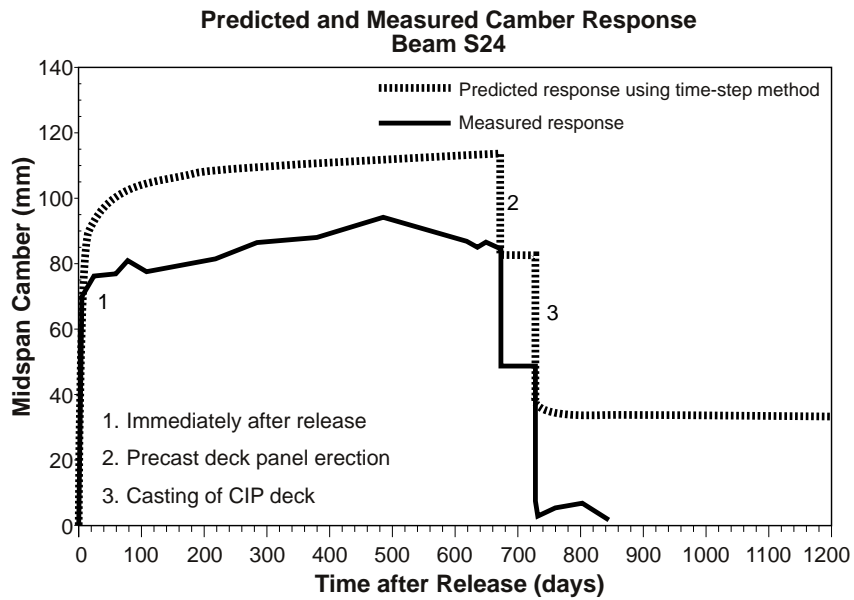


Figure 6.43 Predicted camber for Beam S24 using the time-step method

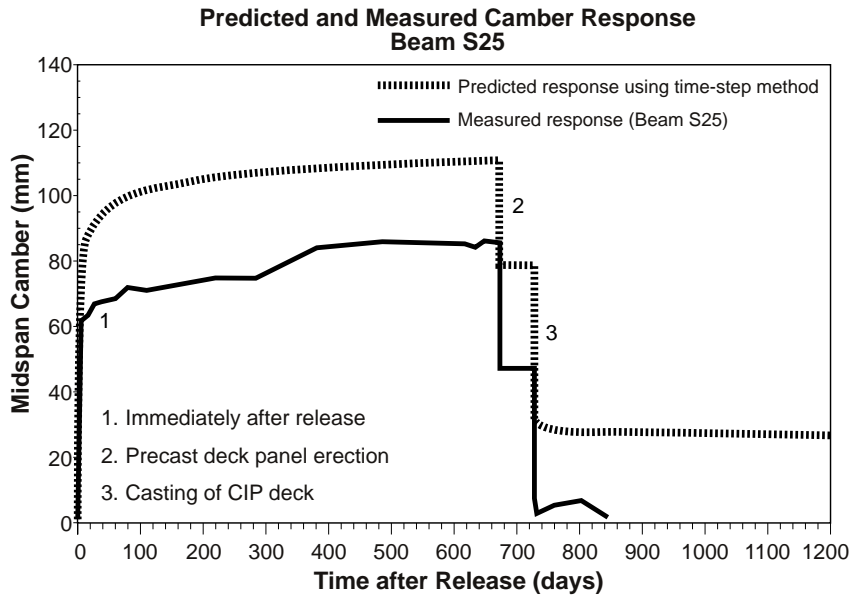


Figure 6.44 Predicted camber for Beam S25 using the time-step method

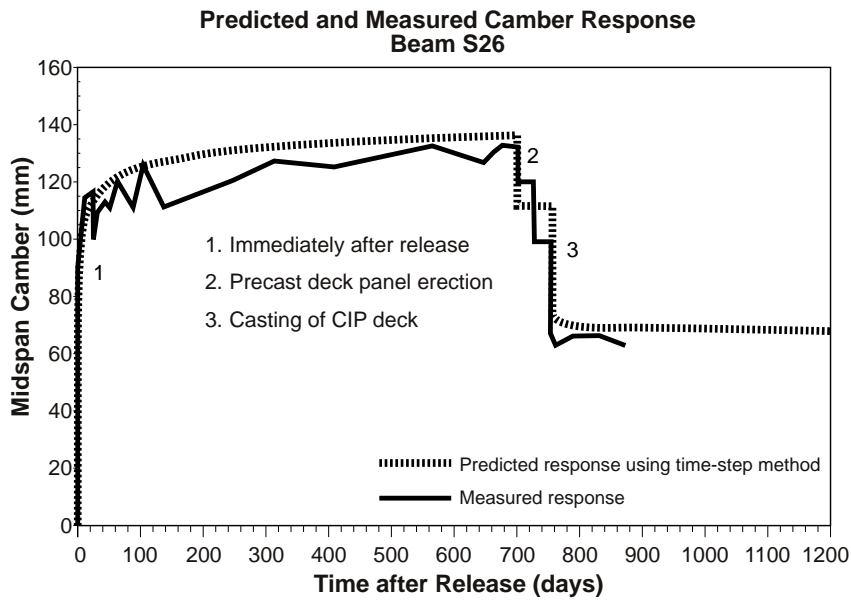


Figure 6.45 Predicted camber for Beam S26 using the time-step method

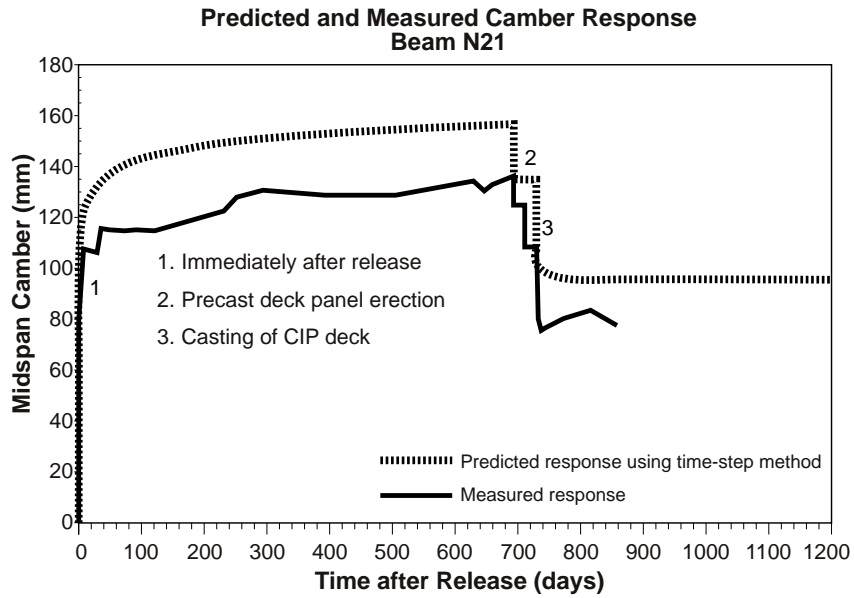


Figure 6.46 Predicted camber for Beam N21 using the time-step method

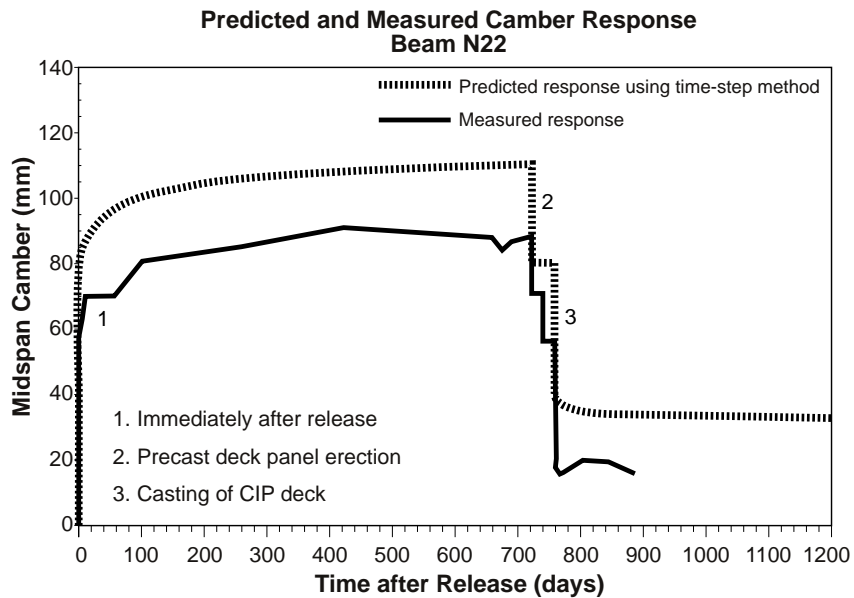


Figure 6.47 Predicted camber for Beam N22 using the time-step method

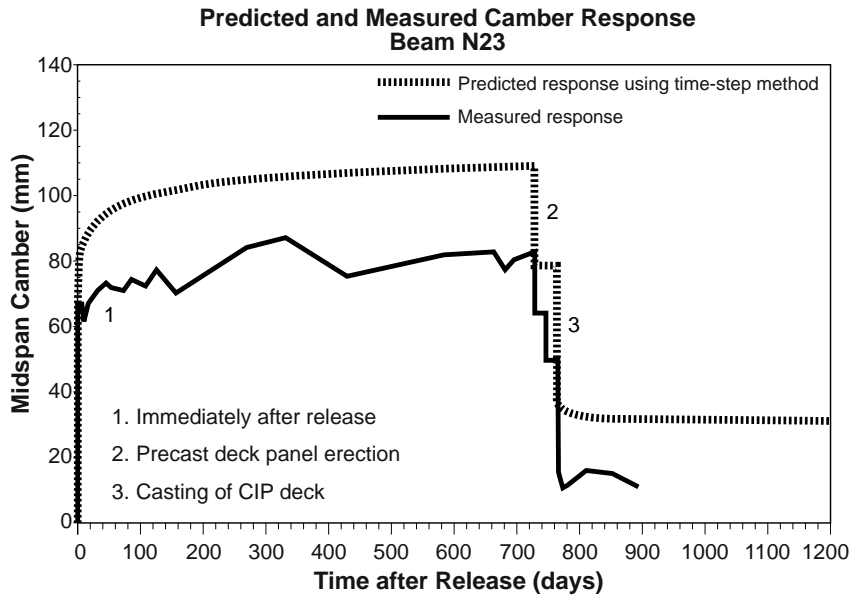


Figure 6.48 Predicted camber for Beam N23 using the time-step method

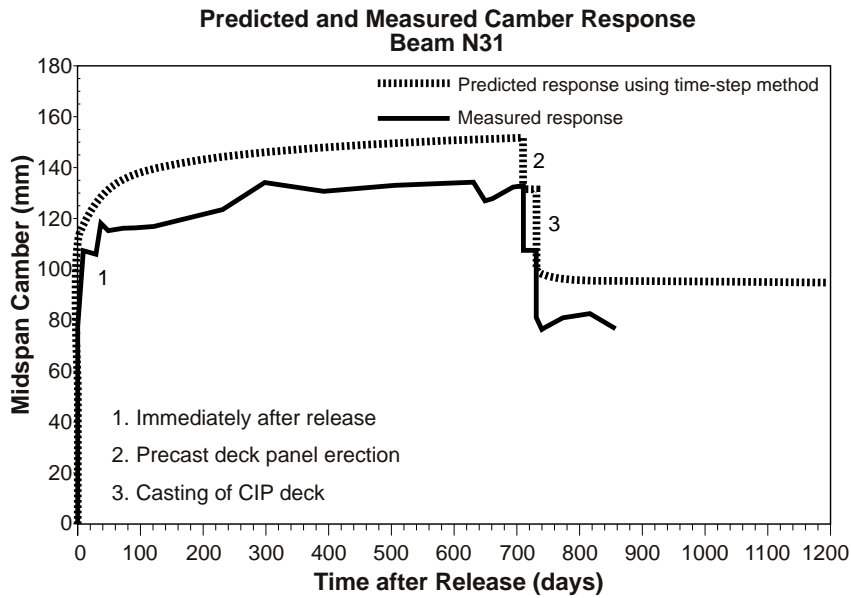


Figure 6.49 Predicted camber for Beam N31 using the time-step method

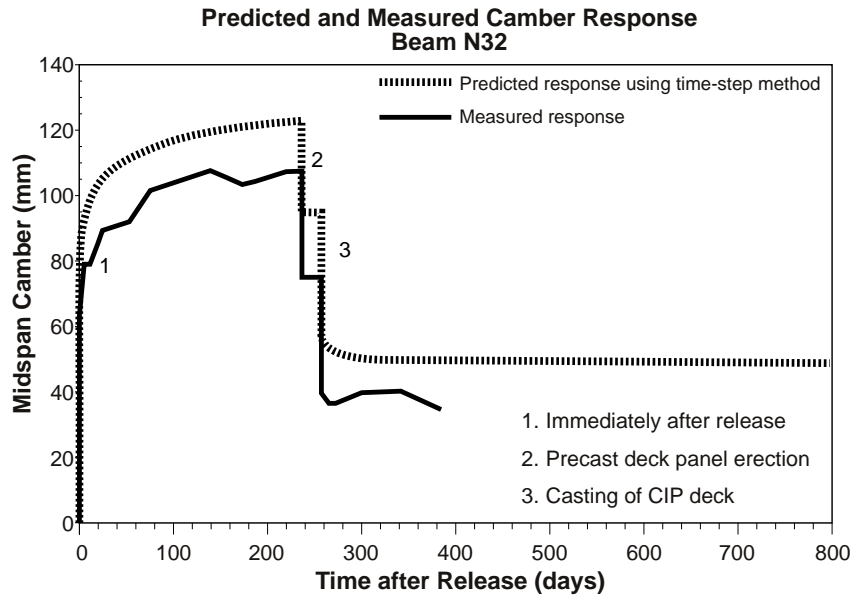


Figure 6.50 Predicted camber for Beam N32 using the time-step method

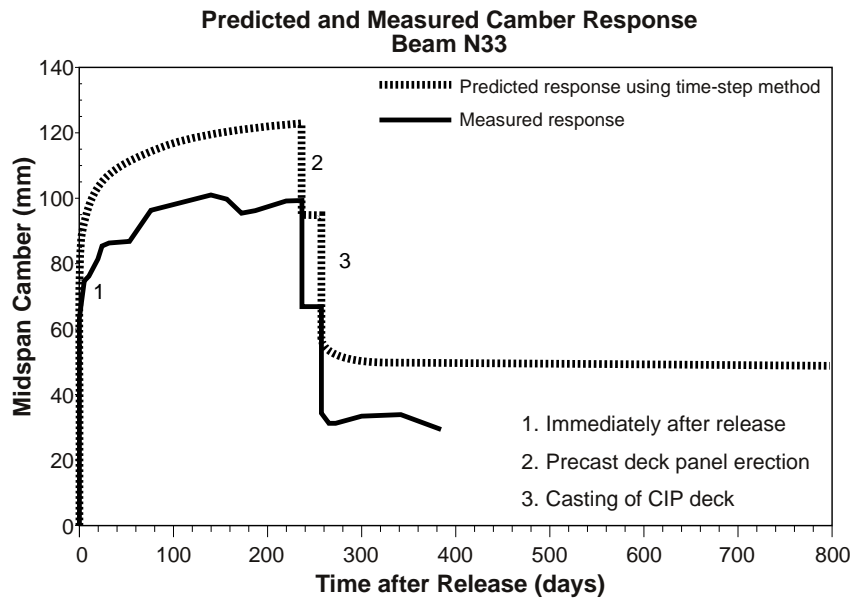


Figure 6.51 Predicted camber for Beam N33 using the time-step method

The average predicted and measured growths of midspan camber from release to erection were 51.7 mm and 43.3 mm, respectively. Low measured camber growth was due to a combination of several possible differences between actual conditions and the analytical model. Some of these possible differences include a higher modulus of elasticity at release, a lower ultimate creep coefficient than what used in the analytical model, and a lower prestressing force transferred to the beams.

Another possible cause for low measured camber from release to erection may have been the effect of early age thermal gradients that developed during hydration. Temperature measurements for Beams S16 and N32 during casting showed the formation of temperature gradient as large as 9 °C between the top and bottom of the beam. After the side forms are removed, the beams will eventually cool to a uniform temperature, causing the top to shorten more than the bottom. The result of this uneven cooling, where the top cools more than the bottom, would be a negative curvature. This would cause a component of deflection. This component of deflection would be present in every camber measurement from release through long-term because the measurements were only corrected for thermal gradients referenced to a uniform gradient, as discussed in Sec. 5.3.1. The proper adjustment may be to use the temperature gradient at some time before the forms are stripped as the reference gradient.

Unfortunately, very few beams were monitored during casting, so corrections based on an early-age temperature gradient were not attempted. The magnitude of this correction based on the gradients observed in Beams S16 and N32 could have been as large as 12 mm, depending on the length of the beam. Offsets of this magnitude were present between nearly all of the predicted and measured camber responses shown in Figures 6.40 to 6.51.

The predicted cambers after placement of the CIP deck varied from 33.2 mm (Beam S25) to 104.3 mm (Beam N21). The interior beams, which had the longest spans, had the lowest cambers at this point. The exterior beams had the highest cambers because the overhangs were not cast with the deck. The measured cambers after placement of the CIP deck varied from 7.1 mm (Beam S25) to 81.0 mm (Beam N31). The average difference between the measured and predicted cambers at this point was 22.1 mm. This was very close to the average difference before erection because the measured and predicted elastic deflections were so close, as shown in Sec. 6.4.3.2.

The predicted long-term cambers varied from 26.1 mm (Beam S25) to 96.1 mm (Beam N21). These values corresponded to the time of the last measured camber for each beam. The predicted long-term camber, shown in Figures 6.40 to 6.51, did not change significantly after the beam section became composite. This was because of the increased stiffness of the section and the small amount of creep occurring at those late ages. The observed decrease in camber was mainly due to differential shrinkage between the CIP deck and the beam. The measured long-term cambers varied from 2.3 mm (Beam S24) to 77.7 mm (Beam N21). The average difference between the measured and predicted long-term camber was 19.8 mm. The maximum difference was 29.9 mm (Beam S24) and the minimum difference was 5.2 mm (Beam S26).

The differences between the predicted and measured long-term cambers for all of the beams are plotted in Figure 6.52. A positive difference indicates that the predicted camber

overestimated the measured camber. This figure shows that all of the beams had long-term camber that was lower than the predicted value. The long-term camber differences were very similar to the differences observed at erection. Based on all of the plots shown in Figure 6.52, measured camber was consistently low from release through long-term for all of the beams. Furthermore, the differences remained fairly close for some of the beams from release to erection and then they remained very close for all of the beams through long-term measurements.

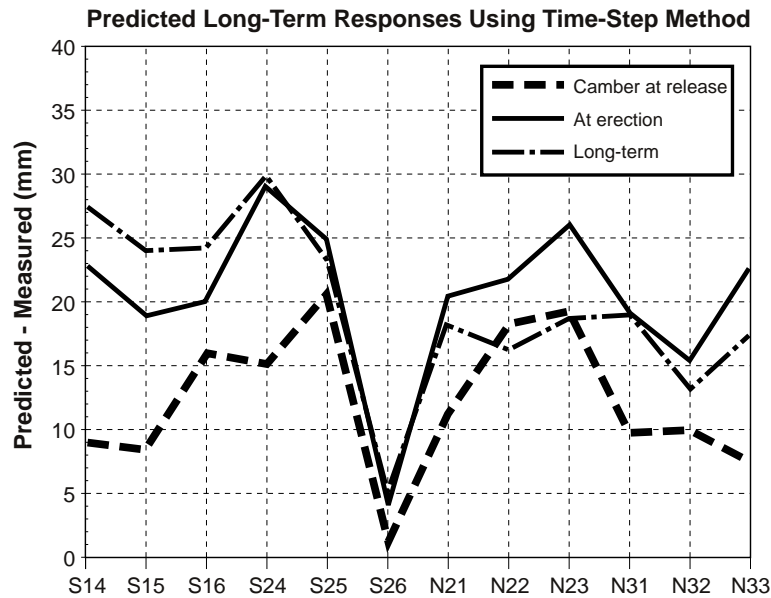


Figure 6.52 Summary of differences between measured and predicted long-term camber and deflection based on the time-step method

6.5 PROPOSED MULTIPLIERS FOR ESTIMATING TIME-DEPENDENT CAMBER AND DEFLECTION

6.5.1 Development of Proposed Multipliers

In this section, a set of camber and deflection multipliers are developed for predicting the time-dependent behavior of prestressed high performance concrete U-beams. The ideas used to develop these multipliers are comparable to those used by Martin (28). The analytical approach is based on the time-step method presented in Sec. 6.4, which was similar to the analytical technique presented by Branson and Kripanarayanan (43).

Time-dependent growth of camber is basically a function of creep and loss of prestress. Since creep is a function of several parameters, including volume-to-surface ratio and relative humidity, accurate prediction of long-term camber and deflection is extremely difficult. The material models for creep, shrinkage, compressive strength, and modulus of

elasticity that were used in the time-step method predicted the time-dependent behavior of the U-beams with acceptable accuracy. The general shape of the predicted camber responses coincided with the measured camber responses, although the measured responses for most of the beams were consistently low from release to several months after completion of the composite decks.

At release, a prestressed concrete beam experiences an upward deflection, or camber, due to the prestressing force, and a downward deflection due to the beam weight. The addition of these two deflections represents the initial camber at release. This relationship is shown in Eq. 6.21.

$$\Delta_i = (\Delta_{ps})_i - (\Delta_{beam})_i \quad (6.21)$$

The initial components of upward and downward deflection at release are elastic responses that happen over a short period of time. As time progresses, these components of deflection increase in magnitude due to creep of the concrete. The camber of a beam at any time after release, without the addition of superimposed loads, is shown in Eq. 6.22.

$$\Delta_t = \lambda_{pt}(\Delta_{ps})_i - \lambda_{bt}(\Delta_{beam})_i \quad (6.22)$$

The coefficients λ_{pt} and λ_{bt} are multipliers of the elastic components of deflection. Their values are greater than unity to account for both the elastic and time-dependent parts of the deflection. As shown in Eq. 6.23, the magnitude of each multiplier is dependent upon several factors (β_j). The factors account for the influences that time-dependent properties and changes in geometric properties have on the increase of deflection components.

$$\lambda_j = 1.0 + \sum \beta_j \quad (6.23)$$

The factor that represents the time function used to model the increase in concrete creep and prestress loss is given by Eq. 6.24. The factor that accounts for the increased moment of inertia when the beam section becomes composite is given by Eq. 6.25. For the U-beams in this study, β_1 was taken as 0.35.

$$\beta_T = \left(\frac{t^{0.5}}{6 + t^{0.5}} \right) \quad (6.24)$$

$$\beta_1 = \frac{I_{nc}}{I_c} \quad (6.25)$$

The time-dependent deflection due to the weight of the beam is only a function of creep. The value for the ultimate creep coefficient, β_{cu} , was taken as 1.40 for all of the U-

beams except Beam S26. For that beam, β_{cu} was taken as 1.05 because transfer occurred 7 days after casting. The deflection due to the weight of the beam at any time after release is shown in Eq. 6.26. The multiplier for the beam weight deflection, λ_{bt} , is shown in Eq. 6.27. If the beam section were to remain non-composite through the end of its service life, λ_{bt} would be equal to one plus the ultimate creep coefficient.

$$(\Delta_{\text{beam}})_t = (\Delta_{\text{beam}})_i (1.0 + \beta_T \beta_{cu}) \quad (6.26)$$

$$\lambda_{bt} = 1.0 + \beta_T \beta_{cu} \quad (6.27)$$

Once the beam section becomes composite, the moment of inertia increases. The factor to account for the increase in moment of inertia is shown in Eq. 6.25. The time-dependent increase in the beam weight deflection that occurs after the beam becomes composite will be reduced by this increase in stiffness. To determine the beam weight multiplier after the beam section becomes composite, the fraction of creep that has occurred up to that point needs to be calculated. The multiplier for beam weight deflection before the beam becomes composite is given in Eq. 6.28.

$$\lambda_{bnc} = 1.0 + (\beta_T)_{nc} \beta_{cu} \quad (6.28)$$

The multiplier for beam weight deflection at any time after the beam section becomes composite is shown in Eq. 6.29. The time-dependent fraction of creep that has occurred before the section becomes composite is represented by λ_{bnc} . The time-dependent creep that occurs after the composite section is represented by the second term in Eq. 6.29.

$$\lambda_{bct} = \lambda_{bnc} + [\beta_T - (\beta_T)_{nc}] \beta_1 \beta_{cu} \quad (6.29)$$

The time-dependent increase in camber due to the prestressing force is a function of creep and prestress losses after release. Since creep is a large contributor to prestress losses after release, the time factor shown in Eq. 6.24 was used to represent the time-dependent loss of prestress. The value for the total loss of prestress after release, β_{pt} , was taken as 12 percent (expressed as a decimal) for all of the U-beams.

The camber due to prestressing any time after release is shown in Eq. 6.30. The multiplier for the camber due to prestress, λ_{pt} , is shown in Eq. 6.31. λ_{pt} will always be less than λ_{bt} because the initial component of camber, $(\Delta_{ps})_i$, is reduced by the total loss of prestress $(1 - \beta_{pt})$. $(\Delta_{ps})_i$ is also directly reduced by the loss of prestress over time, which is represented by the term $(\beta_T \beta_{pt} \beta_E)$. β_E , given in Eq. 6.32, is a factor that accounts for the increase in modulus of elasticity with time. The value of β_E was taken as 0.90 for the HPC U-beams.

$$\left(\Delta_{ps}\right)_t = \left(\Delta_{ps}\right)_i \left[1.0 + \beta_T \beta_{cu} (1.0 - \beta_T \beta_{pl}) - \beta_T \beta_{pl} \beta_E \right] \quad (6.30)$$

$$\lambda_{pt} = 1.0 + \beta_T \beta_{cu} (1.0 - \beta_T \beta_{pl}) - \beta_T \beta_{pl} \beta_E \quad (6.31)$$

$$\beta_E = \frac{E_{ci}}{(E_c)_{56d}} \quad (6.32)$$

The influence of the composite moment of inertia on the time-dependent camber due to the prestressing force is similar to that shown for the deflection due to the beam weight. The factor to account for the increase in moment of inertia (β_I) is shown in Eq. 6.25. The time-dependent increase in the camber due to the prestressing force that occurs after the beam becomes composite will be reduced by the increase in stiffness. To determine the multiplier after the beam section becomes composite, the fraction of creep that has occurred up to that point needs to be calculated. The multiplier for prestress camber before the beam becomes composite is shown in Eq. 6.33.

$$\lambda_{pnc} = 1.0 + (\beta_T)_{nc} \left[\beta_{cu} \left[1.0 - (\beta_T)_{nc} \beta_{pl} \right] - \beta_{pl} \beta_E \right] \quad (6.33)$$

The multiplier for camber due to the prestressing force at any time after the beam section becomes composite is shown in Eq. 6.34. The fraction of creep that has occurred before the section becomes composite is represented by λ_{pnc} . The time-dependent creep that occurs after the composite section is represented by the second term in Eq. 6.34.

$$\lambda_{pct} = \lambda_{pnc} + \left[\beta_T - (\beta_T)_{nc} \right] \beta_I \left[\beta_{cu} (1.0 - \beta_T \beta_{pl}) - \beta_{pl} \beta_E \right] \quad (6.34)$$

Multipliers for the time-dependent deflections due to superimposed deck panels and cast-in-place deck loads are developed similarly to the beam weight multiplier. Deflections due to superimposed loads are only a function of creep. The amount of additional time-dependent deflection due to creep will be determined by the age of loading. The deflection due to a superimposed dead load at any time after its placement on the beam is given by Eq. 6.35. This equation was developed using the time factor (β_T) given in Eq. 6.24, the moment of inertia factor (β_I) given in Eq. 6.25, and the ultimate creep coefficient (β_{cu}). The fraction of creep that occurs before the beam section becomes composite is represented by $(\beta_T)_{nc}$. This equation assumes that no time occurs between placement of the deck panels and casting of the deck slab. The dead load multiplier at any time after placement is given by Eq. 6.36.

$$\left(\Delta_{dl}\right)_t = \left(\Delta_{dl}\right)_i \left[1.0 + \left(\beta_T - (\beta_T)_{nc} \right) \beta_{cu} \beta_I \right] \quad (6.35)$$

$$\lambda_{dlt} = \left[1.0 + (\beta_T - (\beta_T)_{nc}) \beta_{cu} \beta_I \right] \quad (6.36)$$

The beam camber at any time before placement of superimposed loads is given by Eq. 6.22. The beam camber or deflection at any time after the beam becomes composite is shown in Eq. 6.37. This equation includes all components of upward and downward deflection.

$$\Delta_t = \lambda_{pct}(\Delta_{ps})_i - \lambda_{bct}(\Delta_{beam})_i - \lambda_{dlt}(\Delta_{dl})_i \quad (6.37)$$

For superimposed dead loads placed at any time after the beam section becomes composite, such as railings and deck overlays, Eqs. 6.35 and 6.36 would be modified to reflect the increased fraction of creep that has occurred up to placement of the loads. The term $(\beta_T)_{nc}$ would be calculated at the time of placement using Eq. 6.24.

An alternate set of camber and deflection multipliers could be developed based on a different time factor (β_T) and ultimate creep coefficient (β_{cu}). As shown in Sec. 5.2.3, two curves were fit to the creep data that had very close correlation factors. However, the second curve, which was not used in the time-step method, had an ultimate creep coefficient that was quite different from the first curve. The second curve will be used in Sec. 6.5.2 to develop multipliers to compare with the measured responses. This will illustrate the sensitivity of camber and deflection to creep. The ultimate creep coefficient for this curve, (β'_{cu}), adjusted for the U-beams, was taken as 1.10. The time factor for this curve, (β'_T), is given in Eq. 6.38.

$$\beta'_T = \left(\frac{t^{0.6}}{5 + t^{0.6}} \right) \quad (6.38)$$

6.5.2 Prediction of Camber and Deflection using Proposed Multipliers

In this section, multipliers for determining camber (or deflection) at release, at erection, and at the end of service life of the bridge are developed using the equations presented in Sec. 6.5.1. Multipliers were developed using the two creep functions, shown in Eqs. 6.24 and 6.38, and their corresponding ultimate creep coefficients. Both of these curves were fit to the creep specimen data using linear regression analysis and had very similar correlation factors. However, their ultimate creep coefficients were quite different. Using the proposed multipliers, predicted responses were calculated and compared to some of the measured responses. In addition, sensitivity to variations in the modulus of elasticity and prestressing force transferred to the beams are investigated using the proposed multipliers.

The camber and deflection multipliers, calculated based on the equations and assumptions given in Sec. 6.5.1, are summarized in Table 6.13. Multipliers were developed based on the actual times between release and erection for the instrumented beams. It was assumed that the deck panels were simultaneously placed with the cast-in-place deck. Since

the times after release were so large, this assumption introduced minimal error into the values of the multipliers.

Beams were grouped together based on their casting date (1994 or 1996) and assigned a set of multipliers. The calculated multipliers did not vary among beams in the same group because of the ages of the beams. Beam S26 had different multipliers because transfer occurred at 7 days.

There was very little difference between the erection multipliers and final multipliers applied to the elastic components of camber and deflection at release because of the actual construction schedule of the beams. A large percentage of the total creep occurred before the deck loads were placed on the beams. As a result, the multipliers for the superimposed deck loads were very small. The multipliers for the beams cast in 1996 were smaller than those for the beams cast in 1994 because they were in storage approximately 500 days less. The shorter time in storage meant that a larger percentage of the total creep occurred while the beams were composite.

Table 6.13 Proposed camber and deflection multipliers based on actual construction schedule and both creep functions

	Multipliers with creep based on Eq. 6.24 ($\beta_{cu} = 1.40$) ^{1,2}			Multipliers with creep based on Eq. 6.38 ($\beta_{cu} = 1.10$) ^{1,2}		
	S14, S15 N32, N33	S24, S25 N21-N23 N31, S16	S26 ³	S14, S15 N32, N33	S24, S25 N21-N23 N31, S16	S26 ³
At erection:						
Initial camber due to prestress	1.85	1.95	1.69	1.75	1.80	1.57
Initial deflection due to beam weight	2.02	2.15	1.86	1.93	2.01	1.75
Final:						
Initial camber due to prestress	1.96	2.02	1.74	1.80	1.83	1.59
Initial deflection due to beam weight	2.15	2.24	1.93	1.99	2.04	1.77
Deflection due to deck loads	1.13	1.09	1.07	1.06	1.03	1.02
Notes:	<ol style="list-style-type: none"> 1. Number of days between release and casting of the deck slab were used to calculate the multipliers. 2. The multipliers were calculated by assuming that there was no time between erection, placement of the deck panels, and placement of the CIP deck. 3. Ultimate creep coefficients for Beam S26 using Eqs. 6.24 and 6.38 were 1.05 and .80, respectively, because transfer occurred 7 days after casting. 					

The proposed multipliers shown in Table 6.13 were used to investigate the sensitivity of long-term camber prediction. Both sets of multipliers were used to determine the

influence of using different creep functions, which are given by Eqs. 6.24 and 6.38. For each set of multipliers, four different prediction cases were investigated to determine the influence of modulus of elasticity and initial prestressing force transferred to the beams on long-term camber.

The initial case used the camber due to prestress and deflection due to the beam weight at release that were calculated using the PCI Design Handbook equations, measured beam properties, transformed section properties, and the proposed modulus of elasticity equation. This procedure is described in Sec. 6.3.2.1. The values for elastic camber due to the prestressing force, deflection due to the beam weight, and deflections due to the deck panels and cast-in-place deck can be found in Table 6.7. The deck load deflections were the same for all of the prediction cases.

The remaining three cases were based on the PCI release calculations except for variation of some of the properties. The following changes were assumed in these other predictions:

1. Modulus of elasticity increased by 5 percent
2. Initial prestressing force transferred to the beam decreased to $0.86P_i$
3. Modulus of elasticity increased by 5 percent and initial prestressing force transferred to the beam decreased to $0.86P_i$

The 5 percent variation in the modulus of elasticity at release was a valid assumption because of the difficulty in determining the properties of concrete. The use of $0.86P_i$ for the transferred prestressing force was based on the time-step analysis. The average prestressing force at release based on that analysis was $0.88P_i$. This value was reduced slightly to include the possibility of some additional loss of prestress before release.

The results of the predicted midspan camber responses based on the four cases and two sets of multipliers are shown in Figures 6.53 to 6.64. The beams shown in these figures were representative of the instrumented beam. The results for each beam using each set of multipliers are shown in consecutive figures for comparison purposes.

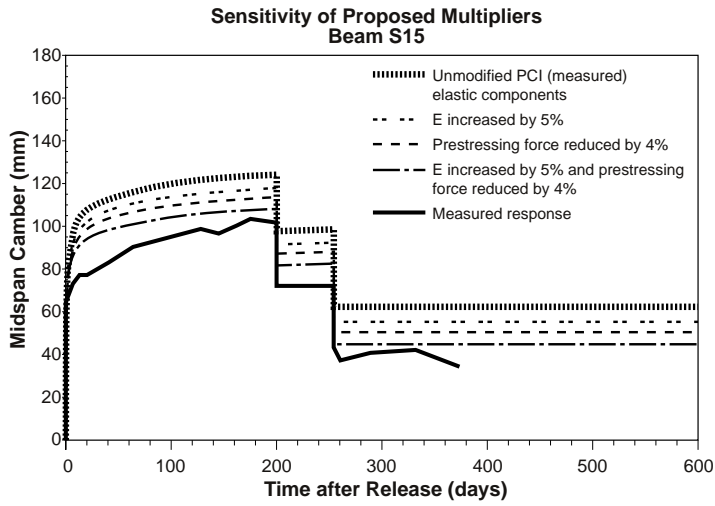


Figure 6.53 Sensitivity of camber prediction for Beam S15 using the proposed multipliers with creep based on Eq. 6.24

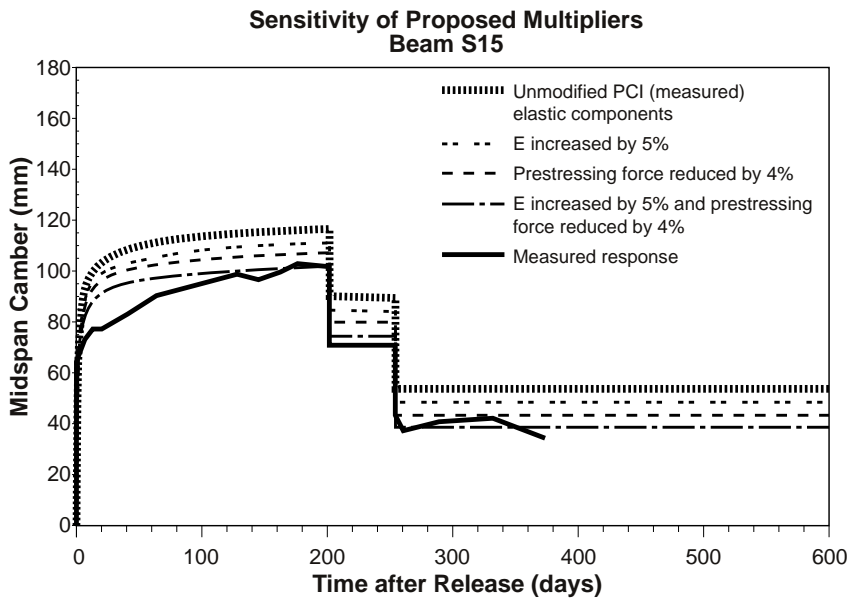


Figure 6.54 Sensitivity of camber prediction for Beam S15 using the proposed multipliers with creep based on Eq. 6.38

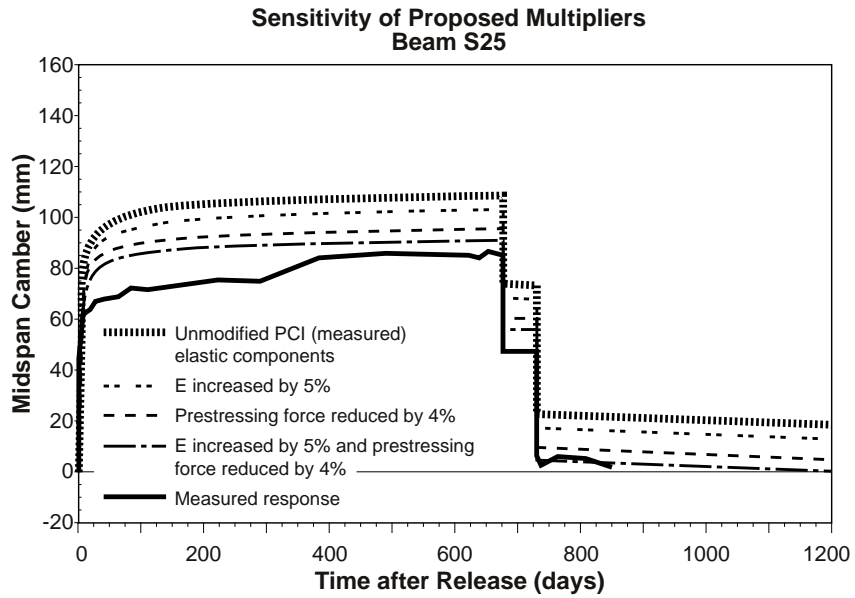


Figure 6.55 Sensitivity of camber prediction for Beam S25 using the proposed multipliers with creep based on Eq. 6.24

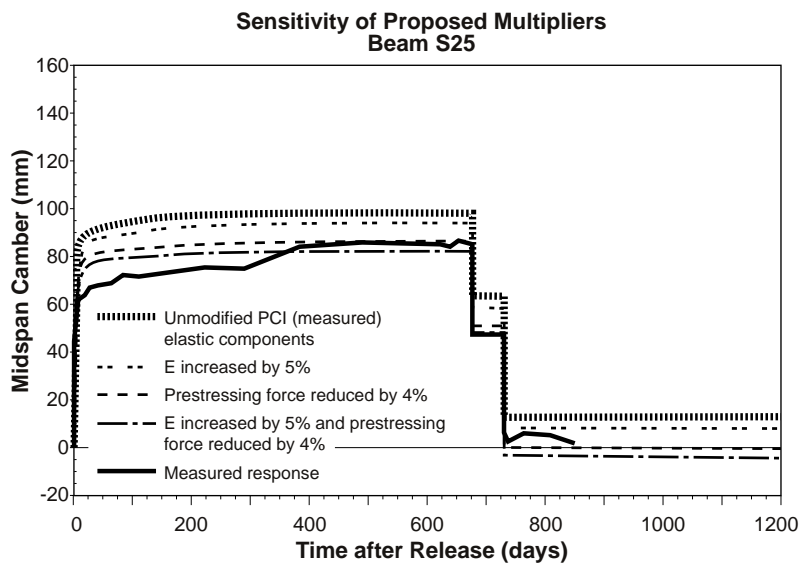


Figure 6.56 Sensitivity of camber prediction for Beam S25 using the proposed multipliers with creep based on Eq. 6.38

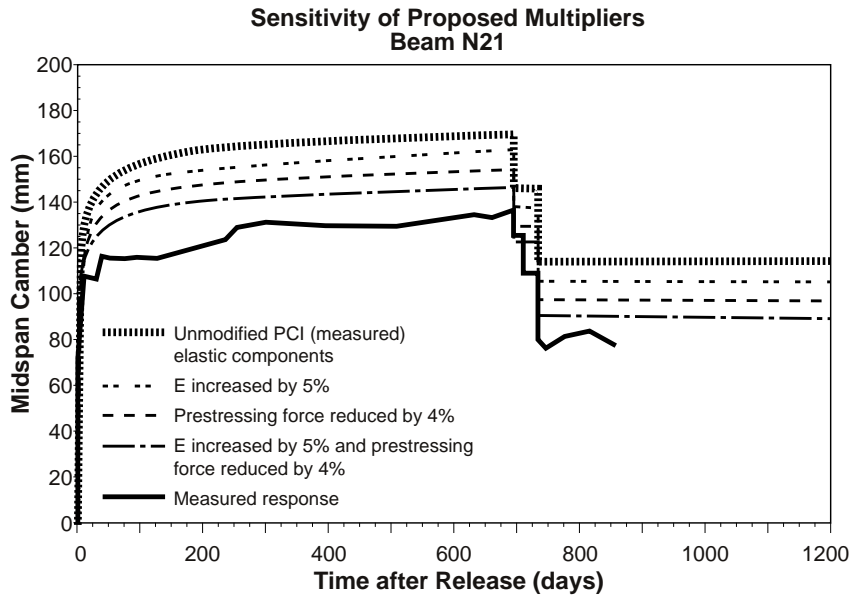


Figure 6.57 Sensitivity of camber prediction for Beam N21 using the proposed multipliers with creep based on Eq. 6.24

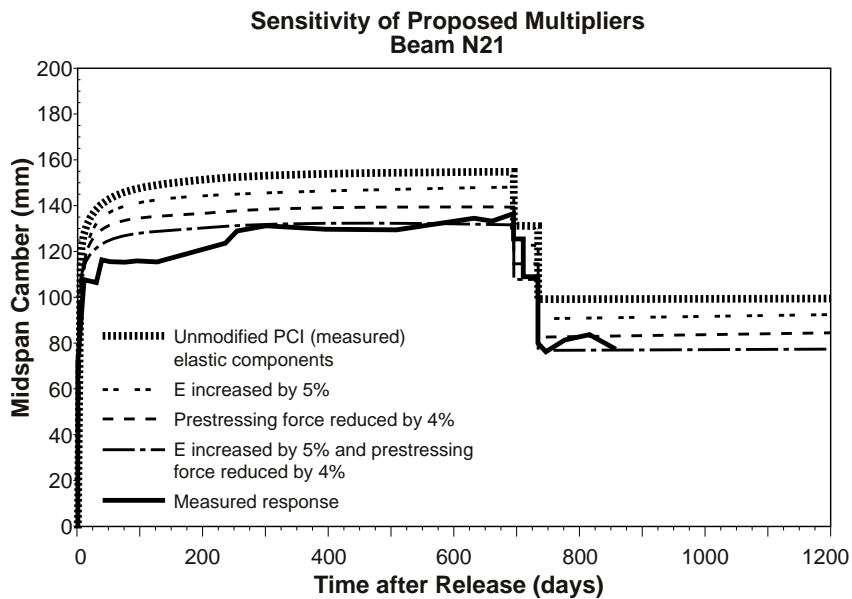


Figure 6.58 Sensitivity of camber prediction for Beam N21 using the proposed multipliers with creep based on Eq. 6.38

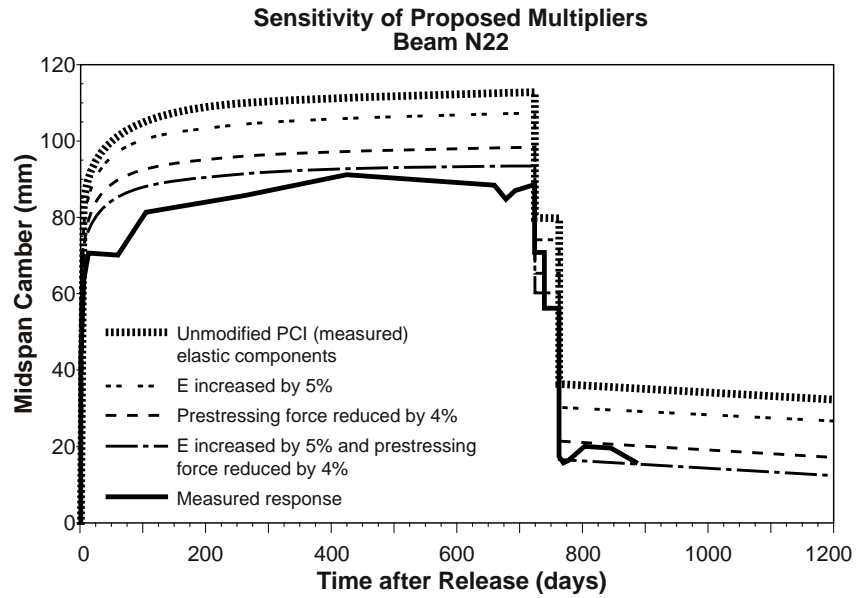


Figure 6.59 Sensitivity of camber prediction for Beam N22 using the proposed multipliers with creep based on Eq. 6.24

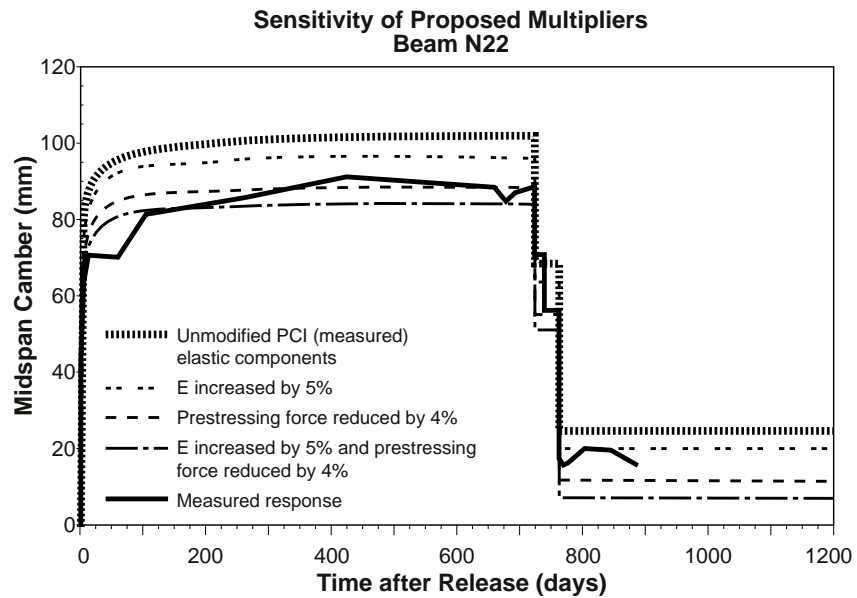


Figure 6.60 Sensitivity of camber prediction for Beam N22 using the proposed multipliers with creep based on Eq. 6.38

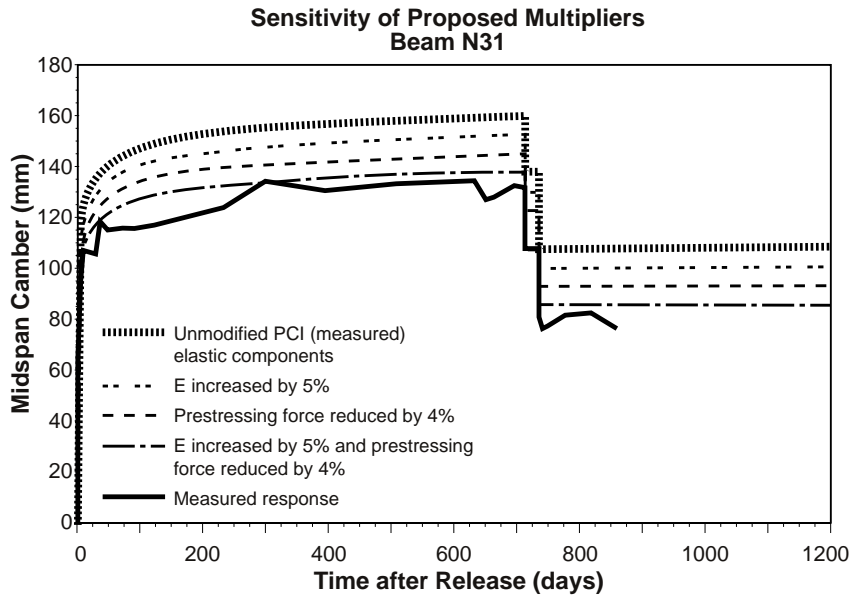


Figure 6.61 Sensitivity of camber prediction for Beam N31 using the proposed multipliers with creep based on Eq. 6.24

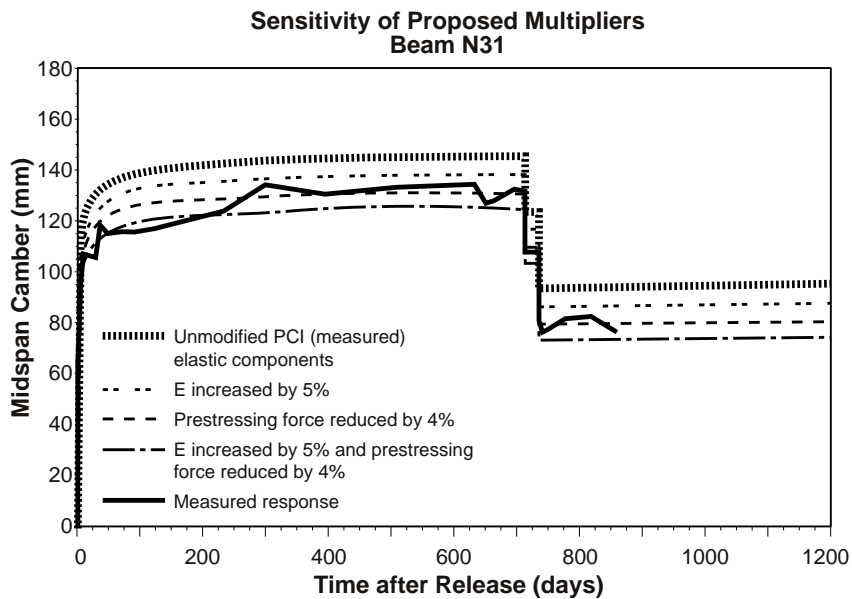


Figure 6.62 Sensitivity of camber prediction for Beam N31 using the proposed multipliers with creep based on Eq. 6.38

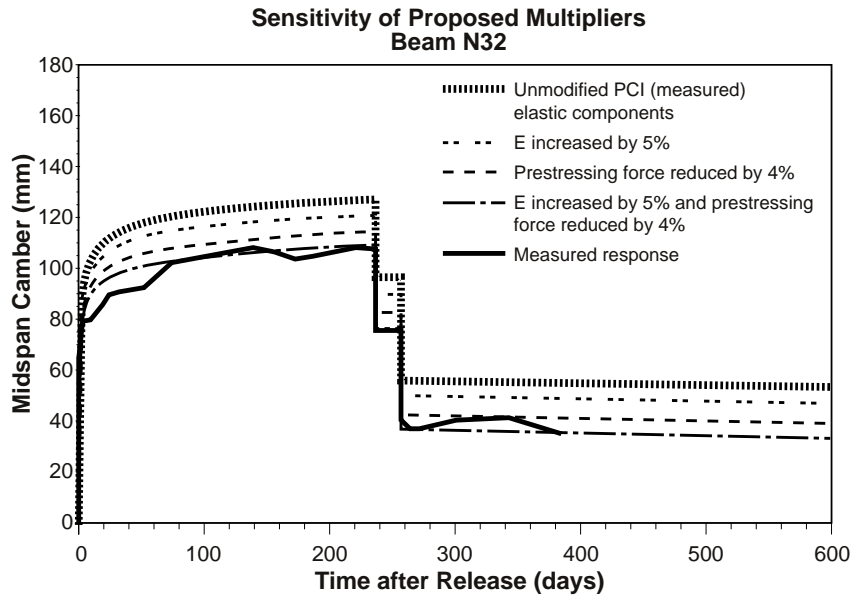


Figure 6.63 Sensitivity of camber prediction for Beam N32 using the proposed multipliers with creep based on Eq. 6.24

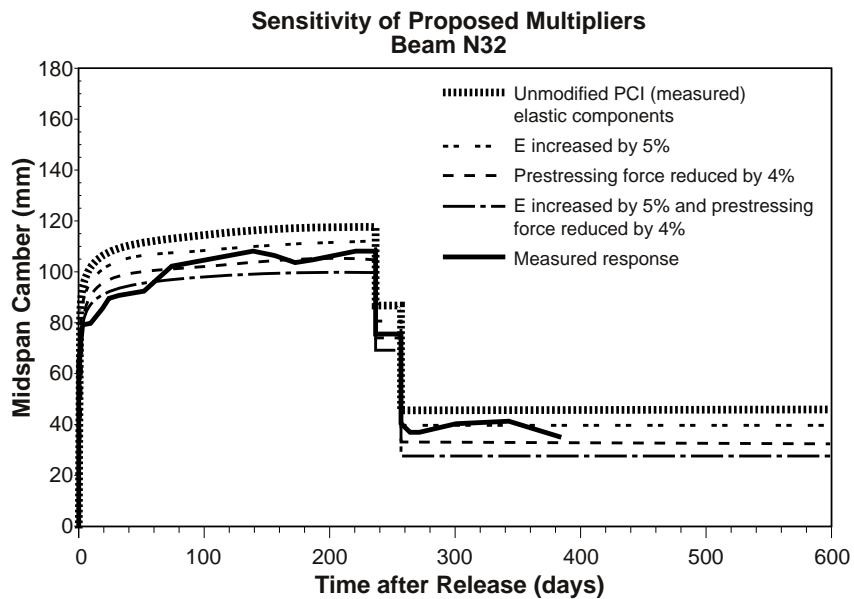


Figure 6.64 Sensitivity of camber prediction for Beam N32 using the proposed multipliers with creep based on Eq. 6.38

The differences between the predicted and measured cambers at release, erection, and long-term for all of the prediction cases are summarized in Tables 6.14 and 6.15. The maximum, minimum, and average of the differences between the predicted and measured camber for all of the beams are shown to provide a general sense of how each prediction case affects the accuracy of the proposed camber and deflection multipliers.

The average predicted camber at release was higher than the average measured camber at release in all four cases. The average difference at release ranged from 15.3 mm for the standard PCI prediction to 5.0 mm for the case with an increased modulus of elasticity and reduced prestressing force. These values applied to each set of multipliers.

The average predicted camber at erection and long-term using the first set of multipliers (based on Eq. 6.24) were higher than the average measured camber under all four prediction cases. For the first two cases (PCI prediction and modulus of elasticity increased), the average difference between the predicted and measured camber increased by 9.6 and 7.1 mm, respectively, from release to erection. The third case (reduced prestressing force) showed more consistency between release and erection because changes in the prestressing force tended to have a greater influence on release camber than changes in the elastic modulus. The fourth case, which combined the effects of an increased modulus of elasticity and a reduced prestressing force, showed consistent agreement with the measured cambers from release through long-term. The average differences at release, erection, and long-term were 5.0, 6.2, and 3.8 mm, respectively. These results show that some of the measured cambers at release may be low due to differences in E_{ci} and P_o and that based upon the lower release cambers, the measured cambers at erection and long-term can be accurately predicted with the proposed multipliers.

Table 6.14 Summary of the differences between measured and predicted midspan camber using proposed multipliers (based on Eq. 6.24 for creep)

Prediction Case		Predicted - Measured (mm)		
		Release	Erection	Long-Term
PCI (meas.)	Max.	21.8	34.7	36.6
	Min.	10.5	16.2	13.0
	Avg.	15.3	24.9	23.2
Increase E_{ci} by 5%	Max.	18.6	26.6	28.2
	Min.	6.8	9.2	7.9
	Avg.	11.6	18.7	16.9
Decrease prestressing force to $0.86P_i$	Max.	14.5	18.6	20.8
	Min.	3.3	2.3	-1.0
	Avg.	8.3	11.8	9.6
Increase E_{ci} by 5% and decrease prestressing force to $0.86P_i$	Max.	11.6	12.6	14.9
	Min.	-0.9	-4.0	-5.5
	Avg.	5.0	6.2	3.8

Table 6.15 Summary of the differences between measured and predicted midspan camber using proposed multipliers (based on Eq. 6.38 for creep)

Prediction Case		Predicted - Measured (mm)		
		Release	Erection	Long-Term
PCI (meas.)	Max.	21.8	20.5	23.9
	Min.	10.5	3.8	6.0
	Avg.	15.3	14.1	14.6
Increase E_{ci} by 5%	Max.	18.6	14.8	18.1
	Min.	6.8	-2.7	-0.5
	Avg.	11.6	8.4	8.8
Decrease prestressing force to $0.86P_i$	Max.	14.5	10.9	14.1
	Min.	3.3	-9.1	-7.0
	Avg.	8.3	1.9	2.1
Increase E_{ci} by 5% and decrease prestressing force to $0.86P_i$	Max.	11.6	5.7	8.8
	Min.	-0.9	-14.9	-12.9
	Avg.	5.0	-3.2	-3.0

The average predicted cambers at erection and long-term using the second set of multipliers (based on Eq. 6.38) were higher than the average measured camber for all of the prediction cases except the last one. For the unmodified PCI prediction, the average differences between the predicted and measured camber at release and erection were nearly identical. The average differences at release, erection, and long-term were 15.3, 14.1, and 14.6 mm, respectively. The other three prediction cases showed a reduction in the average differences from release to erection. The average differences for the fourth prediction case showed a change from 5.0 mm at release to -3.0 mm at erection.

Both sets of multipliers showed consistency between the differences at erection and at release. Errors in the prediction models between release and erection were not magnified because the composite U-beam section was extremely stiff and because the deck loads were placed at a late age. In addition, a majority of the creep for the high performance concrete U-beams occurred within the first 100 days. If future construction schedules using the HPC U-beams are on the order of 50 to 75 days between release and placement of the deck loads, the beams will probably not show significant additional deflection due to creep.

Based on the results of the presented in Figures 6.53 to 6.64 and in Tables 6.14 and 6.15, the prediction of long-term camber and deflection is sensitive to variations in the release camber as well as the variations in the assumed creep function used to model the beams. By altering the modulus of elasticity and the initial prestressing force slightly, the proposed multipliers (based on Eq. 6.24) showed very accurate prediction of the measured midspan cambers from release to erection.

The second set of multipliers (based on Eq. 6.38) showed less accurate prediction of camber growth from release to erection. If the second set of multipliers were assumed to be a better representation of the camber growth during storage, then there would have to be an additional source of deflection at release which would cause an offset between the predictions

and measurements throughout the life of the beam. This pattern was evident in the PCI prediction case shown in Table 6.15. A possible source of this offset may be due to early-age temperature gradients. However, it is more likely that the ultimate creep coefficient for the second set of multipliers was probably an underestimate for the U-beams.

In considering the sensitivity analysis using both sets of multipliers and all four prediction cases, differences between the predicted and measured cambers at release and erection are caused by the inability to precisely model the actual behavior of prestressed concrete beams in the field. Small differences in material properties, prestressing force, and the estimation of thermally induced movements can have a remarkable effect on the accuracy of predictions. In addition, errors in measurement techniques contribute to these differences. The proposed multipliers that were based on the time-step analysis and Eq. 6.24 for creep of the concrete provide a reasonable estimate of long-term behavior of prestressed high performance concrete U-beams with spans ranging from 35 to 42 meters.

CHAPTER 7. SUMMARY, CONCLUSIONS, AND RECOMMENDATIONS

7.1 SUMMARY

Twelve full-scale prestressed high performance concrete Texas Type U54 bridge beams with span lengths ranging from 35.55 to 41.25 meters were instrumented and monitored in the field. The instrumented U-beams were fabricated using 15.2 mm-diameter low-relaxation prestressing strands and concrete with design compressive strengths between 80.0 and 90.3 MPa. Time-dependent camber, deflection, strain at the center of gravity of the prestressing strands, and strain distributions at midspan were measured from transfer of the prestressing force until five months after completion of the composite deck. Internal beam temperatures at midspan were also measured during that time period, allowing for the measurement of temperature gradients over the beam depth. Monitoring of deformation behavior in the bridge will continue for several more years. Companion tests were performed to determine the time-dependent material properties of the high performance concrete used to fabricate the instrumented beams.

The measured time-dependent camber, deflection, and prestress losses at midspan were compared to results obtained using AASHTO and PCI prediction techniques. Predictions were also made using an analytical time-step method that was developed on a computer spreadsheet program by the author. The analytical time-step method used the measured time-dependent material properties for the beams. The analytical time-step method predicted the time-dependent camber, deflection, and prestress losses in the instrumented beams the most accurately.

A set of camber and deflection multipliers were developed based on the analytical time-step method and the measured prestress losses and material properties for the instrumented beams. The equations for these multipliers were well-suited for programming on a computer, although they could also be used for hand calculations.

A second set of camber and deflection multipliers were developed based on an alternative curve fit to the measured creep data for the U-beam specimens. Both sets of multipliers were used to perform a sensitivity analysis on the prediction of long-term camber and deflection behavior. The creep function, the modulus of elasticity at release, and prestressing force transferred to the beams were varied to determine how different combinations of these three variables affected long-term camber of the instrumented U-beams. The different predictions were compared to the measured camber and deflection responses for several representative beams.

7.2 CONCLUSIONS

The conclusions presented in this section are based on the field instrumentation procedures, the measured behavior of the beams, the results of the companion tests, and the results of the analytical techniques for predicting long-term behavior. Conclusions that specify quantities or expressions for time-dependent behavior should only be considered

valid for Texas Type U54 beams that are fabricated using a similar high performance concrete mix and that have span lengths in the range of 35 and 42 meters.

The following conclusions are based upon the results of the field instrumentation of the U-beams and composite deck:

1. Coordination of efforts between the researchers and the contractors was an essential aspect of this field instrumentation study. Lack of proper communication resulted in missed readings and damaged instrumentation. Fortunately, the overall experience was very good in this study and good coordination was generally achieved.
2. The tensioned piano wire camber and deflection measuring system worked well and allowed for very precise measurement. However, the steel ruler at midspan was susceptible to being disrupted during storage and during transportation of the beams. Since this system depended upon an initial reference measurement, disruption of the ruler was a critical problem. A more permanent means of attaching the ruler to the beam should be used in the future to avoid possible movement of the ruler.
3. The precise surveying system that was used for measuring camber and deflection of the beams after they were erected in the bridge worked well and had acceptable accuracy and repeatability. In addition, this system was an efficient method of measuring camber and deflection at the various stages of construction as the bridge was completed. A set of measurements for all twelve beams generally required one hour to complete.
4. The nylon cable ties did not adequately hold the strain gages that were placed in the cast-in-place deck in their intended positions. The various aspects of the deck casting operation, including pouring of the concrete over the gages, tended to move the deck gages with relative ease.
5. Measurement of surface strains using the Demec mechanical gages required the measurement of surface temperatures at the times of the readings. The lack of surface temperature data rendered the surface strain measurements relatively useless for long-term measurements.
6. The bonded electrical resistance strain gages (ERSGs) that were embedded in the beam provided quality data for an average of 150 days after release. ERSGs were not reliable measurement tools for long-term strain behavior in these field instrumented U-beams.
7. The embedded vibrating wire (VW) gages generally provided quality short and long-term strain data. Although VW gages were quite costly, they were very durable and required very little preparation and installation time. Several VW gages are providing valid strain measurements over 900 days after release.

The following conclusions are based on the measured behavior of the beams, the results of the companion tests, and the results of the analytical time-step method for predicting time-dependent camber, deflection, and prestress losses:

1. The AASHTO formula for modulus of elasticity should not be used for the prediction of long-term behavior for the high performance concrete U-beams in this study. Equation 5.2, which is given in Sec. 5.2.2, should be used to calculate the modulus of elasticity for the beam concrete in this study and for other concrete containing limestone aggregate and having compressive strengths greater than 60 MPa.
2. Creep strains were less than those predicted by expressions recommended by ACI Committee 209 for normal strength concrete. The prediction of creep deformation for beams made with the high performance concrete mix used in this study should be based on Eq. 5.3 in Sec. 5.2.3.
3. Shrinkage strains were less than those predicted by expressions recommended by ACI Committee 209 for normal strength concrete. The prediction of shrinkage strain for beams made with the high performance concrete mix used in this study should be based on Eq. 5.6 in Sec. 5.2.3.
4. Temperature gradients were nonlinear in the noncomposite U-beam section and were highly nonlinear in the composite U-beam section. The maximum temperature gradient observed over the depth of the composite U-beams between November of 1996 and March of 1997 was 12 °C.
5. Temperature gradients on sunny days can cause thermal movements of at least 12 mm in the noncomposite U-beams and at least 8 mm in the composite U-beams.
6. Prediction of midspan camber immediately after release was sensitive to the modulus of elasticity and prestressing force used in the calculations. This is illustrated in Sec. 6.5.2.
7. The assumption of four percent prestress losses before release due to shrinkage, relaxation, and an increase in strand temperature after stressing should be used as an estimation of prestress losses before release. In lieu of an exact analysis for elastic shortening, the initial elastic camber for U-beams with low-relaxation strands should be calculated using 0.88 as the ratio of prestressing force immediately after release to the initial force.
8. The AASHTO method for predicting prestress losses using design properties overestimated the measured prestress losses by an average of 8 percent. The AASHTO method should not be used for predicting prestress losses for high performance concrete U-beams similar to those in this study.
9. The analytical time-step method predicted the prestress losses for the U-beams with acceptable accuracy, overestimating the actual prestress losses by an average of only 1.5 percent. This is shown in Sec. 6.4.2.2.
10. The proposed multipliers for predicting camber and deflection based on Eq. 6.24 for creep, which are developed in Sec. 6.5.1, predicted the measured camber and deflection of the U-beams with reasonable accuracy.
11. The time-dependent midspan cambers (or deflections) of the U-beams predicted using the proposed multipliers were sensitive to the creep coefficient function, the

- modulus of elasticity at release, and the initial prestressing force transferred to the beams. This is shown in Sec. 6.5.2.
12. The long-term deflection of the U-beams due to the superimposed deck load is projected to be very small because the composite section was nearly three times as stiff as the noncomposite section and because a majority of the ultimate creep deformation occurred during storage.
 13. Uneven cooling of the beam cross section, which occurred after the forms were stripped, may cause a thermally induced component of deflection in the beam that becomes evident just after release. Based on limited temperature data during casting, the magnitude of this deflection may be as large as 12 mm.
 14. The proper correction for camber or deflection induced by temperature gradients may be in reference to a nonuniform temperature gradient in the beam before the forms are stripped rather than a uniform temperature gradient of 20 °C, which was used for the beams in this study.
 15. Strain measurements at release in the bottom flange of the U-beams may have been artificially high due to restraint offered by the prestressing bed to the beams as they tried to shorten due to cooling and shrinkage. Upon release, the restraint would be removed and an additional compressive strain would be measured by the strain gages.

7.3 RECOMMENDATIONS

1. The precise surveying system for measuring beam camber and deflection after the beams were erected in the bridge, which is described in Sec. 3.3.5, was very efficient and should be used in future projects. It should also be considered for use while the beams are in storage.
2. The vibrating wire strain gages should be used more extensively in field instrumentation projects because of their durability, ease of preparation and installation, and quality of long-term results. The ability to obtain long-term strain data is essential for determining prestress loss behavior in high performance concrete bridge beams.
3. The proposed multipliers (based on Eq. 6.24) should be used to estimate camber and deflection for long-span U-beams made with high strength concrete mixes similar to the one used for the U-beams in this study.
4. Creep and shrinkage tests should be performed on other high performance concrete beam mixes to gain further knowledge of the deformation properties of concretes with very high strength that are used in prestressing applications.

REFERENCES

1. Ralls, M. L., Ybanez, L., and Panak, J. J., "The New Texas U-Beam Bridges: An Aesthetic and Economical Design Solution," *PCI Journal*, Vol. 38, No. 5, Sept.–Oct. 1993, pp. 20-29.
2. Peterman, M. B., and Carrasquillo, R. L., "Production of High Strength Concrete," Research Report 315-1F, Center for Transportation Research, The University of Texas at Austin, October 1983.
3. Russell, B. W., "Impact of High Strength Concrete on the Design and Construction of Pretensioned Girder Bridges," *PCI Journal*, Vol. 39, No. 4, July–Aug. 1994, pp. 76-89.
4. Goodspeed, C. H., Vanikar, S., and Cook, R. A., "High-Performance Concrete Defined for Highway Structures," *Concrete International*, Vol. 18, No. 2, February 1996, pp. 62–67.
5. Cetin, A., and Carrasquillo, R. L., "Effect of Accelerated Heat Curing and Mix Characteristics on the Heat Development and Mechanical Properties of High Performance Concrete," Research Report 580-4 (Preliminary Review Copy), Center for Transportation Research, The University of Texas at Austin, December 1995.
6. Barrios, A. O., Burns, N. H., and Carrasquillo, R. L., "Behavior of High Strength Concrete Pretensioned Girders During Transfer of Prestressing Forces," Research Report 580-2 (Preliminary Review Copy), Center for Transportation Research, The University of Texas at Austin, May 1994.
7. Carlton, M. P. and Carrasquillo, R. L., "Quality Control of High Performance Concrete for Highway Bridges," Research Report 580-3 (Preliminary Review Copy), Center for Transportation Research, The University of Texas at Austin, June 1995.
8. Farrington, E. W., Burns, N. H., and Carrasquillo, R. L., "Creep and Shrinkage of High Performance Concrete," Research Report 580-5 (Preliminary Review Copy), Center for Transportation Research, The University of Texas at Austin, February 1996.
9. Durning, T. A., and Rear, K.B., "Braker Lane Bridge: High Strength Concrete in Prestressed Bridge Girders," *PCI Journal*, Vol. 83, No. 3, May–June 1993, pp. 46-51.
10. Castrodale, R. W., Kreger, M. E., and Burns, N. H., "A Study of Pretensioned High Strength Concrete Girders in Composite Highway Bridges — Design Considerations," Research Report 381-4F, Center for Transportation Research, The University of Texas at Austin, January 1988.

11. Castrodale, R. W., Kreger, M. E., and Burns, N. H., "A Study of Pretensioned High Strength Concrete Girders in Composite Highway Bridges — Laboratory Tests," Research Report 381-3, Center for Transportation Research, The University of Texas at Austin, January 1988.
12. Carrasquillo, P. M. and Carrasquillo, R. L., "Guidelines for Use of High Strength Concrete in Texas Highways," Research Report 367-1F, Center for Transportation Research, The University of Texas at Austin, August 1986.
13. American Concrete Institute Committee 363, "State-of-the-Art Report on High Strength Concrete," *ACI Journal, Proceedings*, Vol. 81, No. 4, July–Aug. 1984, pp. 364–411.
14. Lin, T. Y., and Burns, N. H., *Design of Prestressed Concrete Structures*, Third Edition, John Wiley and Sons, New York, New York, 1981, 646 pp.
15. Carrasquillo, R. L., Nilson, A. H., and Slate, F. O., "Properties of High Strength Concrete Subject to Short-Term Loads," *ACI Journal, Proceedings*, Vol. 78, No. 3, May–June 1981, pp. 171–178.
16. American Association of State Highway and Transportation Officials, *Standard Specifications for Highway Bridges*, Fifteenth Edition, Washington, D.C., 1992.
17. American Concrete Institute, *Building Code Requirements for Structural Concrete (ACI 318-95) and Commentary (ACI 318R-95)*, Detroit, 369 pp.
18. Libby, J. R., *Modern Prestressed Concrete: Design Principles and Construction Methods*, Fourth Edition, Van Nostrand Reinhold, New York, New York, 871 pp.
19. American Concrete Institute Committee 209, "Prediction of Creep, Shrinkage, and Temperature Effects in Concrete Structures," *Designing for Creep and Shrinkage in Concrete Structures*, SP-76, American Concrete Institute, Detroit, 1982, pp. 193–300.
20. Ngab, A. S., Nilson, A. H., and Slate, F. O., "Shrinkage and Creep of High Strength Concrete," *ACI Journal, Proceedings*, Vol. 78, No. 4, July–Aug. 1981, pp. 255–261.
21. American Concrete Institute Committee 517, "Low Pressure Steam Curing," *ACI Report Title No. 60-48*, American Concrete Institute, Detroit, 1963.
22. Hanson, J. A., "Prestress Loss as Affected by Type of Curing," *PCI Journal*, Vol. 9, No. 2, April 1964, pp. 69–93.
23. Swamy, R. N., and Anand, K. L., "Shrinkage and Creep Properties of High Strength Structural Concrete," *Civil Engineering and Public Works Review (London)*, Vol. 68, No. 80, October 1973, pp. 859–868.

24. Arrelaga, J. A., "Instrumentation Systems for Post-Tensioned Segmental Box Girder Bridges," unpublished master's thesis, The University of Texas at Austin, Dec. 1991.
25. Russell, H. G., *Implementation Program on High Performance Concrete-Guidelines for Instrumentation of Bridges*, Report to FHWA, February 1996.
26. Kelly, D. J., Bradberry, T. E., and Breen, J. E., "Time Dependent Deflections of Pretensioned Beams," Research Report 381-1, Center for Transportation Research, The University of Texas at Austin, August 1987.
27. Precast/Prestressed Concrete Institute, *PCI Design Handbook: Precast and Prestressed Concrete*, Fourth Edition, Chicago, 1992.
28. Martin, L. D., "A Rational Method for Estimating Camber and Deflection of Precast Prestressed Concrete Members," *PCI Journal*, Vol. 22, No. 1, Jan.–Feb. 1977, pp. 100–108.
29. Suttikan, C., "A Generalized Solution for Time-Dependent Response and Strength of Noncomposite and Composite Prestressed Concrete Beams," unpublished doctoral dissertation, The University of Texas at Austin, Aug. 1978.
30. Rao, V. J., and Dilger, W. H., "Time-Dependent Deflections of Composite Prestressed Concrete Beams," *Deflection of Concrete Structures*, SP-43, American Concrete Institute, Detroit, 1974.
31. Corley, W. G., Sozen, M. A., and Seiss, C. P., "Time-Dependent Deflections of Prestressed Concrete Beams," *Bulletin No. 307*, Highway Research Board, Washington, D.C., 1961.
32. Furr, H. L., and Sinno, R., "Creep in Prestressed Lightweight Concrete," Research Report 69-2, Study 2-5-63-69, Texas Transportation Institute, Texas A&M University System, College Station, Texas, Oct. 1967.
33. Furr, H. L., Sinno, R., and Ingram L.L., "Prestress Loss and Creep Camber in a Highway Bridge with Reinforced Concrete Slab on Pretensioned Prestressed Concrete Beams," Research Report 69-3 (Final), Study 2-5-63-69, Texas Transportation Institute, Texas A&M University System, College Station, Texas, Oct. 1968.
34. Branson, D. E., Meyers, B. L., and Kripanarayanan, K. M., "Loss of Prestress, Camber and Deflection of Noncomposite and Composite Structures Using Different Weight Concretes," *Iowa Highway Commission Final Report, No. 70-6*, Aug. 1970.
35. Gamble, W. L., "Field Investigation of a Continuous Composite Prestressed I-Beam Highway Bridge Located in Jefferson County, Illinois," *Structural Research Series*

- No. 360, Civil Engineering Studies, University of Illinois at Urbana-Champaign, Urbana, June 1970.
36. Houseshell, D. M., Anderson, T. C., and Gamble, W. L., "Field Investigation of a Prestressed Concrete Highway Bridge Located in Douglas County, Illinois," *Structural Research Series No. 375*, Civil Engineering Studies, University of Illinois at Urbana-Champaign, Urbana, Feb. 1972.
 37. Gamble, W. L., "Long-Term Behavior of a Prestressed I-Girder Highway Bridge in Champaign County, Illinois," *Structural Research Series No. 470*, Civil Engineering Studies, University of Illinois at Urbana-Champaign, Urbana, Dec. 1979.
 38. Zia, P., Preston, H. K., Scott, N. L., and Workman, E. B. "Estimating Prestress Losses," *Concrete International*, Vol. 1, No. 6, June 1979, pp. 32–38.
 39. PCI Committee on Prestress Losses, "Recommendations for Estimating Prestress Losses," *PCI Journal*, Vol. 20, No. 4, July–Aug. 1975, pp. 43–75.
 40. Subcommittee 5, ACI Committee 435, "Deflections of Prestressed Concrete Members," *ACI Journal, Proceedings*, Vol. 60, No. 12, Dec. 1963, pp. 1697–1728.
 41. Tadros, M. K., Ghali, A., and Dilger, W. H., "Time-Dependent Prestress Loss and Deflection in Prestressed Concrete Members," *PCI Journal*, Vol. 20, No. 3, May–June 1975, pp. 86–98.
 42. Tadros, M. K., Ghali, A., and Meyer, A. W., "Prestress Loss and Deflection of Prestressed Concrete Members," *PCI Journal*, Vol. 30, No. 1, Jan.–Feb. 1985, pp. 114–141.
 43. Branson, D. E., and Kripanarayanan, K. M., "Loss of Prestress, Camber and Deflection of Non-composite and Composite Prestressed Concrete Structures," *PCI Journal*, Vol. 16, No. 5, Sept.–Oct. 1971, pp. 22–52.
 44. Sinno, R., and Furr, H. L., "Computer Program for Predicting Prestress Loss and Camber," *PCI Journal*, Vol. 17, No. 5, Sept.–Oct. 1972.
 45. Hernandez, H. D., and Gamble, W. L., "Time-dependent Prestress Losses in Pretensioned Concrete Construction," *Structural Research Series N. 417*, Civil Engineering Studies, University of Illinois at Urbana-Champaign, Urbana, 1975.
 46. Grouni, H. N., "Prestressed Concrete: A Simplified Method for Loss Computation," *ACI Journal, Proceedings*, Vol. 70, No. 2, Feb. 1973, pp. 15–29.
 47. Huang, T., "Study of Prestress Losses Conducted by Lehigh University," *PCI Journal*, Vol. 27, No. 5, Sept.–Oct. 1982, pp. 48–61.

48. Ingram, L. L., and Butler, H. D., "Prestressed Concrete Bridge Girder Design Program," Research Report 149-1 (Final), Texas Transportation Institute, Texas A&M University System, College Station, Texas, Nov. 1970.
49. Texas State Department of Highways and Public Transportation Bridge Division, *Prestressed Concrete Beam Design/Analysis Program User Guide, PSTRS14*, March 1990.
50. American Society for Testing and Materials, "Standard Test Method for Static Modulus of Elasticity and Poisson's Ratio of Concrete in Compression," ASTM C469-87, Philadelphia, 1987.
51. American Society for Testing and Materials, "Standard Test Method for Compressive Strength of Cylindrical Concrete Specimens," ASTM C-39-86, Philadelphia, 1986.
52. American Society for Testing and Materials, "Standard Test Method for Creep of Concrete in Compression," ASTM C512-87, Philadelphia, 1987.
53. Priestly, M. N. J., "Design of Concrete Bridges for Temperature Gradients," *ACI Journal*, Proceedings, V. 75, No. 5, May 1978, pp. 209–217.
54. Potgieter, I. C., and Gamble, W. L., "Nonlinear Temperature Distributions in Bridges at Different Locations in the United States," *PCI Journal*, V. 34, No. 4, July–August 1989, pp. 80–103.
55. Radolli, M., and Green, R., "Thermal Stresses in Concrete Bridge Superstructures Under Summer Conditions," *Transportation Research Record*, No. 547, Transportation Research Board, 1975, pp. 23–36.
56. Committee on Prestress Losses, "Recommendations for Estimating Prestress Losses," *PCI Journal*, Vol. 20, No. 4, July–Aug. 1975, pp. 43–75.

APPENDIX A:
DEBONDING DETAILS

Table A1 Debonding details for instrumented beams in the southbound main lanes bridge

Beam	Row	Total ¹	Debonded Strands and Length from End of Beam ² (m)								
			0.91	1.83	2.74	3.66	4.57	5.49	6.40	8.23	9.14
S14	1	20	7,9	3,5	10,12	8	---	6	4	2	---
	2	4	3,5	---	---	---	---	---	---	---	---
S15	1	20	7,9	3,5	10,12	8	---	6	4	2	---
	2	4	3,5	---	---	---	---	---	---	---	---
S16	1	20	9	3,5,7	8,10,12	4,6	2	---	---	---	---
	2	6	3,5,7	---	---	---	---	---	---	---	---
S24	1	20	9	3,5,7	8,10,12	4,6	2	---	---	---	---
	2	6	3,5,7	---	---	---	---	---	---	---	---
S25	1	20	9	3,5,7	8,10,12	4,6	2	---	---	---	---
	2	6	3,5,7	---	---	---	---	---	---	---	---
S26	1	20	---	7,9	3,5	12	10	8	6	4	2
	2	14	4,7,9,11,13	3,5	---	---	---	---	---	---	---

Notes:

1. Total number of strands debonded in each row at each end of the beam.
2. Numbers correspond to the strand designations defined in Fig. A.1. Debonded strands appear in the column that corresponds to the length from the end of the beam that the debonding was applied.

Table A2 Debonding details for instrumented beams in the northbound main lanes bridge

Beam	Row	Total ¹	Debonded Strands and Length from End of Beam ² (m)								
			0.91	1.83	2.74	3.66	4.57	5.49	6.40	8.23	9.14
N21	1	20	---	7,9	3,5	12	10	8	6	4	2
	2	14	4,7,9,11,13	3,5	---	---	---	---	---	---	---
N22	1	20	9	3,5,7	8,10,12	4,6	2	---	---	---	---
	2	6	3,5,7	---	---	---	---	---	---	---	---
N23	1	20	9	3,5,7	8,10,12	4,6	2	---	---	---	---
	2	6	3,5,7	---	---	---	---	---	---	---	---
N31	1	20	---	3,5,7	9,12	8,10	6	4	2	---	---
	2	12	5,7,9,11,13	3	---	---	---	---	---	---	---
N32	1	20	7,9	3,5	10,12	8	---	6	4	2	---
	2	4	3,5	---	---	---	---	---	---	---	---
N33	1	20	7,9	3,5	10,12	8	---	6	4	2	---
	2	4	3,5	---	---	---	---	---	---	---	---

Notes:

- Total number of strands debonded in each row at each end of the beam.
- Numbers correspond to the strand designations defined in Fig. A.1. Debonded strands appear in the column that corresponds to the length from the end of the beam that the debonding was applied.

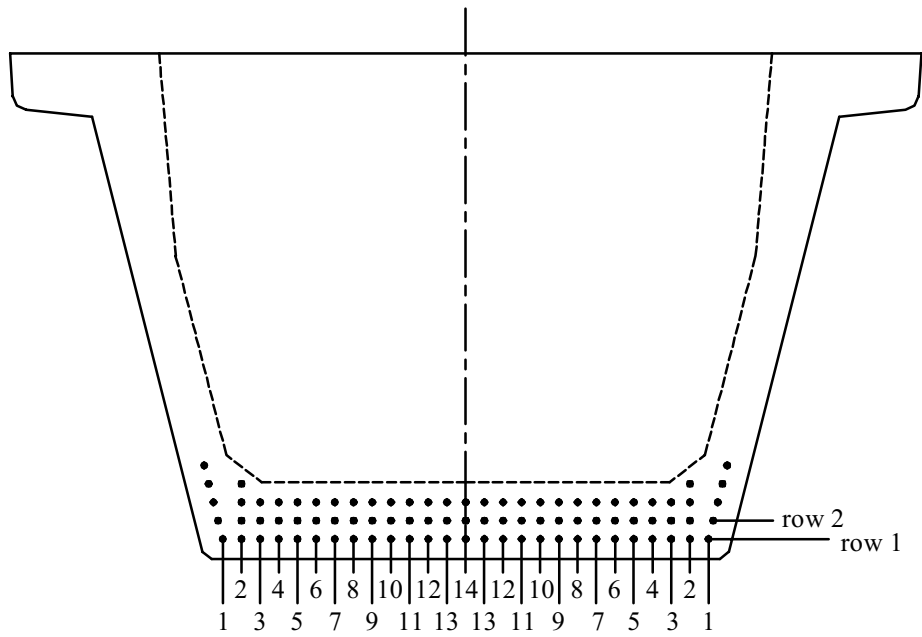


Figure A1 Strand designation for debonding patterns at beam ends